Control and Optimization of a DC-DC Converter for Thermoelectric Generators

vorgelegt von

M.Sc.
Jan Hendrik Hermann Carstens
geb. in Heide (Holstein)

von der Fakultät IV-Elektrotechnik und Informatik
der Technischen Universität Berlin
zur Erlangung des akademischen Grades

Doktor der Ingenieurwissenschaften
-Dr.-Ing.-

genehmigte Dissertation

Promotionsausschuss:

Vorsitzender: Prof. Dr.-Ing. Reinhold Orglmeister

Gutachter: Prof. Dr.-Ing. Clemens Gühmann
Gutachter: Prof. Dr.-Ing. Hans-Christian Reuss
Gutachter: Dr. Thomas Schauer

Tag der wissenschaftlichen Aussprache: 18. März 2016

Berlin, 2016

Abstract

The internal combustion engine is of fundamental importance for individual mobility. The demand for internal combustion engines increases in relation to population growth and fuel consumption. At present, alternative drive concepts using sustainable energies only play a secondary role in mobility. Consequently, the governments enact laws to determine more restrictive emission limit values, thereby aiming to reduce toxic emissions and fossil fuel consumption. To reach those limit values, the efficiency of the internal combustion engine must be increased.

In contrast to the combustion process itself, the thermal loss of the waste gas from the internal combustion engine has a high potential to increase the efficiency and to reduce toxic emissions.

Thermoelectric generators can be used to directly convert thermal energy into electrical energy. For that reason, thermoelectric generators are a suitable technology to recover thermal losses. The recovered energy can be used to relieve the alternator of the on-board power supply. However, to link the energy from thermoelectric generators to the on-board power supply, the voltage potential must be matched. This can be realized with DC-DC converters.

In order to avoid unnecessary losses of energy conversion, different DC-DC converter topologies need to be analyzed. In this thesis, a loss model is presented, which enables to analyze and evaluate the losses of the electrical components of DC-DC converters. An experimental prototype was developed and used to verify this loss model.

Changes of the operation points of an internal combustion engine present a challenge for the integration of thermoelectric generators with DC-DC converters. The voltage potential of thermoelectric generators depends on the engine's operation point. To compensate for the changes in the voltage potential of the thermoelectric generators, DC-DC converters must be controlled.

Furthermore, the aim of the controller is to track the maximum power of a thermoelectric generator and to link the power to the on-board power supply. Therefore, a maximum-power-point-tracking controller with a cascade controller was designed. The analytically designed controller was verified by an experiment.

Finally, the wiring of separated thermoelectric modules of a generator was analyzed to increase the efficiency of the whole thermoelectric generator. Based on this optimization, the potential for saving fuel and CO_2 emissions of an internal combustion engine using thermoelectric generators is simulated.

Kurzfassung

Für die individuelle Mobilität hat die Verbrennungskraftmaschine eine fundamentale Bedeutung. Mit steigendem Bevölkerungszuwachs steigt der Bedarf an Verbrennungskraftmaschinen, sowie der Bedarf an fossilen Brennstoffen. Alternative Antriebskonzepte auf Basis nachhaltiger Energien haben aktuell noch eine untergeordnete Wichtigkeit für die Mobilität. Aus diesem Grund werden immer restriktivere Emissionsgrenzwerte erlassen um den Verbrauch von fossilen Brennstoffen und toxische Emissionen zu reduzieren. Um diese Grenzwerte einzuhalten, steht die Maximierung des Wirkungsgrads der Verbrennungskraftmaschine verstärkt im Fokus der Entwicklung und Forschung.

Im Gegensatz zu dem eigentlichen Verbrennungsprozess von Verbrennungskraftmaschinen, bieten die thermischen Verluste des Abgases ein hohes Potential den Wirkungsgrad zu steigern und somit die Emissionen zu senken.

Mittels thermoelektrischer Generatoren kann thermische Energie direkt in elektrische Energie umgewandelt werden. Aus diesem Grund stellt diese Technologie ein hohes Potential dar die thermischen Verluste der Verbrennungskraftmaschinen zu rekuperieren. Die zurückgewonnene Energie kann in das Bordnetz eingespeist werden um die Lichtmaschine zu entlasten. Um jedoch eine elektrische Potentialanpassung zwischen dem thermoelektrischen Generator und dem Bordnetz vorzunehmen, bedarf es DC-DC Wandlern.

Um unnötige Verluste bei der Einspeisung zu vermeiden, muss untersucht werden, welche unterschiedlichen Topologien von DC-DC Wandlern sich je nach Anwendungsfall eignen. Aus diesem Grund wird in dieser Arbeit ein Verlustmodell präsentiert, welches es ermöglicht, die Verluste einzelner Bauteilkomponenten zu analysieren und zu bewerten. Zur Verifikation dieses Modells wird ein Prototyp entwickelt und der Wirkungsgrad vermessen.

Eine Herausforderung stellt der Wechsel der Betriebspunkte bei einer Verbrennungskraftmaschine dar. Ein thermischer Betriebspunktwechsel wirkt sich auf die Leerlaufspannung von den thermoelektrischen Generatoren aus. Um die Spannungsschwankungen zu kompensieren, wird eine Regelung der DC-DC Wandler entwickelt.

Das primäre Ziel des Regelungskonzeptes ist es, die maximale Leistung vom thermoelektrischen Generator in das Bordnetz zu speisen. Hierzu wird eine Maximum-Power-Point-Tracking Regelung mit einer Kaskadenstruktur entwickelt. Die analytisch ausgelegte Regelung wird durch Experimente verifiziert.

Zum Abschluss dieser Arbeit wird analysiert, wie einzelne Module eines thermoelektrischen Generators mit DC-DC Wandler verschaltet werden müssen um einen optimalen Gesamtwirkungsgrad zu erzielen. Mit dieser Optimierung wird an einem Beispiel das Einsparpotential von Kraftstoff und CO_2 Emissionen an einer Verbrennungskraftmaschine, durch die Nutzung thermoelektrischer Generatoren, simuliert.

Contents

1. Introduction

Mobility is fundamental to our society and has become almost indispensable from economy and social life. For more than one hundred years, the primary drive concept of vehicles has been based on the internal combustion engine (ICE). Conventional ICEs convert chemical energy, stored in fossil fuel, into mechanical energy. In the combustion process toxic emissions and carbon dioxide (CO_2) are released. In recent decades, awareness of sustainability and the protection of the environment have increased significantly. This is reflected in the legal regulations on the limit values for emissions from ICEs. In particular, many governments have enacted additional laws to continuously reduce the CO_2 emissions over the next years. [91]

Currently, commercial availability of alternative drive systems that use electrical energy or hydrogen as primary power source is increasing in personal motor transport. However, due to the current high costs of required technologies and deficits of the infrastructure, they are not an alternative option in the near future.

During the combustion process of the ICE, more than 50 % of the potential energy stored in fossil fuel is converted into heat. The physical efficiency of the combustion process has already reached the optimum. However, the recovery of the waste heat from ICE bears the potential to increase the efficiency significantly. The exhaust gas in particular has a high temperature potential and therefore is suitable for thermal recuperation.

It is possible to recover this waste heat by converting thermal energy into electrical energy with thermoelectric generators (TEGs). In contrast to thermodynamic cycle processes, TEGs allow direct conversion of thermal energy into electrical energy. TEGs are based on semiconductors, and a temperature difference across the TEG causes a heat current. Finally, electric energy is generated in the semiconductors. This electric energy is linked to the on-board power supply through a DC-DC converter. Therefore, the necessary electrical output energy and accordingly the mechanical driving energy of the belt-driven alternator decreases. Consequently, the fuel consumption of the ICE increases.

Thermoelectricity has been known for over 100 years. However, due to the low efficiency of thermoelectric materials, this technology had been developed and explored further only marginal.

In 1956, Joffee [58] published a relevant article about thermoelectric materials and their characteristics. In reference to this article, Tserng wrote the following in 1968 [169]:

> "The enthusiastic tone of this publicity has led many people to believe that simple thermoelectric energy generation would soon begin competing with conventional systems on

an economic basis. A realistic survey of the present state of direct conversion technology, however, indicates that this day is not yet in sight."

More than 50 years later, thermoelectric energy still does not compete with conventional energy systems, but this technology is in the focus of research aiming to increase environmental sustainability of conventional energy.
In recent decades, research projects and pre-developments in the field of integration from TEGs and optimization of thermoelectric materials were performed with the aim to maximize the conversion efficiency from thermal into electrical energy. The simple design of the TEG is an advantage as it can be adapted to the target system by geometric and material variations.
The DC-DC converter is an important factor for the thermoelectric recovery since the power efficiency map and the control structure influence the efficiency of the recovered energy from the TEG.
In the recent years, different control methods and concepts for DC-DC converters used for TEGs have been presented. However, the designs of the controller and the DC-DC converter are mainly based on well-defined TEGs but are not generalized for the parameter variations of the TEG, which are caused by temperature changes.
Depending on the DC-DC converter circuit, the control structure and in particular the integration of TEGs in the electrical system can significantly influence the overall efficiency of the functional chain from the TEG via DC-DC converter to the on-board power supply.
In classical low-voltage on-board power supplies, the alternator is the only energy source. The recovered thermoelectric power of the TEG must be prioritized with an electrical energy management system in the on-board power supply to maximize the relief of the alternator and consequently to reduce CO_2 emission.
The aim of this thesis is to analyze the electrical functional chain from the TEG to the on-board power supply, and to evaluate as well as to optimize the efficiency with generalized boundary conditions. The focus of this work is on the evaluation of DC-DC converters for TEGs and to design a control structure for the converter. In particular, DC-DC converter models are necessary in order to analyze the electrical loss and the dynamic of the converter. These generalized models can be applied to compare different converter topologies and estimate the dimensioned parameters for the power efficiency. Based on this approach, a control design and the electrical wiring of the TEG can be defined and optimized, which is necessary for the integration of TEGs with the DC-DC converters in the on-board power supply.
Finally, a simulation is used to estimate the CO_2 reduction potential of an ICE with a TEG. The electrical components and the alternator are measured and modeled for the simulation of the on-board power supply.

The used measurement data and defined boundary conditions refer to the research project Thermoelectric Generators 2020 (03X3553E), which was supported by the German Federal Ministry of Education and Research (BMBF).

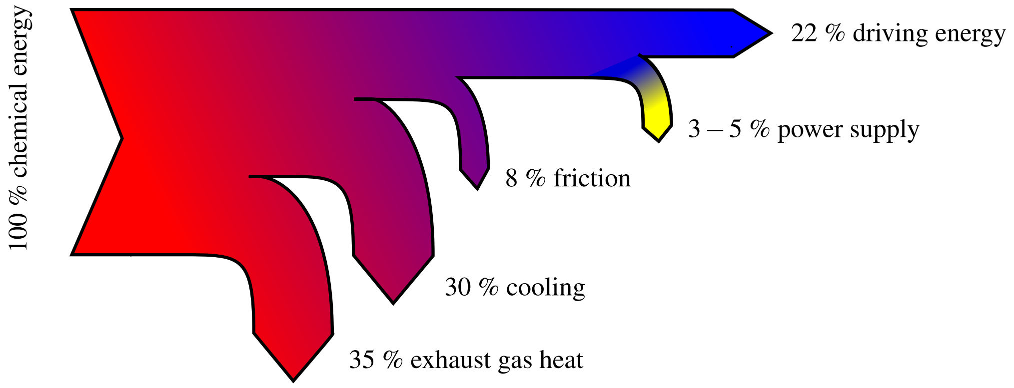

Figure 1.1.: Sankey diagram of the efficiency for a 1.6 L Otto engine in a new European driving cycle [123].

1.1. Literature Review

In this section, a review of literature is presented. At first, the basic principle of exhaust gas recovery is reviewed. After that, the current state of the art of thermoelectric applications is presented. In addition, the state of the art of DC-DC converters for thermoelectric devices is summarized. This includes the control of the maximum power point of the TEG and the integration in an on-board power supply. Finally, the modeling of DC-DC converters is presented and the literature review is summarized. It should be noted that the review is focused on ICEs for automobiles.

1.1.1. Waste Heat Recovery

Over 50 % of the potential energy of the fossil fuel is converted into thermal power during the combustion process in the ICE (see Figure 1.1). The most significant loss of energy during the combustion process is the exhaust gas heat [160].
The research and development are currently focusing on developing methods to recover the waste heat from the ICE in order to save fuel and reduce CO_2 emissions. Table 1.1 provides an overview of the most essential heat recovery methods. In the following, a brief summary of different concepts is presented. A detailed overview of these concepts is presented in [83, 147, 155].

direct mechanical conversion	direct thermal conversion	indirect mechanical conversion	direct electrical conversion
turbocharger turbocompound turbogenerator	absorption chiller adsorption chiller heat exchanger	Clausius-Rankine cycle	thermoelectric

Table 1.1.: Overview of the most popular heat recovery methods.

Turbocharger

The most popular heat recovery method is the turbocharger, which uses the waste gas mass flow to drive the fresh air compressor and consequently to increase the boost pressure of the ICE. The turbocharger can save 15 % - 20 % of fuel [130, 176]. The turbocharger is the most effective method to reduce the fuel consumption of an ICE. However, the turbocharger is mechanically directly coupled to the exhaust system and is controlled through the geometry of the turbine. Concepts with variable geometric turbines or two-stack turbocharger are currently being developed to increase the engine pressure at low engine speeds or to charge the engine with a controlled pre-pressure and an injection outside the cylinder. [147]

In [47], a turbocharger which uses the Rankine steam cycle to decouple the mechanical systems is presented. The advantage of this system is the possibility to control the turbocharger by the Clausius-Rankine steam cycle. The result is a better performance of the turbocharger for the whole speed of the engine with an increased fuel economy by up to 7 % at a 1.6 L Diesel engine.

Turbocompound and Turbogenerator

Another concept which uses the mass flow to drive a turbine is the turbocompound engine. The drive torque of the turbine is transferred to the drive shaft of the ICE via a gearbox. Overall, in this application, the synchronization between the turbine and the engine speed is difficult to achieve [180]. An alternative is to use the drive torque for an alternator [55]. This application, known as a turbogenerator, simplifies the mechanical construction. The drawback of the turbocompound and turbogenerator is the package size and the weight up to 100 kg [177]. With these systems, the fuel economy is increased by up to 6 % at a heavy duty Diesel engines [180, 184]. In [88], a fuel economy improvement by nearly 5 % is estimated through simulations for the new European driving cycle (NEDC) with an 1.6 L Otto engine.

Heat Exchanger

Heat exchangers are important devices for thermal management. The application field includes cooling of the exhaust gas for the exhaust gas recirculation or heating of the engine oil. The heating of oil or mechanic components at the starting phase reduces the fraction loss. Consequently, a fuel economy increase by up to 1.5 % is expected. Additionally, thermal energy can be stored and used explicitly at the starting phase by using a boiler. [54, 125]

However, especially at Diesel engines, pre-heating the intake air can result in a reduction of the emissions [59, 125].

Absorption Chiller

The principle of the absorption system is different to vapor compression refrigeration since it uses thermal energy instead of electrical energy. An absorption chiller can utilize the waste heat to absorb the heat from cooling. In [97], the vapor compression refrigeration is substituted by an

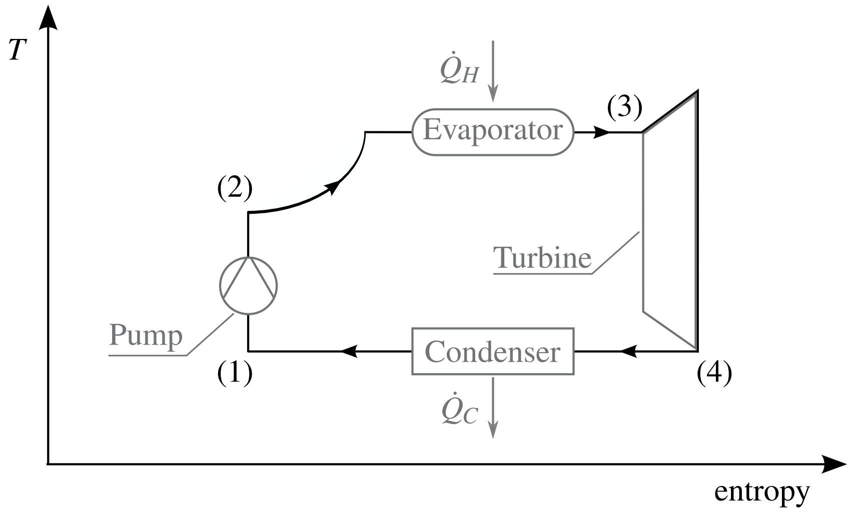

Figure 1.2.: A schematic diagramm of CRC with the heat current $\dot{Q}_H$ of the waste heat and $\dot{Q}_C$ of the cold side in a qualitative relation to the temperature T and entropy [38].

absorption chiller. For steady-state operation points of the ICE, the fuel consumption is reduced between 6 % and 15 %, in relation to a ICE which supply a vapor compression refrigeration.

Adsorption Chiller

In contrast to the absorption, the adsorption chiller uses solid materials for heat exchange. The adsorption chiller is unaffected by acceleration, vibration, and has a compact design [83]. However, adsorption chillers are not commonly used in automobiles because their thermal capacity is too low and the heat transfer is slower than that of an absorption chiller. Hence, this disadvantage depends on the material used for the sorption. For this reason, new materials are currently being explored. [1]

More details of absorption and adsorption concepts are presented in [83, 155].

Six-Stroke Engine

The concept of the six-stroke engine is based on the idea to use a four-stroke cycle principle with two additional cycles. After the exhaust stroke of the four-stroke cycle is finished, water is injected into the cylinder. The injection of the water receives energy from the compressed exhaust gas and cylinder wall heat. Thus, the liquid evaporates and the steam expands. This expansion is an additional power stroke. Finally, the gas is ejected during the last cycle. In [32], an additional mean effective pressure between 0.5 bar and 2.5 bar is calculated for an ICE with 0.5 L cylinder volume. It is remarkable that many patents utilize the six-stroke cycle concept but the scientific articles on this subject are limited. [32, 147]

Clausius-Rankine Cycle

The Clausius-Rankine cycle (CRC) is a steam cycle, which consists of a turbine, a pump, a heat exchanger (evaporator), and a condenser (see Figure 1.2). The CRC is a closed system with a

circulating working fluid. The function of the CRC can be simply illustrated using an ideal thermodynamic cycle with four steps: (1) - (2) the pump compresses the fluid and transfers it to the evaporator (isentropic process); (2) - (3) the fluid evaporates and the exhaust heat is transferred to the vapor (isobaric process); (3) - (4) the steam expands though the turbine - which is coupled with an alternator - and cools down (isentropic process); (4) - (1) the liquid is cooled and condensed (isobaric process).
The working fluid of the CRC is an important factor for the efficiency value of the heat recovery of the ICE. To evaporate fluid, high temperatures are necessary. Water in particular has a high evaporation temperature in contrast to organic fluids with high molecular mass. The exhaust gas can reach temperatures up to 1000 °C, but in the driver cycle the mean temperature is significantly lower [15]. Alternative organic fluids have to be stable, non-fouling, non-corrosive, non-toxic, and non-inflammable. An overview of the characteristics and potential fluids is presented in [19]. Alternatives to water are isentropic fluids.
The advantage of the CRC is the significantly lower exhaust gas back pressure by means of the heat exchanger such as a turbine. The back pressure has a feedback on the combustion process and it can increase the fuel consumption. Additionally, CRCs have a high performance per kilogram. The performance of a commercial CRC is up to 350 $\mathrm{W\,kg^{-1}}$. [38]
In [38], a detailed analysis of the efficiency of the CRC for a 2.6 L Otto engine is presented. The results show that the efficiency significantly depends on the working fluid, the evaporating pressure of the CRC, and the operation point from the ICE. The efficiency of the CRC is below 4 % if it uses water as the fluid. With optimized heat exchangers, evaporator, and fluids, the efficiency increases up to nearly 16 %. It should be noted that this analysis excluded the heat exchanger loss and the power loss to drive the alternator. The efficiency of the CRC to convert thermal energy into mechanic energy lies between 2.17 % and 15.94 % for different operation points of the ICE. [38]
Similar values are presented in the review of CRCs for an ICE by Sprouse and Depcik [158]. An increase of the ICE's efficiency by up to 20 % is possible for simulated and optimized CRC processes. However, the efficiency of a realistic implementation is expected to be below 10 %. [158]
Finally, the mechanic power of the CRC can be used to supply the alternator. Legros et al. [88] present results of a fuel economy simulation of the CRC for the NEDC and the worldwide harmonized light vehicles test cycle (WLTC). The fuel economy is estimated to increase by 3 % for the NEDC and nearly 4.5 % for the WLTC at a 1.6 L Otto engine. An alternator efficiency of 90 % was selected for the simulations. However, commercial alternators have significantly lower efficiencies [140].

Thermoelectrics

Thermoelectrics is the direct conversion of thermal energy into electric energy. A thermoelectric element is an n- and p-doted semiconductor with an electric connection. A temperature gradient across the material causes a thermal force. This force results in a diffusion of electrons and holes in the bulk material. Finally, a voltage potential can be measured at the end of the n- and p-doted semiconductor. This phenomenon is called the Seebeck effect. By combining thermoelectric elements (TEs) and connecting them in series, a higher voltage can be reached. The resulting device is called thermoelectric module (TEM). The connection of these modules to an application is called thermoelectric generator (TEG).

The thermoelectric material is an important aspect of a TEG because the conversion of thermal energy to electric energy depends on the thermoelectric characteristics: Seebeck coefficient, specific resistance, and thermal conductance. The most widely used commercial material for temperatures below 250 °C is Bi_2Te_3 and above up 900 °C is PbTe. Thermoelectrics has the advantage of a simple construction without mechanical components, which is simple to scale for a desired temperature range and thermal performance. Furthermore, TEGs can be combined with other heat recovery techniques. [143]

In the study [187], an overview of thermoelectric applications is presented. This study presents TEGs with efficiencies up to 10 %. In contrast, the analysis of Martínez et al. [100] and Kumar et al. [80, 81] estimates an efficiency between 1.96 % and 4.33 %.

The recovered electric power can be used to relieve the alternator. In [139], a close to the engine integrated TEG concept is presented. The thermoelectric modules and the heat exchangers are integrated in the exhaust manifold. To compensate for the heat flow changes, a control of the exhaust valves is implemented. For this concept, a 200 W TEG based on Fe-Ni TEMs from Toshiba and skutterudite modules from Showa Denko K.K. and Plantec Inc. is simulated. The hardware in the loop simulation has estimated an increase in fuel economy by up to 5 % using an 1.8 L Otto engine for the NEDC. For an 1.8 L Diesel engine, the fuel economy is estimated to increase by 4.5 % in an ARTEMIS (Assessment and Reliability of Transport Emission Models and Inventory Systems) driving cycle [161].

In [102], an overall optimization of a planar TEG system is presented, with two different thermoelectric modules. The low-temperature modules are based on Bi_2Te_3; the high temperature modules are not specified. The simulation has shown a fuel economy of up to 0.6 $\mathrm{g\,km^{-1}}$ CO_2 for the NEDC using a 3 L Otto engine. In this simulation, the TEG uses the engine cooling circuit as heat sink. Additionally, the fuel to compensate for the weight of the TEG is included.

However, the fuel economy depends on the explicit power supply of the vehicle. Only the fuel consumed from the alternator can be saved.

Summary of Waste Heat Recovery

This subsection presented different technologies and concepts that are used to recover the waste heat of an ICE. However, most of the technologies are characterized by an indirect thermal conversion into mechanic or electric energy, such as the Clausius-Rankine cycle or the turbogenerator. As a consequence, these technologies use different components, which are difficult to scale up or

down for a desired power range. The concept of the turbocharger in particular is difficult to adapt to different operation points of the ICE, although the use of this technology leads to the highest increase of the ICE's efficiency.
Another aspect is the risk of damage of the mechanical components, through attrition.
In contrast, direct thermal conversion technologies - chillers and exchangers - can be integrated in a compact space and are passive systems without any additional mechanical components. Therefore, the service and the potential of defects are less when compared to other technologies. Through the selection of material, direct conversion technology can be easily adapted to different requirements such as thermal stress or power range, and the efficiency can be optimized.
However, direct thermal conversion systems can only be used to increase the efficiency of thermal applications. In contrast, TEG systems recover thermal energy and convert it into electric energy with the same advantages like the direct thermal conversion technologies. Electric energy has the advantage of being easily convertible into mechanic or thermal energy. Furthermore, TEGs have a simple design and can be scaled for different applications. Consequently, the TEG has an optimal qualification for the waste heat recovery. The only significant drawback of the TEG is the low efficiency of currently used thermoelectric materials.

1.1.2. Thermoelectric Application

The idea to recover waste heat produced by ICEs is more than a century old. The first patent of waste heat recovery of an ICE using a TEG to charge a battery was granted in 1914 [34]. The first prototype of a TEG to recover waste heat from ICEs was developed in the 1960s for military applications. The thermoelectric material for this application was based on BiTe with an electric power of 500 W and PbTe with 300 W [117, 118].
In the last decades of the 20th century, different prototypes were developed. In 1994, the company Hi-Z Technology integrated a Bi_2Te_3 thermoelectric generator with 1 kW electric power at a 14 L Diesel engine [11]. In the late 1990s, Nissan used SiGe and Bi_2Te_3 material for the TEG with a nominal electric power of 35.6 W and 193 W at a 3 L Otto engine. In 1999, General Motors has integrated a 250 W TEG at an 8 L Otto engine based on Bi_2Te_3. [143, 149]
BWM obtained a 200 W planar TEG for a 3 L Otto engine with Bi_2Te_3 material in 2006 [42]. Furthermore, by cylindrical thermoelectric modules, a TEG with a maximum power of 700 W should be realized [81].
According to Meisner [103], a TEG is designed with the materials skutterudites (for high temperatures above 250 °C) and Bi_2Te_3 (for lower temperatures up to 250 °C) to generate 425 W in light duty vehicles. All those applications use the cooling circuit of the engine as the cold side and the exhaust gas as the hot side for the TEG systems.
Another approach to regain the waste heat for vehicles has been suggested by Kim et al. [75]. The article

presents a TEG concept to recover the waste heat of the radiator from the water cooling system, which achieves a maximum power of 75 W with Bi_2Te_3 material.

1.1.3. DC-DC Converter for Thermoelectric Generator

The voltage of the TEG is proportional to the temperature gradient across the thermoelectric material. The waste heat temperature of an ICE has dynamic characteristics in a drive cycle and, consequently, the voltage of the TEG change [187]. In the patent of 1914 [34], it was already mentioned that the voltage of TEGs can only charge the battery when the voltage amplitudes are adjusted. The presented prototype of [117] used Zener diodes, which clip the maximum voltage to the breakdown voltage and function as linear voltage controllers. Excess power is conducted to ground.

BMW use a diode between a 200 W TEG and an on-board power supply [42]. The TEG only supplies the vehicle electric grid if the voltage of the TEG is higher than the sum of the on-board voltage and the threshold voltage of the diode. The disadvantage of the diode is the electrical loss, which results from the threshold voltage. In addition, the voltage of the TEG up to on-board voltage plus the threshold voltage cannot be used to recover.

An alternative to a diode is a DC-DC converter, which allows to regulate the conversion ratio from input voltage (TEM) to output voltage (vehicle supply voltage) by electrical switches [44]. A comparison of converters with controlled conversion rates or fixed rates is presented in [116].

High-frequency switch signals reduce the necessary nominal semiconductor values, the current ripple, the voltage ripple, and, consequently, the total weight, volume, and costs of a converter. For TEGs, non-isolated DC-DC converters are preferred to avoid the loss of the transformer. In [96], a review of classical DC-DC converters, which are used for TEGs, is presented. The choice of the converter topologies depends on the specified voltage and current amplitude for load and source. The most often selected converters for a TEG are the boost, the buck-boost, and the Ćuk [96]. A good general overview and comparison of the non-isolated DC-DC converters are presented in [20, 21, 22, 39, 132].

Due to the wide range of the input power of a TEG, the used converters and their nominal power can differ significantly. A non-inverted buck-boost converter with a maximal input power of 35 W is presented in [109] for a 12 V battery charging. Montecucco et al. [110] present a buck converter with 93 % efficiency of 22 W input power for a 12 V battery. Huleihel et al. [56] present a boost converter for 1.2 W input power with a flat inductor, which is integrated in the printed circuit board (PCB) to reduce leakage inductance. This circuit reaches an efficiency of 83 %, which includes all driver and semiconductor losses. In addition, a loss model for the converter is proposed, which can serve as a guideline to optimize the boost converter for a desired operation point. A single-ended primary-inductor converter (SEPIC) for a thermoelectric application is presented in [153]. This prototype has only 69 % efficiency for a 2.3 W input power, but with synchronous metal-oxide-semiconductor field-effect transistors (MOSFETs) higher efficiencies can be achieved. In contrast, the SEPIC by [40] reaches up to 95.11 % efficiency for 8.4 W input power. An interesting concept is a 100 W multi-stage Ćuk converter, which is developed for

a combined thermoelectric-photovoltaic hybrid energy grid [186]. This concept reduces the number of necessary semiconductors and sensors in the converter.
The presented boost-buck converter by Wu et al. [182] is designed for a maximal electric power of 500 W with a maximal efficiency of 99 %. To reduce the inductor loss, the boost-buck uses a couple inductor with a single core. The converter is controlled in two modes: either as a boost converter or a buck converter. In boost mode, the buck converter is connected through to the load. In buck mode, the boost converter is connected through to the source. Consequently, the boost-buck converter is controlled only with one controller and an additional battery voltage controller.
Kim [70] also presents a boost-buck converter with a nominal input power of 1.5 kW. However, a decoupling of boost and buck converters is used. Thus, a cascade control concept is implemented, which has the advantage of a better performance to compensate for disturbances and regulate all electrical states of the converter. Kim uses three-phase interleaved synchronous switches to reduce the switching loss.
All of the above mentioned attributes of the converter are designed for a specific operating point and electrical characteristic of the TEM. However, the electrical dynamics of the converters are influenced by the change of TEM's electrical characteristic, which affects the stability and dynamics of the closed-loop controller.
Li et al. [89] propose a DC-DC converter network for the TEG with an overall efficiency of 3.8 % in contrast to 3.4 % for a TEG with a one single stage converter because the network splits the TEG in different operation areas. The single converter must cover all operation points of the TEG, which results in particular decrease of efficiency.
In summary, the electric interface of the TEG and the load is an important device because the efficiency of the electric circuit reduces the entire efficiency of the recovered electric energy. The classical design step of a converter is to select the topology with a maximum efficiency at one steady-state operation point for the application. However, for the waste heat recovery of an ICE, the TEG has multiple operation points. To optimize the DC-DC converter for the TEG to recover waste heat, a general loss model is necessary.

1.1.4. Maximum Power Point Tracking

TEMs are connected to the on-board power supply through DC-DC converters in order to link the recovered electric power to the load. The physical principle of a DC-DC converter is to charge and to discharge electric storage elements like inductors or capacitors. The duration of the charging and discharging is controlled through electric switching elements like MOSFETs. In other words, a DC-DC converter is an adjustable impedance, which can be controlled through the duty cycle of the MOSFETs. An electric equivalent circuit of the TEMs is a DC voltage source u_{tem} with a series resistor r_{tem}. Consequently, the TEM has one maximum power point (MPP), which is reached when the input voltage of the DC-DC converter is $u_{tem}/2$. At this operation point, the input impedance of the DC-DC converter matches the impedance of the TEM. In case the impedances have the same value, the maximize power transfer from source to load is reached. Generally, the exact MPP of the TEM is unknown because the temperature distribution of the waste heat is nonlinear. This means that the electrical characteristic of a TEM is difficult to estimate for a time-varying temperature. In practice, a maximum power point tracking (MPPT) algorithms are used to find the MPP. The MPPT calculates the desired input current of the DC-DC converter to reach the MPP. A direct or indirect control[1] of the duty cycle from the DC-DC converter can be used to match the desired values. The basic idea of an MPPT is a gradient search algorithm, which estimates the power gradient and serves as an indicator to increase or decrease the input current and voltage.

MPPT algorithms are state of the art for photovoltaic modules. A detailed overview of different MPPT algorithms is presented by Esram and Chapman [45] and Salas et al. [148]. Two famous and proven tracking algorithms are the hill climbing (HC) and the perturb and observe (P&O) method. Both methods estimate the gradient of the input power and the new duty cycle value for the MOSFETs, with a fixed step size. To optimize the convergence time of the algorithm, an adaptive gain of the increasing steps can be used. [71, 74]

The incremental conductance method for TEMs is also well-known, and it is based on the input voltage derivation of the power [74, 92, 146].

An alternative to the classic MPPT algorithms is the fractional open circuit method, which disconnects TEMs from the DC-DC converter for a time interval to measure the open-loop voltage u_{tem} of TEMs. Subsequently, the TEMs and converters are re-connected and a controller regulates the converter's input voltage to the half of amplitude of the measured open loop voltage $u_{tem}/2$. The advantage of this method is that no current sensor is necessary. However, the DC-DC converter must be able to disconnect from TEMs, and in this time interval no electric energy can be recovered. Cho et al. [27] present a boost-buck converter with analog fractional open circuit control. Montecucco [107] uses a buck-boost converter prototype for the fractional open circuit and utilized a snubber network to minimize the time interval for the disconnection of the converter. The prototype only needs 110 µs for disconnection, a measurement of the open-loop voltage u_{tem}, and a re-connection of the converter with the TEM. The voltage is measured each 500 ms to track voltage variation of the TEM.

In general, the exact MPP of the TEM cannot be reached with a DC-DC converter due to the AC ripple of current and voltage. This mismatch is used to classify the MPPT efficiency in [27, 107], but the AC ripple also depends on the duty cycle, the semiconductors of the converter, as well as the operation point of the TEM. Hence, the MPPT efficiency value can only be used to compare algorithms with the same hardware and the same operation point.

In summary, the MPPT indeed differs in terms of implementation, but in general all methods can reach the MPP. This means that, the selection criteria of the methods can only be set in relation to the technical application.

[1]To simplify, in this thesis a control without a feedback controller is called direct control. The automatic control is called control or indirect control.

1.1.5. Integration of Thermoelectric Generator

The integration of a TEG into an on-board power supply with a DC-DC converter includes the electric wiring of TEMs and the DC-DC converters. A TEG has a degree of freedom to select a desired interconnection with individual TEMs. A series connection has the advantage to increase the open-loop voltage, whereas a parallel connection increases the short circuit current. The series connection has the drawback that a defect of one TEM results in a total failure of all TEMs. However, the temperature of the exhaust gas decreases significantly in the direction from ICE to the exhaust pipe. Hence, the temperature at TEMs is not distributed homogeneously. Consequently, a TEG is a network of TEMs with nonlinear electrical characteristics. The wiring of TEMs leads to an inherent power mismatch [181]. In [181], a hybrid centralized-distributed power conditioning system is presented, which is based on a boost and flyback converter. In case of voltage, which is too low for the flyback converter, TEMs are connected in series to the boost converter. In order to avoid a significant power mismatch, TEMs can be separated and connected to a flyback converter. A complex interconnection of individual TEMs is not possible with this application.

Furthermore, analyses of the power mismatch of serial or parallel connected TEMs are studied in [111]. A parallel connection increases the load current, which results in higher Joule heating in TEMs and decreases the maximum power. An additional important aspect is the increase of the Peltier effect, which causes a decrease of temperature gradient across the TEMs. For this reason Montecucco [111] concludes that an electrical series connection is more favorable to avoid parasitic loss. Therefore, the balance between the number and costs of DC-DC converters in a distributed system and the expected power loss due to mismatched conditions needs to be optimized.

A switching network which uses relays to connect TEMs parallel is presented in [24] for underheated TEMs. The control of the relays uses a look-up table, which requires a pre-known of the temperature and the electrical characteristics from the TEM. This requirement limits a practical implementation of the switching network for different applications.

An interesting aspect of an optimal integration of a TEG is shown in [186]. The authors present a direct parallel connection of the load with TEMs. A DC-DC converter is used to support the load with a battery or to charge the battery when the TEM generates more power as consumed by the load. However, this concept requires a fundamental reconfiguration of the electric power grid of a vehicle.

In summary, the electrical integration and interconnection of individual TEMs have an influence on the overall efficiency of a TEG. How significantly the electric wiring of TEMs impacts the whole efficiency of a TEG for dynamic temperature changes or a driving cycle has not been investigated in detail.

1.1.6. Modeling of DC-DC Converter

In the 70s, the first analysis and a general model design of basic switched mode DC-DC converter topologies was presented [178, 179]. These fundamental results led to an averaged and linearized model of converters. Middlebrook and Ćuk [105] have proposed a state space averaging (SSA) method, which yields

steady-state and dynamic linearized models of the converters. The basic idea of the SSA is to separate the converter in the electrical equivalent circuits for the the switche on and off time and to average the state space models over one switch period. The same models can also be determined through a circuit averaging or switch network [44, 105]. The SSA models are accurate up to the half of the switching frequency for continuous conduction mode (CCM) [44].
Sun et al. [162] present a detailed analysis and a model of the SSA method for CCM and discontinuous conduction mode (DCM) converters. A similar approach use by Davoudi et al. [37], with the difference that parasitic effects are included. Further, the article shows that high frequency model errors of the SSA method depend on the model accuracy.
However, it is possible to analyze the influence of input and output filters to the converter transfer functions with Middelbrock's extra element theorem [44]. An alternative is the two port theorem which is used to analyze the influence of load and source on the converter [53]. Altowati et al. [4] and Zenger et al. [183] present the interaction of multi-model parallel DC-DC converters, which is based on the SSA method and can be used for the control design.

1.1.7. Conclusion

The literature review shows that waste heat recovery can reduce the CO_2 emissions of the ICE and save fuel. Comparison of the techniques that are used to recuperate waste heat, shows that CRCs and TEGs have the decisive advantage because their integration into the existing vehicle architecture is simple. Additionally, these techniques can be upgraded for already existing ICEs. However, currently both concepts are in the pre-development process. To what extent the two methods are promising for the future particularly depends on the development of thermal fluids and thermoelectric materials.
The already developed TEG prototypes only have low efficiencies, and in the last years the research has been focused on the reduction of thermal loss and the optimization of heat exchanger. The electrical integration of the TEG into the on-board power supply with DC-DC converters was neglected in the concepts in the past. Only TEGs with passive diodes are currently being used, which have the disadvantage that the MPP of the TEG cannot be tracked.
A vehicle simulation with a cooling system, an ICE, and a TEG is presented in [102, 139]. In these simulations, the geometry of the TEG and the heat exchanger are optimized in relation to the additional back pressure of the TEG in the exhaust gas system. Additionally, the fuel economy is calculated in relation to the used alternator. For the electric interface, an ideal DC-DC converter with a fixed efficiency is assumed. What impact the integration of TEG in the electrical system of the vehicle has on the energy management of the vehicle is not apparent from the documentations.
In the literature, electrical circuits to link TEMs to a vehicle power supply are published. However, this circuits are only designed and optimized for well-defined TEMs. Furthermore, the dynamic temperature of the exhaust gas system results in a change of electric characteristic in the TEMs, which has to be

compensated by the converter. In [74] and [107] experiments with changing temperature of the TEMs are presented, but only to verify or motivate the MPPT algorithms. The determined efficiency is only estimated for selected operation points. A detailed analysis of the efficiency for all possible operation points is missing. Therefore, an efficiency analysis, as shown in [56], is necessary to estimate the loss of a converter for entire power range of the TEM.

The electric wiring includes the wiring of individual TEMs with a converter, as well as the entire network of DC-DC converters of the TEG. In [111], the influence of the wiring is analyzed for three different TEMs, but the results indicate a solution for this specific experiment only. The wiring has an influence on the performance of TEG, which is consistent with the results of [24]. Both studies included only empirical results, and a generalization of the results is not possible. The presented bypass network [24], which includes relays to decouple or couple parallel connected TEM, shows that a new configuration of TEM wiring can be useful for underheated TEMs. However, the concept is based on a prior knowledge on how TEMs need to be interconnected.

The SSA method offers the possibility to model and analyze DC-DC converters. Furthermore, an analytical evaluation of the electrical wiring of TEMs for different DC-DC converters is possible. Additionally, the SSA models can be used to develop and design control structures for the electrical network of TEMs and the DC-DC converters.

1.2. Thesis Outline and Summary of Contribution

The literature review shows that TEG systems can be integrated in the waste gas system of a vehicle. The necessary components like thermoelectric material, heat exchangers, and DC-DC converters have been studied in detail. The aim of this thesis is to research the electrical integration of a TEG system in the on-board power supply. This includes the analysis of the electrical components, the interaction of the TEG with the on-board power supply and the TEG during a driving cycle. The focus of this thesis lies on the methodological analysis and the assessment of the electrical interface without any restrictions on used TEMs. The contribution of this thesis can be outlined as follows:

1. Efficiency is an important selection and design criterion for a DC-DC converter. The temperature dynamic of the waste heat leads to a dynamic variation of the electrical operation points of a TEM. An evaluation of the converter for only some operation points is unsatisfactory for this application. For the electrical efficiency analysis of a DC-DC converter, a loss model has been derived. This model can be used to compare different converter topologies. Furthermore, it might serve as a guideline to optimize the efficiency.

2. Experimental results are presented for a DC-DC converter prototype. Theses results are used to verify the loss model and the SSA model of the DC-DC converter.

3. The electric characteristics of a TEM influence the transfer functions of the DC-DC converter. This influence must be considered in the controller's design in order to ensure the stability of the

desired feedback control. A generalized control structure, which is robust and stable for the whole power range of the TEMs, has been derived for a boost-buck converter.

4. Generally, the loss of a converter depends on electrical parameters of the components and the electrical states. The control concept of the boost-buck converter allows to regulate the electrical states. Optimization of the loss has been carried out to increase the efficiency in relation to electrical parameters of the TEM. Measurement results prove increased efficiency of the converter as a result of the optimization.

5. The TEMs present time-variant voltage sources with series resistors, the parameters of which depend on the actual temperature value and the temperature distribution in the exhaust gas system. The fixed wiring of TEMs with a DC-DC converter can result in a mismatch of the maximal power. The interconnection of TEMs and DC-DC converter has been optimized. The results have been generalized for the electric wiring of the TEG in relation to the loss model of the converter.

6. The primary power source of the on-board power supply for an automobile is the alternator with a separate controller. The TEG represents an additional power source. In contrast to the alternator, the output power of the TEG depends on temperature gradient. A new electrical energy management of alternator and TEG has been studied and optimized.

This thesis is structured as follows:

Chapter 2
The basic concepts and functions of thermoelectrics are presented in this chapter for general understanding. Further on, the relations between physical, thermoelectric, and electrical models are illustrated to explain the electric load interaction and feedback of the TEM. The chapter concludes with the presentation of a TEG and a desired system for an automobile.

Chapter 3
To analyse a DC-DC converter for a thermoelectric application, an efficiency model is required. Basic converter topologies are modeled using the SSA method. Parasitic ohmic loss is integrated in these models. Models are derived for dynamic switching loss in MOSFETs and magnetic loss in inductors. These models are used to analyze the efficiency map of the converters. First, the efficiency is analyzed in relation to the switching frequency and, secondly, for an input power range and different output voltage amplitudes. Additionally, a boost-buck converter is developed to verify the efficiency model.

Chapter 4
To integrate the TEM into a vehicle power supply, a control of the boost-buck converter is necessary. A general introduction to a digital control explains the control design and robustness criterion. Based on the SSA models from Chapter 3, the transfer functions of the boost-buck converter

are analyzed and the influence of parameter variation for the TEM can be estimated. Finally, the control parameters can be designed. An alternative concept, which adapts the control parameter to the application, is the self-tuning controller and is studied in this chapter.
To ensure that the maximum power is recovered from the TEG, an MPPT algorithm is designed and used on a current controller. A trickle charge controller protects the battery of the on-board power supply against overcharging. The boost-buck converter is decoupled with a capacitor, and the voltage amplitude of this capacitor can be regulated. This degree of freedom is used to optimize the efficiency of the converter in relation to the input and output voltage. The SSA model of the boost-buck converter, the control design, and the optimization of the efficiency are verified with experiments.

Chapter 5
The electrical integration is analyzed for a TEG with ten PbTe TEMs. Focus of this study is to determine the electrical wiring of TEMs and DC-DC converters with the highest efficiency and minimal count of converters. The electrical parameters of the TEG result from a WLTP driving cycle of a 2 L Otto engine. The optimization of the electric wiring uses an evolutionary algorithm.

Chapter 6
The TEG is an additional power source to the alternator. Both supply the electrical power grid of the vehicle. In this chapter, different energy management strategies are analyzed to estimate the fuel economy of the TEG for a 2 L Otto engine. For the simulation, the electrical necessary system components are measured and modeled. The fuel economy of the TEG depends on the power consumption of the electric load from the on-board power supply and the drive torque of the alternator.

Chapter 7
The derivative methods, estimated analysis, and the results of this thesis are summarized in this chapter. The results are discussed in relation to the ambition of this thesis. Finally, potential future research topics are presented.

2. Thermoelectric Waste Heat Recovery

The thermoelectric effect converts heat energy directly into electric energy and vice versa. The thermoelectric effect was discovered in the 19th century and can be utilized for different application fields like temperature sensors, heat pumps, and thermoelectric generators. This thesis focuses on the application of TEGs. Therefore, this chapter aims to explain the relevant effects and principles in order to understand how a TEG functions. More details are presented in [124, 143, 144, 145]. The thermoelectric effects are briefly defined in Section 2.1. The TEG and the model of this device are explained in Section 2.2 and 2.3. Furthermore, the thermoelectric materials and characteristics are presented in Section 2.4. Finally, the desired TEG system is presented in Section 2.5.

2.1. Basic Principles of Thermoelectrics

The thermoelectric effect is based on three physical phenomena: the Seebeck effect, the Peltier effect, and the Thomson effect. The Thomson relationship describes the relation between these three effects.

2.1.1. Seebeck Effect

When a thermoelectric material is placed between two different temperatures, a voltage is generated. This phenomenon was discovered in 1876 by physicist Alessandro Volta [5]. Thomas Seebeck also discovered this phenomenon 25 years later. Although Volta discovered this phenomenon first, it is known as Seebeck effect. The Seebeck coefficient α is a relation factor between the electrical voltage u and the temperature gradient ΔT. The value of the coefficient depends on the material. The thermoelectric voltage is defined as:

$$u = \alpha \Delta T - \frac{1}{e_c} \Delta \mu_c \quad , \tag{2.1}$$

where e_c is the elementary charge and μ_c the chemical potential difference of the material. The Seebeck effect can be explained qualitative through the Drude theorem. Due to the temperature difference across the thermoelectric material, the electrons and holes diffuse to the cold side with a relative speed caused by the temperature. By collision with other electrons and holes, kinetic energy is converted into thermal energy, and the velocity of electrons decrease. Consequently, the number of electrons increases at the low temperature side and electric field is induced, which causes a drift current to the warm side. For a steady-state, a balance between current and thermodynamics has to be reached. [143]

The connection of a couple of different conductors (n- and p-doted) results in a voltage potential u_{te}

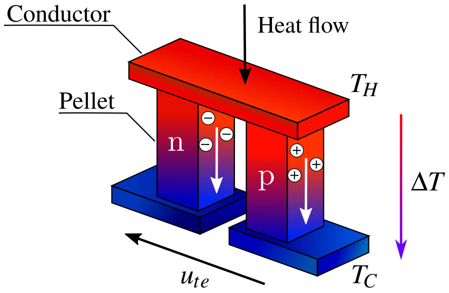

Figure 2.1.: A thermoelectric element with n- and p-doted thermoelectric pellets.

across the open-ends of the couple (see Figure 2.1). For a constant temperature gradient with the assumption, that the electrical contacts have identical chemical potential, the open-circuit voltage u_{te} of a thermoelectric couple with dissimilar materials can be expressed as:

$$u_{te} = \int_{T_C}^{T_H} \alpha_p(T)dT - \int_{T_C}^{T_H} \alpha_n(T)dT = (\alpha_p - \alpha_n)(T_H - T_C) = \alpha_{pn}\Delta T \quad , \tag{2.2}$$

where T_H and T_C are the temperatures of the hot and the cold side of the thermoelectric pellets, ΔT is the temperature gradient, α_n and α_p are the Seebeck coefficients of the n- and p-doted material, and α_{pn} is the difference of the coefficients. [126]

2.1.2. Peltier Effect

The Peltier effect is the reverse Seebeck effect and was discovered by the physicist Jean Peltier in 1834. The Peltier effect can be observed when an external voltage is connected to the couple conductors. Through the current flow from the voltage source, one junction is heated and the other is cooled. Thus, the current transports thermal energy. The relation between the heat current $\dot{Q}_p$ and the electric current i is defined as

$$\dot{Q}_p = \Pi\, i \,, \tag{2.3}$$

where the Peltier coefficient Π has the unit of voltage. An interpretation of this effect is that heat is absorbed or released at each junction when a temperature difference exist. The Peltier effect can result in a closed-loop system if a current flows. Furthermore, the effect is relevant mainly for heat pump applications.

2.1.3. Thomson Effect

This phenomenon was discovered in 1854 by Lord Kelvin (William Thomson). The Thomson effect occurs when the heat current $\dot{Q}_t$ flows from the higher temperature to the lower temperature of a material and absorbs heat:

$$\dot{Q}_t = B_t\, i\, \Delta T \,, \tag{2.4}$$

where B_t is the Thomson coefficient. In contrast to the Peltier and Seebeck effects, the Thomson effect occurs in a single conductor. The Thomson effect is a reversible process and can also result in a heat generation if the current flows from the cold to the hot side.
In most analyses of thermoelectric devices, the Thomson effect in thermoelectric materials is neglected. However, the Thomson effect can significantly affect the heat current of a thermoelectric device with significant temperature differences [23].

2.1.4. Thomson Relationship

In 1854, Lord Kelvin discovered a direct relation between the Seebeck, Peltier, and Thomson effects. The Seebeck and the Peltier coefficient have the following relationship:

$$\Pi = \alpha T \tag{2.5}$$

Consequently, the Peltier heat current can be expressed with the Seebeck coefficient:

$$\dot{Q}_p = \Pi\, i = \alpha\ T\ i \tag{2.6}$$

Furthermore, the Thomson coefficient has a relation to the Seebeck coefficient

$$B_t = T\frac{d\alpha}{dT}\ , \tag{2.7}$$

where T is the absolute temperature. The Thomson relationship can be determined by the Seebeck coefficient and the Thomson coefficient in a conductor made of homogenous material [115].

2.2. Thermoelectric Generator

The TEG is a solid-state energy converter. The first TEG was built in 1947 by Maria Telkes [167]. Its unique characteristics are as follows [115]:

- TEGs are passive without movable components. Thus, TEGs require low maintenance, do not wear out, and do not produce any direct noise.
- TEGs convert energy directly without energy transfer fluids.

Normally, TEGs consist of different TEMs, which are integrated in the application. The TEMs are based on n- and p-doted semiconductors, which have thermoelectric properties. The n- and p-doted semiconductors are electrically connected in series and thermally connected in parallel. An electrical series connection of the n- and p-doted pellets is necessary to generate a higher output voltage because the Seebeck coefficients are mostly below 300 $\mu V\,K^{-1}$ [145].
Commercially available TEMs have a geometric surface of less than 10000 mm^2 [107]. The size of the TEM is kept small in order to prevent excessive temperature differences in the modules. Otherwise, the electric voltage and especially the mechanical stress increase, which can damage the module. Consequently, all materials of the TEM must be chosen with regard to the thermal and electric coefficients.

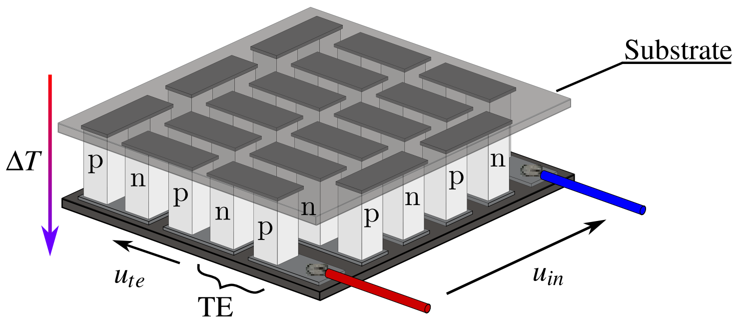

Figure 2.2.: A thermoelectric module.

2.3. Characteristics of Thermoelectric Modules

A TEM is a series connection of TEs. The TEM is mounted between two substrate plates with the material characteristics of an electric insulator and a minor thermal conductivity, such as ceramic. TEMs are electrically connected in series and thermally parallel connected to the heat sources (see Figure 2.2). The heat currents $\dot{Q}_H$ and $\dot{Q}_C$, which flow from the hot temperature to the cold temperature of TEMs are given by the following:

$$\dot{Q}_H = (T_H - T_{Hs})\,\kappa \tag{2.8}$$

$$\dot{Q}_C = (T_C - T_{Cs})\,\kappa \quad , \tag{2.9}$$

where κ is the thermal conductance and T_{Hs} and T_{Cs} are the temperatures of the substrate plates. The electrical resistance of the TEM can be estimated as the summation of all N TE resistance values

$$r_{tem} = \sum_{n=1}^{N} \left(\frac{\rho_p(n)\, l_p(n)}{A_p(n)} + \frac{\rho_n(n)\, l_n(n)}{A_n(n)} \right) , \tag{2.10}$$

where ρ_n, ρ_p are the electrical resistivity, l_n and l_p are the length, A_n and A_p are the cross sectional area of the pellets. The same method can be used to estimate the whole thermal conductance κ_{tem} of TEM

$$\kappa_{tem} = \sum_{n=1}^{N} \left(\frac{\kappa_p(n)\, A_p(n)}{l_p(n)} + \frac{\kappa_n(n)\, A_n(n)}{l_n(n)} \right) , \tag{2.11}$$

where κ_n and κ_p are the thermal conductance of the pellets.
A connection of a ohmic load r_l to the TEM causes a current flow i_{tem}, which is defined as:

$$i_{tem} = \frac{u_{tem}}{r_{tem} + r_l} = \frac{\sum_{n=1}^{N} u_{te}(n)}{r_{tem} + r_l} , \tag{2.12}$$

where u_{tem} is the sum of the open circuit voltage u_{te} of all series-connected TEs. With the first law of thermodynamic at energy equilibrium, the current flow in the TEM (2.8) and (2.9) can be re-written as

$$\dot{Q}_H = \kappa_{tem}(T_H - T_C) + \alpha_{pn} T_H i_{tem} - \frac{i_{tem}^2 r_{tem}}{2} , \tag{2.13}$$

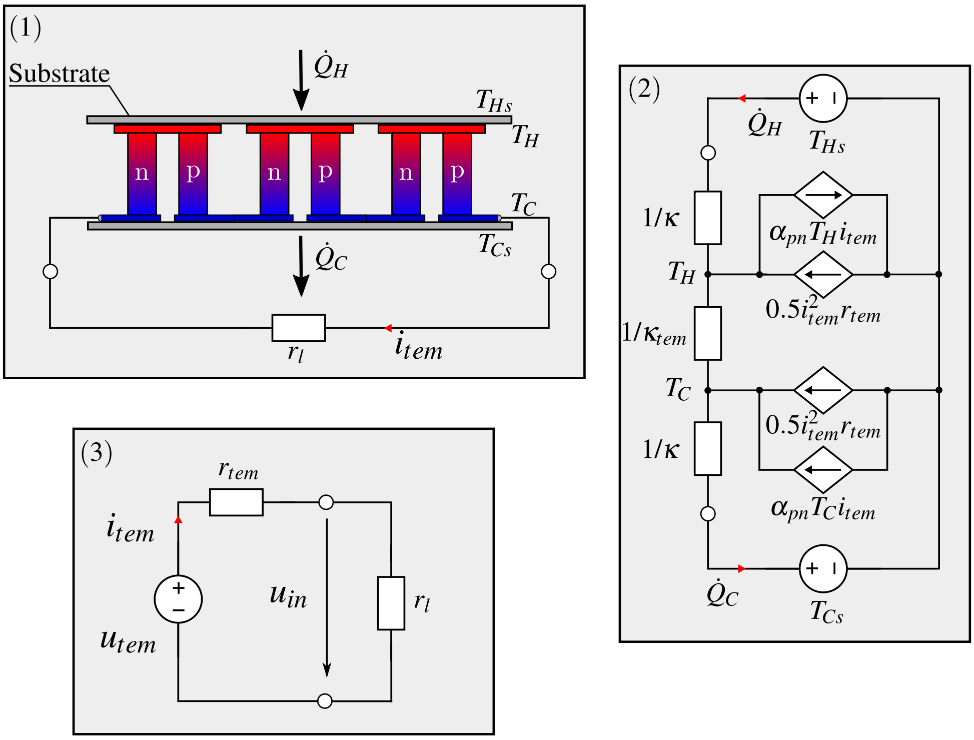

Figure 2.3.: An equivalent presentation of the TEM: (1) the physical device, (2) the equivalent thermoelectric model and (3) the equivalent electrical model.

and

$$\dot{Q}_C = \kappa_{tem}(T_H - T_C) + \alpha_{pn}T_C i_{tem} + \frac{i_{tem}^2 r_{tem}}{2} \ , \tag{2.14}$$

where $i_{tem}^2 r_{tem}/2$ is the Joule heating, while the Thomson effect is neglected. The thermal conduction and heat loss both are irreversible processes and reduce the energy conversion efficiency. Figure 2.3 shows an equivalent presentation of the thermoelectric and the electric model of a TEM. From (2.10) - (2.14) it follows that

$$\Delta T_{tem} = T_H - T_C = \frac{\kappa}{\kappa + 2\kappa_{tem} + \frac{2\alpha_{pn}^2 \overline{T}}{r_{tem}+r_l}} \Delta T_s = \tau_{tem}\Delta T_s \ , \tag{2.15}$$

where $\Delta T_s = T_{Hs} - T_{Cs}$ is the temperature difference across the substrate, ΔT_{TEM} is the temperature gradient across the thermoelectric material, $\overline{T}$ is the mean temperature across the substrates, τ_{tem} is the thermal efficiency and κ is the thermal conductance of the substrate. [36]
From (2.15) it follows that the temperature gradient across the substrate reduces the temperature gradient of the thermoelectric material and finally the open-circuit voltage of the TEM. This effect can be minimized with a high thermal conductance κ of the substrate.
However, the temperature depends also on the current flow i_{tem} in the TEM, which is caused by an electrical load r_l.

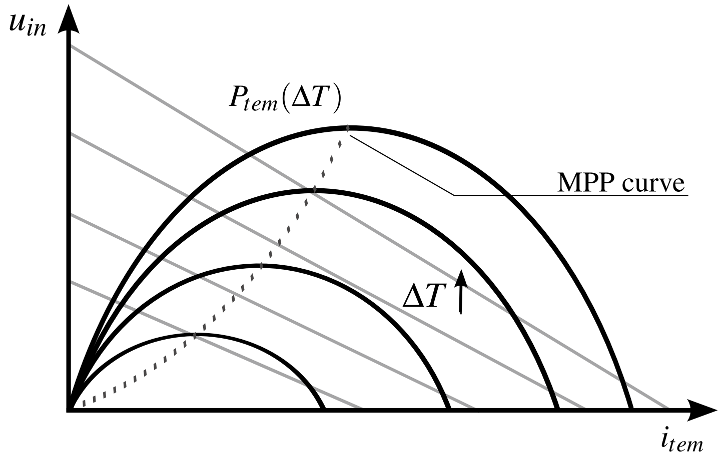

Figure 2.4.: Electrical characteristics from TEM and the electrical output power in relation to the steady-state temperature differences ΔT.

The output power of the TEM is defined as [36]:

$$P_{tem} = i_{tem}\, u_{in} = i_{tem}\,(\alpha_{pn}\,\Delta T_{tem} - i_{tem}\, r_l) = \alpha_{pn}^2\, \tau_{tem}^2\, \Delta T_s{}^2 \frac{r_l}{(r_{tem} + r_l)^2} \tag{2.16}$$

At a constant temperature across the TEM, the module presents an equivalent DC voltage source u_{tem} with a series resistance r_{tem}. The qualitative electrical characteristics depend on the temperature difference. The *u-i* curve of a TEM is shown in Figure 2.4. The power of the TEM is parabolic and has only one maximum power point (MPP) for the case $r_{tem} = r_l$.

It should be noted that for non-ideal heat sources, the value of r_{tem} can be shifted in a closed-loop circuit, depending on the temperature and current [101]. When $r_l < r_{tem}$, the current i_{tem} increase and consequently the Peltier effect and the Joule heating decrease ΔT [108].

2.4. Characteristics of Thermoelectric Materials

From the technical point of view, the quality of TEMs can be defined in terms of the efficiency η_{tem}:

$$\eta_{tem} = \frac{P_{tem}}{\dot{Q}_H} \tag{2.17}$$

The efficiency (2.17) can be re-written with (2.13) to [143]:

$$\eta_{tem} = \frac{i_{tem}^2 r_l}{\kappa_{tem}\,(T_H - T_C) + \alpha_{pn} T_H\, i_{tem} - \frac{i_{tem}^2 r_{tem}}{2}}\ , \tag{2.18}$$

where the temperature-dependent material characteristics are assumed as constants. However, the error of this simplification lies below 10 % [143].

From (2.18) it follows that the maximal efficiency is

$$\eta_{tem}^{+} = \frac{T_H - T_C}{T_H} \frac{\sqrt{1 + Z\overline{\overline{T}}} - 1}{\sqrt{1 + Z\overline{\overline{T}}} + \frac{T_C}{T_H}}\ , \tag{2.19}$$

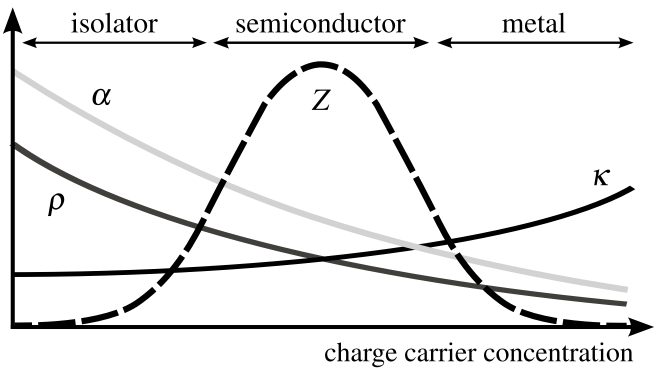

Figure 2.5.: A qualitative representation of the figure of merit in relation to the charge carrier concentration [143].

where $(T_H - T_C)/T_H$ represents the Carnot efficiency and Z is defined as the figure of merit

$$Z = \frac{\alpha^2}{r_{tem}\kappa_{tem}} . \tag{2.20}$$

With the assumption, that the pellets of a TEM have the same geometry and thermoelectric materials, (2.20) can be simplified to

$$Z = \frac{\alpha^2}{\rho\kappa} . \tag{2.21}$$

It should be noted, the electrical resistivity, the thermal conductance, and the Seebeck coefficient depend on the temperature.

The figure of merit is usually normalized to the mean temperature across the thermoelectric material in order to compare this value with other materials:

$$Z\overline{T} = \frac{\alpha^2}{\rho\kappa}\frac{T_H - T_C}{2} \tag{2.22}$$

The figure of merit value depends on the temperature and has only one maximum.

A good Z is defined by a high amplitude for a wide range of desired temperatures. The problem is to handle the electrical resistivity, the thermal conductance, and the Seebeck coefficient as these three parameters depend on the charge carriers of the material.

In generally, the electrical resistivity and the thermal conductance should be small in contrast to the Seebeck coefficient to reach a high figure of merit for a temperature gradient. Since the electrical resistivity and the Seebeck coefficient decrease with higher concentrations of charge carriers, while the thermal conductance increases, a conflict arises within this requirement. In Figure 2.5 is presented the figure of merit for a constant temperature gradient in relation to the charge carriers of the material.

Consequently, a specific thermoelectric material must be selected in relation to the desired temperature gradient of the application. However, the geometry of the pellets can be individual designed to optimize the figure of merit Z (cf. (2.20)). [143]

2.4.1. Overview of Thermoelectric Materials

Generally, all electrically conductive materials can be used for thermoelectrics. However, a particular material is defined thermoelectric material if the $Z\overline{T}$ value is higher than about 0.5. In the following, a brief overview of some thermoelectric materials is presented [49, 52, 143, 156, 157]:

Skutterudites
Skutterudites are crystal structures that are based on the mineral $CoAs_3$. These crystal structures have hollows in the center of the body, which can be used to accommodate large metal atoms to form filled skutterudites. These metal atoms can manipulate the phonon scattering, which results in a reduction of the lattice's thermal conductivity and consequently increases the $Z\overline{T}$ values. In fact, filled skutterudites like $Ce_{0.9}Fe_3CoSb_{12}$ and $Ba_{0.30}Ni_{0.05}Co_{3.95}Sb_{12}$ reach $Z\overline{T}$ higher than 1 for temperatures over 500 °C.

Half Heusler Compounds
The intermetallic half Heusler compounds are crystal structures of the MgAgAs type. Because of the relatively high Seebeck coefficients and electric resistivity, in addition to their potential for material combinations, half Heusler compounds are also interesting thermoelectric materials. They can be easily be produced and have a high chemical stability. $Hf_{0.75}Zr_{0.25}NiSn_{0.975}Sb_{0.025}$ reaches $Z\overline{T} = 0.81$ at 750 °C.

Bismuth Telluride
The most widely used thermoelectric material in commercial devices is Bi_2Te. Because of the low melting point of Bi_2Te_3, the material can only be used for temperature ranges up to 250 °C and reaches $Z\overline{T}$ values up to 1.

Lead Telluride
PbTe is the preferred thermoelectric material for the temperature range from 350 °C up to 700 °C. Its thermoelectric characteristics are well-researched and it can be optimized through appropriate dopants. The combination of silver antimon or germanium results in $AgSbTe_2$ and GeTe with $Z\overline{T} > 1$. Lead telluride materials have been successfully used for TEMs in space missions since 1970s.

Oxide
Oxide has a high mechanic stability and is chemically inert at high temperatures. The oxide material $NaCo_2O_4$ reaches $Z\overline{T} = 0.78$ at 780 °C and is an interesting material for high temperature applications. In the past, the use of this material in thermoelectric devices was disregarded due to the low electrical conductivity of oxides.

The efficiency η_{tem} of thermoelectric modules with $Z\overline{T} = 0.8$ is nearly 6 %. If the $Z\overline{T}$ increases by a factor of four, the predicted efficiency increases by up to 30 % [157]. Currently, the research is focused

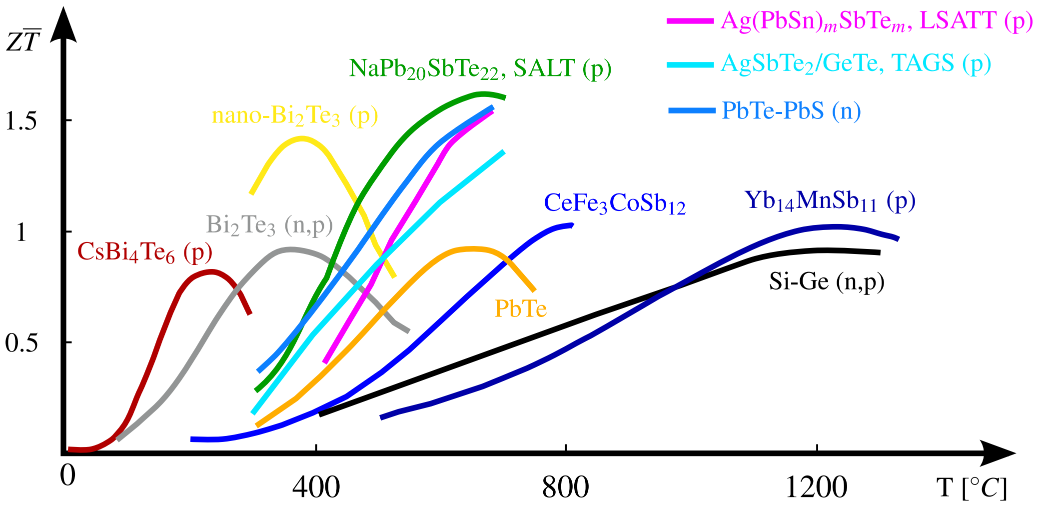

Figure 2.6.: The $Z\overline{T}$ values of some thermoelectric materials, based on [157].

on nanostructured materials, which increase the scatter of the photons without interrupting the motion of electrons. The result is a lower thermal conductance of the material and a higher $Z\overline{T}$ value [157]. In Figure 2.6, the $Z\overline{T}$ values of some thermoelectric materials are presented.

2.5. System of Thermoelectric Generator

A TEG system is based on more than just thermoelectric material and modules. To recover the waste heat in order to completely integrate the system into a vehicle, several components are needed in the system:

- A heat exchanger to maximize the heat transfer from the waste heat to the hot side from TEMs.
- A TEM with a high efficiency in the temperature rang of the waste heat.
- A heat exchanger to emit the heat from the cold side of the TEMs in order to maximize the temperature gradient across the module.
- A frame to integrate the TEG system into the vehicle. This frame has interfaces for electrical and thermal connections.
- An electric interface such as a DC-DC converter to link the electric power of TEMs to the on-board power supply.

Additionally, other devices and functions are required for the integration, for example:

- A pump for the coolant system, which can be regulated.
- A bypass flap to control the mass flow of the waste heat and/or to protect TEMs against temperature limits of the waste heat.
- Sensors to control and monitor the TEG system.
- An electronic control module for the implementation of software and control algorithms.

An overview of the whole TEG system is shown in Figure 2.7.

As shown above, a TEG consists of several components. They have the drawback of contributing an

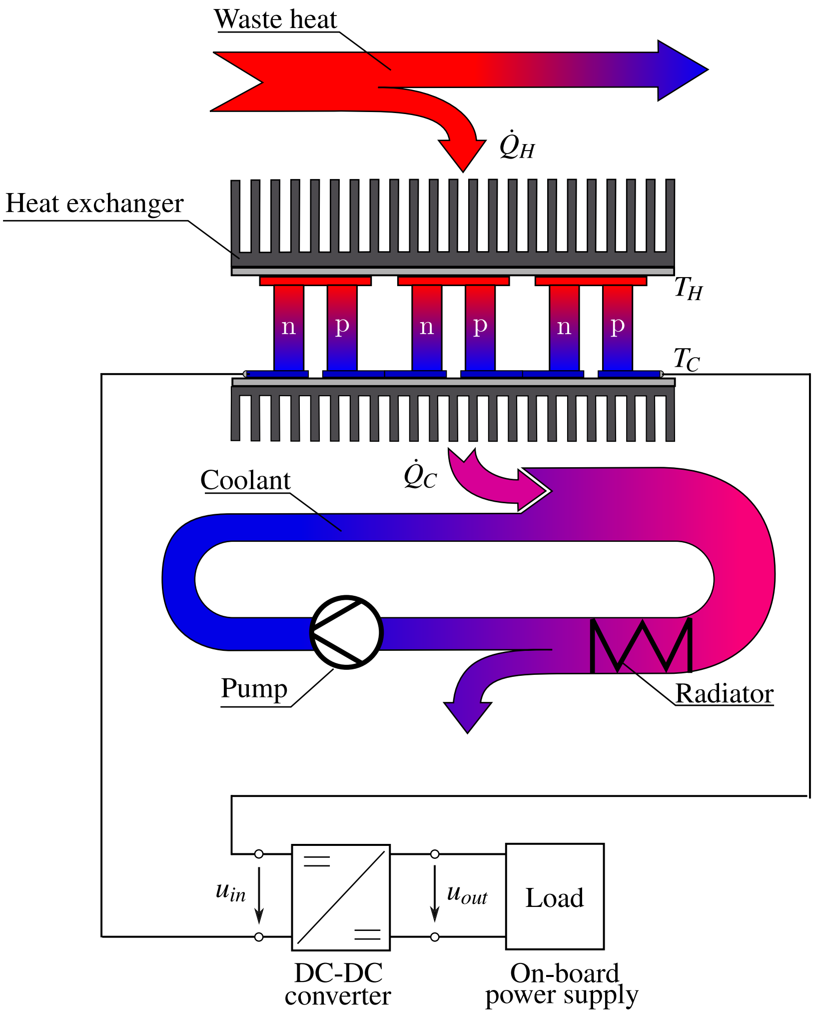

Figure 2.7.: Overview of the TEG system and necessary components for the integration in an automobile.

additional mass to the TEG system, which increases the fossil fuel consumption of the an ICE. Liebl et al. [91] indicate that the CO_2 emission increases by up to 4.57 $\mathrm{g\,km^{-1}}$ for an additional mass of 100 kg. Consequently, this negative influence must be compensated by the TEG system. The thermoelectric material and the $Z\overline{T}$ limit the efficiency of the TEG system. An important point for the integration of TEG systems in vehicles is that the integration space is limited and not every TE material is available in a large amount or might be toxic and therefore not suitable for commercial use.

Additionally, the temperature range of the waste heat, for example, the exhaust gas, can be reach up to 1000 °C depending on the ICE and the driver cycle [15]. This leads to the necessity to optimize the TEMs in particular by considering material mass, temperature, and efficiency (cf. (2.20) - (2.22)).

The $Z\overline{T}$ can be optimized by the selection of the cross section, the length and the number of TEs. Furthermore, different materials can be used to scale the TEs [77].

This optimization can be used to adapted the TEMs of a TEG for a specific application. Thus, the electrical characteristics of TEMs can be differ significantly, depending on the applications.

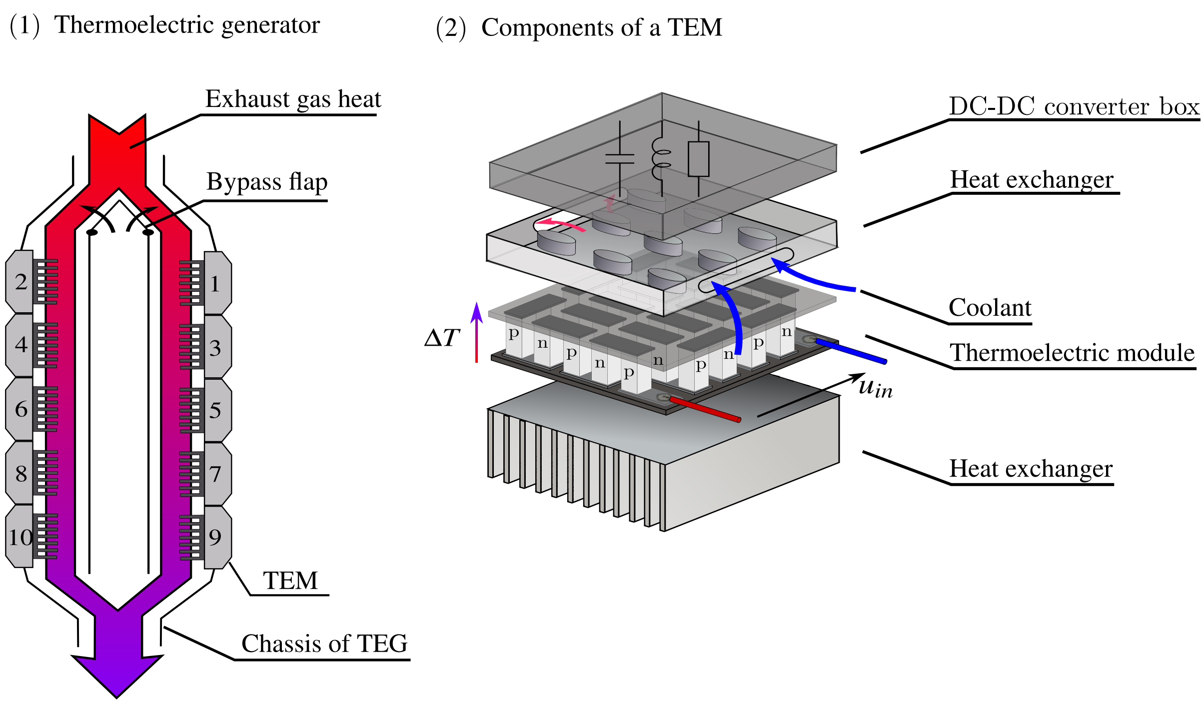

Figure 2.8.: Concept of the desired TEG system with ten TEMs (1), and the structure of the TEM device (2).

Desired Thermoelectric Generator System

In context of the research project “Thermoelectric Generator 2020” (TEG2020), a modular and scalable TEG system is desired. For that reason, a TEM should consist of two heat exchangers and a DC-DC converter for the electrical integration in addition to the TE material. These TEMs can thus be integrated into a chassis system. Consequently, a number of TEMs can be adapted to the TEG and to the target system with a specified thermal power and temperature of the exhaust gas. In the project TEG2020, a TEG system with ten TEMs which should be integrated in the exhaust heat gas system of an automobile with a 2 L Otto engine is desired. Figure 2.8 presents a concept of the system. The bypass flap can be used to protect the TEMs from overheating, which would damage the thermoelectric material. For the coolant, a low temperature circuit of the vehicle, without modifications of the pump or the radiator, should be used.

2.6. Conclusion

In this section, the basic principle of the thermoelectricity, mainly characterized by the Seebeck and Peltier effects, was presented. A thermoelectric module can be modeled as a DC voltage source with a series resistor if there is a constant ideal heat source and sink, which implies that no parasitic heat loss exist. Consequently, the power of a TEM can vary directly according to the number and the size of the used TEs. In practice, the waste heat is not an ideal heat source because the temperature is not homogeneously distributed in the waste gas system of an ICE. The same applies to the heat sink.

Consequently, the number and the size of the TEs is not proportional to the power of the TEM.
Furthermore, a current flow in the TEM decreases the temperature across the module. This effect can be explained by the Peltier effect and the Joule heating.
In terms of the conversion of the heat power into electrical power, the efficiency of a TEM depends on the selected thermoelectric material. The dependance of the $Z\overline{T}$ value on the temperature across the thermoelectric material poses a problem because the highest values are only reached in a specified temperature range. Consequently, the material must be selected in relation to the desired temperature range of the application. Bismuth telluride and lead telluride are favorite materials for temperatures up to 250 °C and 700 °C respectively because of the straightforward manufacturing process. Promising alternative materials for lead telluride are skutterudites and half Heusler compounds.
However, the maximum power of a TEM can be reached when its ohmic load matches the impedance of the TEM. For an application with significant temperature changes, such as the waste heat of an ICE, the impedance of the load must be continuously adapted. Furthermore, the power of the TEM must be linked to the on-board power supply. For this purpose, the DC-DC converters would be an obvious solution.

3. Modeling and Valuation of DC-DC Converters

The energy recovery of the TEG is linked to the vehicle power supply via DC-DC converters. Consequently, the efficiency of the electric device is a crucial factor for ecological and economical relevance of the whole TEG. The topology and electric wiring of a DC-DC converter influence this efficiency.

In recent years, the number of publications on the converters for TEGs has increased. However, most publications focus on the application but neglect the analysis and the comparison of different topologies of converters [70, 121, 172].

Characteristics and comparison options of topologies for a steady-state are presented in [39, 44, 64, 106]. In practice, the converter topologies are evaluated for an operation point with a specified power source and load. Such evaluation strategy is not useful for the TEG, which is integrated in the exhaust gas system of a vehicle, since the temperature profile of the waste heat depends on the ICE and especially the driver cycle. Consequently, detailed prior knowledge of the temperature profile of the exhaust gas and the parameters of the thermoelectric material is required to determine the operation points of a TEM.

An alternative approach is to assume that the TEM is a variable power source with a defined power range. For a defined power range, the electric efficiency maps of converter topologies can be estimated. Finally, the converters can be evaluated in relation to the power losses. This concept has the advantage that converters can also be evaluated for a specified application through the electrical operation points of the TEMs.

In this chapter, a modeling method is used to analyze the power losses and the efficiency of the DC-DC converters is presented. Firstly, the idea is to define the electric hardware requirements in order to specify the possible electrical circuits. Secondly, the converters are analyzed with a mathematical model and rating for different power classes of TEMs. Thirdly, the efficiency of the DC-DC converters are determined under consideration of individual hardware conditions.

The structure of this chapter is as follows. In Section 3.1, the physical principle of a DC-DC converter and its different topologies are outlined. The requirements of hardware, electric power, and the available space of DC-DC converter are defined in Section 3.2. The model method of a converter is presented in Section 3.3.

The dynamic power loss of passive and active semiconductors are separately modeled in Section 3.4. The DC-DC converter topologies are analyzed and evaluated in Section 3.5. After the evaluation of the converters in Section 3.6, the experimental result are used to verify the efficiency model in Section 3.7. Finally, the results are summarized in Section 3.8. The results presented in this chapter have been in part published previously [P1, P5].

3.1. Overview of DC-DC Converters

Power electronics uses the conversion and the control of various electric energies to supply current and voltage loads. Electric systems which realize this transformation are called converters.
Converters are classified depending on the type of energy conversion:

- **Rectifier**: The power flow is unidirectional from the source to the load. The source is AC power, which is converted into DC power.
- **Inverter**: The power flow is unidirectional from the source to the load. The source is DC power, which is converted into AC power.
- **Converter**: The power flow can be bidirectional from the source to the load. The source and the load have the same frequency; only the amplitudes of current and voltage are adapted. The converters are classified according to the energy supply and are called AC-AC or DC-DC converter.

This thesis focuses on the DC-DC converters because the voltage variation of a TEM is nearly constant in contrast to the dynamic changes of electronic states from the DC-DC converters. Furthermore, the load and the battery of a vehicle use DC voltage.
There are two classes of DC-DC converters: regulated and unregulated. Unregulated converters are only used for applications with a defined input power and a higher tolerance for the desired signal quality (such as the amplitude). Most converters are regulated with a feedback controller to compensate power variations of the source and load. The controller regulates an electronic switch to track the desired signal amplitudes.
The controller is based on a linear or switched-mode regulation. The linear controller uses a transistor as a power source. The unnecessary power is converted into heat. The switched-mode converter uses transistors to charge or discharge capacitors and inductors. Finally, the voltage and current amplitudes can be regulated. The efficiency of the switched-mode converters can be significantly higher than that of the linear converters [106], but the switching-mode generates electromagnetic interferences (EMI).
In [106], three classes of switched-mode converters are distinguished (see Figure 3.1):

- **PWM Regulators**: A pulse-width modulation (PWM) signal regulates the switch to continuously charge and discharge the capacitor and the inductor. The PWM-generated EMI is caused by hard switching.
- **Resonant Regulators**: The controller uses an L-C network to turn on and off the switches of the converter in relation to the resonant frequency of the L-C network. The switch-energy of the switches can be charged in a tank-network, which results in soft switching with reduced EMI. This type of converter has the disadvantage of a specified operation point for a limited input voltage and power load variation. However, the tank network can also be used in PWM-regulated converters to reduce switching loss and EMI. This type of converter is called a quasi-resonant converter [44, 64].

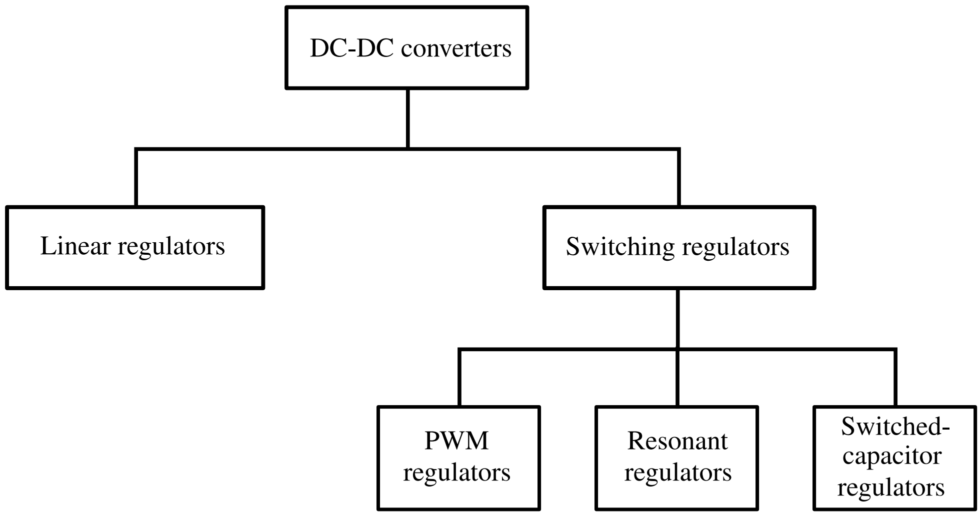

Figure 3.1.: Categorisation of DC-DC converters.

- **Switched-Capacitor Regulators**: The converter only uses capacitors. A pair of switches changes the connection of the capacitors to load and source continuously. This type of converter is also called a charge-pump. The current has a higher ripple in contrast to the current of other converter classes which use inductors. A reduction of the current ripple is possible once the charge-pump works as a quasi-resonant converter [76].

The criteria for the selection of switched-mode converter classes particularly depend on the application and cannot be generalized. For the selection of the converter classes, the requirements for the application must be taken into account.

3.2. Requirements of DC-DC Converter for Thermoelectric Generator

There are two possible approaches to link a TEG to the on-board power supply: a central or a decentral concept. The central concept uses a single high power DC-DC converter. In contrast, for the decentral concept, several separate low power DC-DC converters can be selected. The output power of each converter is connected to the on-board power supply. The advantage of central concept is lower cost for only one power converter when compared to cost of several converters. However, the disadvantage is that the damage of the converter would result in a total failure of the TEG system.
The desired TEG system (cf. Section 2.5) is based on a modular, scalable concept. This means that the TEG can be extended with modules. A decentral concept is not limiting the supported maximum power range of this system. Consequently, this is the only useful concept for the desired TEG system (cf. Section 2.5). The following requirements emerge for this system:

REQ.1 Installation space

The concept of the desired TEG is based on modular, scalable TEMs with an all-in-one

length [mm]	width [mm]	high [mm]
104	68	12

Table 3.1.: Installation space for electric device.

system. This includes a heat exchanger for exhaust gas and cooling water, a thermoelectric module, and the DC-DC converter. The defined installation space for the electric DC-DC converter is presented in Table 3.1.

REQ.2 Temperature
Due to the all-in-one concept, the electrical components are locally integrated near the waste heat. Depending on the application, the temperature ranges from 100 °C to 1000 °C [145]. A sandwich layout with a cooling heat exchanger is used for TEMs to generate a temperature gradient across the thermoelectric material. Additionally, the cooling heat exchanger is used as a heat sink for the thermal loss of the electric devices (see Figure 2.8). In this thesis, it is assumed that the temperature of the cooling water is less than or equal to 100 °C. Consequently, the electrical parts of the DC-DC converter must be specified for this temperature range.

REQ.3 Electric specifications
The electric power range of a TEM is an important criterion for the design and the specification of the converter topology. The general requirement is to support a wide range of input power independently of the thermoelectric materials or the geometry of a TEM. For the contact safety, the open circuit voltage must be lower than 60 V at the maximum current of 20 A. The primary voltage amplitude of a vehicle power supply lies between 12 V and 48 V [63, 120, 127, 128, 129, 151]. The converter should be able to support these output voltages.

3.2.1. Pre-selection of Converter Topologies

Requirements REQ.1 and REQ.2 are conflicting. The compact electric packaging results in higher thermal stress of the electric components at equal input power [62]. For this reason, this thesis exclusively focuses on non-isolated converters because of their smaller package size [64]. However, this decision excludes resonant regulators which use transformers.

Furthermore, switched capacitors [128] use capacitors with high nominal values, such as electrolyte capacitors. Unfortunately, electrolyte capacitors do not satisfy REQ.2. Thus, even switched capacitors are not useful for the desired TEG system.

In the end, only switched-mode converters have the preconditions to satisfy all practical requirements.

Additionally, only basic topologies are selected in this thesis: the buck-boost (BuBo), the boost-buck

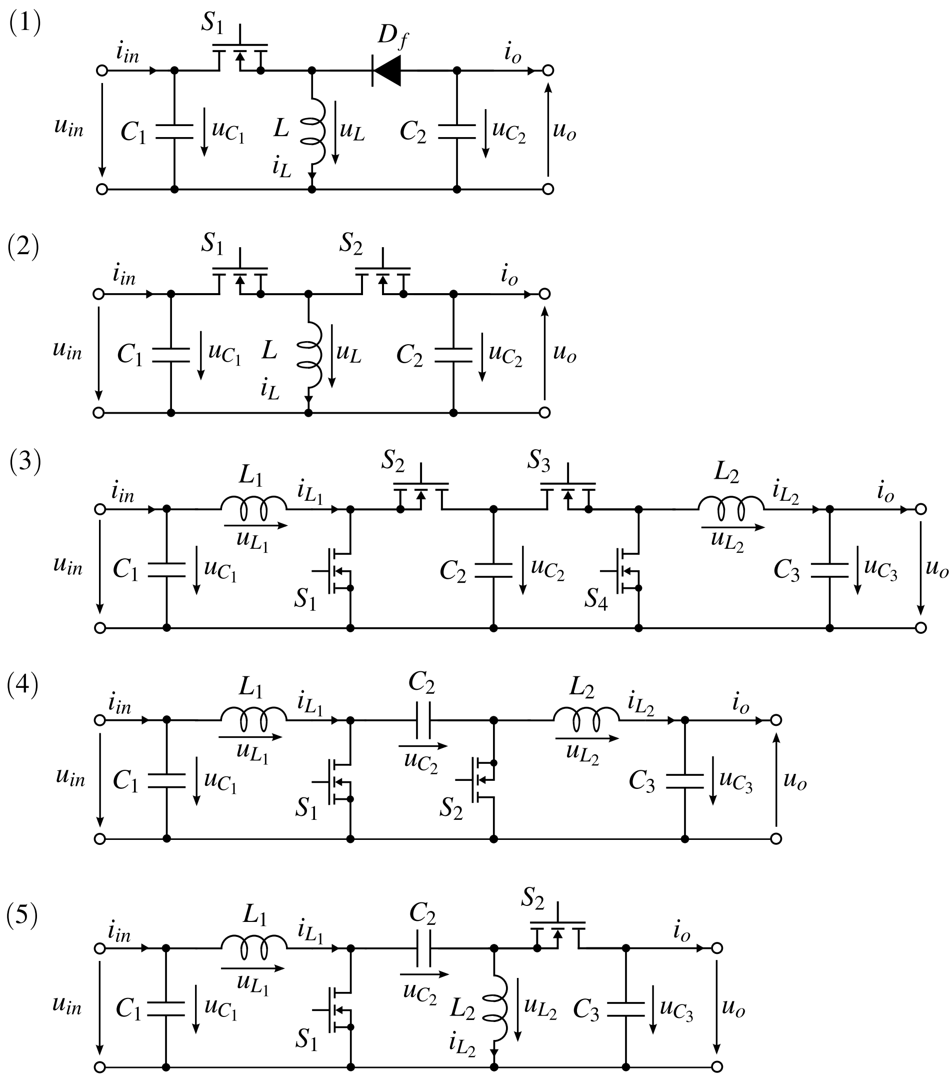

Figure 3.2.: Overview of pre-selected converter topologies: (1) non-synchronous buck-boost, (2) synchronous buck-boost, (3) synchronous boost-buck, (4) synchronous Ćuk, (5) synchronous SEPIC.

(BoBu), the Ćuk, and the SEPIC converter (see Figure 3.2). All off these converters satisfy REQ.3. The SEPIC and the boost-buck converters are non-inverted circuits. In contrast to the other three converters, the boost-buck converter has an interconnected topology based on both the boost and buck converter. Furthermore, a synchronous and a non-synchronous buck-boost converter is shown in Figure 3.2. The difference between both circuits is the selected diode as the switching element. The difference between a diode and a transistor, such as a MOSFET, is the passive and active control as well as the operating quadrant. This means that the MOSFET can be illustrated as an extended regulated diode and operates at a bidirectional current. In contrast, a diode operates only at unidirectional current but has the advantage of not needing a driver and a control signal. However, the desired forward voltage of the diode results in significantly higher power loss in contrast to a MOSFET. Therefore, diodes are less suitable for the realization of high efficiency converters [P1]. For this reason, diodes are not considered for a DC-DC converter in this thesis.

3.2.2. Functions of Converters

The basic principle of the DC-DC converters is the charging and discharging of inductors and capacitors. The magnitude of the charging energy can be regulated with the switching element. In the following, the functional principles of the BuBo, the BoBu, the Ćuk, and the SEPIC converter are briefly explained. More details of the functional principle are presented in the literature [44, 64, 106].

- **Buck-Boost**
  The BuBo converter (see Figure 3.2, (1)) uses an inductor to convert the input power into the output power. If switch S_1 is closed, the source charges the inductor L. In this time period, the output capacitor C_2 must supply the load. If the switch S_1 is open, the inductor is disconnected from the source. Consequently, the diode D_f is forward-biased and the inductor charges the capacitor C_2. This means that the voltage difference across the diode must be greater or equal as the threshold voltage, and consequently, the current amplitude must be positive. In case the voltage difference of the diode falls short of the threshold voltage, the current flow is discontinuous. This mode is called discontinuous conduction mode (DCM).
  Because the inductor current cannot change the polarity, the output voltage is inverted in contrast to the input voltage. The input capacitor C_1 is used to reduce the voltage ripple if the switch S_1 is toggled between the on and off-state.
  In case of synchronous BuBo (see Figure 3.2, (2)), the diode D_f is substituted with a MOSFET. In contrast to the diode, the state of a MOSFET is controlled by an external signal. If the MOSFET switches on, the current flow can be either positive or negative. For this reason, synchronous converters work in the continuous conduction mode (CCM) because the current flow of the MOSFET is bidirectional.

- **Boost-Buck**
  The BoBu converter (see Figure 3.2, (3)) is an interconnection between the boost and the buck converters. The boost converter can only transform the input voltage into a higher output voltage. In contrast, the buck converter can only convert the input voltage into a lower output voltage. In the BoBu converter, the boost and the buck converters are connected with a capacitor C_2. This capacitor serves as an energy buffer, which is charged from the boost converter and is discharged from the buck converter. This interconnection allows to convert the input voltage into a higher or lower output voltage amplitude.
  In the following, the functional principle of the boost and buck converters is briefly explained:

- The boost converter charges the inductor L_1 if the MOSFET S_1 is switched on. S_2 is the synchronous MOSFET to S_1. If S_1 is switched off, S_2 is switched on. Conseqeuently, the current from the inductor flows to the capacitor C_2 and increases the voltage u_{C_2}.
- The buck converter connects the capacitor C_2 to the output capacitor C_3 if the MOSFET S_3 is switched on. In this time period, the inductor L_2 is charged by the current flow of i_{L_2}. If the switch S_3 is open, the synchronous MOSFET S_4 is active. The charged inductor L_2 supplies the output during this time period.

The input and output capacitors C_1 and C_3 are used to reduce the voltage ripple during the switching process of the MOSFETs.

- **Ćuk**

  The Ćuk converter (see Figure 3.2, (4)) uses the capacitor C_2 as the primary storage element to convert the input voltage to the desired output voltage. The inductor L_1 is charged from the source if the MOSFET S_1 is activated. In this time period, the synchronous MOSFET S_2 is disconnected, and the voltage u_{C_2} of the capacitor C_2 supplies the output voltage u_{C_3}. The inductor L_2 is charged during this time periode and prevents a discontinuous current flow of i_{L_2}. To recharge the capacitor C_2 from the source, the MOSFET S_1 must be switched off and MOSFET S_2 must switched on. In this time period, the output is supplied by the current flow of inductor L_2. Since the inductor current cannot change the polarity, the output voltage u_{C_3} is inverted in relation to the input voltage. In contrast to the most of the other converter topologies, like the BuBo or the BoBu, the current i_{in} and i_o flow continuously at all states of the switches. As a result, in contrast to BuBo and BoBu converters, the voltage ripple of the input and output voltages is smaller at the Ćuk converters, albeit all converters have the same design parameters. Consequently, the capacitors of the Ćuk converter can be designed with smaller nominal values.

- **SEPIC**

  The SEPIC (see Figure 3.2, (5)) uses the capacitor C_2 for primary energy conversion between source and load, analogous to the Ćuk converter. In the time span, where MOSFET S_1 is switched on, the inductor L_1 is charged by the source, and L_2 is charged by the capacitor C_2. The load is only support from the output capacitor C_3. If the synchronous MOSFET S_2 is switched on and S_1 is off, the source is connected with the load. Consequently, the current flow from both inductors supplies the load, and the capacitor C_2 is charged simultaneously.

  The SEPIC has the advantage of continuous input current flow. However, the SEPIC has a pulsating output current i_o. In contrast to the Ćuk, the SEPIC has the same input and output polarity.

3.3. Modeling of DC-DC Converter

In Section 3.2.1, the BuBo, the BoBu, the Ćuk, and the SEPIC topologies are selected to satisfy the requirements REQ.1 - REQ.3. The electric efficiency from input power to output power should be used as an objective criterion for converter evaluation. A detailed electrical model of the DC-DC converter is necessary for the efficiency analysis. This model should be used for the dynamic and the steady-state analysis of the converter topology power loss. Furthermore, in this thesis, it is assumed that the input power source (TEM) and the sink (on-board power supply) have a low frequency characteristic in relation to the electric states of the DC-DC converters. Finally, the source and the sink can be assumed as DC values.

3.3.1. State-Space Averaging

The physical principle of DC-DC converters is based on charging and discharging inductors and capacitors with a switch element. Depending on the duration of the charging and discharging time, the magnitudes of current and voltage can be controlled. Different methods used to model switched-mode converters are presented in [37, 44, 105, 163, 179]. These methods have different basic modeling approaches. However, the models have nearly the same accuracy. The basic modeling approach includes the inductor volt-second and the capacitor amp-second balance for the steady-state analysis.
The most famous and proven method is the SSA. This method analyzes each separate state of the PWM-controlled switches and averages the electrical states over the entire switching cycle.
In the following, the SSA method is illustrated using a buck-boost converter. However, the presented modeling steps can be used for all topologies of switched-mode converters.
The PWM has a constant frequency f_{sw} with the time period $T_{sw} = 1/f_{sw}$ and the duty cycle $d = t_{on}/T_{sw}$, where t_{on} is the on-time of the MOSFET S_1. In this time period, the MOSFET conducts electricity. Assuming that the MOSFET is an ideal switch, all electrical components are linear, time-invariant, and frequency-independent.
The electrical circuit can be separated into two circuits for the two states of the MOSFETs. The separated circuits and the ideal waveforms of current and voltage for the steady-states are shown in Figure 3.3. During the period when the MOSFET S_1 is turned on, the input voltage u_{in} drops across the inductor and the current charges the inductor. In this time period, the current increases with the slope of u_{in}/L. The MOSFET S_2 is turned off and blocks the current flow from the load to the inductor. At the time $d\,T_{sw}$, the MOSFET S_1 switches off and disconnects the inductor from the source. At this moment, the MOSFET S_2 switches on and connects the inductor L to the capacitor C. Finally, the inductor charges the capacitor and supplies the load. Figure 3.3 shows that the differential equations can be determined for the inductor and the capacitor.
For the time $0 < t < d\,T_{sw}$ follows:

$$L\frac{di_L}{dt} = u_{in} \tag{3.1}$$

$$C\frac{du_C}{dt} = -i_o \tag{3.2}$$

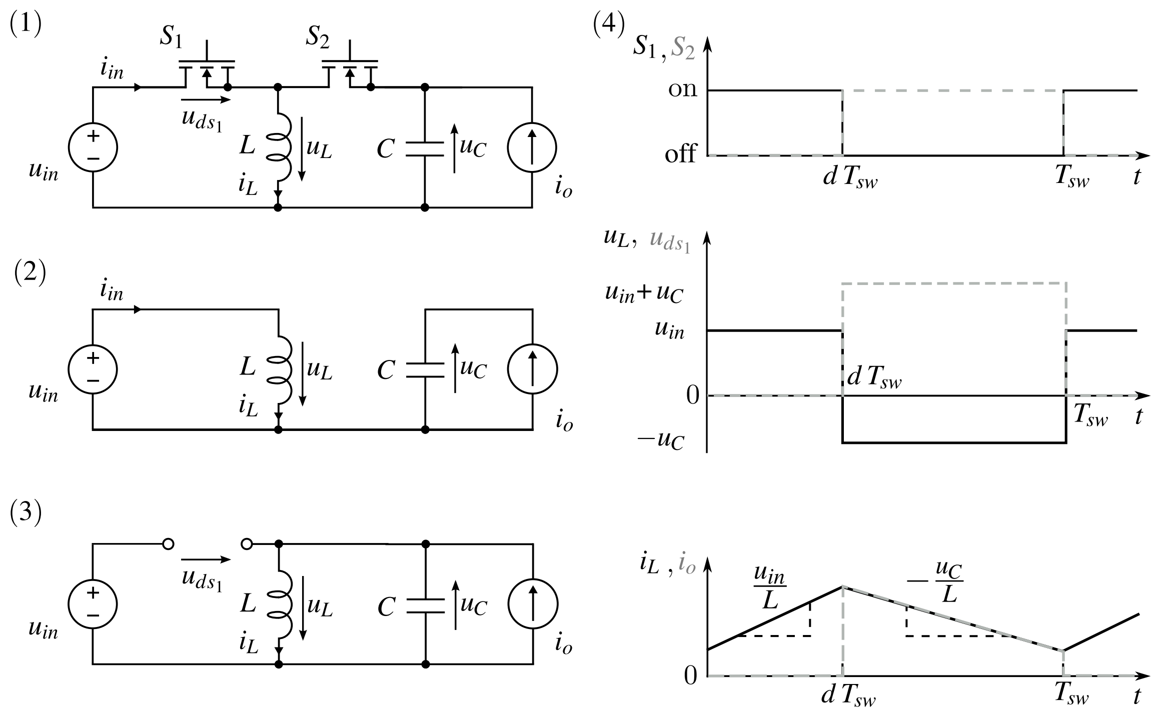

Figure 3.3.: PWM controlled buck-boost converter with separate equivalent circuits and waveforms. (1) electric circuit of boost-buck converter, (2) MOSFET S_1 is switched on and MOSFET S_2 is switched off, (3) MOSFET S_1 is switched off and MOSFET S_2 is switched on. The signal waveforms of the buck-boost converter are presented in (4).

For the time $d\,T_{sw} < t < T_{sw}$ follows:

$$L\frac{di_L}{dt} = -u_C \tag{3.3}$$

$$C\frac{du_C}{dt} = i_L - i_o \tag{3.4}$$

The variable structure between on and off-states of the switches results in a discontinuous system in relation to the switching states. The discontinuity can be neglected by time-averaging the model over one switching period T_{sw}.

Different approaches for time averaging are presented in [35, 44, 105, 163]. However, the accuracy of the models is similar if the electrical circuit is equal [105].

This thesis focuses on the modeling technique by [53, 163], which is based on the first publication of the SSA modeling [179]. Futhermore, in this thesis, it is assumed that converters only operate in the CCM, which is satisfied for synchronous converters. The SSA models with the extension of DCM are presented in [37, 162].

The SSA method assumes that the time average vector $\bar{\mathbf{x}}$ of the state $\mathbf{x}$ can be determined by following:

$$\bar{\mathbf{x}}(t) = \frac{1}{T_{sw}}\int_t^{t+T_{sw}} \mathbf{x}(\tau)d\tau \tag{3.5}$$

Furthermore, the SSA method assumes that the derivation of the state is nearly constant for the time interval T_{sw}. In relation to (3.5), the average state spaces of $\mathbf{x}_{on}$ and $\mathbf{x}_{off}$ for the time-interval $0 < t < d\,T_{sw}$

and $d\ T_{sw} < t < T_{sw}$, follow to:

$$\bar{\dot{\mathbf{x}}}(t) = \frac{1}{T_{sw}} \int_{t}^{t+T_{sw}} \dot{\mathbf{x}}(\tau) d\tau \quad (3.6)$$

$$= d\dot{\mathbf{x}}_{on} + d'\dot{\mathbf{x}}_{off}\ , \quad (3.7)$$

where d is the duty cycle t_{on}/T_{sw} of the switch S_1, and $d' = 1-d$ is the on-time of the synchronous MOSFET. In the buck-boost converter, S_2 is the synchronous MOSFET. The index of the states $\mathbf{x}$ implies the on and off-time intervals of the MOSFET S_1 from the equivalent circuit. Following from (3.1) - (3.4), and (3.7), the SSA of the buck-boost converter yields to:

$$L\frac{d\bar{i}_L}{dt} = d\ u_{in} - d'u_C \quad (3.8)$$

$$C\frac{d\bar{u}}{dt} = d'\ i_L - i_o \quad (3.9)$$

The SSA model is valid up to the maximum bandwidth of $f_{sw}/2$, which corresponds to the Nyquist theorem [P1]. In [37], an extended SSA model and a discussion on a comparison of the accuracy between the SSA and extended SSA model is presented. Nonlinearities of the semiconductors influence the high frequency dynamics of converters, which are not considered in the SSA model. Davoudi et al. [37] show, that the difference between the SSA and a numerical analysis is marginal for significant lower bandwidth of $f_{sw}/2$. However, the model accuracy of the SSA model depends on the equivalent circuit of the converter. For this reason, the equivalent series resistances (ESR) should be integrated into a circuit which presents the contact resistances of the electrical components. Figure 3.4 presents the BuBo, the BoBu, the Ćuk, and the SEPIC converter with the ESR of the electrical components.

3.3.2. Source and Load

Section 3.3.1 presents the modeling method of the converters without defined source and load. A TEM is assumed as DC voltage source u_{tem} with a series resistor r_{tem}. This resistor limits the maximum input current and influences the dynamic of the converter. Furthermore, the load is the vehicle power supply; this power grid contains a storage battery, electric loads, and an alternator. The starter can be neglected because it is only used at the start phase of the ICE, in which the TEM does not generate electric power. The equivalent electric load of the vehicle power supply is presented with voltage source e_{BL}, the equivalent battery voltages, and resistor r_{bl} (see Figure 3.5).
In contrast to the dynamic of the converters, the dynamic changes of the load and source of the converters can be neglected [28, 70].

3.3.3. Models of DC-DC Converters

The SSA models of the converters from Figure 3.4 are presented in the Appendix A.1 with the assumed load and source from Section 3.3.2.

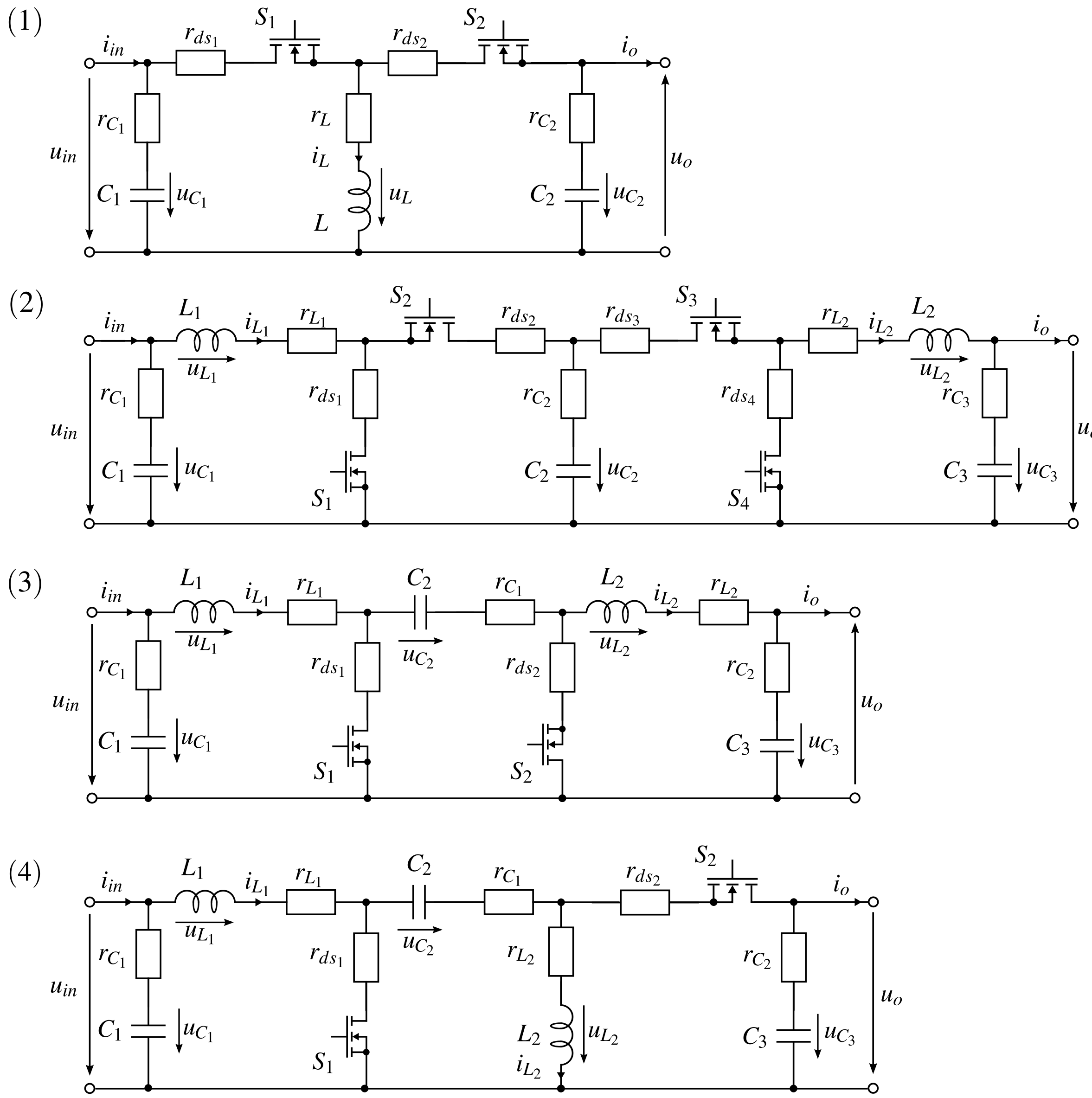

Figure 3.4.: DC-DC converters with ESR: (1) synchronous buck-boost, (2) synchronous boost-buck, (3) synchronous Ćuk, (4) synchronous SEPIC.

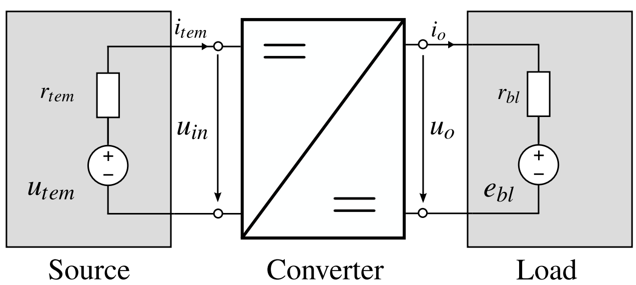

Figure 3.5.: Power grid with a TEM, a converter and an equivalent vehicle power supply.

3.4. Power Losses of DC-DC Converters

Converter power losses are an important criterion for the comparison of different DC-DC converters. Generally, the power loss can be divided into DC and AC components. The DC power loss of electrical components can be simply specified with the data sheets because the values have a high confidence range. In contrast, the dynamic power losses often have higher uncertainties, caused by unknown parameters, inaccurate data, or estimation models. The power loss of a converter P_{loss} is assumed as

$$P_{loss} = P_{dc} + P_{ac} + P_{drv} \ , \tag{3.10}$$

where P_{dc} is the ohmic power loss, P_{ac} is the dynamic frequency dependent loss, and P_{drv} is the driver power loss. The dynamic loss can be divided into three parts:

$$P_{ac} = P_{sw} + P_{sw,sy} + P_{ind} \ , \tag{3.11}$$

where P_{sw} is the loss of the MOSFET, $P_{sw,sy}$ is the loss of the synchronous MOSFET, and P_{ind} is the magnetic loss. In the following, the different models of the power losses are presented. The aim is to determine a power loss model by using known parameters from data sheets. Complex and specific measurements could thus be avoided.

3.4.1. Ohmic Power Loss

The ohmic power loss is a significant characteristic in DC-DC converters. Every electric component has an ohmic value. The current flow causes heat loss and can be determined as follows:

$$P_{dc} = I^2 \ r \ , \tag{3.12}$$

where I is the DC current value in a switching period and r is the resistor. The ohmic power loss is indirectly integrated into the SSA model with the ESR values of the electric components.

3.4.2. Dynamic Power Loss

The minimization of the packing size of converters is associated with the switching frequency of the MOSFETs. The switch time is proportional to the energy charge of the energy storing elements. Along with the reduction of energy charge, the nominal size of the electric components can be reduced. However, a rising switching frequency results in a higher charge and discharge stress of the MOSFETs and the storage elements. Within this time interval, parasitic inductive, and capacitive components cause dynamic power losses. [44]
Consequently, a closer examination of the factors of these losses is necessary. The aim is to determine a loss model for the dynamic power losses caused by the switching.

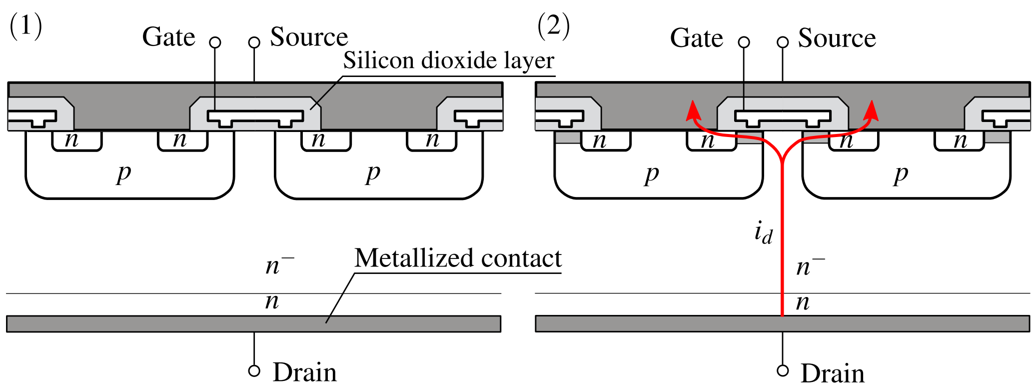

Figure 3.6.: Cross-section of DMOSFET [44]. (1) off-state of power MOSFET. The n^- layer is high-ohmic. (2) a channel is formed under the gate if $u_{gs} > u_{th}$. The n^- layer is low-ohmic; the current i_d flows from drain to source.

Switching Power Loss

To estimate the switching power loss, an analysis of the MOSFET switching process is necessary. In Figure 3.6, a cross-section of a double-diffused metal-oxide semiconductor field effect transistor (DMOSFET) is presented. This type of MOSFET is typically used for higher current amplitudes because of the lower resistor values in the on-state. In case the voltage across drain and source $u_{ds} > 0$ V, the p-n^- and also p-n doted semiconductors[1] are reversely biased, and the MOSFET is in the off-state. The potential from gate to source is u_{gs}. If u_{gs} is higher than the threshold-voltage u_{th}, an inversion layer is formed under the gate in the p junctions. This means that a channel connects the source to the n^- junction and the drain. Due to the direct connection, the n^- region is inundated with free charge carriers. Thus, the resistance of drain to source r_{ds} is drastically reduced. This case is called the on-state of the MOSFET. [44]
The p-n^- junction is called the body-diode, which is parallel to drain and source connectors. Then drain to source voltage $u_{ds} < 0$ V, the diode is forward-biased and the drain current can flow from the source to the drain.
Furthermore, the junctions represent parasitic capacitances: gate to source C_{gs}, drain to source C_{ds}, and gate to drain C_{gd} (see Figure 3.7). These capacitance values depend on u_{ds} and switching frequency f_{sw}. The equivalent circuit model is used for the analysis of the switch time period (see Figure 3.8) [104, 142]. The turn on and off waveforms of a MOSFET are qualitatively shown in Figure 3.9. The turn on and off process of the MOSFET is segmented in ten time periods, which are explained in the following [9, 44, 104, 175]:

$t_1 - t_2$: The PWM signal changes the logical level from 0 to 1. The driver connects the gate to the driver voltage U_{drv}. The driver voltage charges the input capacitance of the MOSFET, and

[1] The index of the doted semiconductors presents the quantity of the dotation [152].

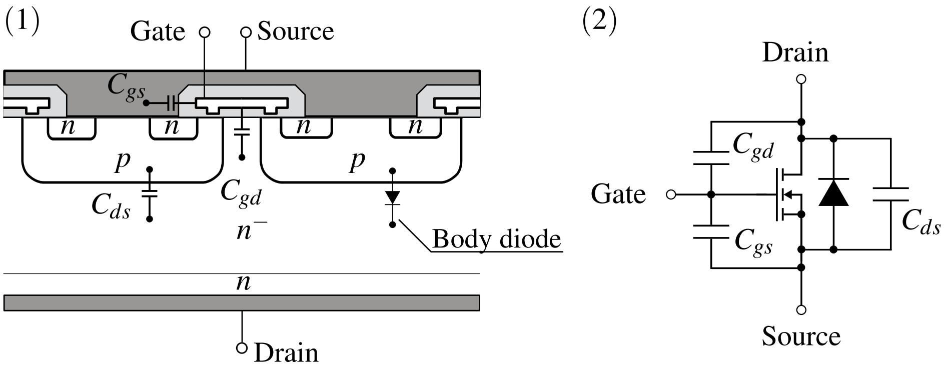

Figure 3.7.: Parasitic effects of a power MOSFET [44]. (1) DMOSFET with the body diode and capacitances. (2) the equivalent circuit of the MOSFET with body diode and capacitances.

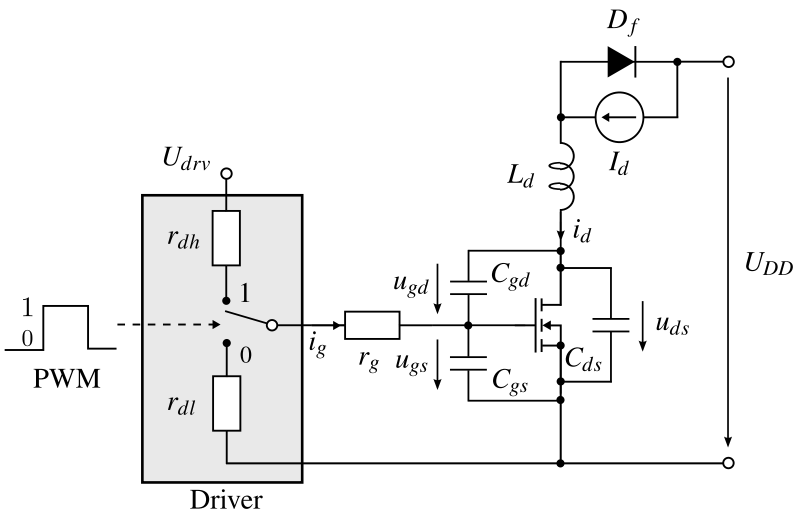

Figure 3.8.: Equivalent circuit of the MOSFET, based on [104, 142].

the voltage signal of the gate source u_{gs} is approximated by

$$u_{gs} = U_{drv}\left(1 - e^{-\frac{t-t_1}{\tau_d}}\right) , \tag{3.13}$$

where $\tau_d = (r_{dh} + r_g)C_{iss}$ is the rise time of the gate voltage to the threshold voltage u_{th} and $C_{iss}(u_{gd}) = C_{gs} + C_{gd}$ is the charge capacitance.

$t_2 - t_3$: If $u_{gs} = u_{th}$, the current i_d increases up to I_d in the time period t_{ri}. In this time period the MOSFET is in the saturation region. The drain current induces the voltage u_{ld} across the parasitic inductor L_d. The voltage u_{ds} is determined by

$$u_{ds} = U_{DD} - u_{ld} = U_{DD} - L_d \frac{di_d}{dt} . \tag{3.14}$$

When i_d reaches I_D, the freewheeling diode D_f switches from the forward to the recovery-biased. This freewheeling diode represents the electrical characteristic of the body diode from the MOSFET in a switch process. The stored minority charge must be removed before

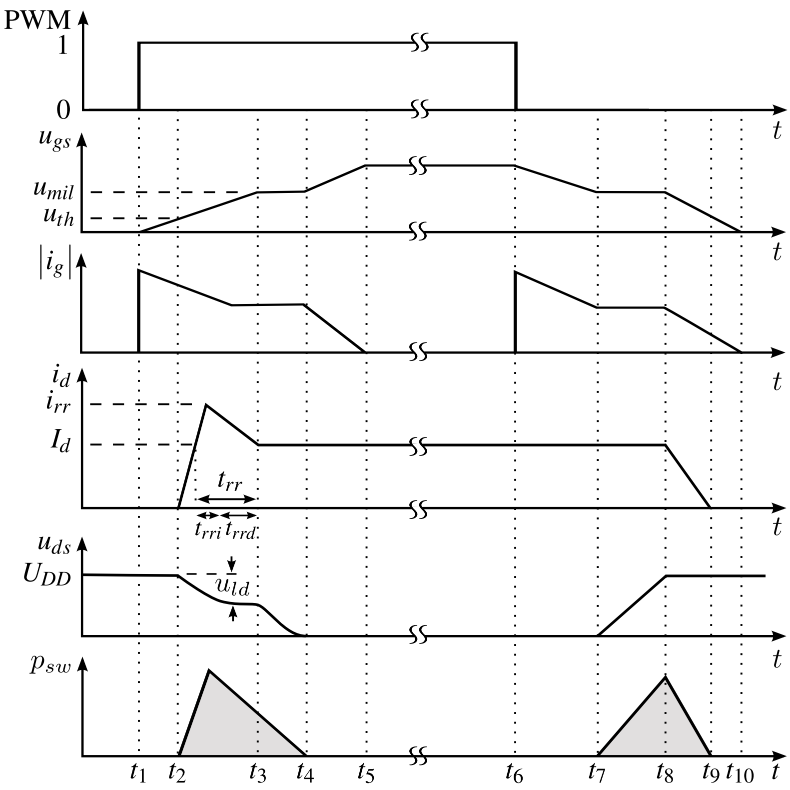

Figure 3.9.: Qualitative switching waveforms with an on and off turn.

the diode changes to the non-conducting state. In the time period (t_{rri}), the current increases to i_{rr} and then drops down to I_d in the time period t_{rrd}. The necessary reverse recovery charge Q_{rr} for the body diode yields to the following:

$$Q_{rr} = \int_{t_2+t_{ri}}^{t_{rr}} (i_d(t) - I_d)dt \tag{3.15}$$

$$\approx \frac{1}{2} t_{rr}(i_{rr} - I_d) \ , \tag{3.16}$$

where $t_{rr} = t_{rri} + t_{rrd}$ is the reverse recovery time.

$t_3 - t_4$: The freewheeling diode D_f starts to block the voltage U_{DD}. The voltage u_{ds} decreases to the Miller voltage u_{mil}. The rapid reduction of u_{ds} changes the polarity of u_{gd} and the current of the driver discharges C_{gd}. In this time periode t_{fu}, the voltage u_{gs} is constant at the Miller plateau voltage. The MOSFET changes from the saturation to the ohmic region. The changing of the drain to source voltage can be approximated with the following:

$$\frac{du_{ds}}{dt} = -\frac{U_{drv} - u_{mil}}{(r_g + r_{dh})C_{gd}} \tag{3.17}$$

$t_4 - t_5$: The capacitor C_{gd} is discharged. The gate to source voltage u_{gs} increases to U_{drv} and the drain to source voltage reaches the minimal voltage magnitude. The turn on process is considered to be completed.

$t_5 - t_6$: In this time period, the current and the voltage of drain to source are nearly constant. Power loss only depends on the drain to source resistor r_{ds}.

$t_6 - t_7$: The PWM signal changes the logic level from 1 to 0. The driver connects the gate to the ground, and the voltage of the capacitance $C_{iss}(u_{ds}) = C_{gd} + C_{gs}$ discharges according to the following approximation curve function:

$$u_{gs} = U_{drv}\left(e^{-\frac{t-t_7}{\tau_i}}\right) , \tag{3.18}$$

where $\tau_i = (r_{dl} + r_g)C_{iss}$.

$t_7 - t_8$: The voltage u_{gs} reaches the Miller plateau. The MOSFET changes from the ohmic region to the saturation region, and the voltage u_{ds} increases. The charge of the gate to drain capacitor discharges to the ground. In this time period, the voltage u_{gs} is nearly constant.

$t_8 - t_9$: The blocked voltage of the diode drops down, and the current I_d is bypassed from the MOSFET to the diode in this time period. At the same time, u_{gs} decreases. At the moment where $u_{gs} = u_{th}$, the inversion layer of the MOSFET collapses.

$t_9 - t_{10}$: The values of the drain current and drain to source voltage are steady. The MOSFET operates in the saturation region. The remaining charge carriers of the C_{iss} discharge to the ground. The turn off process of the MOSFET is accomplished.

In the literature, different model techniques for switching power loss are presented. These models can be classified as physics-based, behavioral, and analytical models. The physics-based and behavioral models are characterized by accurate simulation results. However, detailed material data, which are not specified from the manufacturers, are essential for analysis. In contrast, the analytical models are based on piecewise linear approximation of the signal waveforms from the MOSFET, which is parametrized with data sheet values given by the manufacturers. This method yields closed-form mathematical expressions, which are useful for the following analyses. [41]

It is assumed that parasitic inductance from the PCB or MOSFETs can be neglected since the inductive power loss is not significant for the analysis with a switching frequency up to 500 kHz [41, 137]. This means that L_d (cf. Figure 3.8) is negligible.

From the power loss p_{sw} of the MOSFET (cf. Figure 3.9), the mean switching power loss of the MOSFET P_{sw} follows to:

$$P_{sw} = \frac{1}{T_{sw}} \int_t^{t+T_{sw}} p_{sw}(\tau) d\tau = \frac{1}{T_{sw}} \int_t^{t+T_{sw}} i_d(\tau)\, u_{ds}(\tau)\, d\tau \tag{3.19}$$

The power loss caused from r_{ds} is a DC loss and is estimated with (3.12). The presented turn on waveform (cf. Figure 3.9) illustrates the worst-case scenario for the switching power loss. This means that the voltage u_{ds} falls down to zero after the current i_d has reach the steady-state. The switching loss of turn

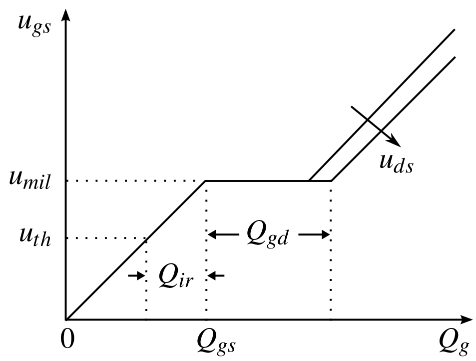

Figure 3.10.: Relation between the gate voltage and gate charge.

on period is approximated as

$$P_{sw,on} = \frac{1}{T_{sw}} \left(\frac{1}{2} U_{DD}\, I_d\, (t_{ri} + t_{fu}) + Q_{rr} U_{DD} + I_d t_{rr} \right) , \tag{3.20}$$

where $t_{ri} = t_3 - t_2$, $t_{fu} = t_4 - t_3$, and Q_{rr} is the reverse recovery charge.
Vice versa, the switching loss in the turn off period yield

$$P_{sw,off} = \frac{1}{T_{sw}} \left(\frac{1}{2} U_{DD}\, I_d\, (t_{ru} + t_{fi}) \right) , \tag{3.21}$$

where $t_{ru} = t_8 - t_7$ and $t_{fi} = t_9 - t_8$.
The fall and rise time of current and voltage ($t_{fi},\ t_{ri};\ t_{fu},\ t_{ru}$) can be estimated by the curve of $u_{gs}(Q_g)$ from the MOSFET data sheet [78]. A qualitative diagram for a constant gate current i_g is presented in Figure 3.10. The necessary charge for the switch process of the MOSFET can be estimated from the diagram. The fall and rise time of the current and voltage are estimated from the gate charge and the equivalent MOSFET circuit (see Figure 3.8) as follows:

$$t_{ri} = \frac{2\, Q_{ir}\, (r_{dh} + r_g)}{2\, U_{drv} - u_{mil} - u_{th}} \tag{3.22}$$

$$t_{fu} = \frac{Q_{gd}\, (r_{dh} + r_g)}{U_{drv} - u_{th}} \tag{3.23}$$

Equally, the time periods for the turn off process yield

$$t_{ru} = \frac{Q_{gd}\, (r_{dl} + r_g)}{u_{th}} \tag{3.24}$$

$$t_{fi} = \frac{Q_{ir}\, (r_{dl} + r_g)}{U_{drv} + u_{th}} . \tag{3.25}$$

Finally, the dynamic power loss of the MOSFET yields:

$$P_{sw} = P_{sw,on} + P_{sw,off} \tag{3.26}$$

Synchronous Switching Power Loss

The MOSFET of the DC-DC converter is used to connect the energy source or load to a storage element. The classic converter topology uses a diode to block a direct current flow from the load to the source.

After the MOSFET is turned off, the diode is forward-biased and connects storage elements to the load. The forward voltage of a power diode is not less than 0.5 V. Consequently, the forward-biased power loss can be significant in a DC-DC converter. [185]
The alternative to a diode is a synchronous MOSFET (SY-MOSFET) (cf. Figure 3.2). It has a parasitic body-diode, which conducts the current from the source to the drain, even if u_{gs} is zero. If $u_{gs} > u_{th}$, the diode is bypassed and the loss only depend on r_{ds}. These loss is typically lower than the diode power loss. Typical values of the drain to source resistor are 10 mΩ to 100 mΩ.
To control the MOSFET and the SY-MOSFET, a dead time t_{dt} between the PWM signals is used to prevent a shoot-through. During this dead time, the body-diode of the SY-MOSFET is forward-biased. The loss for this time period t_{dt} can be approximated with the following [112]:

$$P_{sydt} = \frac{1}{t_{dt}} \int_{t}^{t+t_{dt}} \left(u_F(\tau)\, i_d(\tau) + i_d^2(\tau)\, r_{df} \right) d\tau \,, \tag{3.27}$$

where r_{df} is the internal forward resistor and u_F is the forward voltage of the body diode. During the turn off period, the charge of the body-diode has to recover in order to block the current. The loss can be estimated as follows:

$$P_{syrr} = \frac{1}{T_{sw}} Q_{rr} U_{DD} \tag{3.28}$$

The whole switch power loss of a the SY-MOSFET yields to

$$P_{sw,sy} = P_{sydt} + P_{syrr} \,. \tag{3.29}$$

Magnetic Power Loss

An inductor consists of a wound wire around a core and is used to store energy in the magnetic field. Most inductors use ferromagnetic cores on account of their high permeability. The charging and discharging of energy in the magnetic field cause loss in the core P_{core}, which can be factorized into three parts: the hysteresis P_{hys}, the eddy P_{eddy}, and the excess losses P_{exe}. [135]
The hysteresis loss is caused by changing of the magnetization in a core material. Which can be illustrated as the necessary energy to change the magnetization in the domain walls. This energy is depended on the volume of the core and the permeability of the material. [13, 65].
Furthermore, the magnetic field induces an additional current flow in the core material itself. This current flow is called eddy current and cause a loss P_{eddy} in the resistance of the core. [44]
The excess (or anomalous) loss [13] comprises every loss that results from local non-homogeneous magnetization of the material, which is caused by the grain size, for example [13, 113]. The influence of the grain size on the material is illustrated in [87].
To determine the core loss, different methods are presented in the literature: hysteresis model, empirical equations, and loss-separation. The hysteresis model has the highest accuracy of the methods, although a variety of parameters are necessary for the calculation. However, these parameters must be determined by extensive and accurate measurements. The loss-separation is similar to the empirical equations. Both

methods use a parameter-based calculation to estimate the core loss. The empirical equations are comparable with a curve fitting of the core hysteresis. In contrast, the loss-separation method uses the energy conservation law. [135]

A famous and proven method is the empirical Steinmetz equation (SE), which are used to estimate the loss for sinusoidal signals. Furthermore, the most data sheets include the parameters for the SE. Several modifications of the basic Steinmetz equation [159] are published for non-sinusoidal signals, the modified Steinmetz equation (MSE) [3], the generalized Steinmetz equation (GSE), the improved generalized Steinmetz equation (iGSE) [114], and the improved-improved generalized Steinmetz equation (i^{2}GSE). All these Steinmetz equations have some variety extensions to enclose frequency and non-linear effects. An overview and a comparison of these models are presented in [79, 113].

However, the aim of all approaches is to represent an accurate core loss model. The accuracy of all the SEs depends on the application and, especially, the confidence interval of the model parameters. Due to the relatively simple parametrization, the following MSE has been chosen in this thesis [135]:

$$P_{core} = k_c f_{eq}^{\alpha_c - 1} B^{+\beta_c} + k_{ce} f_{eq}^2 B^{+2} \ , \tag{3.30}$$

where k_c, k_{ce}, α_c, β_c are fitting parameters, f_{eq} is the equivalent frequency for a non-sinusoidal signal, and B^+ is the maximum of the flux density. The flux density is proportional to the volt-second of the inductor voltage u_L:

$$B \sim \frac{1}{T_{sw}} \int_t^{t+T_{sw}} u_L(\tau) d\tau \tag{3.31}$$

The MSE is based on the assumption that the power loss exclusively depend on the changes from the flux density. The voltage signal about the inductor in a DC-DC converter is a square-wave signal. The equivalent frequency for a square-wave signal in relation to a sinusoidal signal can be estimated with Fourier analysis. Comparison of the Fourier components between these both signals result to [135, 171]:

$$f_{eq} = \frac{2 \int_t^{t+T_{sw}} \left(\frac{dB(\tau)}{d\tau} \right)^2 d\tau}{(2\,\pi\, B_{pp}\, 0.5)^2}, \tag{3.32}$$

where B_{pp} is the peak-to-peak value of flux density.

Furthermore, with the relation of the inductor current signal and the duty cycle d of the DC-DC converters, the equation (3.32) can be re-written as [30, 65, 113, 114]:

$$f_{eq} = \frac{f_{sw}}{2\pi\,(d - d^2)} \tag{3.33}$$

Apart from the core loss, the AC current results in an increase of copper loss, which are caused by the proximity and the skin effects.

The magnetic field of a nearby conductor, such as the windings of a multilayer inductor, induces voltage in the conductor and causes an eddy current. Consequently, the current density can be increased or decreased in relation to the current flow direction, which is called the proximity effect. [65]

It is assumed in this thesis, that the inductors only have single layer windings to minimize the packing size, which is necessary to satisfy REQ.1 and REQ.2. Hence, the proximity effect is neglected.
The skin effect is based on the fact that the AC current induces a magnetic field in the conductor. This magnetic field generates an eddy current, which flows in a direction opposite to the center of the conductor. As a result, the current flows cancel each other in the center of the wire, and the AC current is moved to the surface. Consequently, the current is concentrated in a smaller area of the conductor, which increases the resistance [65].
For the assumption of a single layer winding, the AC resistor loss of the inductor causes by the skin effect can be simplified to

$$P_{l_{ac}} \approx \frac{l_w}{2r_w}\sqrt{\frac{\mu_o \rho_w f_{sw}}{\pi}}\frac{1}{T_{sw}}\int_t^{t+T_{sw}} i_L^2(\tau)d\tau \ , \tag{3.34}$$

where ρ_w is the resistivity, μ_o the permeability, l_w is the length, and r_w is the radius of the wire. [65]
Finally, the total AC loss of the inductor is determined as follows:

$$P_{ind} = P_{l_{ac}} + P_{core} \tag{3.35}$$

3.4.3. Driver Power Loss

The power for the direct control of the MOSFET is supply by the driver. With a piecewise linear approximation of the driver circuit (see Figure 3.8), the loss is determined by [9, 78, 99]

$$P_{drv} = P_{drv,on} + P_{drv,off} \tag{3.36}$$

$$P_{drv,on} = \frac{1}{T_{sw}}\frac{1}{2}\frac{r_{dh}U_{drv}Q_g}{r_{dh}+r_g} \tag{3.37}$$

$$P_{drv,off} = \frac{1}{T_{sw}}\frac{1}{2}\frac{r_{dl}U_{drv}Q_g}{r_{dl}+r_g} \ . \tag{3.38}$$

3.5. Analysis and Assessment

For the evaluation of different topologies, a quality value is used to obtain an objective comparison. In contrast to the application requirements outlined in Section 3.2, the electric efficiency η is selected as the evaluation criterion between the different convert topologies. In respect to (3.10), the electric efficiency of a converter is defined as:

$$\eta = \frac{P_{out}}{P_{in}} = \frac{P_{in} - P_{loss}}{P_{in}} \ , \tag{3.39}$$

where $P_{in} = u_{in} \cdot i_{in}$ is the input power, $P_{out} = u_o \cdot i_o$ is the output power, and P_{loss} is the power loss of the DC-DC converter.
The efficiency is a function that depends on the electrical states of the converter, but also on the parameters of the electrical components, and the switching frequency:

$$\eta = f(u_{in}, i_{in}, e_{bl}, f_{sw}, L, C, \ldots) \ . \tag{3.40}$$

In this context, the electrical components need to be defined first in order to reduce the degree of freedoms for the efficiency analysis. The electrical states can be determined for a specific input power. This result can be used to analyze the relation between the efficiency and the switching frequency for different output voltages of the converters. For a specified switching frequency, the converter efficiency is analyzed in detail for a specific load voltage. The aim of the analysis is to select a converter with the optimal fitness for linking the recovered electrical power of the TEG to electrical load.

3.5.1. Parametrization of Electric Components

The efficiency of DC-DC converters depends on the electrical states of the converters as well as the active and passive electrical components. To compare different converters, the components and their ratios to the ESR must be normalized. Tha maximal allowed current ripple Δi and voltage ripple Δu can be defined as parameter criterions for the nominal values of inductors and capacitors. [44, 64]
In this thesis is assumed that the impedance of the inductors and capacitors are frequency-independent. The ESR value depends on the material and type of the components. If material properties and packaging of the inductors are equal, the ESR value r_L depends on the number of turns. Thus, it can be assumed that

$$r_L \sim L\,. \tag{3.41}$$

Furthermore, the relation of the capacitor ESR r_C depends on the dielectric material. However, in practical applications, capacitors are connected in parallel to compensate for the ESR. For this reason, the ESR value of the capacitors r_C is defined as follows:

$$r_C \approx const. \tag{3.42}$$

The parameters of the components must be selected from data sheets. It can be assumed from the analysis in [33] that the DC loss is the significant loss of MOSFETs. For this purpose, MOSFETs with small r_{ds} for the conducting state should be chosen. However, MOSFETs with lower drain source resistor values have higher parasitic capacitance values. For a minimal switching loss, a low capacitance is preferable, but drain-source resistor and capacitance are dependent on the package size. A separated optimization of both values is impossible.
A standard component which supports low and high-side MOSFETs with a bootstrap circuit is selected for the driver. The selected parameters and semiconductors are presented in Table 3.2.

3.5.2. Analysis of Switching Frequency and Output Voltage

Using the selected parameters (see Table 3.2), the efficiency is a function which depends on the states of the converter, the desired output voltage, and the switching frequency:

$$\eta = f(u_{in}, i_{in}, e_{bl}, f_{sw}) \qquad \text{for BuBo, Ćuk, SEPIC} \tag{3.43}$$

$$\eta = f(u_{in}, i_{in}, e_{bl}, f_{sw}, u_{C_2}) \qquad \text{for BoBu} \tag{3.44}$$

parameter	Value	Reference of component
Δu_C	$0.06 \cdot U_C$	-
Δi_L	$0.18 \cdot I_L$	-
L/r_L	$1.1\text{kH}\,\Omega^{-1}$	IHLP-6767GZ (Vishay)
k_c	99.98	IHLP-6767GZ (Vishay)
α_c	1.173	IHLP-6767GZ (Vishay)
β_c	2.213	IHLP-6767GZ (Vishay)
k_{ce}	0.0109	IHLP-6767GZ (Vishay)
r_C	0.1 Ω	CGA9 (TDK)
r_{dh}	4 Ω	UCC27201 (TI)
r_{dl}	4 Ω	UCC27201 (TI)
r_g	1.5 Ω	-
U_{drv}	12 V	-
MOSFETs	-	IPP80N06S2L-07 (Infineon)
r_{bl}	0.1 Ω	-

Table 3.2.: Parameters for analysis. U_C and I_L are the DC values of the capacitor voltage and inductor current.

The input voltage and the current are limited by the requirement REQ.3. The switching frequency and the influence of the output voltage should be analyzed. Generally, the PWM signals of the MOSFETs are generated by an microcontroller (μC). Typically supported switching frequencies of a μC are 50 kHz to 250 kHz. The output voltage e_{bl} range between 12 V up to 48 V, and typical values are 12 V, 24 V, and 48 V. The efficiency η is defined for an operation point only, but REQ.3 allows a wide input power range. To compare the different DC-DC converters for the whole input power range, the average efficiency of the input power is selected

$$\bar{\eta} = \frac{1}{i_{max}} \frac{1}{u_{max}} \int_0^{i_{max}} \int_0^{u_{max}} \eta\left(u_{in}, i_{in}, e_{bl}, f_{sw}, u_{C_2}\right) du_{in}\, di_{in} \ , \tag{3.45}$$

where $i_{max} = 20$ A, $u_{max} = 60$ V, and $\bar{\eta}^+$ is the maximum average efficiency.
In the analysis, the input voltage u_{in} is always the half amplitude of the open circuit voltage u_{tem}. This implies that the TEM operates in its maximum power point.
In Figure 3.11, the average efficiency is presented in relation to the output voltage and the frequency f_{sw}. In all converters, the maximum average efficiency is reached between 50 kHz and 100 kHz. Within this frequency area, the sum of the losses from inductors and MOSFETs reaches its minimum. This is plausible because when frequency increases, the nominal inductor and capacitor values decreases. Consequently, the ESR also decreases. In contrast, the switching loss increases proportionally in relation to the switching frequency. Hence, the dynamic losses of the passive and active electric components have a global minimum; whereas the explicit frequency range of that minimum depends on the electric compo-

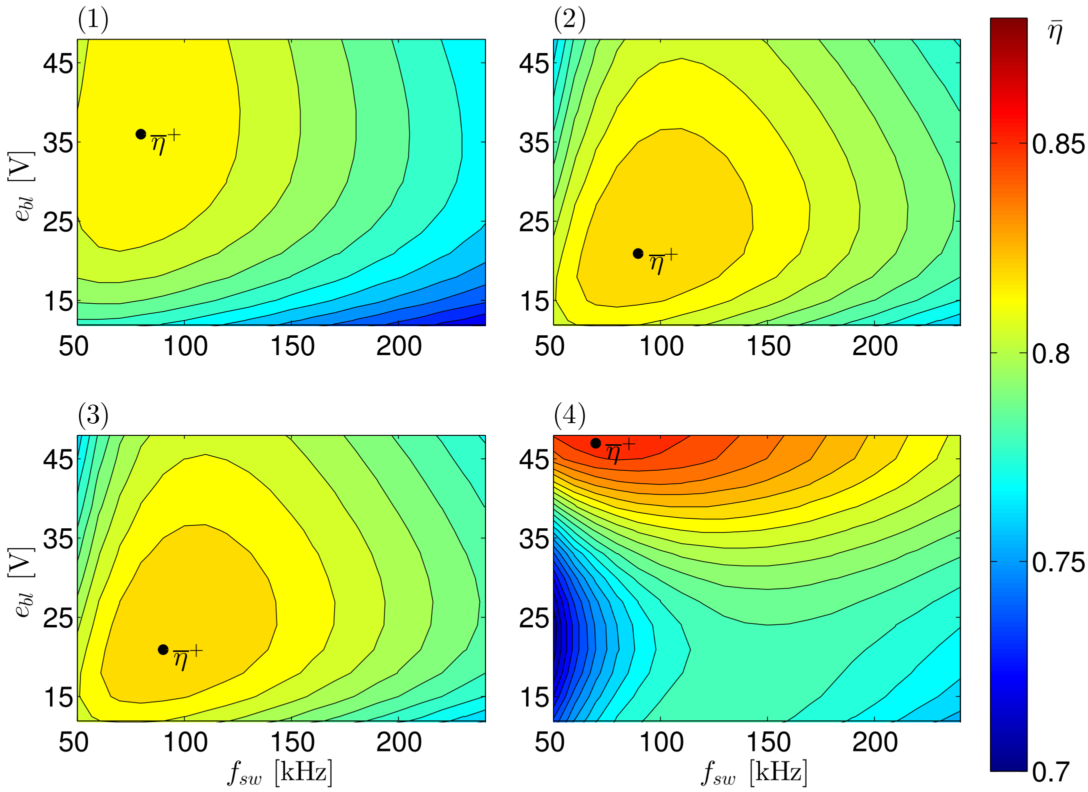

Figure 3.11.: Analysis of efficiency as a function of the output voltage and switching frequency. (1) buck-boost converter, (2) Ćuk converter, (3) SEPIC converter, (4) boost-buck converter with $u_{C_2} = 48$ V.

nents. The mean efficiency of the converters differs by up to 10 % in the analyzed switching frequency range.

The influence of the increasing output voltage results in a general reduction of DC loss in all converters. The DC loss decreases squarely (cf. (3.12)), while output voltage increases and the output current decreases linearly. Therefore, the maximum mean efficiency of converters is reached for a higher output voltage, whereas the output current decreases. This can be best observe in the efficiency map of the boost-buck and buck-boost converters (see Figure 3.11). In contrast, the Ćuk and the SEPIC converters have a maximum efficiency for a output voltage between 20 V and 37 V, although DC loss decreases at higher voltages. The efficiency slightly falls at higher voltages because the conversion ratio from input to output voltage results in higher switching loss. Detailed results regarding the losses are presented in the Appendix A.2.

The boost-buck converter has an additional degree of freedom, the amplitude of u_{C_2}. This value can be selected in the following range: $\max(u_{in}, e_{bl}) < u_{C_2} < 60$ V. The results of the analysis for different u_{C_2} values are presented in Figure 3.12. With the increase of voltage from capacitor C_2, the efficiency of the BoBu converter is shifted as well. The highest efficiency is obtained when the difference between u_{C_2} and the output voltage is minimal. The inductor voltage and the DC current amplitude cause this effect. On the one hand, the voltage drop over the output inductance is minimal if $u_{C_2} \approx u_o$ and, consequently, the

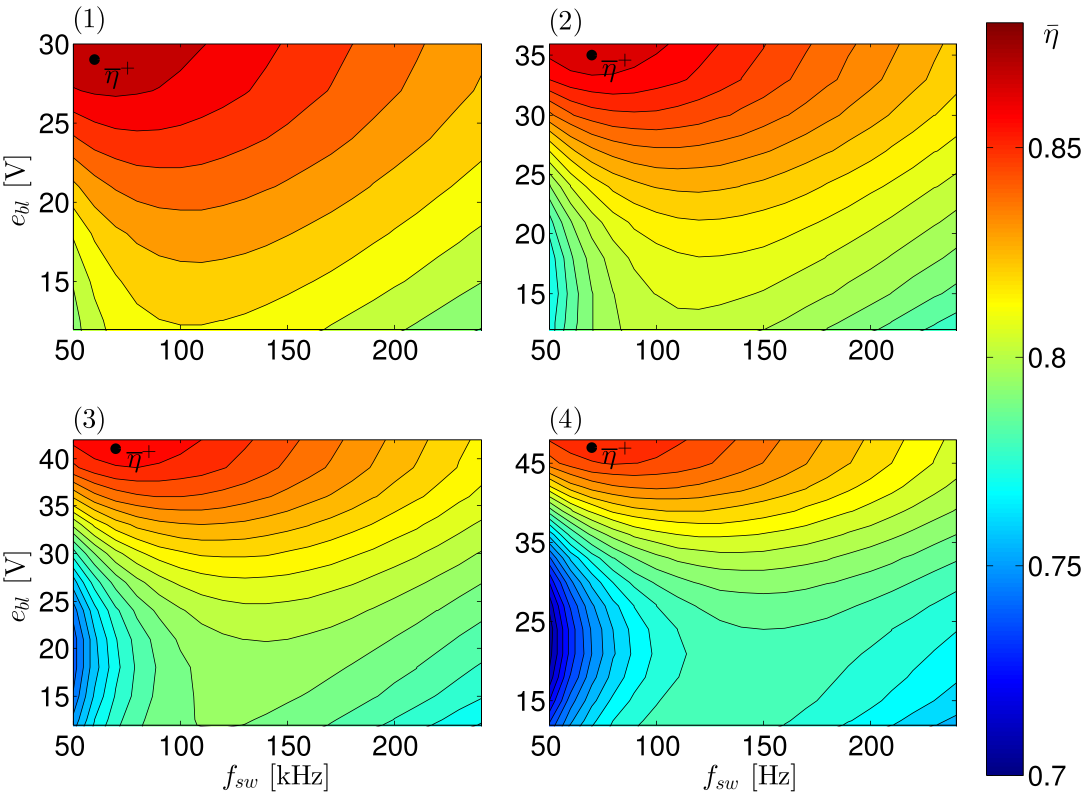

Figure 3.12.: Analysis of efficiency as a function of the output voltage and the switching frequency from a boost-buck converter. (1) nominal voltage of $u_{C_2} = 30$ V, (2) nominal voltage of $u_{C_2} = 36$ V, (3) nominal voltage of $u_{C_2} = 42$ V, (4) nominal voltage of $u_{C_2} = 48$ V.

inductor loss is minimal. On the other hand, DC loss is minimal if the magnitude of the output voltage increases because the output current amplitude decreases (cf. Appendix A.2).

Conclusion

The analysis of the influence of switching frequency reveals that the mean switching loss is contrary to the mean magnetic loss. This is plausible because the core loss and copper loss of the inductor decrease when the switching frequency increases causes by decreased nominal parameter values. As a consequence, the necessary energy for the switching process of the MOSFETs increases simultaneously. The result is a locally bounded switching frequency between 50 kHz to 100 kHz, where efficiency is maximal for all converters. For further analysis, the switching frequency of 100 kHz is selected, because a higher frequency is beneficial for the packing size of the passive electrical components.
In contrast, the DC loss is independent from the selected switching frequency. Hence, for a specified input power, the DC loss decreases at higher output voltage because the output current amplitude decreases. However, the ratio of input voltage to output voltage results in a higher voltage stress of the MOSFETs and increases the switching loss. This effect is significant in the Ćuk and the SEPIC converters for voltages above nearly 30 V. In the boost-buck converter, the desired voltage value u_{C_2} has

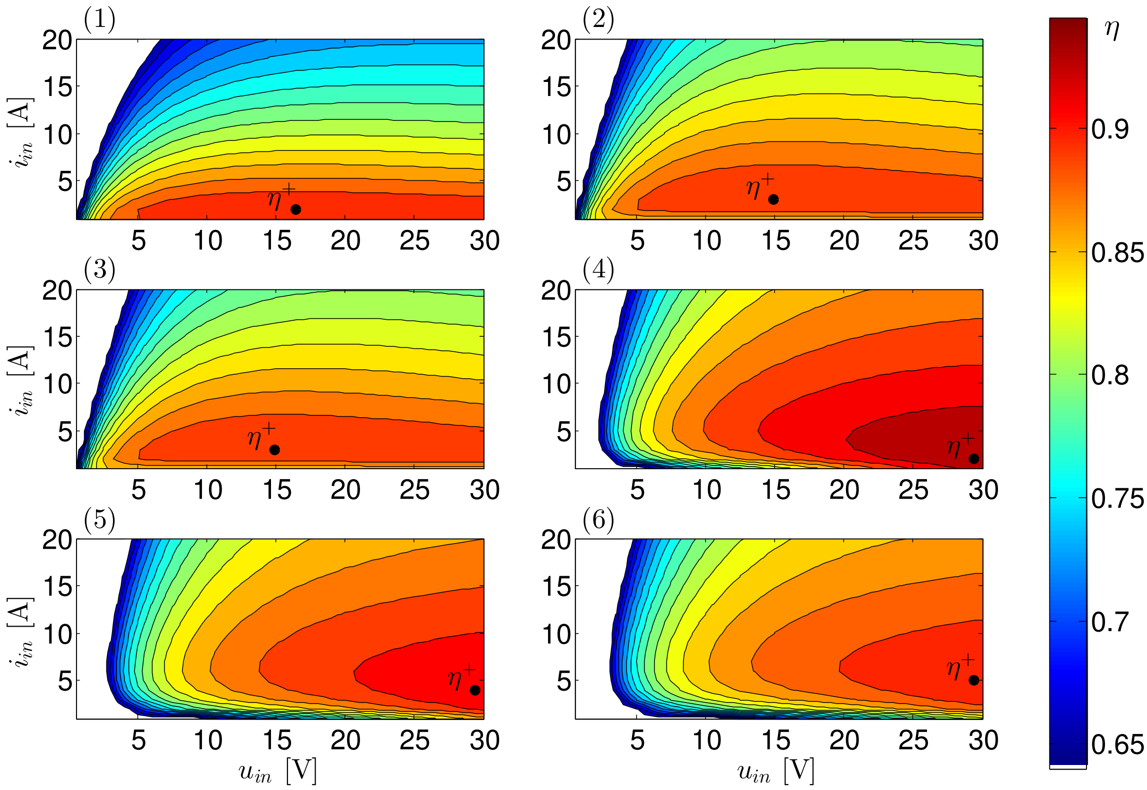

Figure 3.13.: Analysis of efficiency of the converters with $e_{bl} = 12$ V and $f_{sw} = 100$ kHz. (1) buck-boost, (2) Ćuk, (3) SEPIC, (4) boost-buck with $u_{C_2} = 30$ V, (5) boost-buck with $u_{C_2} = 42$ V, (6) boost-buck with $u_{C_2} = 48$ V.

an influence on the mean efficiency because the voltage stress of the inductors can be minimized if the difference between output voltage and u_{C_2} is minimal.

3.5.3. Analysis of Efficiency

In Section 3.5.2, the analysis of the mean efficiency shows the influence on the losses of switching frequency and output voltage. To analyze different converters in relation to the input power and operation points, a switching frequency of 100 kHz is specified. Further, the output voltages for detailed analyses are selected as 12 V, 24 V and 48 V (cf. REQ.3). Consequently, the efficiency of the converter depends on the input power only. In relation to (3.10) and (3.39), the efficiency η for different converter topologies can be determined. In the following, the results of the analyzed efficiency are presented. Detailed results of the losses and the efficiency of the converters are presented in the Appendix A.3.

Comparison of Topologies

The efficiencies of the DC-DC converters for the output voltages 12 V, 24 V and 48 V are presented in Figures 3.13 - 3.15. The results, shown in Figures 3.13 - 3.15, suggest that the BuBo, the Ćuk, and the SEPIC converters reach the highest efficiency at low current amplitudes. In contrast, the input voltage has a minor influence on losses. Fundamentally, the efficiency of the three converters is nearly similar.

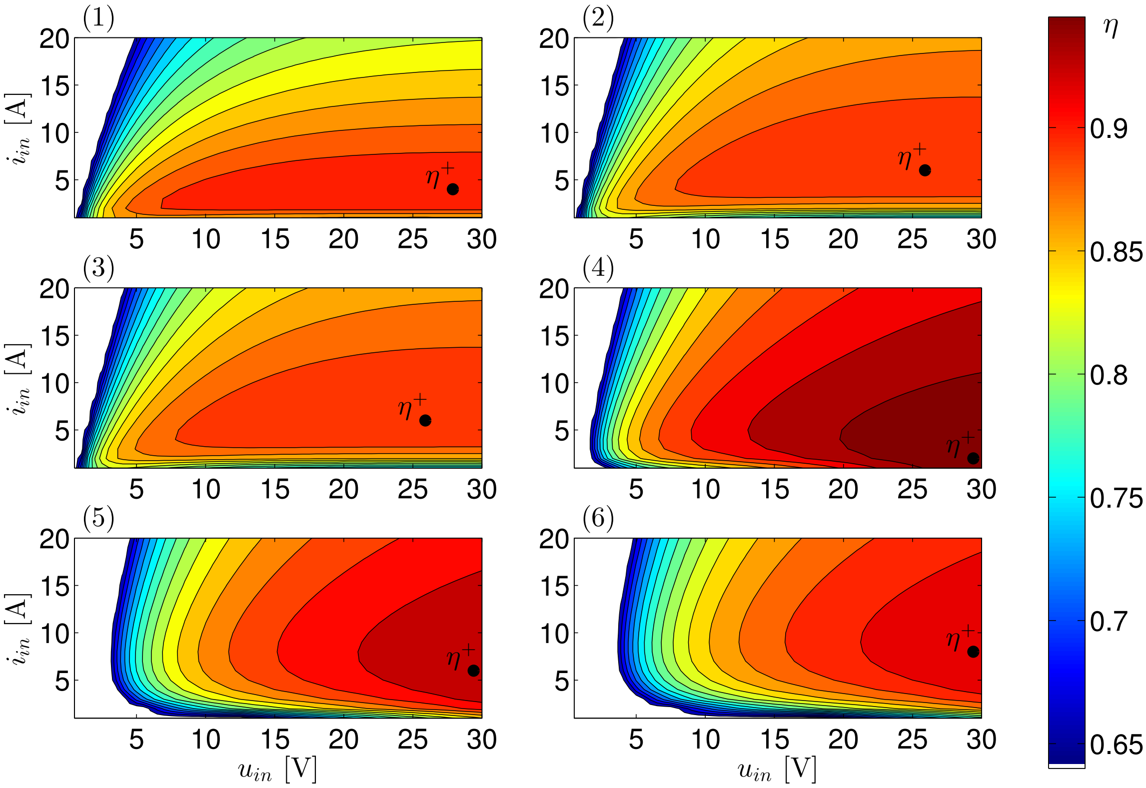

Figure 3.14.: Analysis of efficiency of the converters with $e_{bl} = 24$ V and $f_{sw} = 100$ kHz. (1) buck-boost, (2) Ćuk, (3) SEPIC, (4) boost-buck with $u_{C_2} = 30$ V, (5) boost-buck with $u_{C_2} = 42$ V, (6) boost-buck with $u_{C_2} = 48$ V.

The main part of their losses is caused by the DC loss (3.12), which rises quadratically in relation to the current amplitude. Depending on the topology of the BuBo, the Ćuk, and the SEPIC converters, the loss of MOSFET, inductor, and synchronous MOSFET are significantly different. Generally, the drain to source voltage of the MOSFETs increase if the input voltage increases. Consequently, the switching loss increases in relation to the input voltage.

The body-diode resistance dominates the loss of the SY-MOSFET. In comparison to the synchronous switching power loss in BuBo converter, the losses in the Ćuk and the SEPIC converters are higher because the current flow of both inductors L_1 and L_2 is in part overlapping and causes a higher current stress in the SY-MOSFET.

The significant part of the inductor loss is caused by the core loss, which depends on the duty cycle of the converters (cf. (3.30) and (3.32)). The duty cycle of the BuBo, the Ćuk, and the SEPIC converter depends on the ratio of input to output voltage. Consequently, the inductor loss is nearly constant for different input current amplitudes for all three converters (cf. Appendix A.3).

The BoBu converter has a significantly different efficiency map in comparison to the BuBo, the Ćuk, and the SEPIC converter, besides ohmic and synchronous switching losses. The difference of the efficiency maps is caused by the degree of freedom of the middle voltage u_{C_2}. The middle voltage is selected as constant in the analysis. Hence, the switching loss exclusively depends on the current since the drain

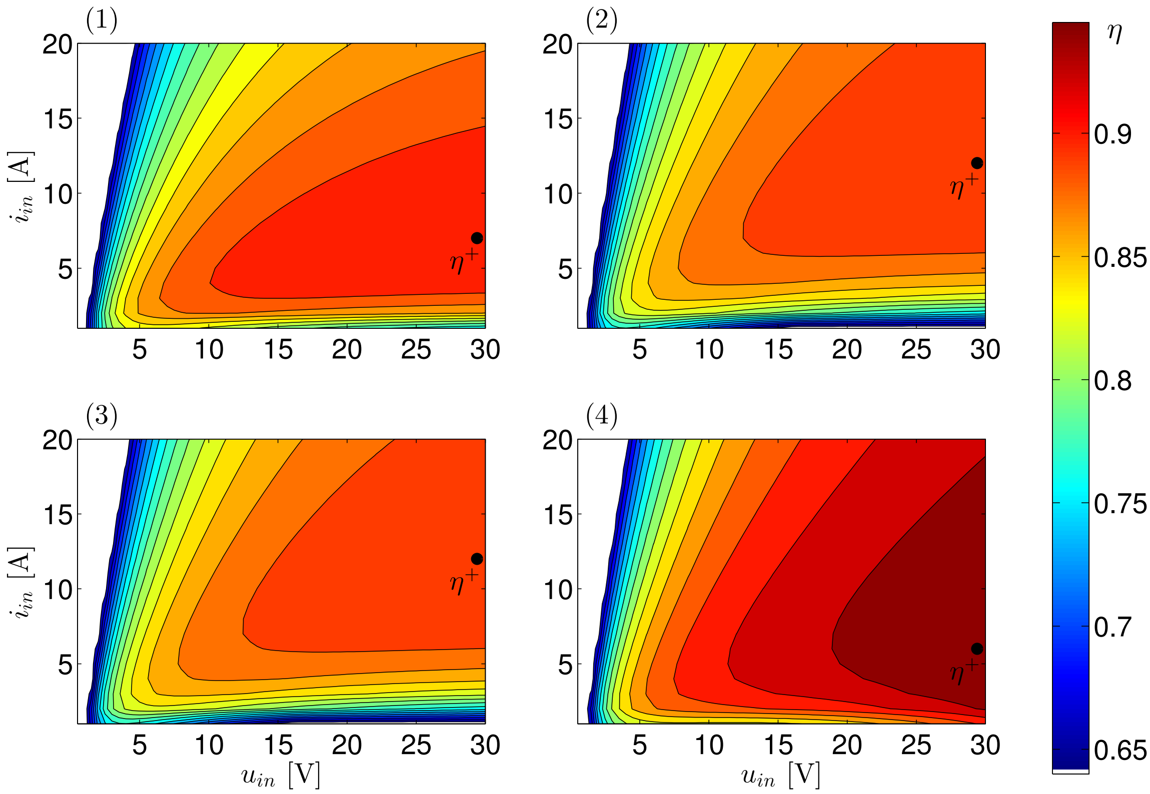

Figure 3.15.: Analysis of efficiency from the converters for $e_{bl} = 48$ V and $f_{sw} = 100$ kHz. (1) buck-boost, (2) Ćuk, (3) SEPIC, (4) boost-buck with $u_{C_2} = 48$ V.

to source voltage is nearly constant, besides the voltage ripple. Furthermore, the inductor loss reaches maximum if the duty cycle is 0.5. In this operating point, the current ripple has the maximum magnitude and causes the highest eddy current loss. With respect to the middle voltage, the location of this point can be shifted. This effect can be observed from analysis results in Appendix A.3 and Figures A.11 - A.14. Therefore, the ratio of u_{C_2} to u_{in} should more or less be 0.5 to reduce the inductor loss.
The average efficiency $\overline{\eta}$ and the maximum efficiency $\eta^+ = max(\eta)$ of the converters are presented in Table 3.3. These results show that the BoBu converter has the highest efficiency. In particular, the efficiency can be manipulated by the degree of freedom of the middle voltage u_{C_2}.
Furthermore, the efficiencies of all converters depend on the output voltage. The efficiency tends to increase for higher output voltage. In the following, this effect is analyzed in detail.

Influence of Output Voltage

The variation of the output voltage influences the efficiency of the converters. This is in part shown in Section 3.5.2. From the detailed analysis of the losses from the DC-DC converters (cf. Appendix A.3), the following relationships can be determined:

converter	$e_{bl} = 12$ V		$e_{bl} = 24$ V		$e_{bl} = 48$ V	
	$\overline{\eta}$	η^+	$\overline{\eta}$	η^+	$\overline{\eta}$	η^+
BuBo	0.777	0.912	0.812	0.915	0.81	0.915
Ćuk	0.812	0.905	0.826	0.909	0.809	0.907
SEPIC	0.812	0.905	0.826	0.908	0.809	0.907
BoBu$\|_{u_{C_2}=30\text{ V}}$	0.821	0.949	0.852	0.972	-	-
BoBu$\|_{u_{C_2}=36\text{ V}}$	0.806	0.938	0.824	0.956	-	-
BoBu$\|_{u_{C_2}=42\text{ V}}$	0.794	0.926	0.799	0.943	-	-
BoBu$\|_{u_{C_2}=48\text{ V}}$	0.782	0.915	0.776	0.932	0.853	0.961

Table 3.3.: Average and maximum efficiency ($\overline{\eta}$, η^+) of the converters for different output voltage amplitudes e_{bl}.

DC Loss

The ohmic loss is dependent on the current amplitude. DC loss becomes the dominant loss as the result of the square weighting of the current. Due to the increase of the output voltage, the output current is reduced proportionally. Therefore, the current amplitude for the electrical components decreases, which leads to a reduction of the DC loss. When the output voltage changes from 12 V to 48 V, the average DC loss of the converters decrease by up to 55 % (cf. Table A.1 and Table A.11).

Switching Loss

The magnitude of the switching loss is different for the converters. In general, the loss depends on the drain to source voltage of the MOSFETs. Hence, the switching loss increases for higher output voltages. This effect can be clearly observed in the estimated losses of the BuBo, the Ćuk, and the SEPIC converters (see Table A.1 and Table A.11). The average switching loss increases by up to 139 % if the load voltage changes from 12 V to 48 V. In contrast, the loss of the switches decrease in the BoBu converter when the output voltage increases. The middle voltage u_{C_2} is selected as constant voltage. Consequently, the drain to source voltage is nearly constant. However, the drain current for the MOSFETs S_3 and S_4 decrease at a constant input power if the input voltage increases. Consequently, the average switching loss is reduced by up to 7 %, when the output voltage changes from 12 V to 48 V (cf. Table A.1 and Table A.11).

Inductor Loss

The inductor loss is characterized by the magnetic flux density. The maximal flux amplitude B^+ is proportional to the volt-second across the inductor. The input and the output voltage amplitudes of the converter significantly influence the voltage amplitude across the inductor.

When the input voltage increases at a constant output voltage at the BuBo, the Ćuk, and the SEPIC converters, the volt-second of the inductor increases proportionally. Consequently, the inductor loss also increases in relation to the input voltage (see Figures A.8 - A.10).
When the output voltage changes from 12 V to 48 V, the maximal inductor loss increases by up to 300 % (cf. Table A.1 and Table A.11).
The BoBu converter has electrical characteristics that are different from the other converters. The BoBu is an interconnection of the boost and the buck converters. The maximal magnetic density flux of the boost converter is reached when the duty cycle is 0.5. At this operation point, the ratio of u_{C_2} to u_{in} is nearly 0.5. If the duty cycle of the boost converter is smaller or higher, the density flux decreases (see Figures A.11 - A.14).
In contrast, the buck converter operates in a nearly constant operation point cause by the selected amplitude of u_{C_2}. Consequently, the magnetic flux amplitude of the buck converter influences the magnetic loss only when the output voltage changes. The lowest magnetic flux at the buck converter is reached when the duty cycle is nearly one. To achieve this duty cycle, the output and the middle voltage amplitudes must have the same value. For a load change from 12 V to 48 V at $u_{C_2} = 48$ V, the maximal inductor loss decreases by up to 224 % (cf. Table A.1 and Table A.11).

Synchronous Switching Loss

The synchronous switching loss primarily causes from the dead time of the direct control signal of the MOSFET. In this time span, the body-diode of the SY-MOSFET is forward biased. As already noted from the DC loss, the current stress decreases for higher output voltages. This leads to a reduction of the synchronous switching loss at all converters, because the synchronous switching loss is characterized by the current amplitude (cf. (3.27)). The synchronous loss is reduced by up to 81 % if the output voltage changes from 12 V to 48 V (cf. Table A.1 and Table A.11).

3.6. Evaluation of Converters

In Section 3.2, different DC-DC converters which satisfied the technical requirements REQ.1, REQ.2 and REQ.3 for the desired TEG system are presented. The analysis of the efficiency in Section 3.5.3 shows, that switching frequency between 50 kHz and 100 kHz yields the maximum efficiency for all selected converters. For a detailed analysis of the efficiency map, a switching frequency of 100 kHz is selected, although lower frequencies can partially achieve a higher mean efficiency. The advantage of a higher switching frequency is that smaller packing sizes of the electrical semiconductors can be used. Consequently, the selected switching frequency is a practical design parameter to satisfy REQ.1.
The detailed analysis in Section 3.5.2 presents the efficiencies and losses of each converter for different operation points. The result is that the Ćuk and the SEPIC converter have almost the same efficiencies

and losses. Only signal flows and the values of capacitance and inductor are different. The maximum efficiency is reached for low input current amplitudes, which is similar to the BuBo converter. In comparison, BoBu converter reaches the maximum efficiency at higher input voltage and higher current amplitudes.
Furthermore, the analysis shows that the maximum efficiency of all converters shifts in relation to the output voltage e_{bl} towards higher input current and voltage. The reasons for this behavior are the decrease of the DC loss and the increasing voltage stress of the inductors.
Nevertheless, the analysis of the converters shows that the efficiency decreases significantly for high input current and low voltage amplitudes, which is caused by the DC loss. This loss can be reduced with multiphase converters, which decrease the average current stress at the semiconductors [98, 136]. However, this implementation requires more installation space and is in direct conflict with REQ.1.
The BoBu converter has the highest mean efficiency, in comparison to the BuBo, the Ćuk, and the SEPIC converters. The BoBu has the disadvantage of a more complex electrical circuit in contrast to the other topologies. However, the additional degree of freedom to select the middle voltage of the BoBu converter shows that the efficiency can be maximized by the variation of this voltage amplitude. This additional feature can be used to optimize the efficiency of the BoBu in relation to TEMs with different nominal electric specifications, without a hardware modification. For this reason, the BoBu converter is selected as the electrical interface between TEMs and the on-board power supply.

3.7. Model Verification

The scope of this section is to verify the presented modeling and analysis results of the BoBu converter from Sections 3.3 - 3.5. The semiconductor parameters and electrical parts of the converters are defined by the requirements of the current and the voltage ripple from Table 3.2.

3.7.1. Prototype of Boost-Buck Converter

The prototype was developed in relation to the selected boost-buck converter from Section 3.6. To satisfy conditions REQ.1, REQ.2 and REQ.3, the electric circuit is realized with surface-mount device (SMD) capacitors, inductors, and semiconductors. All parameters are specified for temperatures between -55 °C and 125 °C. The direct control of the MOSFETs is realized with a μC. To measure the electrical states of the converter, the voltage and the current signals are conditional for the μC and are filtered with a second order low-pass. The cut-off frequency f_c is 1 kHz. The sample frequency f_s of the analog digital converter (ADC) from the μC is selected to 10 kHz. The electric circuit with μC and filters of the boost-buck converter is presented in Figure 3.16. The selected electric components with nominal values are presented in Appendix A.4, and the final electrical circuit is shown in Figure 3.17.

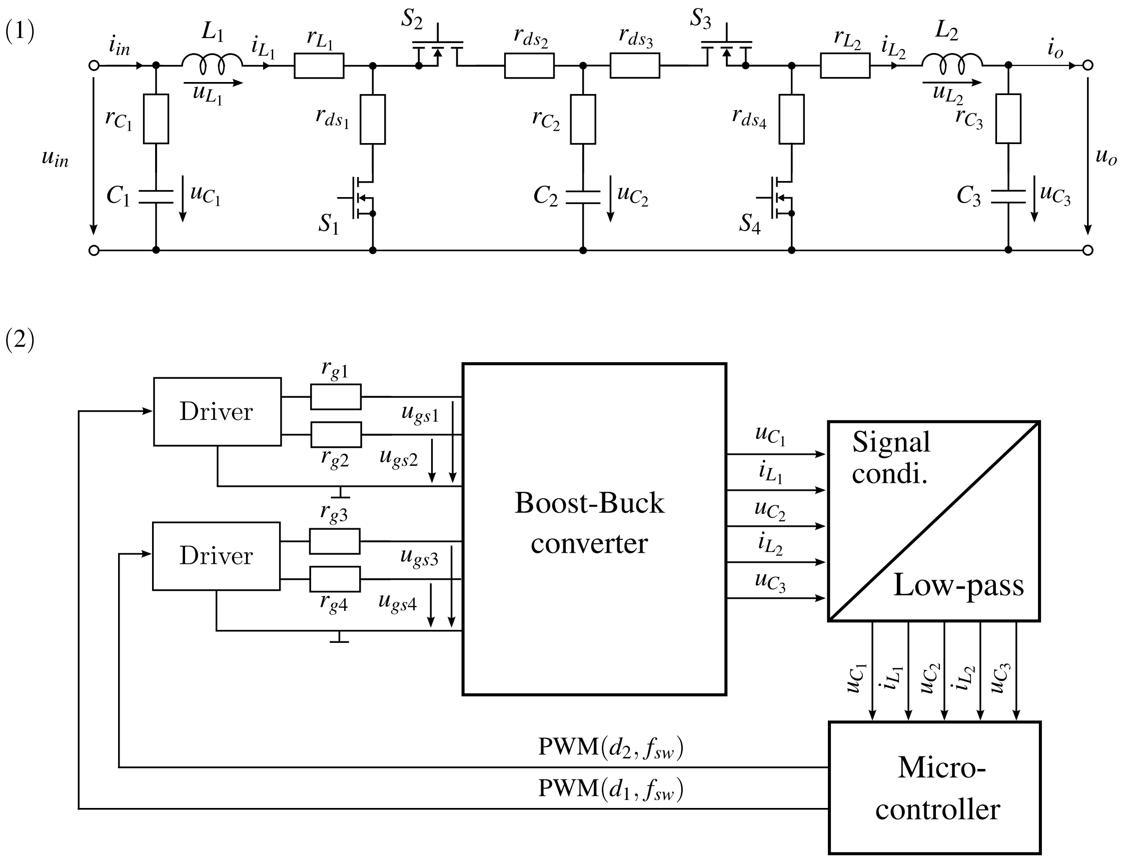

Figure 3.16.: Electrical circuit of boost-buck converter with ESRs is presented in (1). Overview of logic modules is presented in (2).

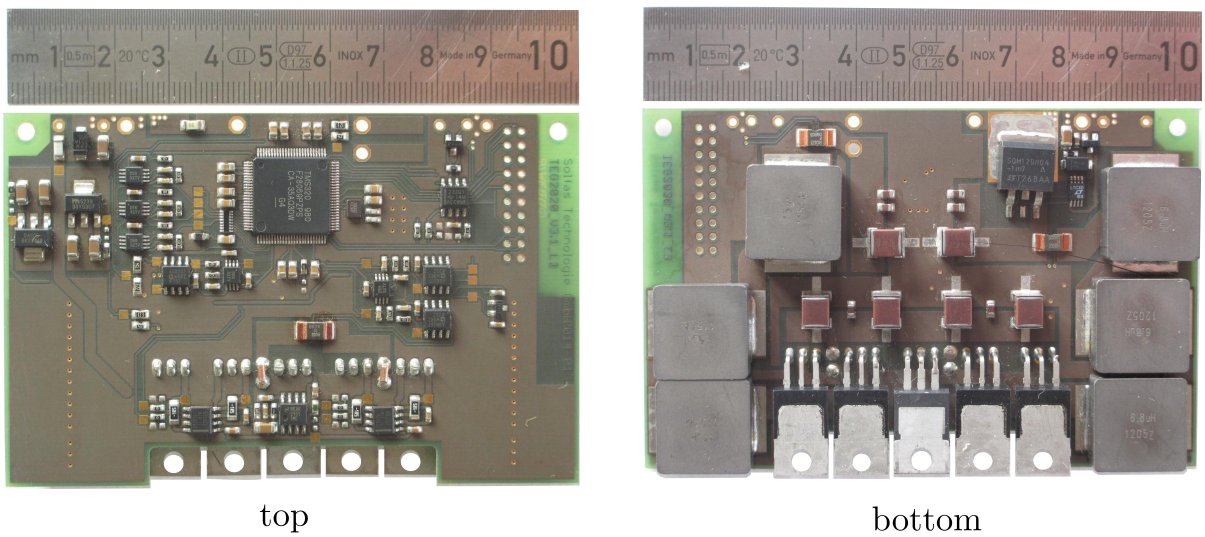

Figure 3.17.: Prototype of the boost-buck converter.

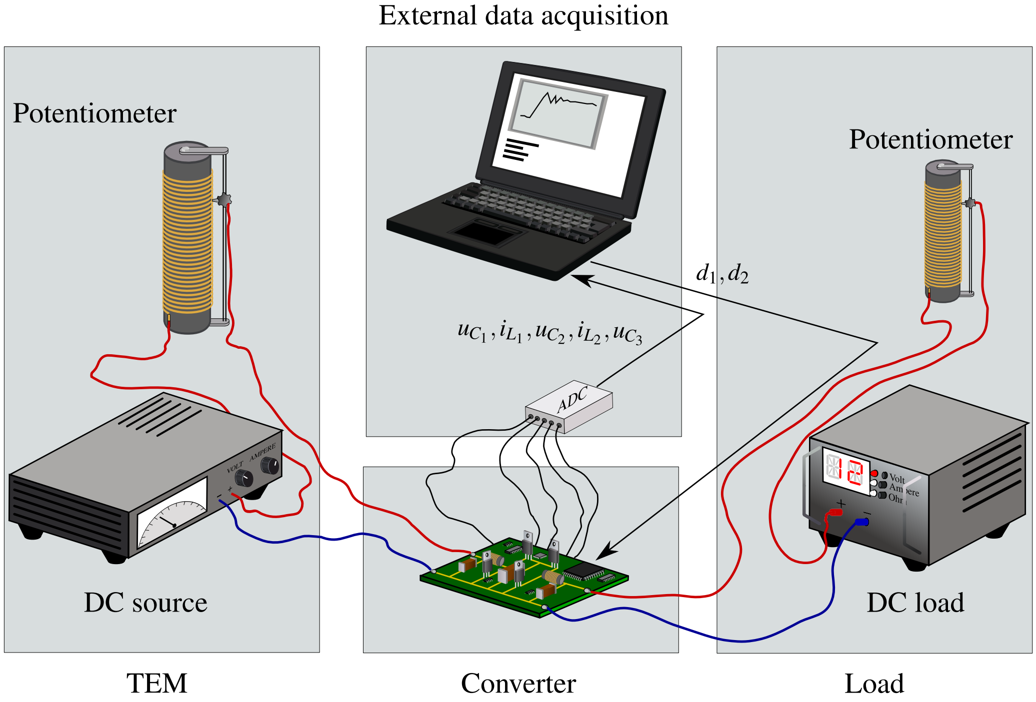

Figure 3.18.: Structure of the test bench. The TEM is simulated with an DC voltage source and a series-connected power potentiometer. The on-board power supply is simulated with a regulated electric load and a series-connected power potentiometer. The electrical states of the DC-DC converter are measurement with an external ADC. The desired duty cycles of the converter are transmitted from an computer to the DC-DC converter.

3.7.2. Experimental Measurement

To verify the electrical efficiency of the converter, a test bench is used to simulate the TEM and the load. The TEM is simulated by a regulated DC voltage source and a series-connected power potentiometer. Besides, the on-board power supply is simulated with a regulated electric load (DS 3606 from Höcherl & Hackl) and a series-conneted power potentiometer. In contrast to a battery, this load can be precisely conditioned.

To measure the input and output power, external data acquisition (DAQ) devices are selected (USB-6009 from National Instruments). The advantage of an external DAQ is a higher measurement resolution (14 bit) in contrast to the measurement resolution of the internal ADC of the selected μC (12 bit). However, the regulation of the duty cycles d_1 and d_2 is implemented in the μC. The desired duty cycles are determined for $u_{C_2} = 48$ V and transmitted from a computer to the controller via serial interface. The structure for the test bench is illustrated in Figure 3.18.

In the experiment, 60 operation points were selected for the verification of the efficiency model. The measured values of the efficiency in comparison to the analytical results are presented in Figure 3.19. The errors between the measured and the analytical efficiency are presented in Table 3.4. In comparison, the

$\overline{e}$	e^{+}	$\overline{e}_{\%}$	$e^{+}_{\%}$
0.04	0.12	5.29 %	24.99 %

Table 3.4.: Errors between the measured and the analytical efficiency of boost-buck converter. $\overline{e}$ is the mean error, e^{+} is the maximal mean error, $\overline{e}_{\%}$ is the relative error, and $e^{+}_{\%}$ is the maximal relative error.

results show that the maximum relative error $e^{+}_{\%}$ between measurements and model is 24.99 %. However, most errors between measurement and model are significantly lower. Consequently, the relative mean error $\overline{e}_{\%}$ between measurements and model is only 5.29 %. Regarding the results, it is remarkable that the highest errors $e^{+}_{\%}$ only occur at low input current amplitudes of nearly 1 A.
There are different reasons for the errors between the model and the measured efficiency, among other things, the quantization error of DAC and the parameter tolerance of electrical components.
The quantization of the duty cycles has a significant influence on the operation point of the converter. Since the PWM has only 450 quantization steps, a quantization error results in a mismatch between the desired and the actual operation point of the converter. Additionally, the necessary dead time t_{dt} of the PWMs for short-circuit protection of the MOSFETs decreases the effective quantization steps to only 430.
Assuming that in the experiment a simple quantization error occurs, the maximum relative error between the experimental and the modeled efficiency decreases from 24.99 % up to 17.37 % (see Appendix A.5). However, the quantization effect has a lower influence on the operation points with a nearly constant efficiency (cf. Figure 3.19 and Figure A.44).
Taking into account that the parameters of the electric components have a nominal tolerance of 20 % and assuming that this only influences the parasitic ohmic losses, the mean error between the measured and the analytical efficiency decreases by up to 4.18 % (see Appendix A.5). If the component tolerances and quantization error take into account, the relative mean error $\overline{e}_{\%}$ is only 3.41 % in the best case (see Appendix A.5).
However, the measurement results in Figure 3.18 show that the efficiency of the experimental converter correspond to the efficiency of the analytical model.

3.8. Conclusion

A structured model to analyze the efficiency of DC-DC converters was presented in this chapter. The state-space averaging model technique, which includes the ohmic loss of the converter, was used to determine the steady-state operation points. Inductor loss was estimated with the Steinmetz equation, which are based on a curve fitting of the core loss.
The approach to determine the switching loss uses differential equations, which base on a piecewise linear signal analysis. The advantage of the presented models is that the parameters can be selected from

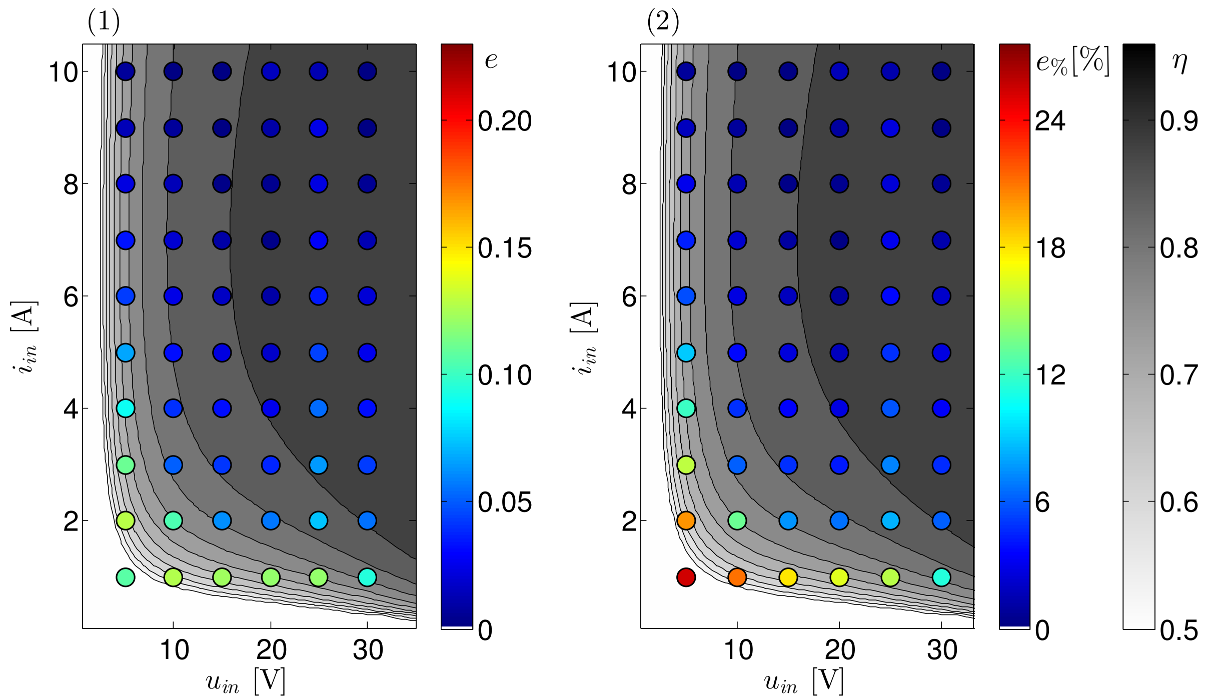

Figure 3.19.: Comparison between the experimental measurements and the analytical efficiency model of the converter for $u_{C_2} = 48$ V. The dotted markers present the measurement points in relation to the error between the measurement and the model. (1) the absolute error e between the measurement and the model. (2) the relative error $e_{\%}$ between the measurement and the model.

data sheets provided by the manufacturers. The disadvantage of the data sheet parametrization is often inaccurate values.

The benefit of the data sheet parametrization is reflected in analyses and assessments of different DC-DC converter topologies. With specified boundary conditions for power range and components, analysis of characteristic losses can be performed and efficiency can be estimated without any measurements.

The presented analysis of the efficiency map of the different converters starts with the study of the switching frequency and the output voltage amplitude. The results show that the loss of MOSFETs increase and that the loss of the inductors decrease when the switching frequency increase. As a consequence, there is a global maximum of mean efficiency in relation to the switching frequency. Depending on the analyzed switching frequency range, the average efficiency of the the converters differed by up to 10 %. From the results it follows that the optimal switching frequency to maximize the efficiency for all converters is between 50 kHz and 100 kHz. A higher frequency has the benefit to select semiconductors with smaller package size. Consequently, for a detailed analysis of the losses, a switching frequency of 100 kHz was selected. Another important factor is the output voltage amplitude, which in general is in conflict with the switching loss because the output voltage is proportional to the source to drain voltage of the MOSFETs. In contrast, the DC loss decreases in relation to higher output voltages. However, for all converter topologies, the highest loss is caused by the DC loss, followed by the switching, inductor,

and synchronous switching loss.
The comparison between the buck-boost, the boost-buck, the Ćuk, and SEPIC converters shows that the BoBu has the highest average efficiency of 85.3 % with a maximum efficiency of up to 96.1 %. The BoBu has the advantage of the additional degree of freedom to select the amplitude of the middle-voltage. The analysis shows, that the middle-voltage can be used to optimize the efficiency at different output voltage amplitudes. The main drawback of the BoBu is the number of necessary components, which is higher by a factor of up to 1.5 in relation to the other converters. Furthermore, the converter uses four MOSFETs, which must be controlled. This results in a complex control structure. However, the BoBu has the potential to increase the efficiency for a defined TEM without any changes of hardware components.
The results of the efficiency analysis were verified with an experimental prototype of the boost-buck converter. The comparison of the measurement and the model results shows an mean error of 5.29 %. Taking into account the component tolerances, and the quantization errors, the mean error decreases to 3.41 %. Therefore, it can be stated that the presented model results are a good prognosis for the DC-DC converter efficiency.

4. Control of the DC-DC Converter

Control of the DC-DC converter enables to regulate the states of the system to a desired reference. Additionally, feedback control can be designed to eliminate disturbances and to stabilize the system. For the electrical integration of the TEMs into a power grid with DC-DC converter, control of the DC-DC converter is necessary. One aim of the regulation of the DC-DC converter is to track the current of the TEM at MPP. This means that TEMs must be loaded with a specific current to recover the maximum electric power. Taking into account that the precise electrical characteristics of the TEM are unknown, a search and tracking algorithm for the MPP and, in particular, a control of the desired current and voltage amplitudes are required.
Generally, the electric parameters of TEMs depend on the temperature gradient across the module. Temperature variations have an impact on the parameter of the TEMs and influence the stability of the converter. However, such effects are neglected in [40, 70, 72]. Due to the requirement REQ.3, the parameters may differ significantly depending on the type of TEM. Consequently, neglect of parameter variations is not applicable.
The aim of this chapter is to design a control structure, which is stable and robust in spite of significant parameter changes. For this reason, the criteria of robustness should be defined. In addition, a control concept has to be developed to optimize the efficiency of the converter depending on the actual input power and output voltage. The structure of this chapter is as follows. General digital control and design criterions are defined in Section 4.1. In Section 4.2, the control structure of the boost-buck converter is presented. This includes the dynamic model of the boost-buck converter and the analysis of the plants. Furthermore, the plant models and the control designs are verified by experiments. The approach to extend the control concept with an adaptive control concept is presented in Section 4.3. The maximum power point tracking algorithm is given in Section 4.4. Furthermore, an optimization of the efficiency by regulating of the middle voltage u_{C_2} of the BoBu converter is shown in Section 4.6. Finally, the control concept and results are summarized in Section 4.7. Partial results have previously been published in [P3, P2, P4, P5].

4.1. Digital Control Design

The control design for the BoBu converter is based on a digital control structure, which uses a μC. A μC requires a finite time to convert input signals and calculate control signals. Consequently, the measurement signals and actuator signals are determined only in discrete time steps. Generally, this time period is equal to the sampling frequency of the ADC from the measurement signal. The selection of a digital control restricts the possible control structures. This includes, amongst others, the popular peak current control, which has the advantage of its controller directly regulating the MOSFETs without duty cycle control [26]. This leads to a simplification of the control system, the analysis, and the parametrization. Approaches of digital and mixed-signal peak current control are presented in [18, 51].

In contrast to an analog control design, the usage of a μC has several advantages. It should be noted that the parameters and the control algorithm of the programming can be modified. This allows to use of non-linear and adaptive controllers as well as optimization algorithms and a rapid prototyping in the design of the control parameters. For this reason, a digital control concept is useful for the DC-DC converter prototype [93].

Different linear and nonlinear digital control methods of the DC-DC converters are described in the literature. The most popular methods are backstepping, exact linearization, flatness, gain-scheduling, linear, and sliding mode control.

The aim of the exact linearization is to cancel the nonlinearity of the plant with the feedback control law. However, a disadvantage of the method is the mathematical analysis, which is in part difficult to handle for higher order systems. Furthermore, the exact linearization requires detailed system models. Parameter variations can hardly be compensated. [82, 90]

The backstepping is a similar concept, but the system is split into nonlinear and linear terms and, consequently, into a simpler system, which can also be modeled as a strict feedback form. This allows for a separated manipulation of the nonlinearity. The compensation of parameter variations can be extended with an adaption of the control parameters. [7, 43]

One of the famous nonlinear controls of a converter is the sliding mode approach. Sliding mode is a variable structure control method, which attempts to move the states of the system to a defined sliding surface. Originally, this control concept is developed for linear systems and can only be used for input affine nonlinear systems [170]. The general advantage of this method is the robustness against parameter variations of the control system [66]. Sliding mode controllers with a linearized nonlinear plant are presented in [14, 95, 164, 165, 166] to satisfy the conditions of an input affine system. As a consequence, the robustness of the sliding mode converter is only guaranteed for this linearized operation point.

The aim of the flatness controller is to compensate the nonlinearity through a feed-forward control. The stabilization of the system is often accomplished with linear control [46, 168].

The gain-scheduler belongs to a family of linear controllers, which are designed for different operation points of the plant. Depending on the actual state of the plant, the control parameters can be changed [61].

The classical linear control design can not compensate the nonlinear characteristics of the controlled plant, but the robustness against parameter variations can be considered in the design. Additionally, the linear control concept has the advantage that the control structure can be extended to an adaptive, gain-scheduling, or flatness controller. The adaptive linear controller in particular uses identification algorithms to redesign control parameters in order to compensate of variation effects [7, 85].

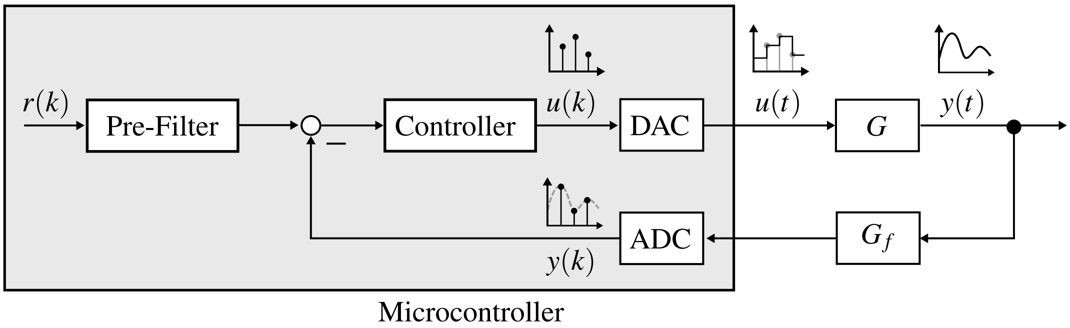

Figure 4.1.: Digital closed-loop.

Considering the fact that the control strategy must be robust against parameter variations of the TEMs, a linear control approach proves to be promising. In the following, the digital closed-loop system and the design steps for a linear controller are presented.

4.1.1. Digital Control System

A general digital closed-loop system is shown in Figure 4.1. The system's output $y(t)$ is the response of the signal $u(t)$ from the linear, time-invariant system $G(s)$. The signal $y(t)$ must be filtered with a analog low-pass at the frequency f_c, by anti-aliasing filter $G_f(s)$, to avoid the aliasing effect. Following, the low-pass filtered signal is sampled from the ADC with the sampling rate f_s or sampling time T_S. From the Nyquist criterion it follows that $f_c \leq f_s/2$. This requirement is necessary to allow reconstruction of the continuous-time signal $y(t)$ in relation to the samples $y(k)$. The argument k is the index of the samples. [6, 86]

The control signal $u(k)$ takes into account the error $e(k)$ between the reference $r(k)$ and the measurement signal $y(k)$. The sampled signal $u(k)$ is converted from a discrete-time to a continuous-time signal $u(t)$ by a DAC, with a zero-order hold (ZOH). The discrete transfer function from the control $u(k)$ to the output signal $y(k)$ is given by

$$G(z^{-1}) = \frac{y(z)}{u(z)} = \frac{z-1}{z}\mathscr{Z}\left\{\mathscr{L}^{-1}\frac{G(s)\,G_f(s)}{s}\right\} \tag{4.1}$$

$$= \frac{z^{-d_e}B\left(z^{-1}\right)}{A\left(z^{-1}\right)} \tag{4.2}$$

where $\mathscr{Z}$ is the z-Transform ($z = e^{s\,T_S}$), $\mathscr{L}^{-1}$ is the inverse Laplace-Transform, d_e is the time-delay, and $A(z^{-1})$, $B(z^{-1})$ are polynomials [6]:

$$A(z^{-1}) = 1 + a_1 z^{-1} + \ldots + a_{n_a} z^{-n_a} \tag{4.3}$$

$$B(z^{-1}) = b_0 + b_1 z^{-1} + \ldots + b_{n_b} z^{-n_b} \tag{4.4}$$

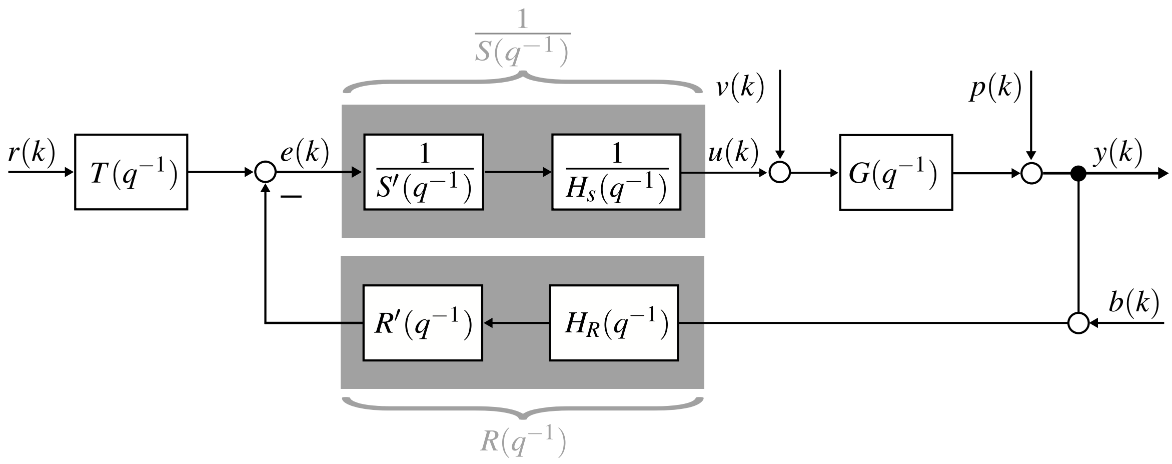

Figure 4.2.: Digital control system with disturbance $p(k)$, control input disturbance $v(k)$, and noise signal $b(k)$.

A linear discrete-time model can also illustrated as a difference equation. Hence, the time shift operator $q^{-1} = z^{-1}$ can be used [6]:

$$q^{-1} f(k) = f(k-1) \tag{4.5}$$

Consequently, (4.2) can re-written to:

$$G(q^{-1}) \quad = \quad \frac{y(k)}{u(k)} = \frac{q^{-d_e} B\left(q^{-1}\right)}{A\left(q^{-1}\right)} \tag{4.6}$$

It should be noted, the z-domain must be used for a frequency analysis.

4.1.2. Two-Degree of Freedom Controller

A two degree of freedom controller (2DOF) allows to specify the disturbance and the tracking response of a closed-loop system. The control structure of Figure 4.1 can be transformed into the structure in Figure 4.2, which is called RST controller [86, 150]. The control equations yield:

$$u(k) \quad = \quad \frac{T(q^{-1})}{S(q^{-1})} r(k) - \frac{R(q^{-1})}{S(q^{-1})} y(k) \tag{4.7}$$

$$S(q^{-1}) \quad = \quad S'(q^{-1})\, H_S(q^{-1}) \tag{4.8}$$

$$R(q^{-1}) \quad = \quad R'(q^{-1})\, H_R(q^{-1}) \,, \tag{4.9}$$

where $S'(q^{-1})$, $H_S\left(q^{-1}\right)$, $R'\left(q^{-1}\right)$, $H_R\left(q^{-1}\right)$ are the controller polynomials and $T(q^{-1})$ is a pre-filter. The polynomials $H_S\left(q^{-1}\right)$ and $H_R\left(q^{-1}\right)$ can be pre-specified to damp frequencies in the measured signal, and well-damped poles as well as zeros of the transfer function $G(q^{-1})$ can be canceled. The desired closed-loop dynamics are determined by the polynomials $S'\left(q^{-1}\right)$ and $R'\left(q^{-1}\right)$. The design of controllers starts with the pre-definition of $H_S\left(q^{-1}\right)$ and $H_R\left(q^{-1}\right)$. Afterwards, $S'\left(q^{-1}\right)$ and $R'\left(q^{-1}\right)$ are calculated to ensure the desired closed-loop dynamics and stability. At last, $T\left(q^{-1}\right)$ can be used as gain or as a filter for the reference signal $r(k)$ [150].

Stability and Robustness

The closed-loop transfer functions from Figure 4.2 yield:

$$y(k) = \underbrace{\frac{q^{-d_e}TB}{A_{cl}}}_{T_{ry}(q^{-1})} r(k) + \underbrace{\frac{SA}{A_{cl}}}_{S_{py}(q^{-1})} p(k) + \underbrace{\frac{q^{-d_e}SB}{A_{cl}}}_{S_{vy}(q^{-1})} v(k) + \underbrace{\frac{q^{-d_e}RB}{A_l}}_{S_{by}(q^{-1})} b(k) \quad (4.10)$$

$$u(k) = \underbrace{\frac{TA}{A_{cl}}}_{T_{ru}(q^{-1})} r(k) + \underbrace{\frac{RA}{A_{cl}}}_{S_{pu}(q^{-1})} p(k) + \underbrace{\frac{SA}{A_{cl}}}_{S_{vu}(q^{-1})} v(k) + \underbrace{\frac{RA}{A_{cl}}}_{S_{bu}(q^{-1})} b(k)\ , \quad (4.11)$$

where $A_{cl}(q^{-1})$ is the characteristic polynomial of the closed-loop dynamics:

$$A_{cl}(q^{-1}) = S(q^{-1})A(q^{-1}) + q^{-d_e}R(q^{-1})B(q^{-1}) \quad (4.12)$$

The transfer function $S_{py}\left(q^{-1}\right)$ is the output sensitivity function and represents the transfer response of the disturbance $p(k)$ to the output signal $y(k)$. The transfer response $S_{vu}\left(q^{-1}\right)$ from input disturbance $v(k)$ to the control signal $u(k)$ has the same characteristic as $S_{py}\left(q^{-1}\right)$. Furthermore, the transfer function $S_{vy}(q^{-1})$ (input-disturbance output-sensitivity function) describes the response from $v(k)$ to the output signal $y(k)$. The influence of measuring noise $b(k)$ of the output signal $y(k)$ is represented by the noise-output sensitivity function $S_{by}\left(q^{-1}\right)$. The input signal sensitivity functions $S_{pu}\left(q^{-1}\right)$ and $S_{bu}\left(q^{-1}\right)$ that affect the control signal $u(k)$ are also significant. Thereby, the transfer functions of the disturbance and the measurement noise have the same influence on the control signal. The transfer function $T_{ry}\left(q^{-1}\right)$ presents the command response from the reference signal $r(k)$ to the output signal $y(k)$.
These functions show a direct influence of disturbances and noise on the output signal.
The choice of the zeros of $H_S\left(q^{-1}\right)$ and $H_R\left(q^{-1}\right)$ can be used to damp or to eliminate signals at a specified frequency.
Basically, it is assumed that disturbances affect the output of the closed-loop system. This leads to the requirement that the output sensitivity function $S_{py}\left(q^{-1}\right)$ and the noise-output (also called complementary) sensitivity function $S_{by}\left(q^{-1}\right)$ must damp in the respective frequency ranges. The relationship of both sensitivity functions is as follow:

$$S_{py}\left(q^{-1}\right) + S_{by}\left(q^{-1}\right) = 1 \quad (4.13)$$

This means that the desired sensitivity functions are conflicting because both transfer functions cannot be designed independently. For most practical applications, it is assumed that the disturbance is low-frequent and the noise is high-frequent. Hence, the output sensitivity function is designed to damp low-frequent and to pass high-frequencies. Consequently, the input-output sensitivity function is designed vice versa.
Besides the question of how disturbance and noise affect the system, the focus lies on the most important requirement, which is the stability of the closed-loop system. The closed-loop system is asymptotically stable only if all transfer functions of (4.10) and (4.11) are asymptotically stable. This means that all

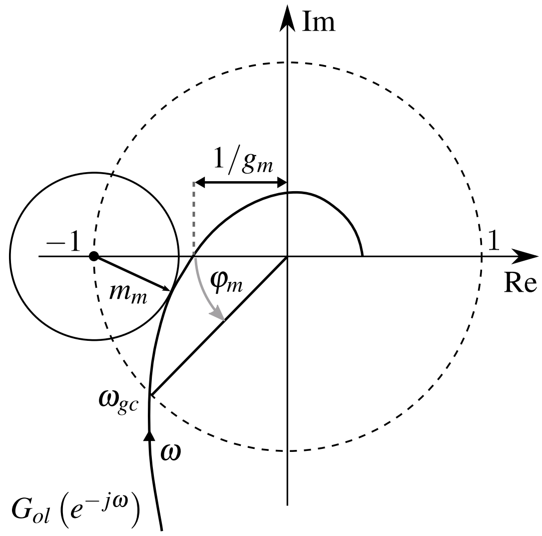

Figure 4.3.: Nyquist plot of the open-loop system $G_{ol}\left(e^{-j\omega}\right)$.

poles of the closed-loop system have to be inside the unit circle of the z-plane

$$|z_i| < 1, \qquad \text{for } A'_{cl}(z) \stackrel{!}{=} 0 \text{ and } i = 1 \ldots \deg A'_{cl} , \tag{4.14}$$

where A'_{cl} is denominator of the closed-loop transfer function. [86, 150]

Initially, the analysis of stability is based on a known, deterministic system only. However, in the practice parameter deviations, variations, and non-modeled dynamics affect the closed-loop system. Therefore, the criteria of stability from the control loop (4.14) have to be extended. The system has to be stable and should be robust against the uncertainties in the modeling. The Nyquist plot can be used in the frequency analysis to explain the robustness. Gain and phase margins are indicators of robustness of the closed-loop system at the critical point $(-1, j0)$ of the Nyquist plot, where the closed-loop system is unstable [86]. In Figure 4.3, the Nyquist plot for the open-loop system

$$G_{ol}\left(z^{-1}\right) = \frac{z^{-d_e} B\left(z^{-1}\right) R\left(z^{-1}\right)}{A\left(z^{-1}\right) S\left(z^{-1}\right)} \tag{4.15}$$

is shown.

The gain margin g_m is defined as the inversion of the open-loop transfer function at the frequency ω_{180} where the open loop gain is negative reel:

$$g_m = \frac{1}{\left|G_{ol}\left(e^{-j\omega_{180}}\right)\right|} \tag{4.16}$$

Furthermore, the phase margin φ_m is defined as

$$\varphi_m = 180° - \arg\left\{G_{ol}\left(e^{-j\omega_{gc}}\right)\right\} , \tag{4.17}$$

with the lowest frequency ω_{gc} at $\left|G_{ol}\left(e^{-j\omega_{gc}}\right)\right| = 1$. The relation of phase margin to ω_{gc} can also be interpreted as a time-delay margin $d_m = \varphi_m/\omega_{gc}$ of the system. The gain and phase margins are quantitative values to indicate the greatest difference between the gain and the phase until the system becomes unstable.

Both margins are definable criteria, but have the disadvantage of describing only two points in the Nyquist plot. A general definition is the modulus margin m_m, which is the minimum distance between $G_{ol}\left(e^{-j\omega}\right)$ and the critical point $(-1, j0)$

$$m_m = \min\left\{\left|1 + G_{ol}\left(e^{-j\omega}\right)\right|\right\} = \min\left\{\frac{1}{\left|S_{py}\left(z^{-1}\right)\right|}\right\} . \tag{4.18}$$

The gain and phase margin can be determined with the modulus margin:

$$g_m = \frac{1}{1 - m_m} \tag{4.19}$$

$$\varphi_m = 2\arcsin(0.5\, m_m) \tag{4.20}$$

The robustness values are a degree of freedom in the control design. A widely proven criterion is:

ROB.1 Robustness Criterion

The choice of $m_m \geq -6$ dB implies a gain margin $g_m \geq 6$ dB and a phase margin $\varphi_m \geq 29°$.

In this thesis, this criterion is used for the design of the controller.

Design of Pole Placement Controller

The RST controller can be designed to influence the characteristic closed-loop dynamics. This means that the poles of the closed-loop can be shifted with control parameters. This allows to design a controller for both stable and unstable systems as well as to determine the bandwidth frequency of the closed-loop dynamics. Taking into account the digital closed-loop control from Figure 4.2, the characteristic polynomial follows to:

$$A_{cl}\left(q^{-1}\right) = S\left(q^{-1}\right)A\left(q^{-1}\right) + q^{-d_e}R\left(q^{-1}\right)B\left(q^{-1}\right) \tag{4.21}$$

This polynomial is essential for the closed-loop dynamics and also for the disturbance sensitivity. Generally, the parameters $S\left(q^{-1}\right)$ and $R\left(q^{-1}\right)$ can be pre-specified in part with $H_S\left(q^{-1}\right)$ and $H_R\left(q^{-1}\right)$ (cf. (4.8) and (4.9)). This degree of freedom can be used, for example, to pre-specify an integrator $H_S\left(q^{-1}\right) = 1 - q^{-1}$ to achieve zero steady state error in presence of constant disturbances or parametric uncertainties. Consequently, the desired polynomial (4.21) follows to:

$$A_{cl}\left(q^{-1}\right) = S'\left(q^{-1}\right)H_S\left(q^{-1}\right)A\left(q^{-1}\right) + q^{-d_e}R'\left(q^{-1}\right)H_R\left(q^{-1}\right)B\left(q^{-1}\right) \tag{4.22}$$

With a desired specified stable polynomial $A_{cl}\left(q^{-1}\right)$, the control parameters can be determined by solving the Diophantine equation (4.22) for the polynomials R' and S'. [6, 86].

The minimal degree $n_{a_{cl}}$ of the desired polynomial A_{cl} is

$$n_{a_{cl}} = \deg\left\{A_{cl}\left(q^{-1}\right)\right\} \leq \deg\left\{A\left(q^{-1}\right)H_S\left(q^{-1}\right)\right\} + \deg\left\{q^{-d_e}B\left(q^{-1}\right)H_R\left(q^{-1}\right)\right\} - 1 \tag{4.23}$$

$$n'_s = \deg\ S'\left(q^{-1}\right) = \deg\left\{q^{-d_e}B\left(q^{-1}\right)H_R\left(q^{-1}\right)\right\} - 1 \tag{4.24}$$

$$n'_r = \deg\ R'\left(q^{-1}\right) = \deg\left\{A\left(q^{-1}\right)H_S\left(q^{-1}\right)\right\} - 1 \tag{4.25}$$

if (4.21) is coprime [150]. Finally, the coefficients of $R' = r'_o + r'_1 + \ldots + r'_{n'_r}$ and $S' = s'_o + s'_1 + \ldots + s'_{n'_s}$ can be determined by writing the Diophantine equation (4.22) in vector-matrix notation:

$$n_{a_{cl}} + 1 \left\{ \underbrace{\overbrace{\begin{bmatrix} \overline{a}_0 & 0 & \ldots \\ \overline{a}_1 & \overline{a}_0 & \ldots \\ \vdots & \vdots & \ddots \end{bmatrix}}^{\deg S'+1}\!\!\overbrace{\begin{bmatrix} \overline{b}_0 & 0 & \ldots \\ \overline{b_1} & \overline{b}_0 & \ldots \\ \vdots & \vdots & \ddots \end{bmatrix}}^{\deg R'+1}}_{} \right. \begin{bmatrix} s'_0 \\ \vdots \\ r'_0 \\ \vdots \end{bmatrix} = \begin{bmatrix} a_{cl_0} \\ \vdots \\ a_{cl_{na_{cl}}} \end{bmatrix} \tag{4.26}$$

where $\overline{A}(q^{-1}) = A(q^{-1})H_S(q^{-1})$ and $\overline{B}(q^{-1}) = B(q^{-1})R_S(q^{-1})$ are polynomials:

$$\overline{A}(q) = \overline{a}_0 q^{n_{AB}} + \overline{a}_1 q^{n_{AB}-1} + \ldots + \overline{a}_{n_{AB}} \tag{4.27}$$

$$\overline{B}(q) = \overline{b}_0 q^{n_{AB}} + \overline{b}_1 q^{n_{AB}-1} + \ldots + \overline{b}_{n_{AB}} \tag{4.28}$$

with

$$n_{AB} = \max\ \deg\left\{\overline{A}S', \overline{B}R'\right\}\ . \tag{4.29}$$

The calculation method of the polynomials $H_R\left(q^{-1}\right)$ and $H_S\left(q^{-1}\right)$ to cancel poles and zeros of the closed-loop transfer functions are presented in [150].
The guideline for the controller design can be split into three parts:

1. Perform stability analysis of the plant (poles and zeros). Define $H_R\left(q^{-1}\right)$ and $H_S\left(q^{-1}\right)$ in order to cancel and/or to minimize the steady-state error.

2. Define the characteristic polynomial for the desired closed-loop dynamics. Calculate $S'\left(z^{-1}\right)$ and $R'\left(z^{-1}\right)$ utilizing the Diophantine equation.

3. Check the desired stability and robustness criteria with frequency analysis. If the criteria are not satisfied, modify $H_S\left(q^{-1}\right)$ and $H_R\left(q^{-1}\right)$ and/or select another desired closed-loop dynamic.

Detailed design guidelines for determination of control parameters are presented in [86] and [150].

Anti-Wind-Up

Practical applications have actuators with saturations, for example, a PWM. These saturations can affect the performance of the controller, especially if the controller has an integral part. In case that the

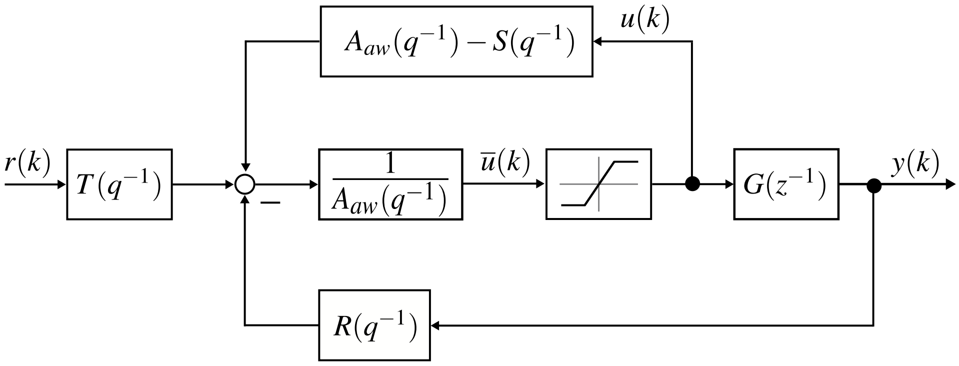

Figure 4.4.: Modified controller to prevent the wind-up effect.

saturation of the actuator is reached and the error of the controller is unequal to zero, the control signal increases to infinity, which is caused by the integrator. This effect is called wind-up and can lead to an unstable closed-loop system. A suitable countermeasure against the wind-up is to integrate the nonlinear actuator characteristic into the controller (see Figure 4.4). [6]
This modification yields to

$$A_{aw}\left(q^{-1}\right)\overline{u}(k) = T\left(q^{-1}\right)r(k) - R\left(q^{-1}\right)y(k) + \left[A_{aw}\left(q^{-1}\right) - S\left(q^{-1}\right)\right]u(k)\ , \tag{4.30}$$

where $u(k)$ is a saturation function with the limited value u_{sat} and is defined as:

$$u(k) = \mathrm{sat}\,\overline{u}(k) := \begin{cases} \overline{u}(k)\ , & |\overline{u}(k)| < u_{sat} \\ u_{sat}\ , & \overline{u}(k) \geq u_{sat} \\ -u_{sat}\ , & \overline{u}(k) \leq -u_{sat} \end{cases}\ , \tag{4.31}$$

The polynomial $A_{aw}\left(q^{-1}\right)$ can be specified as a first or a second order system. The polynomial $A_{aw}\left(q^{-1}\right)$ must be stable and the degree of $A_{aw}\left(q^{-1}\right)$ is smaller or equal to $S\left(q^{-1}\right)$. [86, 150]
In this thesis, $A_{aw}\left(q^{-1}\right)$ is selected as $A_{cl}\left(q^{-1}\right)$.

4.1.3. Conclusion

In this section, the design concept of a linear digital control is presented. This concept has the advantage of two degrees of freedom. The first degree of freedom is to design the poles and the zeros of the closed-loop control. The second degree of freedom can be used to design the gain or the dynamics of the reference signal of the control loop. An important aspect of the control parameter design is the stability of the control loop, which depends on the transfer functions from reference, noise, and disturbance signal to output signal. Design criteria as the sensitivity and the complementary transfer function can be used to ensure stability. The general problem is to handle parameter variations of the control transfer functions. These variations lead to a mismatch of the desired closed loop dynamic. To ensure the stability of the control loop in this case, a robustness criterion can be designed, which should be involved in the design of the control parameters. A drawback of this design concept is the mismatch of the desired closed-loop

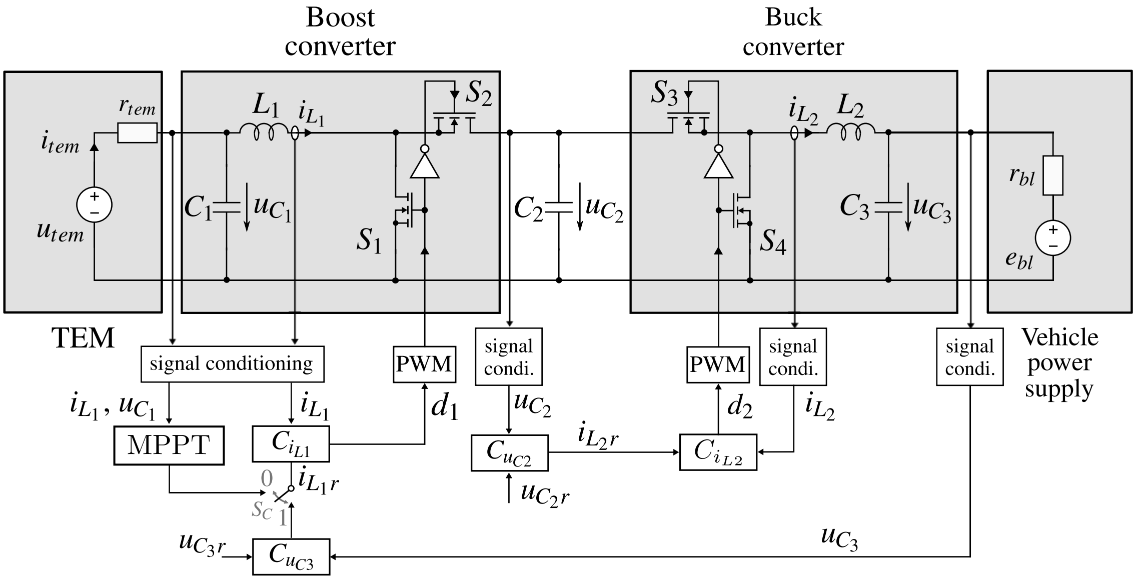

Figure 4.5.: Control structure of the boost-buck converter without ESR values.

dynamics if the parameters vary.
An alternative is an online adaption of the control parameters, which requires the identification of the gain, the poles, and the zeros of the plant.
However, the design of the linear digital control requires a detailed analysis of the plants from the DC-DC converters.

4.2. Control Structure

The used control structure (see Figure 4.5) for the boost-buck converter is presented in [70]. To charge the battery and supply the load, a cascade control structure is used. Control of the capacitor voltage u_{C_2} by the voltage controller $C_{u_{C2}}$ between boost and buck converters ensures that electrical fluctuations or changes of the TEM are compensated. The capacity C_2 functions as an energy buffer and decouples high frequency feedbacks from boost and buck converters. A subsidiary controller $C_{i_{L2}}$ regulates the charge current i_{L_2}. The advantage of a cascade control is the compensation of the disturbance of the current control with a lower settling time as the voltage controller. Hence, the voltage controller $C_{u_{C2}}$ is used to regulate the reference voltage of the capacitor C_2 and has a higher settling time to smooth the reference value for the subsidiary current controller. A feature of this control structure is a degree of freedom to choose the reference voltage u_{C_2}. Consequently, the control structure is able to supply all battery voltage levels if $u_{C_2} > u_{C_3}$. The input current controller $C_{i_{L1}}$ is used to regulate the load current of the TEM. In case the battery voltage is lower than the maximum allowed charging voltage of the vehicle power supply (e.g. 13.6 V), the MPPT algorithm searches the MPP of the TEM and calculates the current setpoint i_{L_1r}. If the output voltage is higher than the allowed charging voltage, the MPPT is disabled through the logic

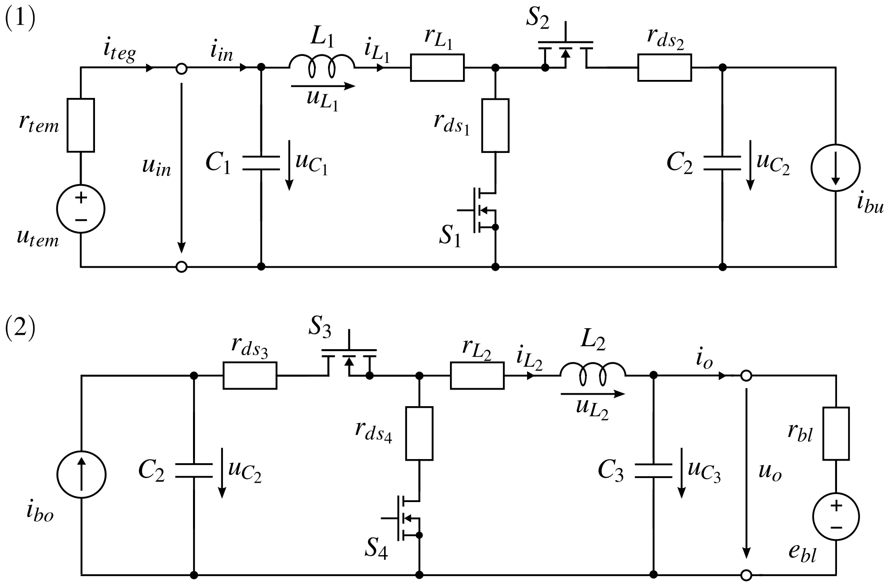

Figure 4.6.: Separation of the boost-buck converter in a boost converter with a current sink (i_{bu}) and a buck converter with a current source (i_{bo}).

switch $S_C = 1$. In this case, the new current reference value is determined by the control loop C_{uC3}. The controller $C_{u_{C3}}$ reduces the reference input current to keep the charging voltage (e.g. 13.6 V) at the vehicle supply. To re-enable the MPPT, the logic switch must selected to $S_C = 0$. All measurement signals of the BoBu converter are filtered with a second order low-pass. The signals i_{L_1}, i_{L_2}, u_{C_1}, u_{C_2} and u_{C_3} have a bandwidth of $f_c = 1$ kHz and are sampled with $f_s = 10$ kHz from a 12 bit ADC in the μC.
In the following, the Subsection 4.2.1 presents the system model of the boost-buck converter in detail. The SSA model is verified with measurements of a test bench. The design of the control parameters and experimental step responses of the control closed loops are presented in Subsection 4.2.2.

4.2.1. Analysis of Dynamic Model for Boost-Buck Converter

The design of the controller is based on the analysis of the plants. The modeling uses the SSA method, which is presented in the Section 3.3. In this section, the modeling and the analysis of the BoBu converter is presented in detail. For simplification, the ESR values of the capacitors are neglected, because the values are marginal in relation to all other ESR values (cf. Appendix A.4). The buffer capacity C_2 of the BoBu converter serves as a decoupling between the boost and buck converter. Therefore, the modeling can be separated to a boost converter with an ideal approximate current sink and a buck converter with an ideal approximate current current source (see Figure 4.6). The current sink and source are defined as:

$$i_{bu} = i_{L_2} d_2 \tag{4.32}$$

$$i_{bo} = i_{L_1} (1 - d_1) \tag{4.33}$$

With (4.32) and (4.33), the differential equations of the BoBu converter are:

$$\frac{du_{C_1}}{dt} = -\beta_1\, u_{C_1} - \beta_2\, i_{L_1} + \beta_3\, u_{tem} \tag{4.34}$$

$$\frac{du_{C_2}}{dt} = \delta_1\, i_{L_1} - \delta_2\, i_{L_1} d_1 - \delta_3\, i_{L_2}\, d_2 \tag{4.35}$$

$$\frac{du_{C_3}}{dt} = \gamma_1\, i_{L_2} - \gamma_2\, u_{C_3} + \gamma_3\, e_{BL} \tag{4.36}$$

$$\begin{aligned}\frac{di_{L_1}}{dt} = {} & \alpha_1\, i_{L_1} + \alpha_2\, u_{C_1} - \alpha_3\, u_{C_2} + \alpha_4\, u_{tem} + \alpha_5\, d_1\ i_{L_1} + \alpha_6\, d_2\ i_{L_2} + \alpha_3\, d_1\, u_{C_2} \\ & \alpha_6\, d_1\, d_2\, i_{L_2}\end{aligned} \tag{4.37}$$

$$\frac{di_{L_2}}{dt} = -\varepsilon_1\, i_{L_2} - \varepsilon_2\, u_{C_3} + \varepsilon_3\, e_{BL} - \varepsilon_4\, i_{L_2} d_2 - \varepsilon_5\, d_2\, i_{L_1} + \varepsilon_6\, d_1\, d_2\, i_{L_1}\ , \tag{4.38}$$

where α_{1-6}, β_{1-3}, γ_{1-3}, δ_{1-3} and ε_{1-6} are system parameters (see Appendix A.1). To determine the linearization of the state space model, the Jacobian matrix can be used. This matrix involves the partial derivations of the nonlinear state functions (4.34) - (4.38) [50].

The linearization of the state spaces at the operation points $\mathbf{X} = [U_{C1}, I_{L1}, U_{C2},\ I_{L2},\ U_{C3}]^T$ and $\mathbf{U} = [U_{tem},\ E_{bl},\ D_1,\ D_2]^T$ yield the small signal SSA model

$$\dot{\mathbf{x}} = \mathbf{A}\mathbf{x} + \mathbf{B}\mathbf{u} \tag{4.39}$$

$$\mathbf{y} = \mathbf{c^T}\mathbf{x} \tag{4.40}$$

$$\mathbf{A} = \begin{bmatrix} \beta_1 & \beta_2 & 0 & 0 & 0 \\ \alpha_2 & \alpha_5\, D_1 + \alpha_1 & \alpha_3\,(1-D_1) & \alpha_6\,(D_2 - D_1\, D_2) & 0 \\ 0 & \delta_2\, D_1 + \delta_1 & 0 & \delta_3\, D_2 & 0 \\ 0 & D_1\, D_2\, \varepsilon_6 + D_2\, \varepsilon_5 & 0 & D_2\, \varepsilon_4 + \varepsilon_1 & \varepsilon_2 \\ 0 & 0 & 0 & \gamma_1 & \gamma_2 \end{bmatrix} \tag{4.41}$$

$$\mathbf{B} = \begin{bmatrix} \beta_3 & 0 & 0 & 0 \\ \alpha_4 & 0 & -\alpha_3\, u_{C2} - \alpha_6\, D_2\, I_{L2} + \alpha_5\, I_{L1} & -\alpha_6\, D_1\, I_{L2} + \alpha_6\, I_{L2} \\ 0 & 0 & \delta_2\, I_{L1} & \delta_3\, I_{L2} \\ 0 & \varepsilon_3 & D_2\, \varepsilon_6\, I_{L1} & \varepsilon_4\, I_{L2} + D_1\, \varepsilon_6\, I_{L1} + \varepsilon_5\, I_{L1} \\ 0 & \gamma_3 & 0 & 0 \end{bmatrix} \tag{4.42}$$

$$\mathbf{c^T} = \begin{bmatrix} 0 & 1 & 0 & 0 & 0 \\ 0 & 0 & 1 & 0 & 0 \\ 0 & 0 & 0 & 1 & 0 \\ 0 & 0 & 0 & 0 & 1 \end{bmatrix}\ , \tag{4.43}$$

where $\mathbf{x} = [\tilde{u}_{C1}, \tilde{i}_{L1}, \tilde{u}_{C2},\ \tilde{i}_{L2},\ \tilde{u}_{C3}]^T$ is the state vector, $\mathbf{u} = [\tilde{u}_{tem},\ \tilde{e}_{BL},\ \tilde{d}_1,\ \tilde{d}_2]^T$ is the input vector and $\mathbf{y} = [\tilde{i}_{L1}, \tilde{u}_{C2},\ \tilde{i}_{L2},\ \tilde{u}_{C3}]^T$ is the output vector. The tide symbols the changes of the signals and states in relation to the operation points **U** and **X**

From (4.39) it follows that the system is a multi-input multi-output system. It can be determined using frequency analysis that the amplitude of the plants

$$G_{d_1 i_{L1}}(s) = \frac{\tilde{i}_{L1}(s)}{\tilde{d}_1(s)} \tag{4.44}$$

$$G_{d_1 u_{C3}}(s) = \frac{\tilde{u}_{C3}(s)}{\tilde{d}_1(s)} \tag{4.45}$$

$$G_{d_2 i_{L2}}(s) = \frac{\tilde{i}_{L2}(s)}{\tilde{d}_2(s)} \tag{4.46}$$

$$G_{d_2 u_{C2}}(s) = \frac{\tilde{u}_{C2}(s)}{\tilde{d}_2(s)} \tag{4.47}$$

are dominant in the frequency range up to $f_s/2$ [70]. Hence, the plant can be assumed as a single-input single-output system.

For simplification, the tilde symbol of the vector elements **x** and **u** is neglected.

From (4.39) - (4.42) it follows, that the eigenvalues and DC gains of the system depend on the system parameters. The series resistor r_{tem} value affect the system coefficients of the converter (cf. Appendix A.1). The effect of a resistor variation to the transfer functions dynamics (4.44) - (4.47) is shown in the frequency analysis (see Figure 4.7). The resistor r_{tem} is thereby sequentially varied from 0 to 3 Ω. In case r_{tem} increases, the DC gain of (4.44) and (4.47) increases and in contrast, (4.45) and (4.46) decreases. This in particular leads to a shift of the gain crossover frequency by up to 1.5 kHz. The most significant influences of the resistor can be observed at $G_{d_1 u_{C3}}$ and $G_{d_2 i_{L2}}$. Due to the increase of the r_{tem} value, the input voltage u_{C_1} is reduced at constant operating points. From the law energy conservation it follows that the transformation ratio between the input and the middle voltage increases and the current i_{L_2} decreases at the same time. Consequently, the amplitude of $G_{d_1 u_{C3}}$ reduces.

It follows from the bode plot of $G_{d_2 i_{L2}}$ that higher values of the resistor r_{tem} reduce the DC-gain. Consequently, the charge and discharge time of the buffer capacitor increases.

Verification of Transfer Functions

Generally, the complexity of a parameter-based model increases with the accuracy of the model. In particular, nonlinearities or saturations lead to extensive models. To verify the SSA model, the plants should be measured. For this reason, a test bench was established with a direct control of the MOSFETs and an external data acquisition of the signals via a MicroAutoBox II from dSPACE. For this measurement, the μC of the converter was disabled. A representation of the measurement configuration and data processing principle is shown in Figure 4.8. The test bench for the simulation of TEM and load had the same configuration as the test bench presented in Section 3.7. Voltage source and series power potentiometers were used for the TEM along with electric load for the stimulation of the on-board power supply.

In order to perform a spectral analysis, the duty cycles of the MOSFETs were change with a sinusoidal input signal at the operating point with the amplitude of $\tilde{d}_1$ and $\tilde{d}_2$. The states were measured and conditioned with sensors as well as anti-aliasing filters. Finally, a discrete Fourier transformation (DFT) was performed, which calculates the amplitude and the phase of each excitation frequency. The selected

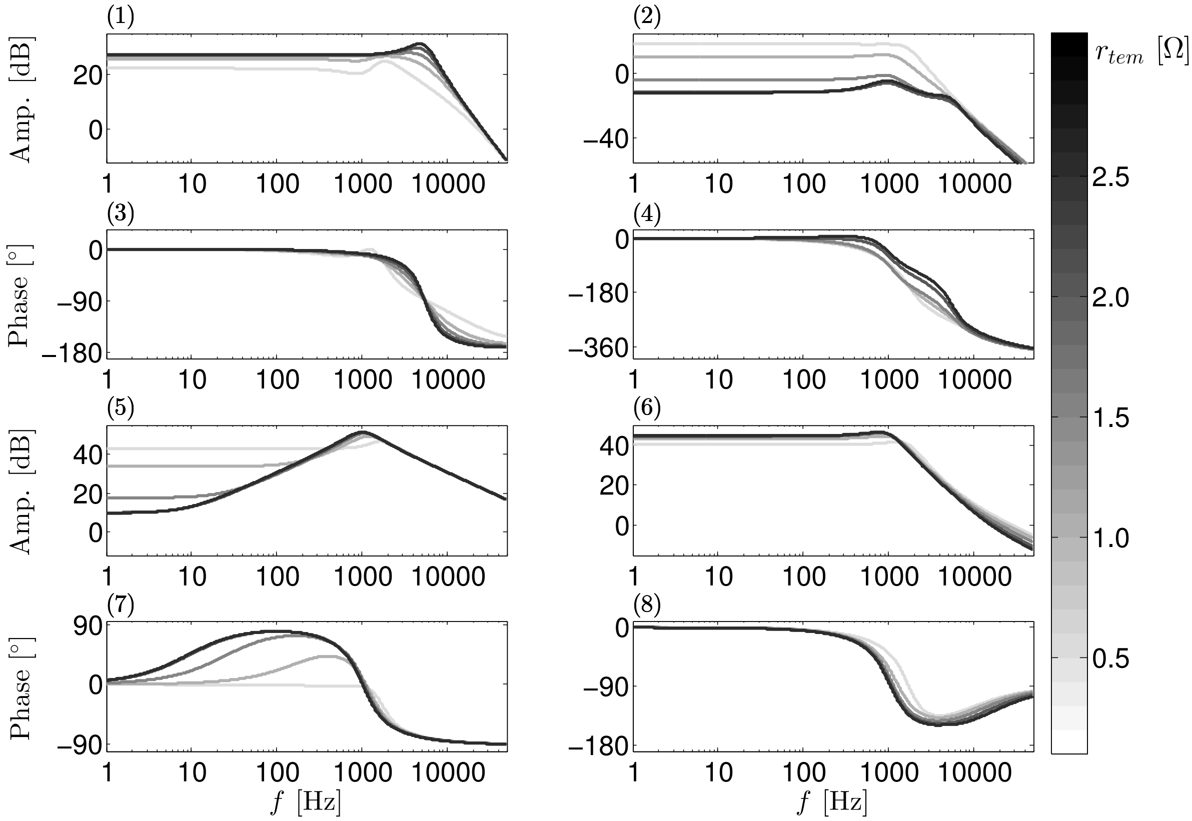

Figure 4.7.: Bode plot of $G_{d_1 i_{L1}}$, $G_{d_1 u_{C3}}$, $G_{d_2 i_{L2}}$, $G_{d_2 u_{C2}}$ for different values of r_{tem}. The amplitude and phase of $G_{d_1 i_{L1}}$ are presented in (1) and (3). The amplitude and phase of $G_{d_1 u_{C3}}$ are presented in (2) and (4). The amplitude and phase of $G_{d_2 i_{L2}}$ are presented in (5) and (7). The amplitude and phase of $G_{d_2 u_{C2}}$ are presented in (6) and (8).

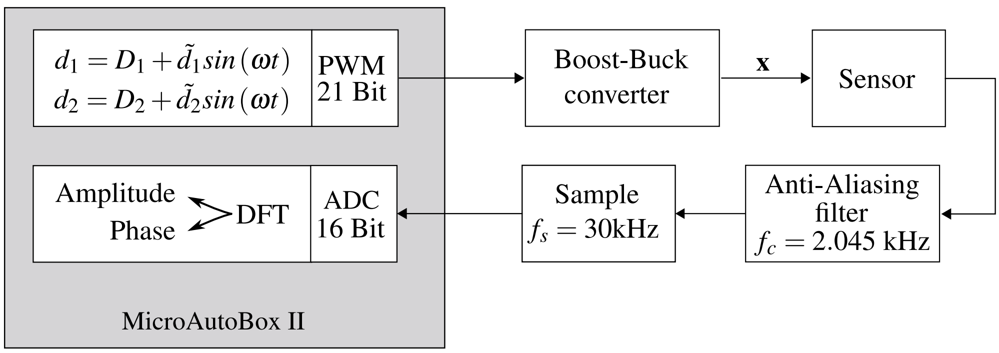

Figure 4.8.: Measurement configuration and data processing principle of the frequency analysis of the BoBu converter. The MicroAutoBox II controls the MOSFETs with the duty cycles d_1 and d_2. The states were measured and conditioned for the ADC of the MicroAutoBox II. The measurement data were analyzed with a DFT.

operation points of the converter and the parameters of the measurement are shown in Table 4.1. The maximum confidence interval of the measurement data was limited by the measurement chain. The maximum confidence interval of the measurements was defined as the least significant bit voltage of

operation point	value	operation point	value
U_{tem}	30 V	r_{tem}	0.1 Ω
E_{bl}	12.5 V	U_{C_1}	29.5 V
I_{L_1}	5 A	U_{C_2}	48 V
I_{L_2}	10.6 A	U_{C_3}	13.6 V
D_1	0.40	D_2	0.28
$\tilde{d}_1$	0.020	$\tilde{d}_2$	0.014

Table 4.1.: Parameters and specification of the boost-buck converter for the frequency analysis.

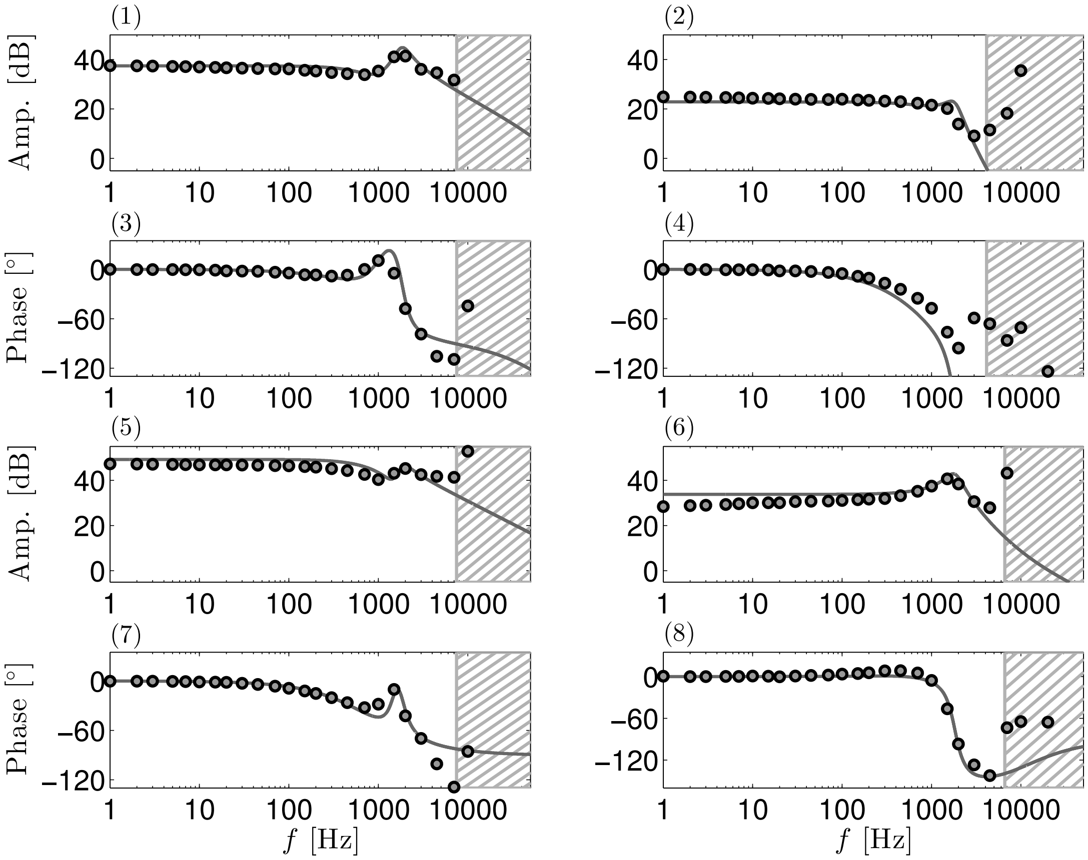

Figure 4.9.: Bode plot of $G_{d_1 i_{L1}}$, $G_{d_1 u_{C3}}$, $G_{d_2 i_{L2}}$, $G_{d_2 u_{C2}}$ (black line) in relation to the experimental measurements results (dotted markers). The amplitude and the phase of $G_{d_1 i_{L1}}$ are presented in (1) and (3). The amplitude and the phase of $G_{d_1 u_{C3}}$ are presented in (2) and (4). The amplitude and the phase of $G_{d_2 i_{L2}}$ are presented in (5) and (7). The amplitude and the phase of $G_{d_2 u_{C2}}$ are presented in (6) and (8). The measurements in the criss-cross gray area are outside of the confidence interval.

the ADC [17]. Therefore, the theoretical confidence interval is marked in the measurement results (see Figure 4.9). The root-mean-square (RMS) error of the amplitude e_{rms_a} and the phase e_{rms_p} between the model and the measurement in the confidence interval is shown in Table 4.2. From the comparison of the

transfer function	e_{rms_a} [dB]	e_{rms_p} [°]
$G_{d_1 i_{L1}}$	1.27	7.23
$G_{d_1 u_{C3}}$	2.22	23.86
$G_{d_2 i_{L2}}$	2.61	6.62
$G_{d_2 u_{C2}}$	3.41	5.13

Table 4.2.: Root-mean-square error between model and measurement results of the frequency analysis. The error of the amplitude is e_{rms_a} and of the phase is e_{rms_p}.

results from Figure 4.9 it follows that, besides from $G_{d_2 u_{C2}}$, the amplitudes of the transfer functions have marginal differences lower than nearly 2.6 dB. The amplitude error of $G_{d_2 u_{C2}}$ reaches up to 4 dB (see Figure 4.9). The mismatch between the model and the measurement can be caused by selected values of the power potentiometer and/or additional contact resistor values from the test bench. An additional uncounted contact resistor of only 80 mΩ between the TEM and the converter reduces the an RMS error to nearly 1.88 dB (cf. Appendix A.6).

In contrast, the RMS errors of the phase from the transfer functions show significantly higher errors between the measurements and the models. However, from Figure 4.9 it follows that the highest differences occur only by up to nearly 1000 Hz. Under 1000 Hz, the RMS phase errors are below 1.4 °. These errors can also be caused by uncounted resistor values. The errors in the frequency range over 1000 Hz could be caused by the internal controller of the electrical load from the test bench. This equipment uses a controller to regulate the desired source load. The maximal band frequency is only 2 kHz, which influences the phase and the amplitude of the signals above this frequency. This would also explain the significantly higher RMS error of the transfer function from the duty cycle d_2 to the output voltage u_{C_3} of the DC-DC converter. Albeit the measurement results of the transfer functions show differences compared to the model results, a qualitative consistency can be determined. Finally, it can be stated that there is a qualitative correspondence between the measurements and the model. The accuracy of the mathematical model is sufficient for the controller design, because the deviations of the model and the converter prototype can be compensated by the robustness requirement ROB.1 of the controller.

4.2.2. Design of Controller

The control structure of the converter is presented in Figure 4.5. The closed-loop control are digital feedback circuits with two degrees of freedom. The design rules and syntheses of the controllers are presented in this section. To get a better overview, the feedback controllers of the BoBu converter can be separated in two cascade controllers. The first is used to stabilize and regulate the buffer voltage u_{C_2} ($C_{u_{C2}}$) and to charge the load with the current controller ($C_{i_{L2}}$) of i_{L_2}. In contrast, the second cascade controller uses a subsidiary current controller ($C_{i_{L1}}$) to regulate the input current i_{L_1} of the TEM. In case the load of the converter exceeds the maximum charging voltage, an output voltage controller ($C_{u_{C3}}$) is

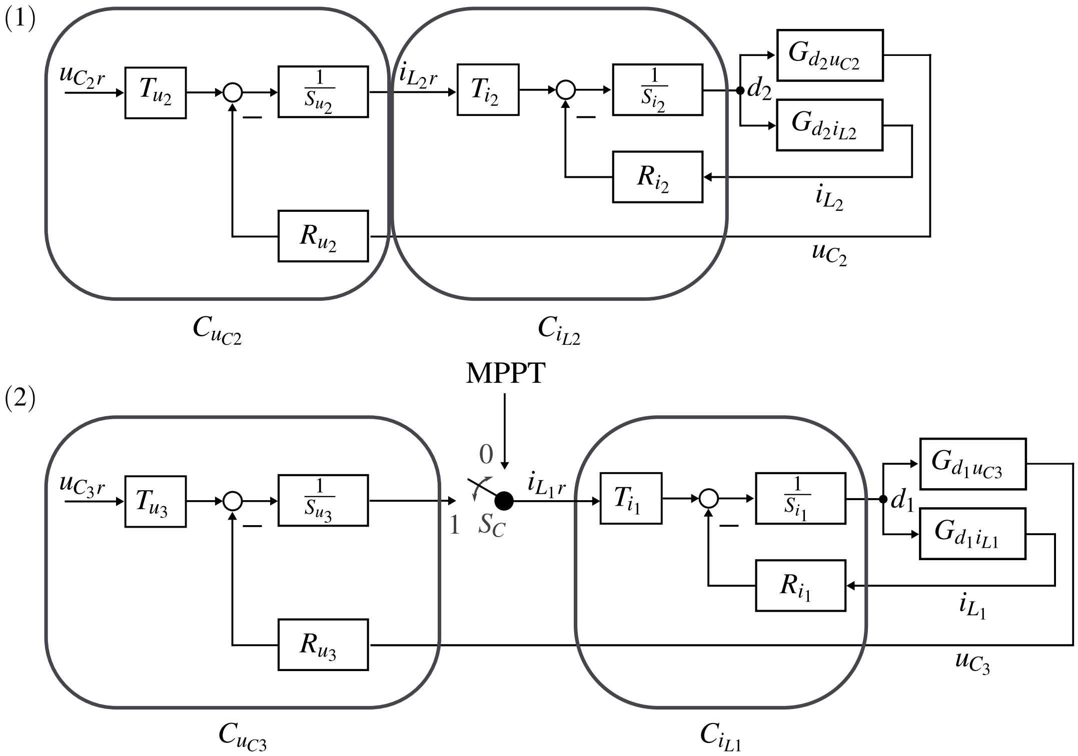

Figure 4.10.: Control structure of the boost-buck converter in detail. The cascade controller $C_{u_{C2}}$ of the buffer voltage u_{C_2} with the subsidiary output current controller $C_{i_{L2}}$ is shown in (1). The cascade controller $C_{u_{C3}}$ of the over-voltage charging controller u_{C_3} with the subsidiary input current controller $C_{i_{L1}}$ is presented in (2).

used to regulate the trickle charging of the battery. In case, that the voltage is lower than the maximum charging voltage, the reference signal of the current controller is determined from an MPPT algorithm. This algorithm ensures that the maximum power is recovered from the TEM.

The two cascade controllers are shown in Figure 4.10. In contrast to (4.44) - (4.47), the plants $G_{d_2 u_{C2}}$, $G_{d_2 i_{L2}}$, $G_{d_1 u_{C3}}$, and $G_{d_1 i_{L1}}$ additionally include the anti-aliasing filter $G_f(s)$

$$G_f(s) \quad = \quad \frac{\omega_c}{s^2 + 2\,\xi_c \omega_c s + \omega_c^2}\,, \tag{4.48}$$

where $\omega_c = 2\pi f_c$ is the cut-off natural frequency and ξ_c is the cut-off damping. For the application, $f_c = 1$ kHz and $\xi_c = 1$ are selected.

Parametrization

The basic design and parametrization of the controllers are based on the presented principles in Section 4.1. The selection of the desired polynomial A_{cl} is fundamental. A typical definition of the desired closed-loop dynamics S_{by} from reference $r(k)$ to output signal $y(k)$ is a first or second order system. In this thesis, a system of second order is chosen because of the degree of freedom of the damping factor ξ

and the bandwidth of the closed-loop system. The second order system is defined as:

$$G_{PT2}(s) = \frac{\omega_o^2}{s^2 + 2\xi\,\omega_o s + \omega_o^2} \tag{4.49}$$

$$G_{PT2}(z^{-1}) = \mathscr{Z}\left\{\mathscr{L}^{-1}\left(\frac{G_{CL}(s)}{s}\right)\right\} = \frac{b_{pt2_1}\,z^{-1} + b_{pt2_2}\,z^{-2}}{1 + a_{pt2_1}\,z^{-1} + a_{pt2_2}\,z^{-2}}\,, \tag{4.50}$$

where b_{pt2_i} and a_{pt2_i}, with $i = 1,2$ are the coefficients, $\omega_o = 2\pi f_o$ and f_o are the natural frequencies [86]. In relation to (4.50), the desired closed-loop dynamics follows to:

$$T_{ry}(q^{-1}) = \frac{y(k)}{r(k)} \tag{4.51}$$

$$T_{ry}(q^{-1}) \overset{!}{=} \frac{q^{-d_e}T(q^{-1})B(q^{-1})}{A_{cl}(q^{-1})} = \frac{q^{-d_e}T(q^{-1})B(q^{-1})}{1 + a_{cl_1}\,q^{-1} + a_{cl_2}\,q^{-2}} = \frac{q^{-d_e}T(q^{-1})B(q^{-1})}{1 + a_{pt2_1}\,z^{-1} + a_{pt2_2}\,z^{-2}} \tag{4.52}$$

From the analysis in Subsection 4.2.1 it follows that the plants have not an integral part. To ensure that the steady-state error between the reference and the measurement signal converges to zero, an integrator has to be used. Hence, the polynomial $H_s(q^{-1})$ is preselected as $1 - z^{-1}$.

The two cascade controllers of u_{C_2} and u_{C_3} are based on the design requirement for the current controllers to have a higher bandwidth. This means that the rise time of the subsidiary control is significantly smaller than that of the voltage controller. Therefore, disturbances at the output of the current closed-loop control can be compensated faster. Hence, the closed-loop dynamics of the subsidiary control can be neglected when designing voltage controllers.

Before the polynomials are determined, the electrical behavior and the requirements must be defined to select the necessary design criterion for the controller.

The input current controller can be designed as low-frequency, because the temperature changes of the waste heat in the TEG system and, consequently, the electrical parameters of the TEM are low-frequency in contrast to the electric dynamic of the converter. However, the bandwidth of the current closed-loop limits the convergence time of the MPPT algorithm. In the initial phase of the converter, the voltage u_{C_2} has to reach the reference value before the current controller $C_{i_{L2}}$ starts to supply the load of the converter. When the current controller $C_{i_{L2}}$ starts to supply the load, the voltage u_{C_2} of the buffer capacitor C_2 decrease. If the capacity is not charged from the input controller with the same bandwidth, it could lead to undesirable oscillations in the starting phase. Thus, it is favorable to design the closed-loop system of i_{L_1} with the same or greater bandwidth as the closed-loop system of i_{L_2}.

The dynamic behavior from the closed-loop system of i_{L_2} can be neglect, in case the bandwidth of the closed-loop system of the voltage u_{C_2} is significant lower. This choice is useful to simplified the control design of the cascade controller. In this thesis, the bandwidth of closed-loop system of u_{C_2} should be less than five times than the subsidiary closed-loop of i_{L_2}.

In contrast, the bandwidth requirement of the control loop $C_{u_{C3}}$ is uncritical. The bandwidth of $C_{u_{C3}}$ has to be smaller than that of the controller $C_{i_{L1}}$ to change the desired reference values for the current controller smoothly. However, the loop should be able to react adequately to on-board power supply changes like the connecting and disconnecting of power consumers. Consequently, the bandwidth can be selected

controller	f_o [Hz]	ξ	t_r [ms]
$C_{i_{L1}}$	500	0.95	1
$C_{i_{L2}}$	500	0.95	1
$C_{u_{C2}}$	100	0.95	5
$C_{u_{C3}}$	250	0.95	2.5

Table 4.3.: Design parameters for the cascaded controllers. Presented is the natural frequency f_o and the damping factor ξ of the reference system $G_{CL}(s)$ for the closed-loop dynamics $S_{by}(q^{-1})$. The equivalent rising time t_r of the closed-loop is the time which is needed for the output signal to pass 10 % to 90 % of the reference value.

between 100 Hz and 250 Hz.
The selected reference values for the closed-loop dynamics are presented in Table 4.3. Based on this criterion, the controller parameters are calculated with the Bézout identity (cf. (4.26)).
A separation from the reference and disturbance rejection is not necessary. For this reason, $T(q^{-1})$ is selected to ensure a DC gain of one for the reference $r(k)$ to output $y(k)$ signal

$$T(q^{-1}) = \frac{A_{cl}(1)}{B(1)} \,. \tag{4.53}$$

The determined polynomials of the controllers are presented in the Appendix A.7. The selected operation points of the TEM and the load for the control design are $u_{tem} = 60$ V, $r_{tem} = 0.1$ Ω, $e_{bl} = 12$ V, $r_{bl} = 0.1$ Ω.

Robustness

The variation of the internal resistor r_{tem} or the voltage u_{tem} from the TEM affects the dynamics of the control plants (cf. Section 4.7). Hence, the desired closed-loop dynamics and also the poles of the transfer functions can differ from the analysis at the assumed operation point. In [70, 72, 73, 122], a controller for a DC-DC converter is presented with the assumption that the internal resistor r_{tem} and u_{tem} is well-known. Hence, this assumption restricts the allowed application of TEMs with different electrical characteristics.
In this thesis, the closed-loop dynamics should be stable, for all variations of the parameters from the TEM. The influence of the closed-loop control can be analyzed with the SSA model of the DC-DC converter and parameter variations of the TEM. Furhter, the close-loop systems must be satisfy the robustness criterion ROB.1, to ensure a gain and phase margin. In case that the designed controller does not satisfy the robustness criterion ROB.1, the polynomials H_s and H_r must be redesigned to eliminate or damp the critical frequency ranges of the sensitivity and the complementary sensitivity function. The advantage of this straightforward methods is that it requires only moderate effort. In contrast, numerical analyzes like the H_∞ are difficult to handle for systems with time-delays and results in a complex modeling, especially by high order converters like the BoBu converter [16].

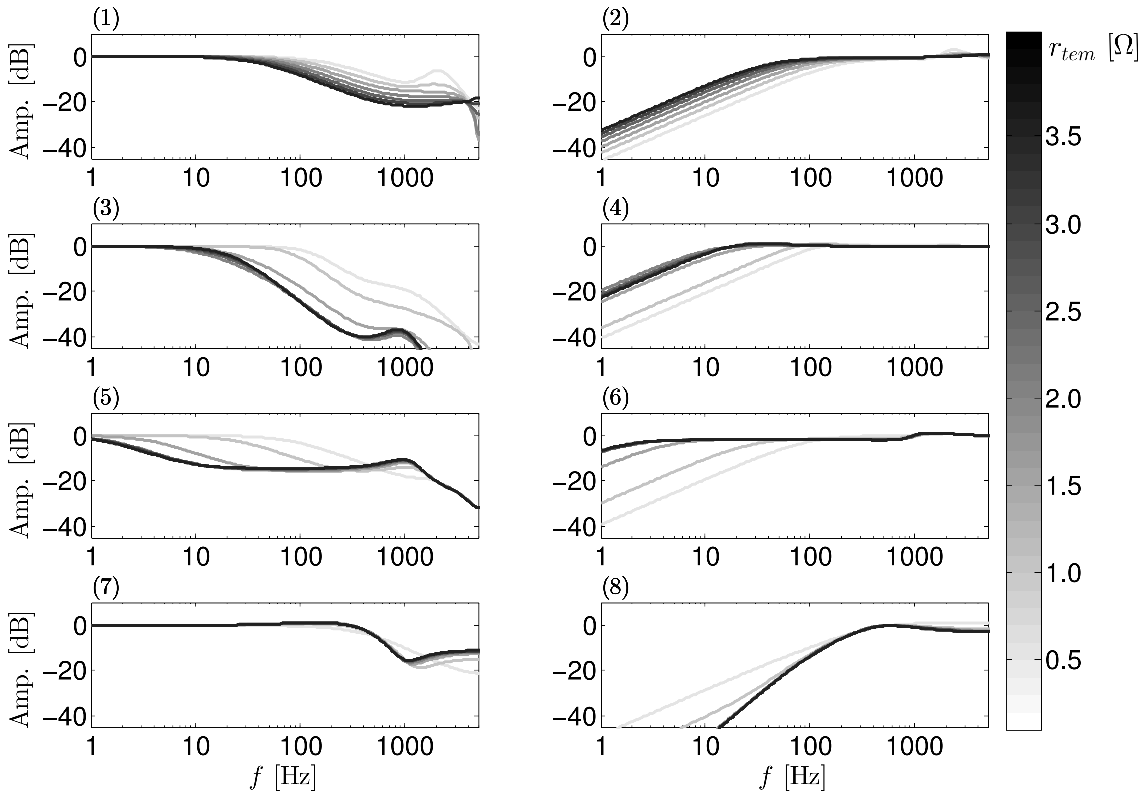

Figure 4.11.: Bode plot of the sensitivity $S_{py}(z^{-1})$ and complementary sensitivity $S_{by}(z^{-1})$ for the controllers for different resistor values r_{tem}. The amplitudes of $S_{by}(z^{-1})$ and $S_{py}(z^{-1})$ of the current controller $C_{i_{L1}}$ are presented in (1) and (2). The amplitudes of $S_{by}(z^{-1})$ and $S_{py}(z^{-1})$ of the voltage controller $C_{u_{C3}}$ are presented in (3) and (4). The amplitudes of $S_{by}(z^{-1})$ and $S_{py}(z^{-1})$ of the current controller $C_{i_{L2}}$ are presented in (5) and (6). The amplitudes of $S_{by}(z^{-1})$ and $S_{py}(z^{-1})$ of the voltage controller $C_{u_{C2}}$ are presented in (7) and (8). In all cases, the variations of the internal resistor influence the sensitivity functions.

The result of the analysis of the sensitivity functions of the controllers for r_{tem} between 0 Ω and 4 Ω and $u_{tem} = 30$ V is presented in Figure 4.11. The result shows that ROB.1 guarantees stability of the closed-loop systems for a variation of r_{tem} and that the sensitivity functions converge for higher r_{tem} values up 3 Ω. The reason for this effect is that higher values of r_{tem} increase the damping of the eigenvalues from the converter. Consequently, the eigenvalues and the dynamics of the DC-DC converter are nearly independent from the TEM when r_{tem} is significantly above 3 Ω. Further, all open-loop systems satisfy the robustness criterion ROB.1, which is illustrated in the Nyquist plot (see Figure 4.12).
Furthermore, the closed-loop dynamics are also stable and satisfy the robustness criterion ROB.1, for all variations of parameter variations of allowed TEM parameters (cf. REQ.3). However, the closed-loop dynamics of the controllers is influenced by the resistor. The robustness criterion ensures a stable closed-loop, but not a constant bandwidth of the desired feedback system.

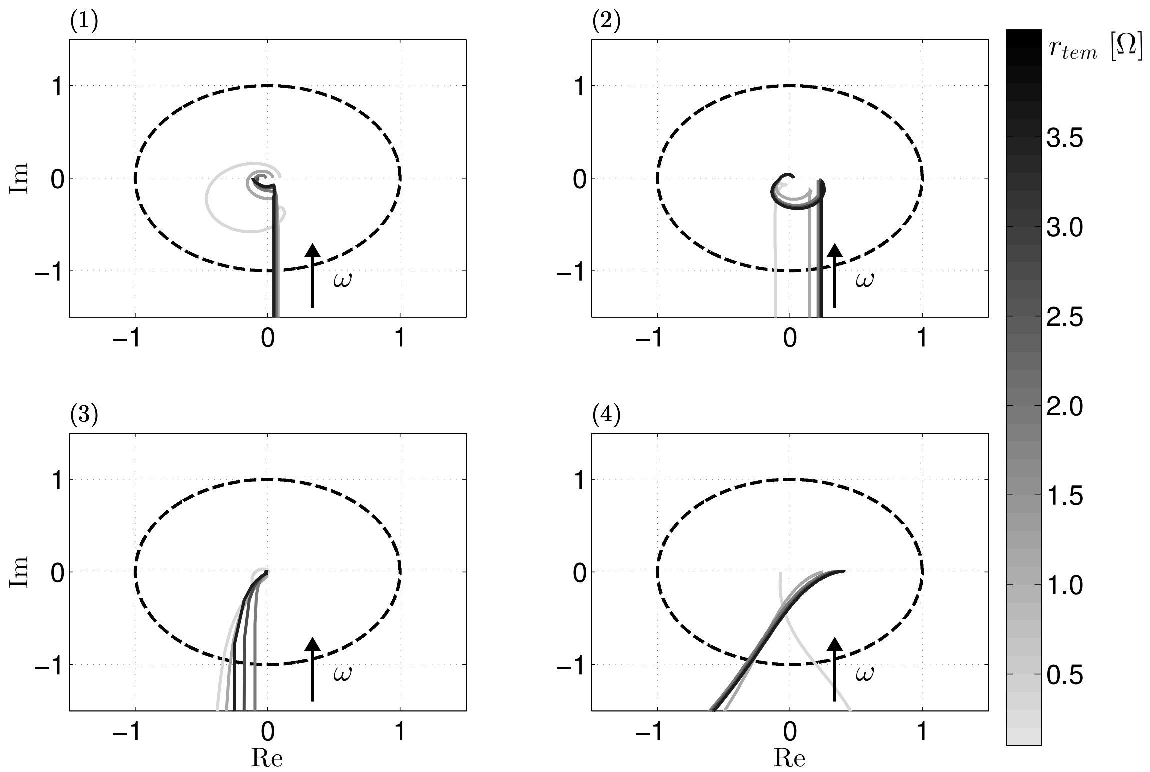

Figure 4.12.: Nyquist plot of the open-loop systems with variable resistor value r_{tem}. In (1) is presented the open-loop dynamics of the input current controller $C_{i_{L_1}}$. In (2) is presented the open-loop dynamic of the output current controller $C_{i_{L_2}}$. In (3) is presented the open-loop dynamics of the output voltage controller $C_{u_{C_3}}$ and in (4) is presented the open-loop dynamics the middle voltage controller $C_{u_{C_2}}$. The dashed line presents the unit circle.

Verification

At first, step response of the reference signal was measured to verify the control design of the DC-DC converter. The operation points of the converter, the parameters of the sources, and the load are presented in Table 4.1. These are the values received by the plant analysis in Section 4.2.1. In contrast to this experiment, the electrical load was changed again to a lead-acid-battery in order to avoid frequency feedback of the internal controller from the electrical load (cf. Section 4.2.1). The step responses of the closed-loop systems, the error between the desired closed-loop dynamics and the measurements are shown in Figure 4.13. In a direct comparison to the measurements, only marginal errors e can be observed. However, at the time frame between 15 ms and 18 ms it can be recognized that the error of i_{L_1}, i_{L_2}, and u_{C_3} increase. These errors correlate with the step signal of the reference values and suggest that the desired closed-loop dynamics are not exactly matched. The reason for the mismatch is the erroneous estimation of the plant parameters (cf. Section 4.2.1), which result from the parameter uncertainty of the electrical components or unconsidered contact resistor values. In relation to the RMS errors e_{rms} and the maximal RMS error values e^{+}_{rms} of the measurements (see Table 4.4), such differences are negligible and tolerable. A second test for the verification is the disturbance rejection. For this test, a step signal was

controller	e_{rms}	e^{+}_{rms}
$C_{i_{L1}}$	52.1 mA	185.5 mA
$C_{i_{L2}}$	49.4 mA	131.7 mA
$C_{u_{C2}}$	34.0 mV	112.9 mV
$C_{u_{C3}}$	10.6 mV	29.8 mV

Table 4.4.: RMS error e_{rms} and maximal RMS error value e^{+}_{rms} between simulation and measurement of step response of reference signal.

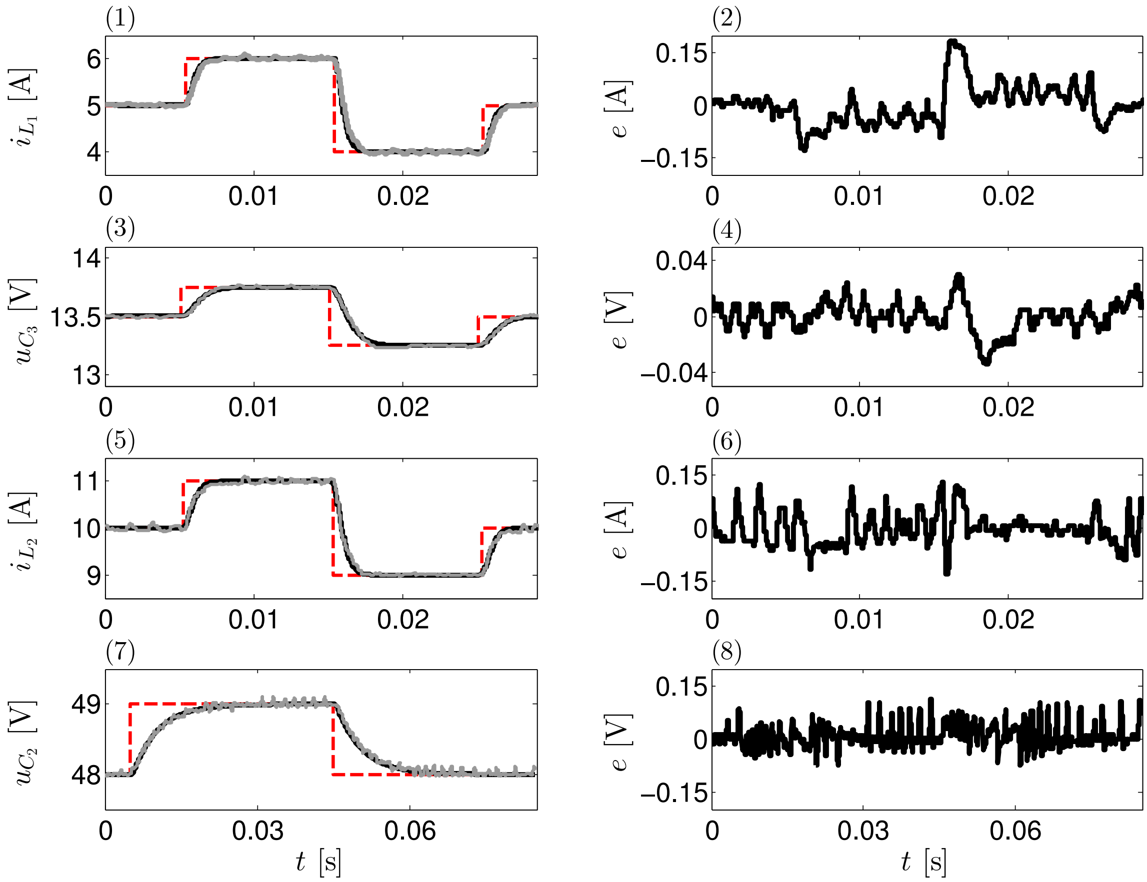

Figure 4.13.: Comparison between the simulation (black line) and the measurement (gray line) step response from command variable change of the control loops. The dashed line is the reference signal. The signals of the current control loop of i_{L_1} are presented in (1) and the error e between the simulation and the measurement is presented in (2). The signals of the voltage control loop of u_{C_3} are presented in (3) and the error e between the simulation and the measurement is presented in (4). The signals of the current control loop of i_{L_2} are presented in (5) and the error e between the simulation and the measurement is presented in (6). The signals of the voltage cascade control loop of u_{C_2} are presented in (7) and the error e between the simulation and the measurement is presented in (8).

added to the digital measurement signal in the μC and the disturbance reaction of the closed-loop control was measured. The disturbance responses of the controllers are presented in Figure 4.14. In this case,

significant peaks of the errors can detected when the step signal of the disturbance is enable and disable in the time periods of 4 ms - 7 ms and 25 ms - 27 ms.
In contrast to the command response of the feedback controller, the numerator of the sensitivity functions is characterized by the poles of the plants (cf. (4.10)). The poles of the transfer functions are sensitive for parameter uncertainty in contrast to the zeros of the plants (cf. Appendix A.1). This explains the higher maximum RMS error values e^{+}_{rms} of the disturbance responses (see Table 4.5), as opposed to the command reference step responses.
However, the step and disturbance responses show that the desired closed-loops are matched. The errors can be caused by the faulty nominal parameters of the model or contact resistor values of the test bench (cf. Section 4.2.1).

controller	e_{rms}	e^{+}_{rms}
$C_{i_{L1}}$	45.8 mA	246.0 mA
$C_{i_{L2}}$	37.5 mA	175.0 mA
$C_{u_{C2}}$	58.7 mV	244.9 mV
$C_{u_{C3}}$	14.6 mV	50.7 mV

Table 4.5.: RMS error e_{rms} and maximal RMS error value e^{+}_{rms} between simulation and measurement of step response of disturbance signal.

4.3. Approach of Adaptive Controller

The control design presented in Section 4.2.2 uses an analytical method to evaluate the robustness and stability of the closed-loop control. This method assumes that a detailed model from the DC-DC converter is known. Furthermore, the variation of the series resistor r_{tem} from the TEM influences the eigenvalues of the plants. The control design is able to ensure a stable closed-loop system for the variation of the eigenvalues, but is incapable to compensate the influence on the closed-loop dynamics. A possibility to compensate these effects is to use for an adaptive control, which is able to adjust control parameters online. The aim of the adaptive control is to ensure the desired stable and constant closed loop bandwidth.
The adaptive control method can be divided into two domains: the direct and the indirect adaptive control. The essential difference is the quality criterion of how the control parameters are adjusted. The direct method uses the error between the model and the measurement of the plant and directly adapts the control parameters in order to reduce this error. This concept is based on the assumption that the plant parameter and eigenvalues are fixed. The indirect method uses the error between the desired and the closed loop dynamics. The poles and zeros will be identified on the basis of the measurement. Subsequently, the control parameters can be adapted like the pole placement design. [7, 85]

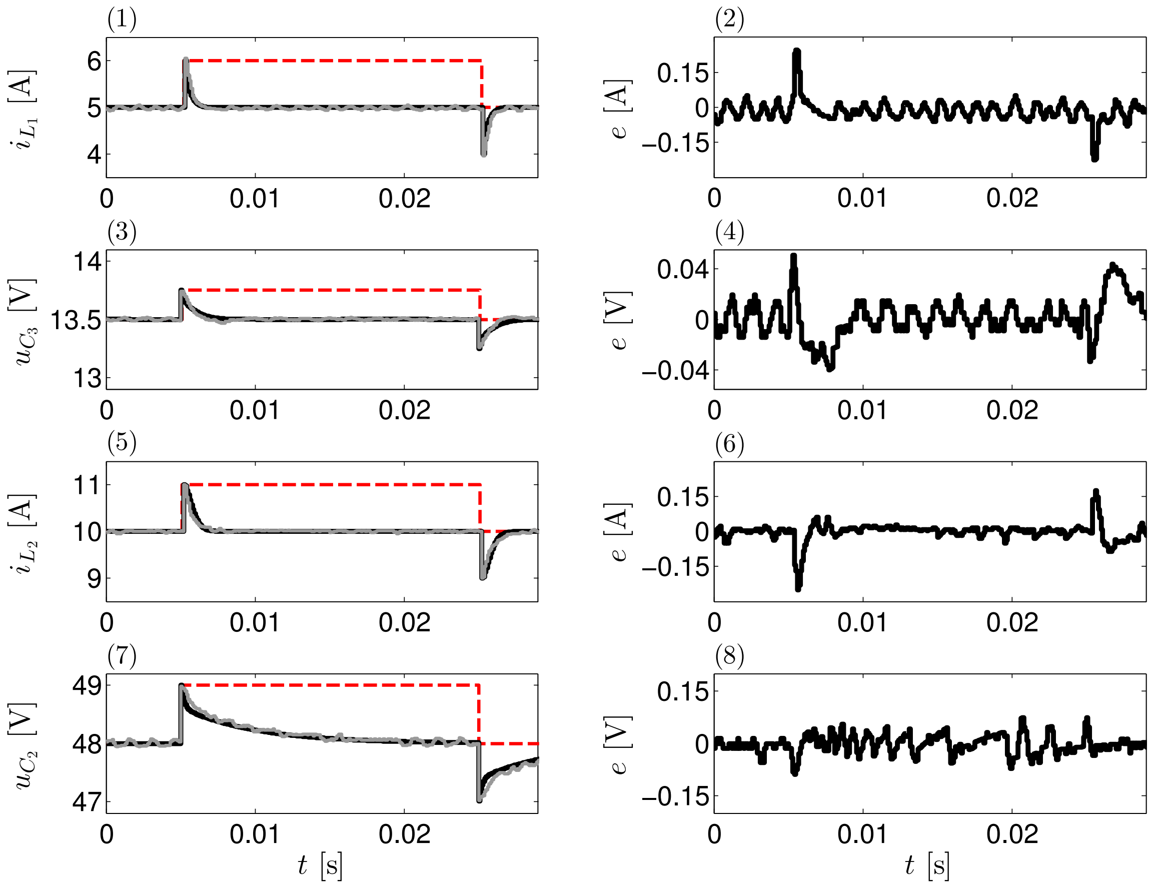

Figure 4.14.: Comparison between the simulations (black line) and the measurement (gray line) of the control loop disturbance reaction. The dashed line is the disturbance signal at the ADC. The signals of the current control loop of i_{L_1} are presented in (1) and the error e between the simulation and the measurement is presented in (2). The signals of the voltage control loop of u_{C_3} are presented in (3) and the error e between the simulation and the measurement is presented in (4). The signals of the current control loop of i_{L_2} are presented in (5) and the error e between the simulation and the measurement is presented in (6). The signals of the voltage cascade control loop of u_{C_2} are presented in (7) and the error e between the simulation and the measurement is presented in (8).

Generally, the indirect method is more complex because identification is necessary. However, the indirect method has the following advantage: the system dynamic is identified and the control parameters can be selected for defined conditions. This means that the parameters can be chosen in relation to eigenvalues of the transfer function or a defined control problem. [85]
Due to the large variance of the self-dynamics of the plants (cf. Figure 4.7), the indirect method has a significant advantage and is therefore considered further. In general, the indirect identification is based on three steps. At first, the plant is to be identified. Second, the poles and the zeros of the plant are to be estimated. Third step involves the tuning of the control parameters.

4.3.1. Closed Loop Identification

The basis of indirect adaptation is the parameter identification. For identification, the plant input $u(k)$ is stimulated with a sufficient bandwidth signal, typically a step-signal or a pseudo-random binary sequence. The output of the plant $y(k)$ is measured simultaneously. For a discrete linear time-invariant system, the output model follows to [119]:

$$y(k+1) = \frac{q^{-d_e} B(q^{-1})}{A(q^{-1})} u(k) + p(k) = G(q^{-1}) u(k) + p(k) \tag{4.54}$$

The parameters of $B(z^{-1})$ and $A(z^{-1})$ can be estimated with a parameter adaption algorithm (PAA). This implies that the input and output signals are not correlated and the disturbance $p(k)$ is an unbiased white noise signal. [85]

The use of parameter identification (also called system identification) is often calculated offline. In this case, it is possible to open the closed-loop system in order to stimulate the input signal of the plant and to measure the output signal. This is not practical for the application of the TEM and the DC-DC converter because opening of the controllers could lead to a drift of the output signal or a damage of the components. However, in a closed loop, the control signals $u(k)$ and output signal $y(k)$ are correlated, and consequently, the system parameters cannot be identified. Therefore, the idea is to identify the closed loop system

$$T_{ry}(q^{-1}) = \frac{y(k)}{r(k)} = \frac{q^{-d_e} T\, B(q^{-1})}{A_{cl}(q^{-1})} \,. \tag{4.55}$$

The transfer function $G(q^{-1})$ of the plant can be calculated with the known control parameters $S(q^{-1})$ and $R(q^{-1})$. For the online identification, a closed-loop output error (CLOE) algorithm can be used [85]. The goal of the CLOE algorithm is to find an optimal predictor in order to minimize the expectancy value of the prediction error

$$\underset{\hat{y}}{\operatorname{argmin}} \mathbb{E}\left\{ \varepsilon_{cl}(k+1)^2 \right\} \,, \tag{4.56}$$

where ε_{cl} is the prediction error

$$\varepsilon_{cl}(k+1) = y(k+1) - \hat{y}(k+1) \tag{4.57}$$

between the measurement $y(k+1)$ and the prediction output $\hat{y}(k+1)$ of the closed loop system. For the closed loop identification, (4.57) must be re-written. The output of the closed loop system is given by

$$y(k+1) = -A^*(q^{-1}) y(k) + B(q^{-1}) u(k-d_e) + A(q^{-1}) p(k+1) \tag{4.58}$$

$$A^*(q^{-1}) = a_1\, q^{-1} + \ldots + a_{n_a}\, z^{-n_a} \,, \tag{4.59}$$

where A is a monic polynomial. A compact form of (4.58) is:

$$
\begin{aligned}
y(k+1) &= \boldsymbol{\theta}^T \boldsymbol{\Theta}(k) + A(q^{-1})p(k+1) && (4.60)\\
\boldsymbol{\theta}^T &= [a_1, \ldots, a_{n_a}, b_0, \ldots, b_{n_b}] && (4.61)\\
\boldsymbol{\Theta}^T(k) &= [-y(k), \ldots, -y(k-n_a), u(k-d_e), \ldots, u(k-d_e-n_b)] && (4.62)\\
u(k) &= \frac{T(q^{-1})}{S(q^{-1})} r(k) - \frac{R(q^{-1})}{S(q^{-1})} y(k) && (4.63)
\end{aligned}
$$

Accordingly, the prediction output $\hat{y}$ results in

$$
\begin{aligned}
\hat{y}(k+1) &= -\hat{A}^*(q^{-1})\hat{y}(k) + \hat{B}(q^{-1})\hat{u}(k-d_e) && (4.64)\\
\hat{y}(k+1) &= \hat{\boldsymbol{\theta}}^T \hat{\boldsymbol{\Theta}}(k) && (4.65)\\
\hat{u}(k) &= \frac{T(q^{-1})}{S(q^{-1})} r(k) - \frac{R(q^{-1})}{S(q^{-1})} \hat{y}(k)\ , && (4.66)
\end{aligned}
$$

where it is assumed, that the disturbance $p(k)$ is a white unbiased signal and $\hat{u}(k)$ is estimated with the reference signal $r(k)$. In relation to (4.58) - (4.66), the prediction error equation (4.57) can be re-written to [84]:

$$
\varepsilon_{cl}(k+1) = \frac{S(q^{-1})}{A_{cl}(q^{-1})} \left(\boldsymbol{\theta}(k) - \hat{\boldsymbol{\theta}}(k)\right)^T \boldsymbol{\Theta}(k) \tag{4.67}
$$

To determine the predicted parameters $\hat{\boldsymbol{\theta}}$, the following recursive CLOE algorithm can be used [85]:

$$
\begin{aligned}
\hat{\boldsymbol{\theta}}(k+1) &= \hat{\boldsymbol{\theta}}(k) + \mathbf{L}(k)\varepsilon_{cl}(k+1) && (4.68)\\
\mathbf{L}(k+1) &= \frac{\mathbf{P}(k)\boldsymbol{\Theta}(k+1)}{\lambda + \boldsymbol{\Theta}(k+1)^T \mathbf{P}(k)\boldsymbol{\Theta}(k+1)} && (4.69)\\
\mathbf{P}(k+1) &= \frac{1}{\lambda}\left[\mathbf{P}(k) - \frac{\mathbf{P}(k)\boldsymbol{\Theta}(k+1)\boldsymbol{\Theta}^T(k+1)\mathbf{P}(k)}{\lambda + \boldsymbol{\Theta}^T(k+1)\mathbf{P}(k)\boldsymbol{\Theta}(k+1)}\right]\ , && (4.70)
\end{aligned}
$$

where $\mathbf{L}(k)$ is the adaption gain, $\mathbf{P}(k)$ is the covariance matrix, and λ is the forgetting factor. For a linear time-invariant system with constant parameters and $\lambda = 1$, the covariance matrix converges to zero. Hence, variations of the parameters or operating points are not detected. For this reason, selection of the forgetting factor $\lambda < 1$ ensures sensitive parameter estimation. In practical application, the forgetting factor is selected between 0.9 and 1. [84]

The choice of λ also has an effect on the sensitivity of the measurement signal noise. For higher values of the forgetting factor the noise is damped more, and for smaller values the algorithm converges faster. The initial value of $\hat{\boldsymbol{\theta}}$ can be selected to zero and $\mathbf{P} = F\mathbf{I}$, where $\mathbf{I}$ is a unit matrix and F is a constant value between 100 and 1000. A high value of F implicates a marginal confidence interval of the predicted parameters for the first interval of the CLOE algorithm. [84, 119]

4.3.2. Validation

Before the self-tuning of the control parameters can be performed, the parameters must be verified. The error ε_{cl} is a criterion that is used to check the identification. In practice, the identification succeeds if the error is lower than a limit value. However, this criterion provides no information about the correlation of the parameters. For this purpose, a confidence test between the error and prediction signal can be used [84]:

$$RN_{\varepsilon x}(i) = \frac{R_{\varepsilon x}(i)}{\sqrt{[R_{xx}(0)\; R_{\varepsilon\varepsilon}(0)]}}, \quad x = \hat{y}, \hat{u}; \;\; \forall i \neq 0 \tag{4.71}$$

$$= \frac{\sum\limits_{k=1}^{N} \varepsilon_{cl}(k) x(k-i)}{\sqrt{\left[\sum\limits_{i=1}^{N} x^2(k) \sum\limits_{k=1}^{N} \varepsilon_{cl}^2(k)\right]}}, \tag{4.72}$$

where $R_{xx}(0)$ and $R_{\varepsilon\varepsilon}(0)$ are the auto-correlations and $R_{\varepsilon x}$ is the cross-correlation for N-samples. The confidence test for the whiteness of the disturbance signal $p(k)$ is defined as [84]:

$$RN_{\varepsilon\varepsilon}(i) = \frac{R_{\varepsilon\varepsilon}(i)}{R_{\varepsilon\varepsilon}(0)}, \;\; \forall i \neq 0 \tag{4.73}$$

The system identification can be considered as succeeded for the following condition

$$|RN_{\varepsilon x}(i)| \leq \frac{\tau}{\sqrt{N}}, \quad x = \hat{y}, \hat{u}, \varepsilon; \;\; \forall i \neq 0 \tag{4.74}$$

where τ implies the confidence interval. In other words, the confidence test is a statistical criterion for a predefined allowable error between the measurement and the model.

4.3.3. Self-Tuning of Control Parameters

The parameters of the controller (see A.7) are calculated using the design rules outlined in Section 4.2.2.

4.3.4. Experiment

In the first step, an adaptive algorithm was implemented for the current controller $C_{i_{L2}}$. The default control parameters were designed with the assumption that the internal resistor is $r_{tem} = 0.1\ \Omega$. The desired closed loop polynomial has a rising time of 1 ms (cf. Section 4.2.2). The TEM was simulated with a voltage source and a resistor. The value of the resistor was 1.9 Ω and the value differed significantly from the design parameter $r_{tem} = 0.1\ \Omega$.

After the control system had reached the steady-state, the last reference value $i_{L_2 r}$ of the voltage controller u_{C_2} was kept constant with an additional square-wave signal of 0.4 A. The CLOE algorithm was initialized with the model order $n_a = 3$, $n_b = 1$, $d_e = 1$, $P(0) = 1000$, and $\lambda = 0.998$. The parameter estimation is shown in Figure 4.15, (1). After nearly 60 iteration steps the parameters converted to a steady-state value. The validation started on every 40th iteration and was based on the correlation analysis (4.71) and (4.73). The confidence interval $|RN| < 0.196$ was selected. This means that 95 % of the measurements had to be within 2σ standard deviation with N=100 samples and $\tau = 1.96$. The confidence value of the output prediction and the control signal prediction in relation to the error is $\left|RN_{\varepsilon\hat{i}_{L_2}}\right| = 0.065$

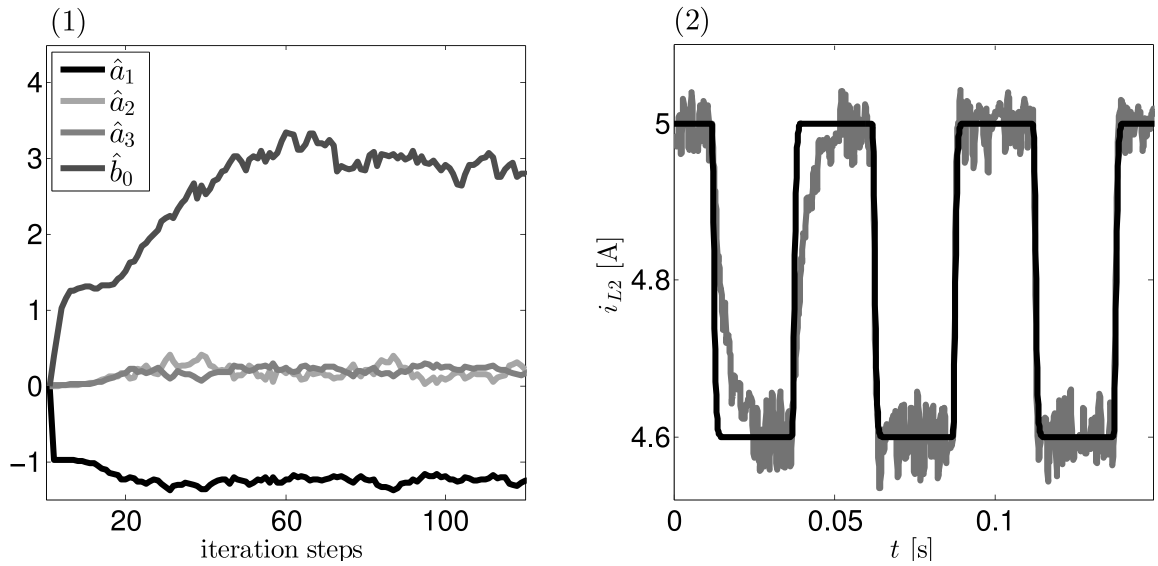

Figure 4.15.: Estimated parameters of the plant for each iteration step are presented in (1). The adaption of the control parameters is presented in (2). The controller is designed for $r_{tem} = 0.1\ \Omega$. In the experiment, the resistor was selected with $r_{tem} = 1.9\ \Omega$. The black line is the desired closed loop, the gray line is the current closed loop. At 60 ms, the control parameters are adapted on the basis of the parameter identification.

and $\left|RN_{\varepsilon\hat{d}_2}\right| = 0.102$. The residual prediction error is $|RN_{\varepsilon\varepsilon}| = 0.151$. The results imply that the identification is successful. Based on these values, the control parameters were re-designed online, in order to match the desired closed loop dynamics shown in Table 4.3. The successful adaption of the controller is shown in Figure 4.15, (2).

4.3.5. Conclusions and Discussion

The feasibility of the indirect adaptive controller is demonstrated experimentally. The robust control design can compensate parameter variations of the TEM with fixed control parameters. In contrast, the self-tuning allows to adapt the control parameters to ensure the desired closed-loop dynamics. Furthermore, a detailed analysis of the parameter variations of the TEM are not necessary for the control design. However, the eigenvalues of the plants can vary for different operation points of the TEM. As a result, the dominating system order of the plants has been adapted for each iteration. The complexity of the algorithms increases with the number of the used controllers, especially the parameter variation of the TEM. It is possible to extend the presented adaptive controller to a multi-model controller [85]. The multi-model concept corresponds to a gain-scheduler controller with a self-tuning algorithm.

In summary, the adaptive controller ensures a defined closed-loop dynamics of the controllers, which are independent of the TEM parameters. The algorithms have to be extended with a self-estimation of the system order to estimate all dominating eigenvalues of the plant.

For the practical implementation of the control parameters adaption an adequate computing performance or essential optimization of the algorithms is required. The selected μC for the prototype does not have

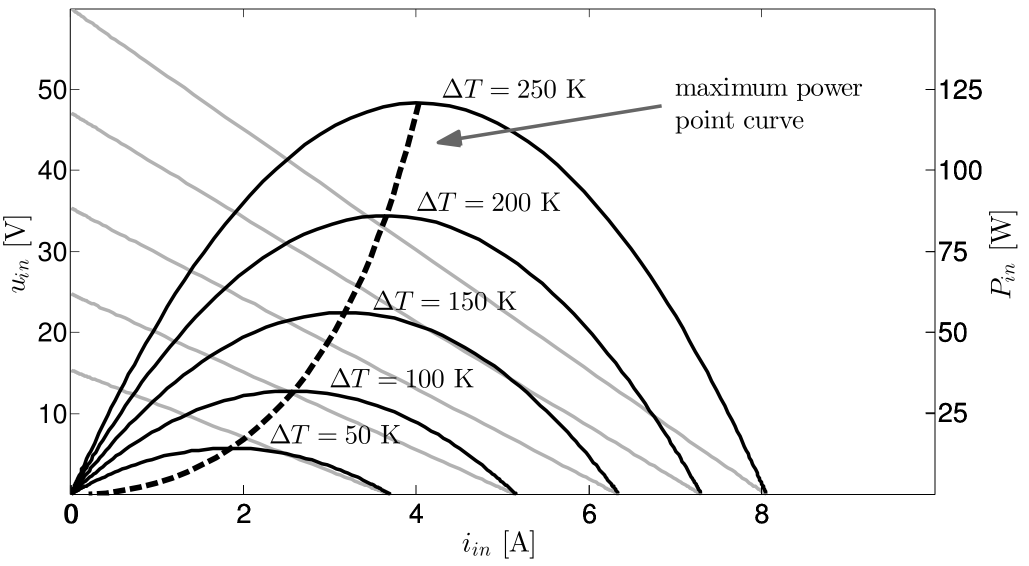

Figure 4.16.: Electrical characteristics of PbTe-based TEM, at different temperatures. The gray line represents the voltage u_{in} of the TEM at the connectors. The black line shows the power of the TEM, and the dashed line is the maximum power point curve for different temperature gradients ΔT.

enough computing performance to implement this concept for the controller concept of the BoBu converter. For this reason, the robust control concept with constant control parameters is used for the BoBu converter.

4.4. Maximum Power Point Tracking

The proposed control structure of the BoBu converter in Section 4.2 can switch between two reference signals for the input current controller. When the maximum charge voltage u_o^+ of the battery is reached, a cascade controller regulates the output voltage. Here, it is necessary that the controller reduces the input power by decreasing the input current i_{L_1}. If the output voltage collapses under the voltage level u_o^-, the reference signal of the current controller switches to an MPPT algorithm. The voltage difference between u_o^+ and u_o^- implied a tolerance band to avoid a switch back and forth between the charge control and MPPT algorithm.

The aim of the MPPT algorithm is to identify the operation point of the input current at which the maximum power is recuperated from the TEM.

The qualitative relationships between the electrical characteristic parameters and the output power of a TEM are shown in Figure 4.16. The power curve $P_{tem}(u_{in}, i_{in} = i_{tem}, \Delta T)$ is parabolic and always has one maximum power point (MPP) at a constant temperature gradient across the TEM. The operation point of the MPP is reached in case the terminal voltage u_{in} is the half amplitude of the TEM's open voltage. At this operation point, the load impedance of the TEM is equal to its internal series resistor.

Generally, the MPPT is based on a gradient search algorithm. Esram and Chapman [45] present a detailed overview of different MPPT techniques with their advantages and disadvantages. In principle, all MPPT algorithms can be used to search the MPP of a TEM. A widely-used MPPT algorithm is the perturb and observe (P&O) algorithm. The P&O algorithm determines at each iteration step the actual input power of the DC-DC converter $P_{in}(k) = P_{tem}(k)$ and compares this value with the previous power sample value $P_{in}(k-1)$. If the difference $\Delta P_{in}(k) = P_{in}(k) - P_{in}(k-1)$ is positive, the input current is increased. If $\Delta P_{in}(k) < 0$, the input current is decreased. The MPP is reached when $\Delta P_{in}(k)$ is zero. The algorithm yields to:

$$i_{L_1}(k+1) = i_{L_1}(k) + \mu(k)\mathrm{sign}\left[\Delta P_{in}(k)\right] \tag{4.75}$$

$$\mathrm{sign}\left[\Delta P_{in}(k)\right] := \begin{cases} +1, & \Delta P_{in} > 0 \\ 0, & \Delta P_{in} = 0 \\ -1, & \Delta P_{in} < 0 \end{cases}, \tag{4.76}$$

where μ is the step size.

In contrast to classical P&O algorithms [60, 92, 146, 172, P2], the presented P&O algorithm uses an input current controller, which regulates the desired current $i_{L_1}(k+1)$. This has the advantage that disturbances of the signals are compensated by the controller (cf. Section 4.2.2).

In order to optimize the convergence time of the MPPT, an adaptive step size is defined as:

$$\mu(k+1) = \mathrm{sat}\left(\frac{|\Delta P_{in}(k)|}{\mu(k)}\right) := \begin{cases} S_\mu, & S_\mu\ \mu(k) < \frac{|\Delta P_{in}(k)|}{\mu(k)} \\ \frac{|\Delta P_{in}(k)|}{\mu(k)}, & \frac{\mu(k)}{S_\mu} \leq \frac{|\Delta P_{in}(k)|}{\mu(k)} \leq S_\mu\ \mu(k) \\ \frac{\mu(k)}{S_\mu}, & \frac{|\Delta P_{in}(k)|}{\mu(k)} < \frac{\mu(k)}{S_\mu} \\ \mu(k), & |\Delta P_{in}(k)| = 0 \end{cases}, \tag{4.77}$$

where S_μ is a tuning factor to limit the adaption size. Generally, $S_\mu = 2$ is a good selection for practical application.

Furthermore, the sum of $sign\left[\Delta P_{in}(k)\right]$ and $sign\left[\Delta P_{in}(k-1)\right]$ is used to detect an oscillation of the P&O algorithm. If the sum is zero, oscillation is detected and the step size is selected as $\mu(k+1) = \mu(k)/4$.

However, all gradient search algorithms are based on the assumption that the input power has reached a steady-state. Otherwise, the transient response of the signals result in an incorrect calculation of the input power. To ensure a steady-state before the new reference signal of the input current is estimated, the MPPT algorithm is updated once every 100 ms.

4.4.1. Experiment

The aim of the MPPT is to detect the maximum power of the TEM and to calculate the necessary reference current for the input current control loop. To verify the P&O algorithm, the test bench of the converter (cf. Section 3.7) was used. The TEM was simulated with a nominal voltage $u_{tem} = 15$ V and a series resistor $r_{tem} = 3.1\ \Omega$. If the MPP was reached, the resistor of the test bench r_{tem} was changed

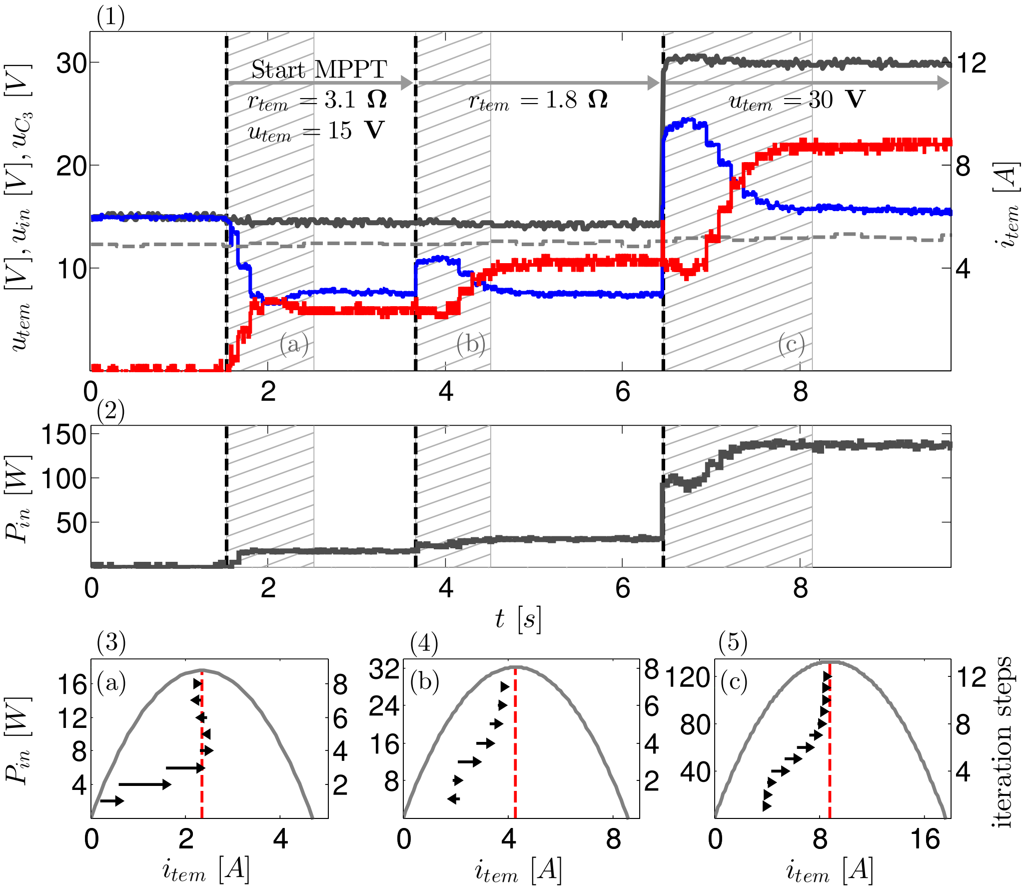

Figure 4.17.: Verification of maximum power point tracking algorithm. The MPPT starts at nearly 1.5 s. The TEM is simulated with $r_{tem} = 3.1\ \Omega$ and u_{tem}=15 V. At 3.7 s, the resistor r_{tem} is changed to 1.8 Ω and at 6.5 s the voltage u_{tem} is changed to 30 V. The time signals of voltage u_{tem} (gray line), u_{in} (blue line), u_{C_3} (gray dashed line) and current i_{tem} (red line) are presented in (1). The input power of the converter is presented in (2). The calculated input current amplitudes from the MPPT algorithm in relation to the iteration steps are presented in (3), for the time spans (a), (b) and (c) from (1). Additionally, the gray line represents the power characteristics of the simulated TEM. The red dashed line marks the current amplitude of the maximum power point.

to $r_{tem} = 1.8\ \Omega$. Finally, the voltage u_{tem} was changed from 15 V to 30 V. The results are presented in Figure 4.17. The MPPT algorithm was enabled at 1.5 s and the desired load current i_{tem} of the TEM was updated each 100 ms to ensure a steady-state of i_{tem} and u_{in}, which was necessary to determine the DC power of P_{in}. The measurement results in Figure 4.17 (1) show that the input current i_{tem} is adapted after the internal resistor or the voltage of the simulated TEM changed and the current i_{tem} converges to a steady-state. At this operation point, the amplitude of the input voltage is $u_{in} = 1/2\ u_{tem}$. This implies that the input impedance of the converter (u_{in}/i_{tem}) matches the serial TEM resistor r_{tem} value. Consequently, the maximum power point of the TEM is reached.

The convergence time of the MPPT algorithm depends on the input power gradient ΔP_{in} and especially of the adaptive step size μ of the MPPT algorithm (cf. (4.75) - (4.77)). Figure 4.17 shows that the input current i_{tem} increases significantly at the first iteration in the time span (a). At the 4th iteration, the step size suddenly decreases, which was caused by the small input power gradient. After the resistor r_{tem} changed from 3.1 Ω to 1.8 Ω, the input current i_{tem} increased marginally for the first iteration steps (see time span (b) from Figure 4.17), although the input power P_{in} significantly changes. The reason is the actual value of the step size μ, which depends on the previous adaption during the time span (a). In the time span (a), the initialize step size was 0.1 and converge to nearly zero. Consequently, at the start of the time span (b), the step size is nearly zero. However, from (4.77) it follows that the step size is sensitive in relation to the input power gradient. After the third iteration, the step size reached a significant higher value, which resulted to higher amplitude changes of the input current i_{tem}. This effect can also be observed during the time span (c), where the voltage u_{tem} changes from 15 V to 30 V, because the MPPT also converges in the time span (b) to the maximum input power and its step size converges to nearly zero.

However, the MPPT algorithm always reached the MPP. The time span to reach the MPP depends on the step size values of the MPPT. In this experiment, the time span is lower as 1 s.

4.5. Trickle Charge Control

When the battery voltage reaches the maximal allowed charge voltage u_o^+, the input current i_{L_1} must be decreased in order to reduce the charge current i_{L_2}. Generally, the reference input current value is determined by the MPPT. If the output voltage reaches u_o^+, a trickle charge control (TCC) is activated, which disables the MPPT algorithm and enables the voltage control of the output u_{C_3}. For the selection of the MPPT and the TCC, the hysteresis function S_C is defined as follows:

$$S_C := \begin{cases} 1\,, & u_{C_3} \leq u_o^- \,,\, \dot{u}_{C_3} < 0 \\ 0\,, & u_{C_3} < u_o^- \,,\, \dot{u}_{C_3} < 0 \\ 1\,, & u_{C_3} > u_o^+ \,,\, \dot{u}_{C_3} > 0 \\ 0\,, & u_{C_3} \geq u_o^+ \,,\, \dot{u}_{C_3} > 0 \end{cases} \,, \tag{4.78}$$

where u_o^-, u_o^+ are the lower and the upper voltage limits of the trickle charge, $S_C = 1$ enables the TCC, and $S_C = 0$ enables the MPPT (see Figure 4.18). This activation function is used to avoid a switch back and forth between the TCC and MPPT algorithm.

4.5.1. Experiment

To verify the TCC, a 12 V lead acid battery was used as load in the test bench of the BoBu converter (cf. Section 3.7). At the beginning of the experiment, the 12 V battery was charged to 13.3 V. A DC voltage source and a series resistor simulated the TEM. At the beginning of the experiment, $u_{tem} = 15$ V and $r_{tem} = 3.1$ Ω were selected and the MPPT was activated ($S_C = 0$) (see Figure 4.19). After 40 ms, the resistor of the test bench changed to $r_{tem} = 1.8$ Ω. Consequently, the MPPT increased the input current and also the battery was charged with a higher output current i_{L_2}. Finally, the battery voltage reached

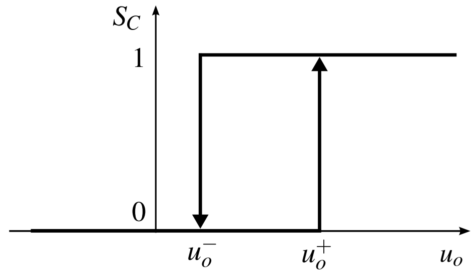

Figure 4.18.: Activation function S_C for the trickle charge controller.

the selected maximum trickle voltage $u_o^+ = 13.6$ V. The activation function resulted into $S_C = 1$ and the TCC was enabled. The desired battery voltage was selected as $u_{C_3r} = 13.4$ V. To match this voltage, the output voltage controller reduced the reference input current value of $C_{i_{L1}}$ to 2.1 A. At 0.5 s the resistor changed back to $r_{tem} = 3.1\ \Omega$ and the input power was not sufficient to maintain the trickle voltage. As a consequence, the output voltage decreased and the TCC increased the input current to match the desired battery voltage. At the point where the output voltage u_{C_3} dropped down to the selected minimum trickle voltage $u_o^- = 13.3$ V, the activation function changed to $S_C = 0$ and the MPPT was reactivated.

4.6. Optimization of Efficiency

The middle voltage u_{C_2} of the boost-buck converter is a degree of freedom. The selection of u_{C_2} is only limited by the input and output voltage of the converter. The requirement for the boost converter is $u_{in} \leq u_{C_2}$, and $u_{C_2} \geq u_{C_3}$ for the buck converter. The default value is selected as $u_{C_2} = 48$ V (cf. REQ.3). However, the selection of the regulated middle voltage u_{C_2} influences the efficiency of the converter (cf. Section 3.5). In contrast to the input voltage, the output voltage can be assumed to be nearly constant. The idea is to optimize the efficiency through the adaption of the reference value u_{C_2} in relation to the input voltage u_{in}, and the input current i_{in} of the converter. The optimization function yields to:

$$\underset{u_{C2} \in \{u_{in}, i_{in} = i_{tem}\}}{\text{argmax}} \quad \eta\left(u_{in}, i_{in}, u_{C_2}\right)\big|_{e_{bl}=const, f_{sw}=const} \tag{4.79}$$

In case of electrical steady states, it follows that $u_{in} = u_{C_1}$ and $i_{in} = i_{L_1}$.
An offline analysis, based on the DC-DC converter model from Chapter 3, can successively determine all variations of u_{C_2} in relation to the input power. Finally, the reference signal u_{C_2r} for the middle voltage controller $C_{u_{C2}}$ with the highest efficiencies in relation to the input power of the converter is saved in a lookup table (see Figure 4.20). The efficiency of the BoBu converter for a constant value and an optimized value for u_{C_2} at a nominal source voltage of 12 V is shown in Figure 4.21. The maximum efficiency of the converter η^+ increases up to 0.967, and additionally, the arithmetic mean efficiency $\bar{\eta}$ increases to 0.858. In relation to the default selected reference value $u_{C_2} = 48$ V (cf. Table 3.3), the mean efficiency increases by nearly 8 % with an optimized value of u_{C_2}.

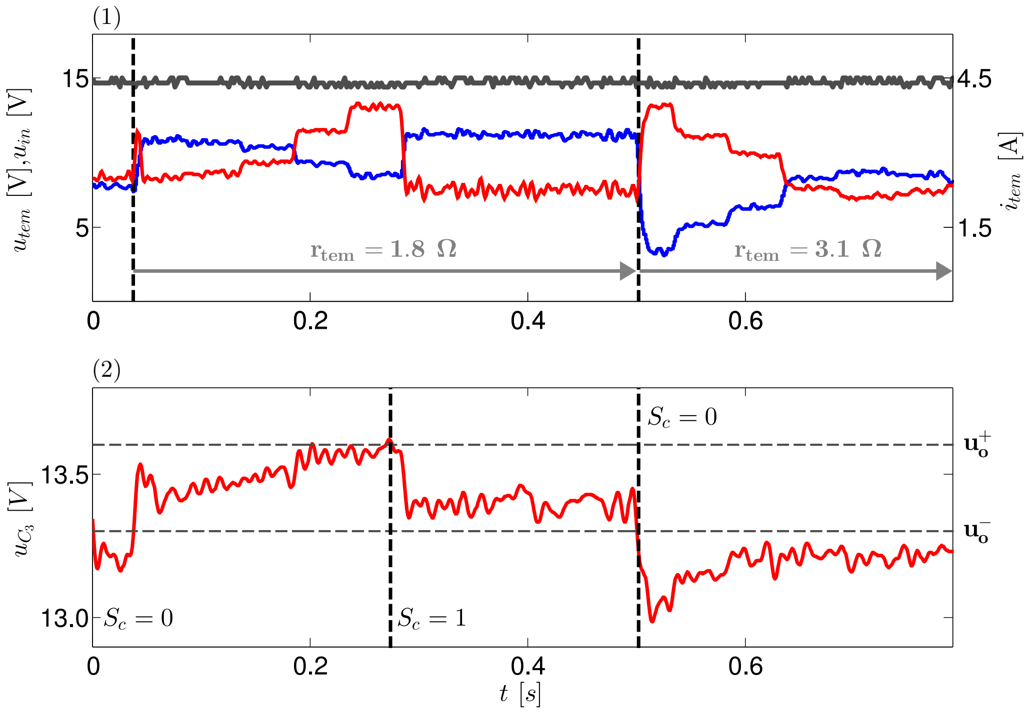

Figure 4.19.: Experiment results of the TCC. In (1) input current i_{tem} (red line), input voltage u_{in} (blue line), and u_{tem} (gray line) are presented. In (2), the output voltage u_{C_3} with the states of the activation function S_C are presented.

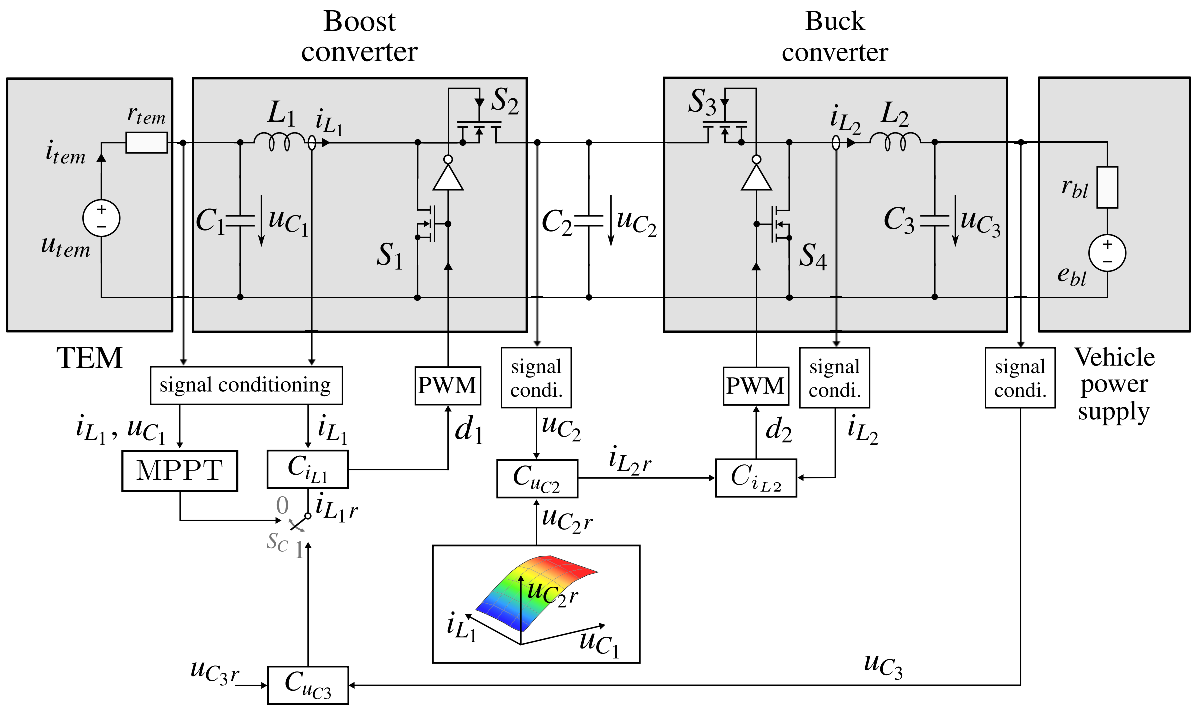

Figure 4.20.: Control structure of the boost-buck converter with look up table for middle voltage controller and without ESR values.

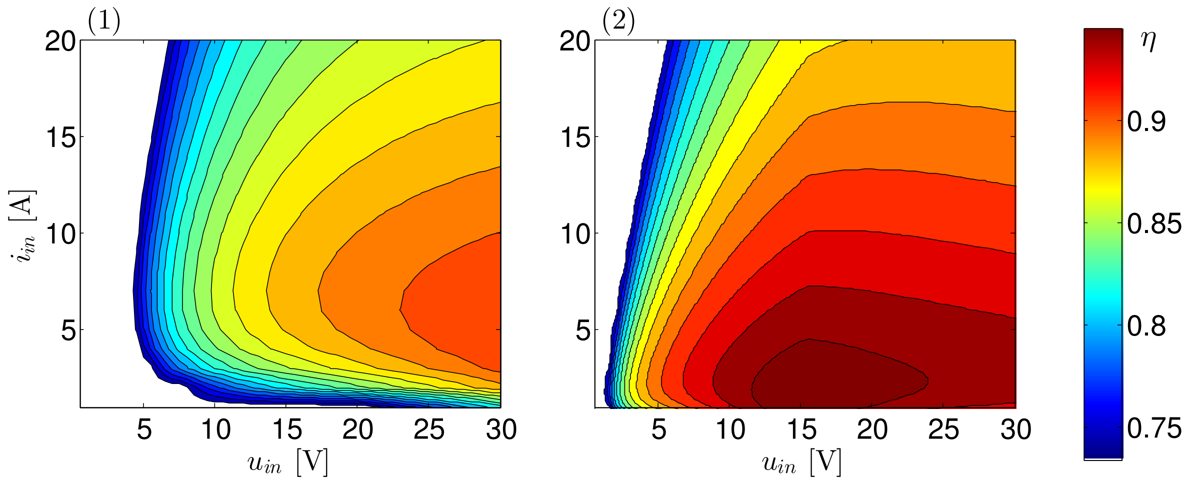

Figure 4.21.: Comparison between boost-buck efficiency with fixed and variable u_{C_2}. The efficiency with a constant reference value $u_{C_2} = 48$ V is presented in (1). The optimize efficiency with the variable u_{C_2} is presented in (2).

4.6.1. Verification

The test bench in Section 3.7.2 was selected to verify the optimized efficiency in relation to the middle voltage. In this experiment, the reference values of u_{C_2} were determined with (4.79). The values were saved in a lookup table. In relation to the measured input voltage u_{in} and input current i_{in}, the reference value for the controlled u_{C_2} was selected from the lookup table. The measurement results of the test bench are presented in Figure 4.22. The error e and the relative error $e_{\%}$ between the measured and analytical efficiency are selected as the evaluation criteria. The error between model and measurement has a maximum relative error of 4.8 %. All error values e are significantly lower than 0.05. Additionally, the mean error of the measurements is 1.67 %. Furthermore, the maximal efficiency of the BoBu converter from the measurements is 0.981. Consequently, the measurements confirm the analytical model and the optimization of the boost-buck converter through the adaption of the middle voltage u_{C_2}.

4.7. Conclusion

This chapter presented a digital control concept of the boost-buck converter to link the recovered thermoelectric energy to a load or a battery. The linear controllers were designed in relation to the SSA model of the boost-buck converter. In contrast to control concepts like [70], robustness criteria are introduced in the control design to support TEMs with different electric parameters. The results of the experiment shows that the design controller satisfied the robustness and the stability criteria for a parameter variation of a TEM.

However, the design concept of the linear controller with the aim to satisfied a robust and stable feedback control is straightforward but requires detailed knowledge about the converter parameters and the load. In contrast, the linear controller was extended to an adaptive controller. This requires an online identification of the plant parameters and an adaption of the control parameters. Depending on the possible drift

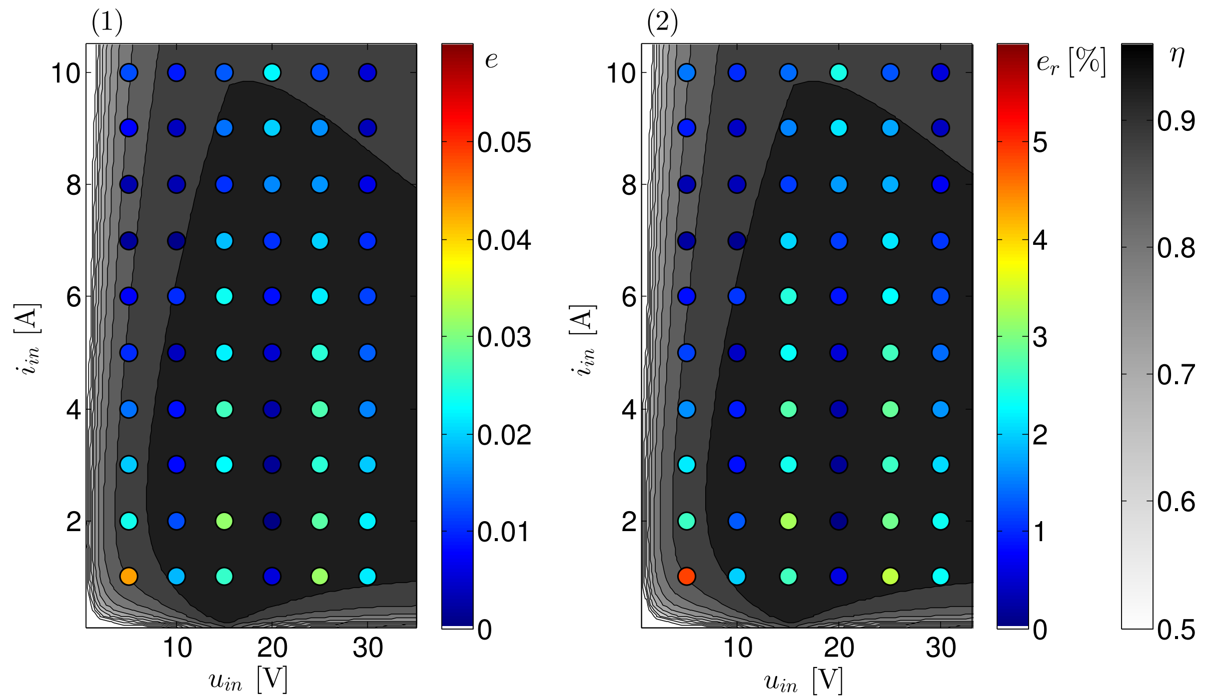

Figure 4.22.: Comparison between analytical model and experimental measurements, with optimized reference values of u_{C_2}. The absolute error e between measurement and model is presented in (1). The relative $e_{\%}$ error between measurement and model is presented in (2). The doted markers presented the measurement points.

of the eigenvalues, the identification and the self-tuning algorithm are complex and require sufficient computing power. Therefore, a full implementation in the prototype wasn't entirely completed because the calculation power is limited. The multi-model adaptive control can be considered as an alternative in contrast to the RST controller. This structure can also be used for a gain-scheduling control, and its offers a concept to change the identification algorithm with the scheduling of the operation points for the controller.

An MPPT algorithm was presented in order to recover the MPP of the TEM. The selection of the MPPT algorithm is based on the numerical accuracy and on the quality of the measurement signals. The presented MPPT is a combination of the perturb and observe algorithm with a controller, which regulate the desired input current of the boost-buck converter. To compensate for the oscillation nature of the algorithm, an adaptive step size was implemented, which also reduces the convergence time.

However, the MPPT algorithm depends on the measurement accuracy and the estimation of the actual input power. An accurate measurement reduces the complexity to detected the exact MPP with the MPPT algorithm and vice versa.

The implemented control concept has the degree of freedom to select the reference value u_{C_2}. This value has a direct influence on the efficiency of the boost-buck converter. Hence this relation was used to optimize the efficiency for a specified battery voltage.

Based on the offline calculation, the reference values u_{C_2} for an optimal efficiency were saved in a lookup table and implemented in the μC. The results of the experiment shows that the mean efficiency of the BoBu converter increases by up to 8 % with the optimized middle voltage in contrast to the efficiency map with a fixed u_{C_2} value. A maximum efficiency of 98.1 % was measured in this experiment.

5. Electrical Integration

The selected assessment of the DC-DC converter (cf. Chapter 3) is based on the assumption that the electrical characteristic of the TEM is unknown. The boost-buck converter has the highest average efficiency in comparison to the other three topologies (buck-boost, Ćuk, SEPIC) for the analyzed input power. However, for a defined input power, the other converters can have a higher local efficiency as compared to the BoBu converter. This can be observed by the calculated efficiency of converters in Chapter 3. In contrast to the BuBo, the Ćuk, and the SEPIC converter, the BoBu has an additional degree of freedom to choose the reference value of the middle voltage u_{C_2}. This feature is used in Section 4.6 to adapt the efficiency of the converter for a defined input power. However, this manipulation is limited by the voltage amplitudes of the load and the source.

As already mentioned, a TEG is based on a number of TEMs. The integration of a TEG into an electrical vehicle grid has a degree of freedom to select the wiring of the TEMs for a boost-buck converter. In other words, the input power - more precisely, the input current and the voltage amplitude of a converter - can be manipulated with the selected number and interconnection of the TEMs.

The aim of this chapter is to define a network configuration of explicate TEMs, which yields to an electrical operation point where the BoBu converter has a maximal efficiency. The idea is to use an optimization algorithm to evaluate the electrical efficiency of different interconnection variations of TEMs with the converters.

For this purpose, the necessary components for waste heat trajectory of ICE and TEG must be defined. With the optimized functional chain from the recuperating thermal power up to the integration in the electrical system, explicit simulations and analyses of the on-board power supply can be performed.

The structure of this chapter is as follows. The TEG is presented in Section 5.1. The parameters of the TEMs, the drive cycle, and the ICE are defined in Section 5.2. The electrical efficiency of the initial wiring of TEMs and DC-DC converters is simulated in Section 5.3. Based on these results, an optimization algorithm uses to determine the electrical wiring of the TEMs and the number of converters with the maximal efficiency for the electrical function chain is presented in Section 5.4. In Section 5.5, the results are summarized and discussed.

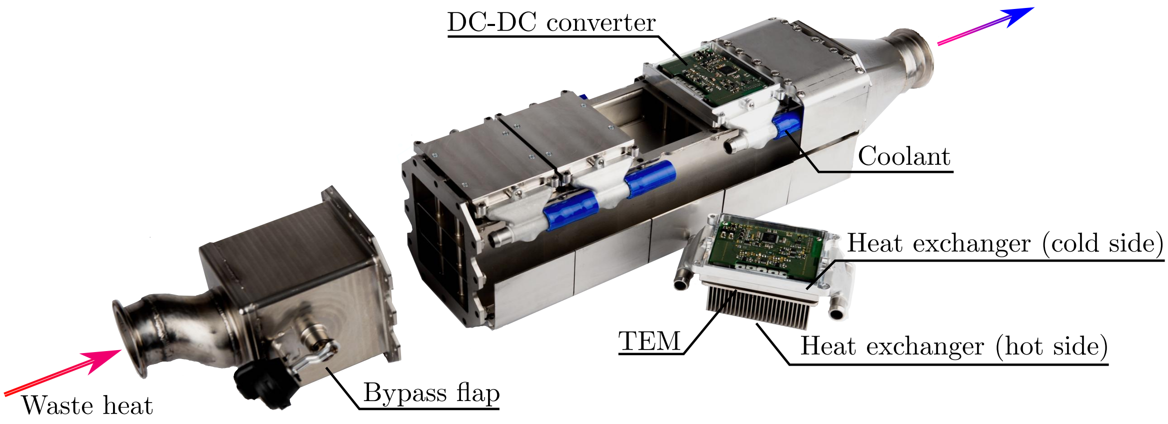

Figure 5.1.: Prototype of the thermoelectric generator from the research project TEG2020 [57] (cf. 2.8).

5.1. Prototype of Thermoelectric Generator

The prototype of the TEG from the research project TEG2020 is presented in Figure 5.1. The mechanical chassis was developed to integrate ten TEMs with ten DC-DC converter boxes (cf. Section 2.5). An integrated bypass can be opened and closed with the bypass flap to protect the thermoelectric material from overheating. The cooling is plugged in the cooling circuit of the vehicle. The weight of the prototype is 30 kg. The TEG is integrated behind the catalytic converter (CAT) to avoid the influence of the exhaust gas after treatment.

5.2. Definition of Simulation Parameters

In the following, the necessary parameters and conditions for the simulation of the thermoelectric characteristic in a driver cycle are listed.

5.2.1. Parametrization of Internal Combustion Engine

For the simulation, a 2 L Otto engine is selected. The nominal characteristic parameters are presented in Table 5.1. The efficiency of the ICE can be defined via the brake specific fuel consumption (BSFC). The BSFC is defined as

$$BSFC = \frac{FC\rho_f}{P_e} , \tag{5.1}$$

where P_e is the effective power of the engine, FC is the fuel consumption rate in liter per hour, and ρ_f is the mass density of the fuel in gram per liter. In this thesis, ρ_f is defined as 0.72 kg L^{-1}. The BSCF map is required to calculate the fuel consumption and also to determine the fuel saving potential of a TEG. Figure 5.2 illustrates the assumed BSFC map in relation to the brake mean effective pressure (BMEP) p_{me} and the engine speed n, which is used for all engine simulations in this thesis.

cylinder	engine displacement $[\mathrm{cm}^3]$	max. torque $[\mathrm{N\,m}]$	max. engine power $[\mathrm{kW}]$
4	1984	280	147

Table 5.1.: Parameters of the ICE.

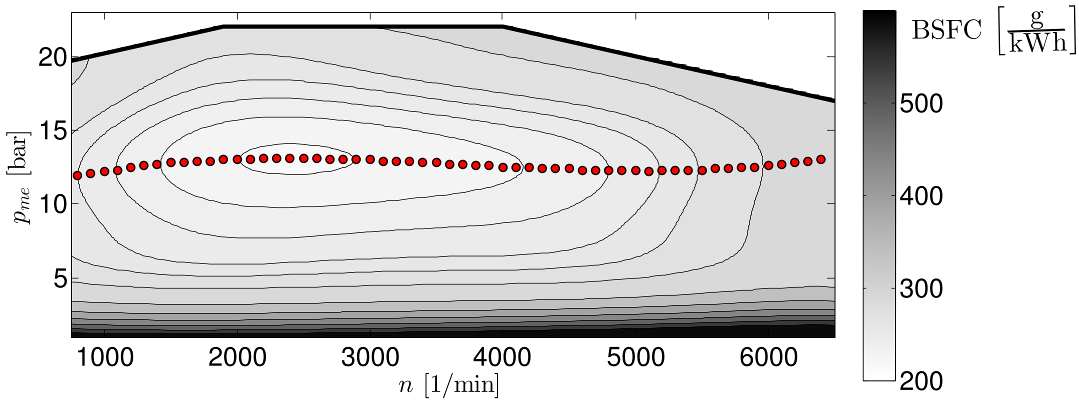

Figure 5.2.: Assumed specific fuel consumption map for the ICE. The dotted line presents the minimal BSFC in relation to the speed.

5.2.2. Definition of Driver Test Cycle

The potential energy of the waste heat depends on the actual operation point of the ICE. Therefore, a drive cycle must be defined, to compare the fuel consumption with and without a TEG system. In this thesis, the WLTC, version 1, is selected. This cycle is defined for upper-class vehicles and is divided in four parts low, medium, high, and extra high (see Figure 5.3). The WLTC has a time span of 1800 s and a total distance of nearly 23 km.

5.2.3. Definition of Nominal Vehicle Voltage

The boost-buck converter is able to support up to 48 V on-board power supply voltage. However, for the electric integration, only a 12 V electric vehicle grid is analyzed.

5.2.4. Definition of Temperature Trajectory of Waste Heat

The temperature of the waste heat depends on the actual operation point of the ICE. For the WLTC, only the vehicle speed v is defined. Generally, the selection of the gear is a degree of freedom, which can be determined by the driver. In this thesis, it is assumed that the engine is integrated in a vehicle with a six-speed automatic gearbox. It is assumed, that the total mass of the vehicle with the TEG system is 1500 kg. Consequently, the engine speed is clearly defined for the WLTC, which results into a well-defined temperature trajectory of the waste heat. For this thesis, the waste heat temperature is based on the simulation results from Kühn et al. [68].

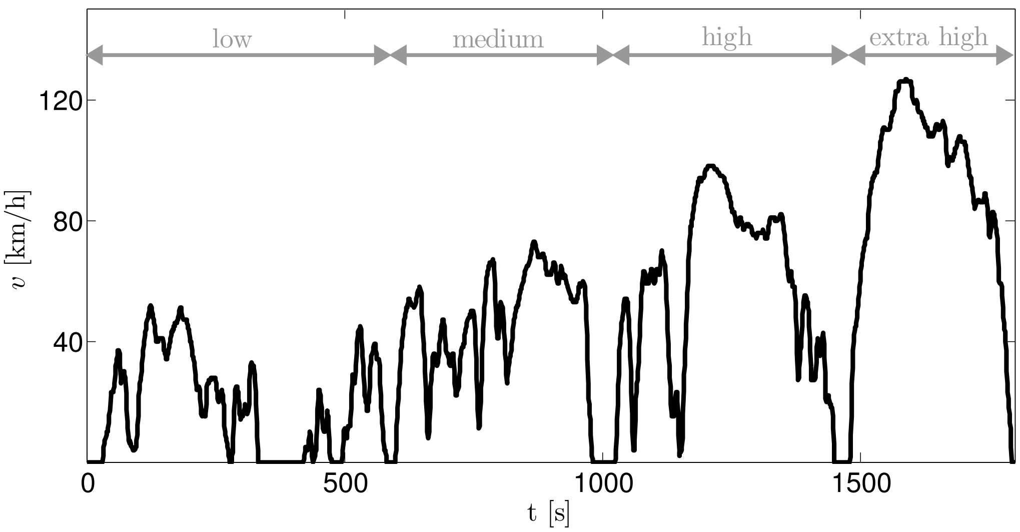

Figure 5.3.: Speed profile v of the worldwide harmonized light vehicles test cycle.

5.2.5. Parametrization of Thermoelectric Module

The electrical characteristics of TEMs depend on the material characteristics as well as the geometrical parameters of modules and the heat exchanger. The temperature of the exhaust gas of an Otto engine can rise up to 1000 °C [15]. For this reason, lead telluride (PbTe) is selected as thermoelectric material. In particular, this material has been well-examined and characterized in the literature [2, 48, 144, 157].
The geometrical parameters of thermoelectric pellets are 5 mm for length, width, height; one TEM consists of 108 TEs. The TEs are connected in series in order to reach a higher voltage amplitudes because the efficiency of the converter increases in relation to the voltage (cf. Section A.3.1).

5.2.6. Simulated Parameters of Thermoelectric Modules

The voltage and resistor values of the TEMs are determined with the selected parameter of the TEs and the exhaust waste heat temperatures of the internal combustion engine. These data are simulation results of the research project TEG2020. The method uses for the simulation is presented in [77]. The electrical characteristics, the temperature, the mass flow rate $\dot{m}$ of the exhaust gas and the engine speed n are presented in Figure 5.4. From (2.17) it follows that the mean efficiency of the conversion of thermal power into electric power of the TEMs is $\overline{\eta}_{tem} = 3.34$ %.
It should be noted that the TEG contains ten TEMs in total, and two modules arranged in pairs, parallel to waste heat (cf. Section 2.5 and Figure 2.8). In this thesis, it is assumed that the TEG has a symmetric construction and the thermoelectric materials are ideal. Consequently, the temperature across module pairs 1 - 2, 3 - 4, 5 - 6, 7 - 8 and 9 - 10 have the same values as well as the same electrical characteristics.

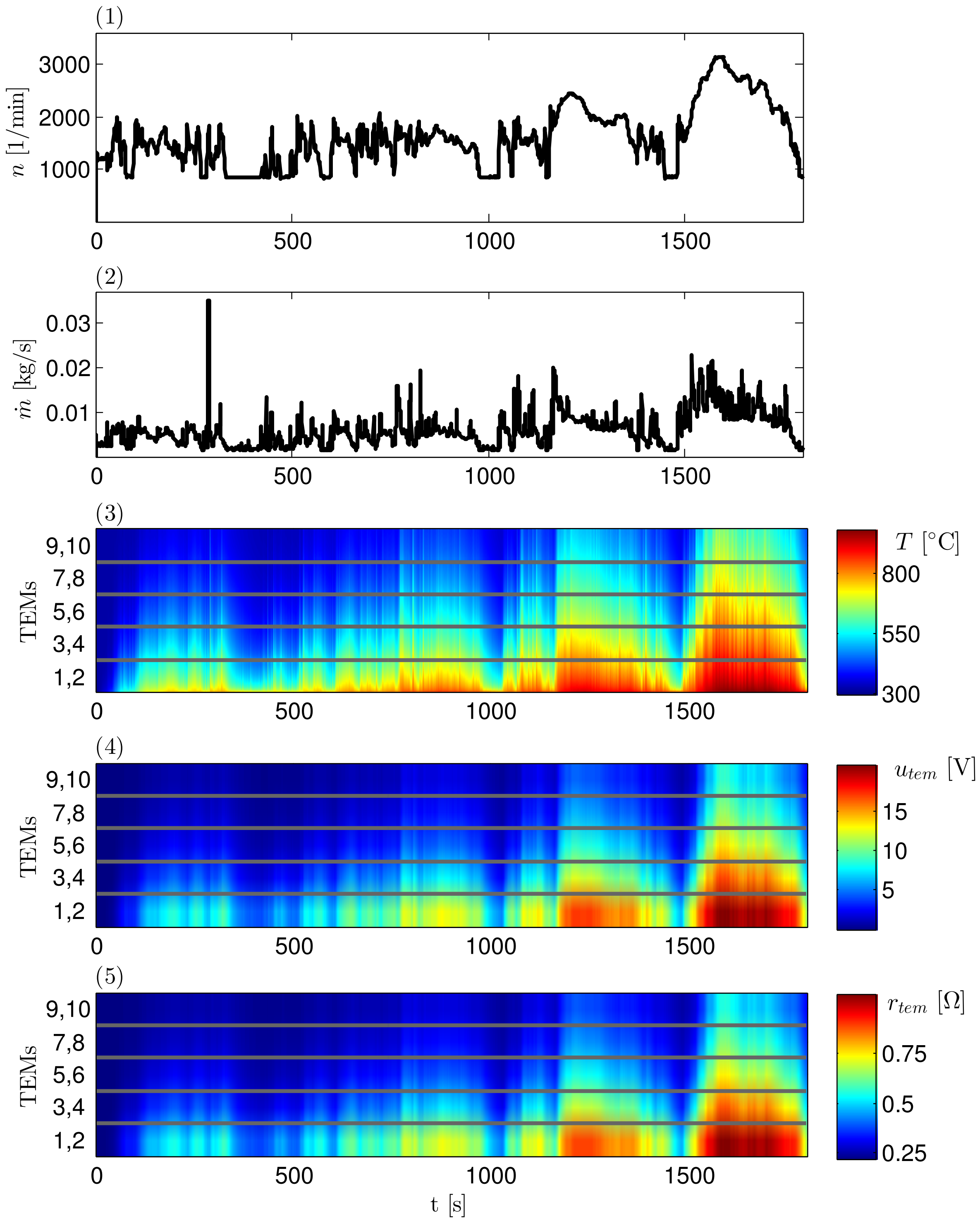

Figure 5.4.: Simulated data of the exhaust gas from the ICE and the electrical characteristics of the TEMs for a WLTC. The engine speed n for a vehicle mass of 1500 kg is presented in (1). The mass flow $\dot{m}$ of the exhaust gas is presented in (2). The temperature gradient across the ten TEMs is presented in (3). The open circuit voltage u_{tem} and the internal series resistor r_{tem} of the TEMs is presented in (4) and (5).

5.3. Interconnection of TEM

The desired concept of the TEG provides an installation space for a DC-DC converter for each TEM. Consequently, ten converters can be integrated in the desired TEG system. The initial situation is a one-to-one concept - one converter for one TEM. This concept is restrictive for an interconnection of the TEMs to the on-board power supply. Thus, only a direct connection is possible. In this situation, the selection of the reference signal from u_{C_2} at the control structure only allows to influence the efficiency of the functional chain from TEG to the load of the on-board power supply. The electric power efficiency η_{TEM_w} of the wired TEMs with DC-DC converter and the whole efficiency η_{TEG} of the TEG yield:

$$\eta_{TEM_w} = \frac{P_{out}(t)}{\frac{1}{N_M - i_M}\sum_{i_M}^{N_M} P_{TEM,i_M}(t)} \tag{5.2}$$

$$\overline{\eta}_{TEM_w} = \frac{\overline{P}_{out}}{P_{TEM_w}} = \frac{\int_0^{1800} P_{out}(t)\, dt}{\int_0^{1800} \frac{1}{N_M - i_M}\sum_{i_M}^{N_M} P_{TEM,i_M}(t)\, dt} \tag{5.3}$$

$$\eta_{TEG} = \frac{P_{TEG}}{P_{\sum TEM_w}} = \frac{M}{N}\frac{\sum_{i=1}^{N} P_{out,i}(t)}{\sum_{i=1}^{M} P_{TEM_w,i}(t)} \tag{5.4}$$

$$\overline{\eta}_{TEG} = \frac{\overline{P}_{TEG}}{\overline{P}_{\sum TEM_w}} = \frac{\int_0^{1800} P_{TEG}(t)\, dt}{\int_0^{1800} P_{\sum TEM_w,i}(t)\, dt} \quad , \tag{5.5}$$

where P_{TEM} is the power of a thermoelectric module, P_{out} is the output power of the DC-DC converter, N is the number of the converters, M is the number of the modules, P_{TEM_w} is the output of the wired TEMs, i_M is the index of the module from a TEM network, and N_M is the number of TEMs in a network. The sum of the wired module power is $P_{\sum TEM_w}$ and the output power of all DC-DC converters is P_{TEG}. For the initial situation - one converter for one TEM - is $N_M = 1$ and $M = N = 10$.

The efficiency of the TEG with the initial configuration in a WLTC is presented in Figure 5.5 with a constant reference signal $u_{C_2} = 48$ V and adaptive reference signal for the BoBu (cf. Section 4.6). From Figure 5.5 it follows that the electrical efficiency from the 4th to the 10th TEM is marginal in the low and middle drive cycle. In those time spans, the efficiency of the whole TEG is only dominated by the efficiency of the first and the second TEM. In the extra and extra high time spans, nearly all modules have an efficiency of about 65 %. The low efficiencies at low and middle drive cycles are reasonably related to the electrical parameters of the TEMs (cf. Figure 5.4), since the ratio of voltage to current of the TEMs lies between 0.25 Ω and 0.5 Ω at the MPP. The efficiency of the converter can also be represented in relation to the input resistor value of the TEM (see Figure 5.6). Therefore, higher resistor values in a TEM lead to an increase of the efficiencies of the converter and the whole TEG.

Furthermore, the adaptive reference value u_{C_2r} significantly increases the efficiency (see Figure 5.5, (2)).

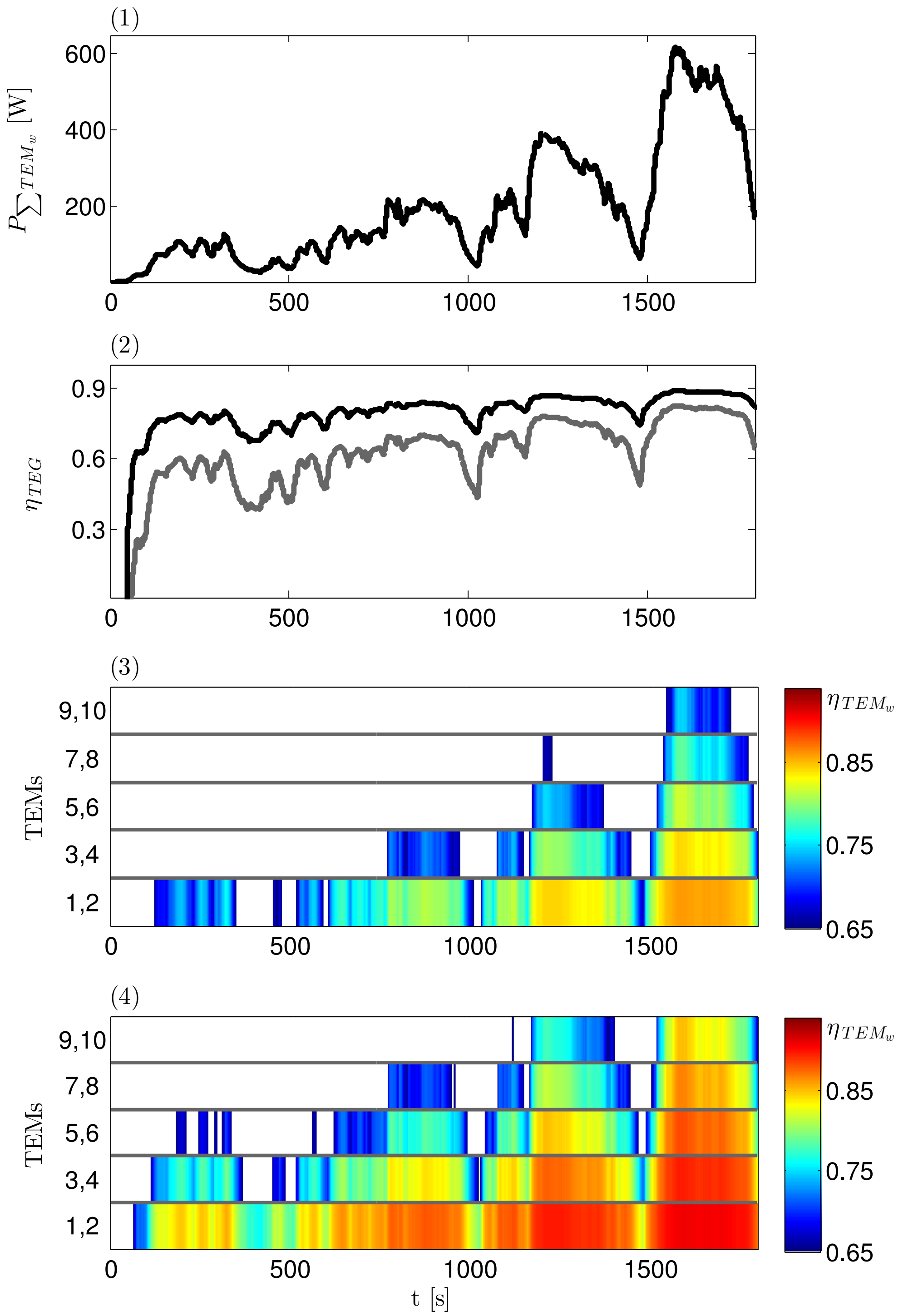

Figure 5.5.: Simulated power efficiency of the electric wiring of TEMs with DC-DC converters for a WLTC. (1) presents the total power of the TEMs $P_{\sum TEM_w}$. The efficiency η_{TEM} of the BoBu with $u_{C_2r} = 48$ V (gray line) and adaptive reference value of u_{C_2r} (black line) are presented in (2). The efficiency of the separated TEMs with each converter η_{TEM_w} for $u_{C_2r} = 48$ V is shown in (3) and for adapted u_{C_2r} in (4).

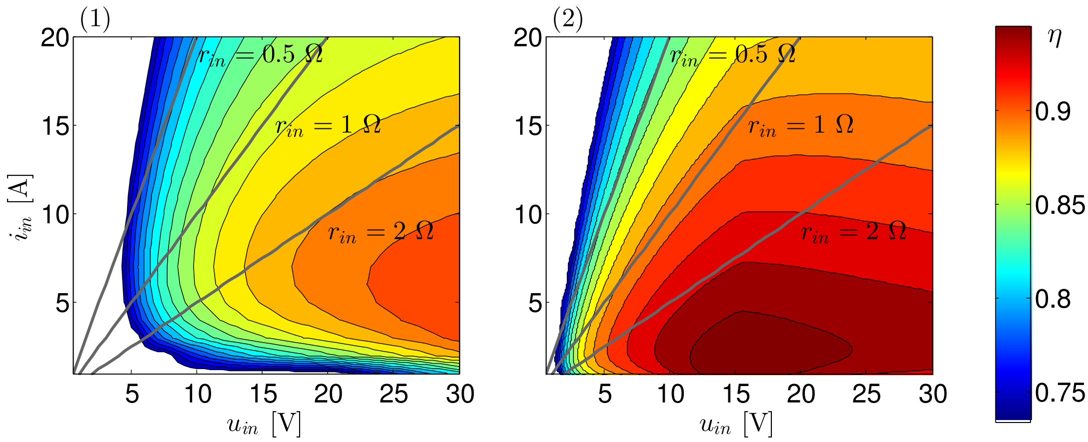

Figure 5.6.: Comparison between the boost-buck efficiencies for fixed and variable u_{C_2r} with presentation of the internal resistor r_{in}. The efficiency with the reference value $u_{C_2r} = 48$ V is shown in (1). The optimized efficiency with the adapted u_{C_2r} is shown in (2).

The nominal characteristic values of the simulation are summarized in Table 5.2. Due to the adaption of the voltage amplitude, the average efficiency of the whole TEG increases by up to 16 %.
In summary, the adaptive middle voltage control results in higher values of η_{TEM_w} in comparison to the control with fixed reference value of u_{C_2}. However, the efficiency of the TEG in low and medium driver cycle intervals are the lowest in the WLTC because the converter is operating at very unfavorable operating points.
Furthermore, it can be seen that the temperature in the TEG is very inhomogeneous. Consequently, the TEMs have significantly varying efficiencies, which depend on their position in the TEG.

5.4. Optimization of TEM Interconnection

The efficiency of the converters depends on the selected semiconductors, the electrical parts, and the electrical operation points. Due to the adaptive control of the middle voltage u_{C_2}, the efficiency optimization of the converter was successful. The realized hardware of the converter was selected without a specific electrical characteristic of the TEM. In practice, the wiring of the TEM and the converter could be suboptimal for a selected TEM. For example, the converter might work at an operation point in which the efficiency is lower than at other possible operation points. However, in the application, the electrical wiring is a degree of freedom. The selection of the one-to-one concept is only one choice.
The electrical wiring of TEMs to a DC-DC converter influences the operation point of the TEMs and, finally, the overall efficiency of the function chain from the TEM to the load.
The possible interconnection of TEMs results in a significant number of solutions. The selection of the number of TEMs, the DC-DC converter, and the electrical wiring of the TEMs is a nonlinear combination problem. The aim is to find the optimal combination of TEMs and converters to reach the maximum electrical efficiency of the TEG system. Unfortunately, the objective function is not given in a closed

module	P_{out}^{+} [W]	$\overline{P}_{out}$ [W]	$\eta_{TEM_w}^{+}$	$\overline{\eta}_{TEM_w}$	P_{TEG}^{+} [W]	$\overline{P}_{TEG}$ [W]	η_{TEG}^{+}	$\overline{\eta}_{TEG}$
	$u_{C_2r} = 48$ V							
1,2	83.08	35.38	0.86	0.80	-	-	-	-
3,4	64.57	18.04	0.84	0.73	-	-	-	-
5,6	48.40	9.23	0,82	0.65	-	-	-	-
7,8	35.04	4.89	0.79	0.58	-	-	-	-
9,10	24.97	2.71	0.75	0.51	-	-	-	-
TEG	-	-	-	-	512.12	140.50	0.83	0.72
	adaptive middle voltage u_{C_2r} (cf. (4.79))							
1,2	87.67	38.81	0.91	0.88	-	-	-	-
3,4	68.66	20.98	0.90	0.85	-	-	-	-
5,6	52.15	11.62	0,88	0.82	-	-	-	-
7,8	38.52	6.62	0.87	0.78	-	-	-	-
9,10	28.29	3.96	0.85	0.75	-	-	-	-
TEG	-	-	-	-	550.58	163.98	0.89	0.84

Table 5.2.: Nominal values of the simulated TEG with one-to-one connection of TEMs and BoBu converters for fixed and adaptive middle voltage reference u_{C_2r}.

form since the analytical model of the temperature profile and of the TEMs is not a component of this thesis. To solve such nonlinear global problems, heuristic optimization algorithms can be used. Well-known algorithms are the simulated annealing (SA), the evolutionary algorithm (EA), Branch and Bound (B&B), as well as Tabu Search (TS). [8, 10, 119]

Although all methods can be used to solve the optimization problem, none guarantees a global optimization. In this case, an EA solver is selected because of its intuitive structure and the possibility to implement prior knowledge [119].

5.4.1. Evolutionary Algorithm

The EA is a stochastic optimization method based on evolution strategies seen in the nature. The principle of the natural evolution is represented by, for example, a human - an individual. The information of the structure of this individual is saved in chromosomes and corresponds to a string of binary coding (genotype). The biological organism - the individual - is a representation of the information encoded in chromosomes.

Each individual has a certain quality. The result of the evolution strategy is the survival of the individual, which bears a certain level of fitness. In other words, the result of the evolution is to put forth a human with the best adaption to survive in its environment.

Algorithm 1 Evolutionary Algorithm

$k := 0;$
$fit[k] := 0;$ ▷ initialize fitness value
initialize $pop[k]$; ▷ initialize population of individuals
evaluation $fit[k]$; ▷ calculate fitness of individuals
$k++;$
while terminate criterion = false **do**
    $pop[k]$:= mutation/recombination $pop[k-1]$;
    evaluation $fit[k]$;
    $pop[k+1]$:= select $\langle pop[k] \cup \max fit[k] \rangle$ ▷ select individuals with highest fitness
    $k++;$
end while

In nature, the evolution starts with a population - a quantity of individuals. The start population is a stochastic selection of individuals. Each of these individuals are associated with a fitness value. The evolution is based on different mechanisms, such as recombination and mutation, to procreate individuals with the highest survival odds. Therefore, when the chromosomes of two individuals are combined, a new individual is generated. It also has a certain fitness value. Additionally, mutations can change different parts of the individual's chromosomes.

The evolutionary structure, like iteration, evolves through generations. Thus, from the actual population, the individuals with the highest fitness value are advantaged and will generate a new population because they have a better chance to survive or to satisfy the defined requirements. For a technical or mathematical problem, each individual represents a result from the solution space. The iteration of the evolution repeats until the maximum of the fitness or another termination criterion is reached. The evolution strategy can be illustrated as a pseudo-code (see Algorithm 1). This simple structure is ideal for adapting nonlinear optimization problems and can directly be implemented into software. Further, the stochastic characteristics of the EA allows a parallel implementation for computer in order to reduce the calculation time [8]. A particular advantage of the EA is the option to define constraints, which reduces the solution space. Furthermore, prior knowledge can be considered at the fitness calculation as well as mutation, recombination, and selection.

In the literature, several EA approaches are distinguished: genetic algorithms (GA), evolutionary programming (EP), and evolution strategies (ES). These three approaches are based on the evolution method. The difference between these methods is the representation of the coding in the genotype space and the utilization of individual evolutionary methods (mutation, recombination, and selection). The GA traditionally uses binary coding in contrast to the EP and the ES, which use real values and are more problem-orientated. Furthermore, the GA and EP are based on a stochastic selection of the individuals for each new iteration in contrast to the deterministic selection of the ES.

In practice, those three approaches are often combined to a hybrid approach. [8]

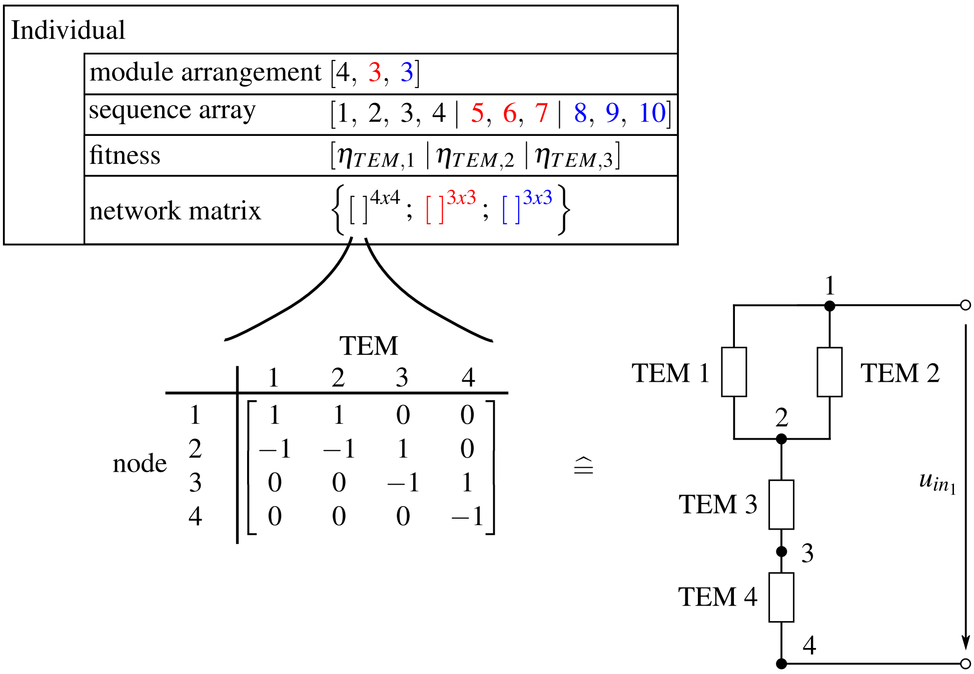

Figure 5.7.: Example of a representation of an individual. This individual represents three DC-DC converters. The first converter uses TEMs 1 - 4, the second TEMs 5 - 7, and the third TEMs 8 - 10. For illustration, the network matrix for the first converter is presented for an explicit electrical wiring of the TEMs.

In this thesis, a combination of GA and ES, which uses stochastic and deterministic methods for the optimization of the internal connection from the TEMs with the DC-DC converter, is selected.

Representation of Individuals

The coding of individuals is an important factor. Individuals represent configuration of the TEG. Figure 5.7 shows a representation of an individual.
An individual includes one DC-DC converter, a number of TEMs, the electric wiring of the TEMs, and the fitness value. The information of the selected TEMs for an individual is represented in the module sequence array. This array has the information on the TEM numbers. The network matrix presents the electrical wiring for the selected TEMs of a DC-DC converter. The coding of this matrix is based on the direct graph of the electrical wiring of the modules [29]. Each module is a branch and has two nodes, which are depicted as ± 1. The network matrix illustrates the connection of each node in relation to their particular branch. Each individual also has a fitness value, which represents the criterion for the selection.

Recombination

For the recombination of two individuals to produce a new individual, a one-point crossover algorithm is implemented [8, 119]. However, in this implementation the crossover can only combine the whole string of the module arrangement with another sequence array of the individual. Individuals are selected with a random selection function.

Mutation

Two types of mutations are distinguished: the arrangement and the sequence mutation. Both mutations are random alterations of the array coding. By mutations of the arrangement individual elements can be combined or an individual can be divided. This means that a converter with four TEMs can be separated in two converters with two TEMs, for example. These mutations are reversible.

Evaluation of Fitness

The aim of the EA is to find the electrical wiring of the TEMs and the necessary number of DC-DC converters with the highest TEG efficiency. Each result for the electrical wiring of an individual can be evaluated with the fitness $\overline{\eta}_{TEG}$, which based on the module wiring efficiency η_{TEM}.
The fitness is particularly based on the wiring of the TEMs for the DC-DC converter. For this reason, all combinations of the TEMs internal wiring are sequentially calculated and the combinations with the highest fitness are saved in the individual's network matrix.

Selection

With each iteration of the EA, a new population is generated from the previous population. There are different selection rules, which are stochastic (e.g., roulette wheel selection) or deterministic (e.g., ranking) [8]. For the used EA, a ranking method which selects only the individuals with the highest fitness values is selected. These individuals are the basis for the next population.

Termination Criterion

The EA is terminated if the iteration of the EA is greater than a fixed selected value N. In this thesis, $N = 30$ is selected.

5.4.2. Result of Optimization

The evolutionary algorithm is used for optimization of the electrical internal wiring of the TEMs with the DC-DC converter in relation to the assumed electrical characteristics of the TEMs and the WLTC (cf. Section 5.2.5 and 5.2.6). For the optimization, the WLTC is segmented in the sub-cycles low, medium, high, extra high, and the complete WLTC. This segmentation leads to a local and a global optimization. The results of the thermoelectric module network (TEMN) from the EA are presented in Table 5.3. The electrical efficiency of the TEG for the local and global optimization in relation to the one-to-one concept is presented in Figure 5.8. An illustration of the electric wiring of the TEMs and the DC-DC converters for the global optimization is shown in Figure 5.9.

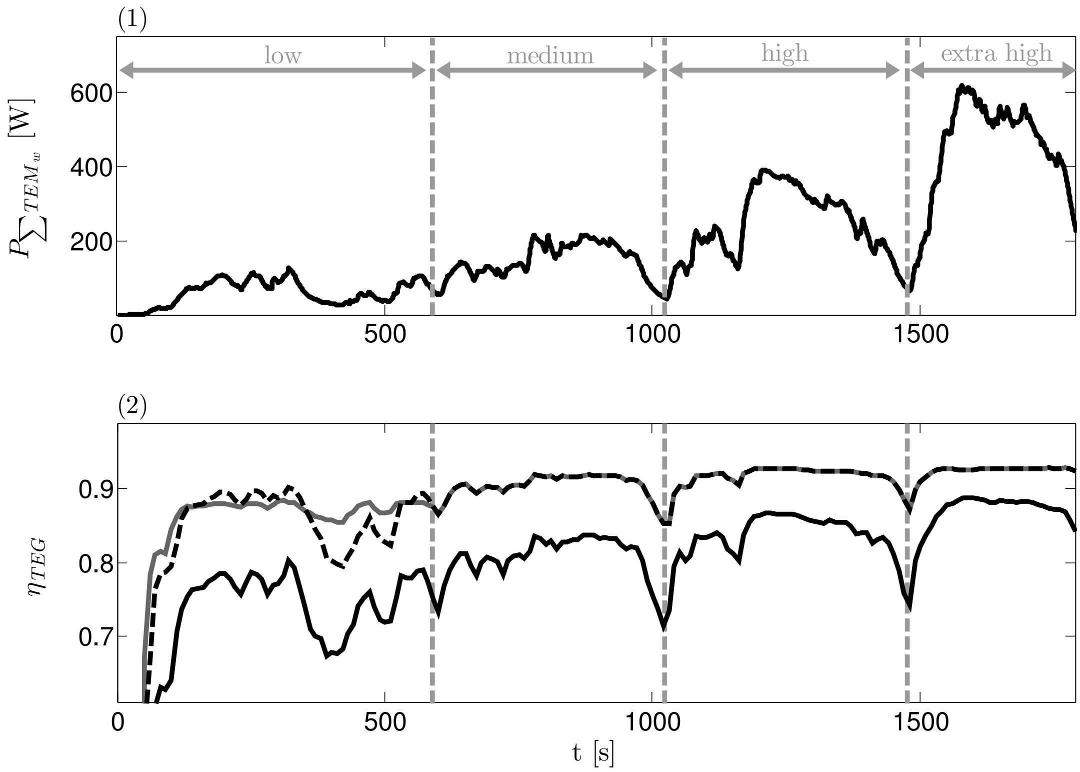

Figure 5.8.: Results of the optimized power efficiency of the electric wiring of the TEMs with DC-DC converters for a WLTC. (1) presents the whole power of of all TEMs $P_{\sum TEM_w}$. The efficiency η_{TEG} of different electrical wirings of TEMs and DC-DC converters is presented in (2). The black line represents the efficiency of the one-to-one concept. The black dashed line presents the optimized result of the EA for the complete driver cycle and the gray line presents the results for the optimized sub-cycles.

Two conclusions can be draw from the results shown in Table 5.3 and Figure 5.8. First, the series connection is dominating in the results for the internal wiring of the TEMs for a converter. Secondly, only TEMs are connected in parallel in the low cycle of the WLTP, where temperature gradients across the TEMs have the lowest amplitudes in the TEG (cf. Figure 5.5). These two conclusions are plausible in relation to the following facts.

In general, a series connection of TEMs results in an increase of the open circuit voltage. A parallel connection increases the current value of the short circuit current. According to the efficiency map of the converter (cf. Figure 4.21), the efficiency increases at higher input voltages and decreases at higher input currents. Furthermore, the TEMs have only one maximum power point at a defined current load. In case of an inhomogeneous temperature distribution of waste heat in the TEG, the current load in the MPP can be widely distinguished between the individual TEMs. Through a wiring of parallel and series connection, the current load can be distributed to operate the TEMs nearly at their individual MPP.

Consequently, a parallel connection is useful to separate the current load in a TEMN if the operation current at the MPP is significantly different.

A series connection has a positive influence on the efficiency of the BoBu converter because the input

WLTC	TEMN	number of BoBu	η^{+}_{TEG}	$\overline{\eta}_{TEG}$	$\bar{P}_{\sum TEM_w}$	$\bar{P}_{TEG}$
low	TEM 1+TEM 2+(TEM 3 ∥ TEM 4) TEM 5+TEM 6+TEM 7+TEM 8 TEM 9+TEM 10	3	0.89	0.88	59.2 W	52.0 W
medium	TEM 1+TEM 2+TEM 3 TEM 4+TEM 5+TEM 6 TEM 7+TEM 8+TEM 9+TEM 10	3	0.92	0.91	145.43 W	132.3 W
high	TEM 1+TEM 2+TEM 3 TEM 4+TEM 5+TEM 6 TEM 7+TEM 8+TEM 9+TEM 10	3	0.93	0.92	241.2 W	222.3 W
extra high	TEM 1+TEM 2+TEM 3 TEM 4+TEM 5+TEM 6 TEM 7+TEM 8+TEM 9+TEM 10	3	0.93	0.93	437.8 W	405.7 W
complete	TEM 1+TEM 2+TEM 3 TEM 4+TEM 5+TEM 6 TEM 7+TEM 8+TEM 9+TEM 10	3	0.93	0.92	194.2 W	178.1 W

Table 5.3.: Results of the optimized interconnection of the TEMs for the sub-cycles and complete WLTC. The wiring is depicted as + (series connection) and ∥ (parallel connection).

voltage increases. However, the load current in the TEMs connected in series is equal in the modules. In case the temperature gradient of the waste heat is nearly constant across the modules, the current load at the MPP is nearly the same.
However, the results in Figure 5.8 show that the TEMNs of the EA have a significantly higher efficiency than the one-to-one concept. The mean efficiency of the global optimized wiring is 92 %. In contrast, the one-to-one concept reaches an efficiency of only 84 % (cf. Table 5.2).

5.5. Conclusions and Discussion

This chapter presented the optimization of the electrical wiring from the TEMs to reach a maximal efficiency of the DC-DC converter. The design of the DC-DC converter is based on the requirement to support a wide power class of TEMs. The drawback of this requirement is that the efficiency of the boost-buck converter decreases in relation to the ratio between the input voltage and the input current of the converter. Based on the selected parameters of the TEMs and the waste heat temperature profile of a 2 L Otto engine, the simulation results show that the electrical wiring of the one-to-one concept is

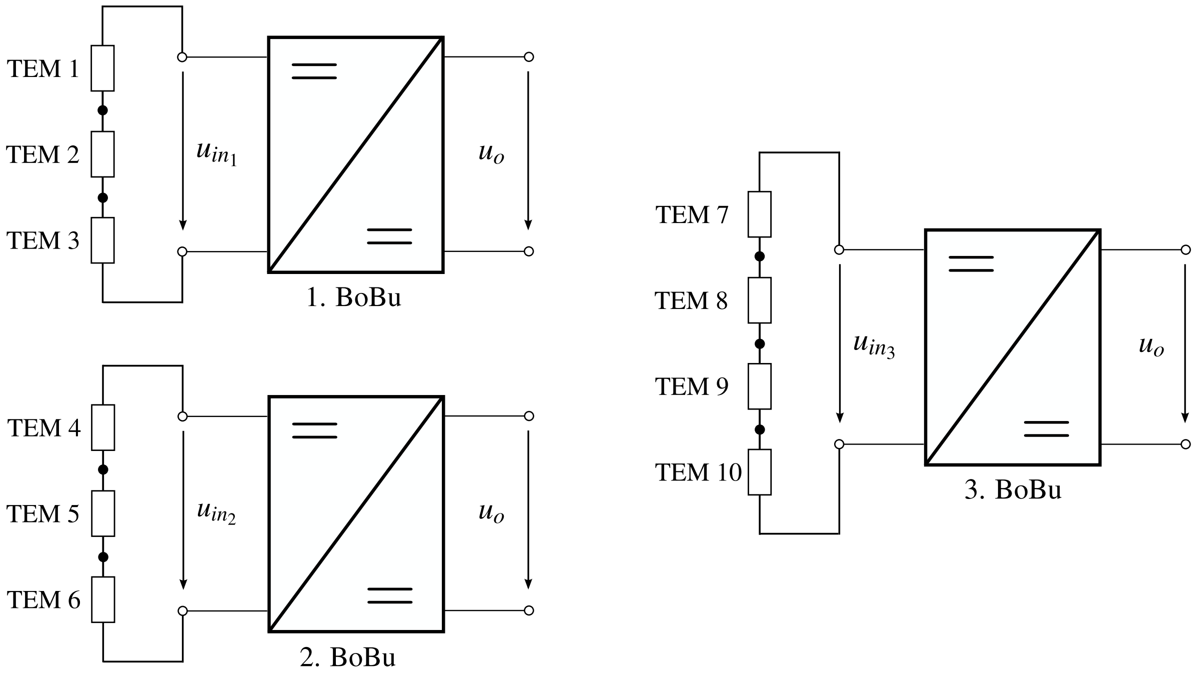

Figure 5.9.: Optimal interconnection of the DC-DC converters with TEMs for the complete WLTC.

sub-optimal for the TEG system. The efficiency of the wiring is marginal at a low temperature, which is caused by the low-impedance of the TEMs. The adaptive of the middle-voltage reference value u_{C_2r} was used to shift the efficiency map in relation to the operation point of a TEM. Hence, the performance of this method is limited to the physical parameters of the converter.

However, at the practical application of a TEG, the electrical wiring of TEMs and the connection with DC-DC converter can also be used as degree of freedom. An evolution algorithm was selected to find the ideal electrical wiring and the number of converters to optimize the efficiency of the TEG. The advantage of this approach is the fact that parallel computation can be used to decrease the calculation time of the optimization. This optimization algorithm also offers the possibility to take application requirements into account, like the maximal open-loop voltage for the DC-DC converter (cf. REQ.3).

However, a global optimum cannot be ensured because the EA is based on a stochastic concept. The selection of the iteration steps and integration of prior knowledge, like practical requirements, limit the search area and increase the likelihood of a global optimum validation.

Besides, the EA was used to optimize the wiring for different segments of the WLTC. The results show, that determined electrical interconnection could differ from the actual electrical characteristic and the temperature distribution in the TEMs. The EA selected a serial interconnection of TEMs for the presented application. This led to a relocation of the operation points at higher input voltages, where efficiency of the converters is maximal. Consequently, the whole efficiency increased significantly in relation to the one-to-one concept. Therefore, fewer converters are necessary, which is a positive aspect from an economic point of view.

In summary, the electrical wiring of the TEMs is an opportunity to adjust the electrical characteristic of the TEMs to the operation points of a DC-DC converter with the highest efficiency values.

6. Electrical Energy Management

The integration of TEGs into the vehicle electrical systems is useful if fuel is saved and, consequently, a reduction of CO_2 emissions of the engine can be achieved.

The primary electrical energy from an on-board power system is generated by an alternator. The direct coupling of the alternator to the internal combustion engine with a V-belt results into an increase of the fuel consumption when the alternator generates electrical power. In modern on-board power supply systems, electrical energy management strategy (EEMS) is integrated, which provides the necessary energy by the use of the secondary battery and the alternator. The task of a EEMS is to ensure that the alternator produces electric energy in the operation points of the ICE where the additional fuel consumption for the electric generator is minimal. This includes methods such as the start-stop function and the recovery of the braking energy.

The TEG is the second power source that is integrated in the on-board power supply. The additional energy of the TEG requires reassessment and adaption of the EEMS in order to prioritize the use of the recovered energy from the TEG.

The aim of this chapter is to analyze the fuel consumption of the alternator for the vehicle power grid and to derive an EEMS to integrate the TEG in the power grid. With regard to this management, the potential to reduce the CO_2 emissions of an ICE should be simulated. The components of a 12 V automotive energy grid are modeled and characterized in Section 6.1. The fuel consumption of the alternator for the ICE is analyzed in Section 6.2. Based on this result, different EEMS are defined and integrated in the fuel consumption simulation in Section 6.3. The focus is to determine the potential of the TEG to reduce the emissions of the ICE. Finally, the results are discussed and summarized in Section 6.4.

6.1. Structure of Energy Grid

An automobile with an ICE classically has a 12 V power supply. The basic components of the on-board power supply are the alternator, which generates the primary electric energy, and the accumulator, generally a lead-acid-battery, which is essentially required to supply the engine starter, electrical load and to compensate load changes [12]. Additionally, the TEG system is integrated into this on-board power system (see Figure 6.1). For the simulation of the on-board power supply, all components must be characterized by models or maps. Figure 6.2 presents an equivalent network of on-board power supply, which is used for detailed simulations of the vehicle's power supply. The components and their characteristics are explained and illustrated in the following subsections.

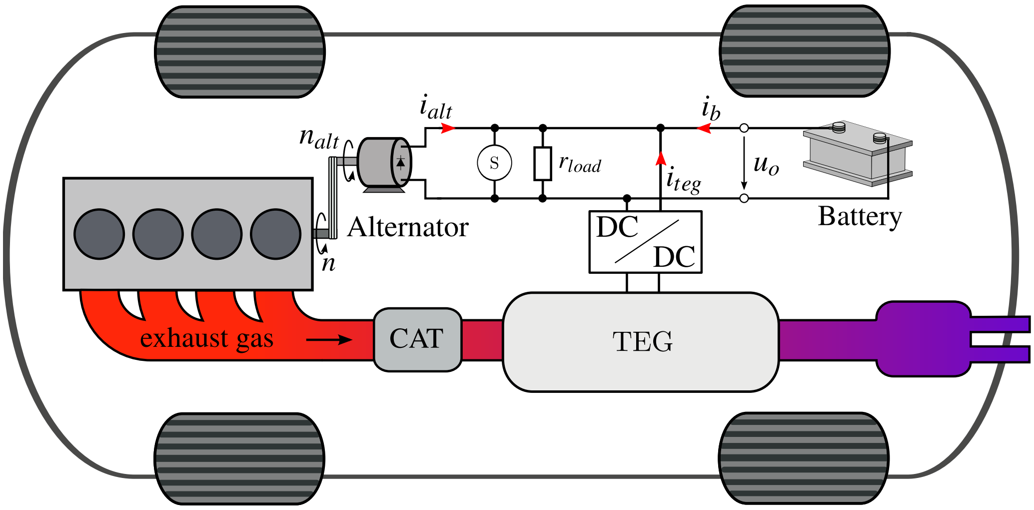

Figure 6.1.: Overview of 12 V classical energy grid with TEG system in an automobile, where S is the starter.

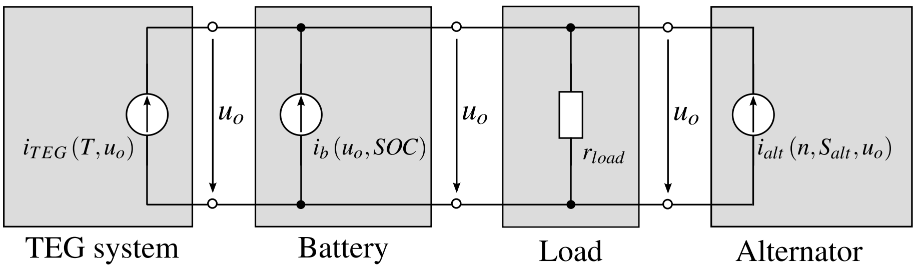

Figure 6.2.: Network of the electrical components for the simulated on-board power supply. The supplied current of the alternator i_{alt} depends on the actual engine speed, the voltage of the on-board power supply u_o, and the direct control signal S_{alt}. The battery current i_b depends on the current state of charge (SOC) and the voltage u_o. The TEG system is also illustrated as a current source, which depends on the waste heat temperature T and the voltage u_o.

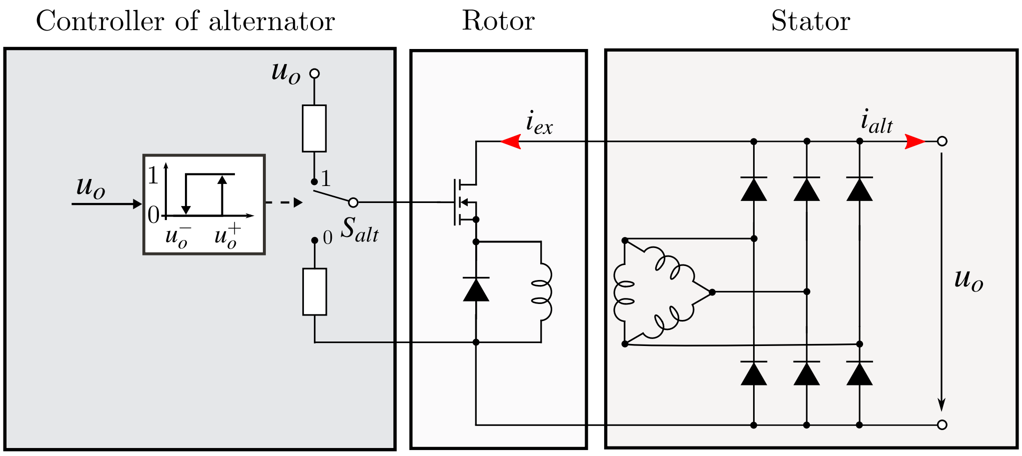

Figure 6.3.: Equivalent electrical circuit of an alternator.

6.1.1. Alternator

An alternator is a three-phase generator. The basic principle of the alternator is, that the rotor generates a rotated magnetic field, which according to Faraday's induction law results in a voltage in the stator. The induced voltage is sinusoidal. For this reason, AC voltage is converted into DC voltage with a three-phase bridge rectifier. The structure and the operating principle of the generator are described in detail in the literature [15, 140, 141, 174].

Depending on the type of automobile and equipment, different power classes of alternators are used. The maximal electric power of an alternator is 3 kW to 4 kW. Higher output values are limited by electrical losses, which depend on the current amplitude, the temperature and the compact design of the alternator. [15, 28, 131, 141]

Due to the direct mechanical connection between ICE and alternator by a V-belt, the power output of the generator can only be controlled by the exciting current i_{ex} of the rotor. The controller for the alternator has the task to regulate the vehicle power supply voltage u_o and to charge the battery to the desired voltage level u_o^+. The control variable of the exciting current i_{ex} is a switch element (like a MOSFET), which can be turned on and off. The control law of the current regulator is a hysteresis controller, which activates the switch when the voltage u_o is lower than u_o^- and switches it off when u_o^+ is reached. The hysteresis limit values (u_o^+, u_o^-) depend on the temperature [140, 174]. A general overview of the equivalent electrical circuit in the alternator is presented in Figure 6.3.

Characterization of Alternator by Measurement

To study the energy grid of a vehicle, a 12 V alternator made by Robert Bosch GmbH with a maximum output current i_{alt} of 140 A was selected. The characteristic map of the alternator was measured. In contrast to a physically based model, characterization with a map is simple because necessary unknown components of the alternator must not be estimated by identifications.

The only drawback to use the characteristic map for simulation is that the time dynamic behavior is not

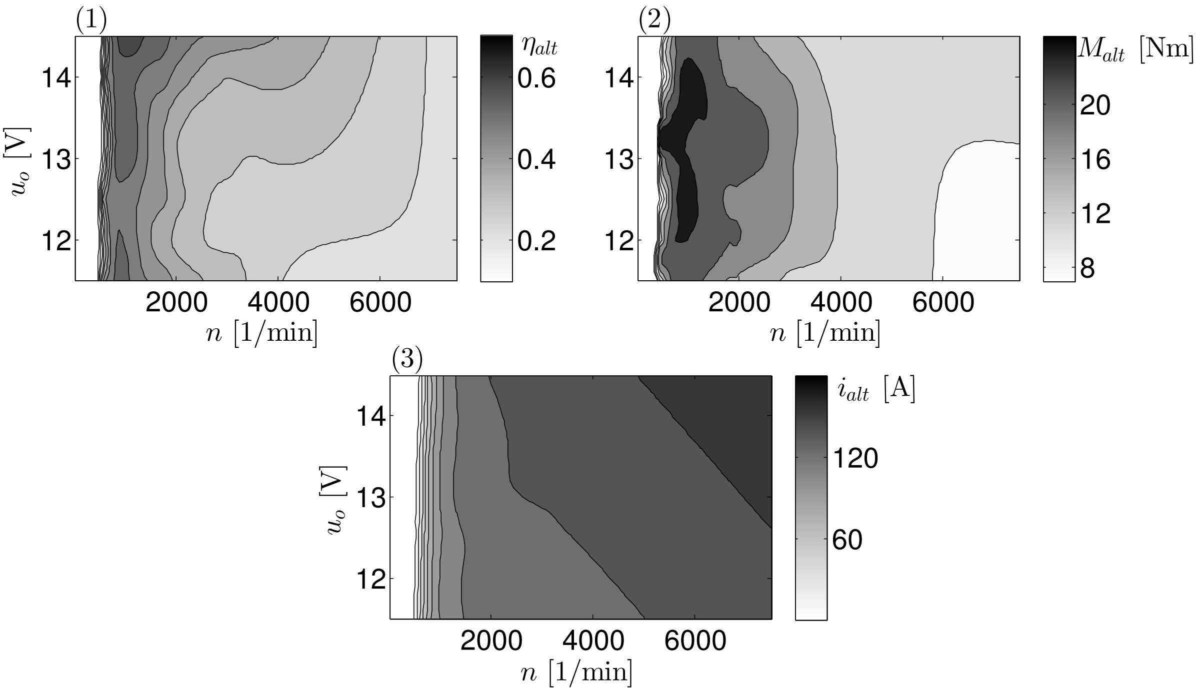

Figure 6.4.: Measurement of the on-board power voltage level (u_o) at the maximum current load i_{alt} for variable engine speeds (n) [P5]. The efficiency map η_{alt} is presented in (1). In (2) the measured drive torque M_{alt} and in (3) maximum current amplitude i_{alt} of the alternator are presented.

included.

For the measurements, the excitation circuit was separately supplied with a constant voltage source and the electrical system was simulated by an adjustable power load. The Figure 6.4 shows the efficiency η_{alt} of the alternator

$$\eta_{alt} = \frac{P_{ele}}{P_{alt}} = \frac{i_{alt} u_o}{2\pi n M_{alt}} \ , \tag{6.1}$$

where M_{alt} is the torque and i_{alt} is the output current of the generator. The static and rolling friction were determined by a separate measurement in order to adjust these values from the torque measurement. From the measurement results, the following conclusions are derived:

- If the terminal voltage u_o of the on-board power supply increases, the excitation current i_{ex} and the magnetic excitement increase as well. Consequently, the stator voltage and also the output current i_{alt} are rising at constant rotation speed.
- The terminal voltage u_o has direct influence on the magnetic excitation. The efficiency of the alternator increases through the maximization of the magnetic field depending on rotation speed. The chopper and mechanical losses of the alternator are disproportionate to the rotation speed, which results in a significant decrease of the efficiency η_{alt} [140].

It should be noted that influences of the temperature were not compensated in the measurements.

However, the control limits (u_o^+, u_o^-) depends on the temperature to match the trickle charge of the

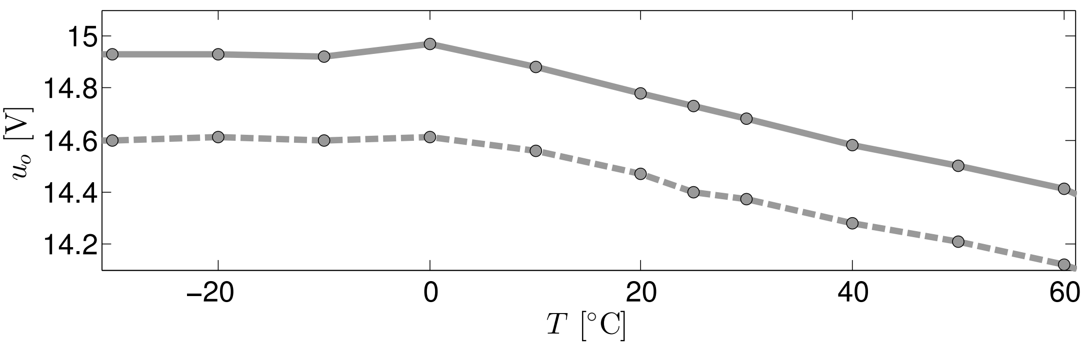

Figure 6.5.: Hysteresis band of the controller for the alternator is shown in relation to the ambient temperature. The dashed line is the value curve for u_o^- and the gray line for u_o^+. The measurement values are market with dots.

accumulator. The characteristic curve of the controller hysteresis was measured separately in a regulated temperature cabinet (see Figure 6.5). From this measurements follows that the charge voltage is inversely proportional to temperature. This characteristic is plausible, because the internal resistor value of a lead-acid battery is also inversely proportional to the temperature [69].

6.1.2. Battery

The electrochemical theory, the functional principle, and the state of the art of lead-acid batteries are presented in detail in [69, 133].

The nominal voltage of the lead-acid battery used for the on-board power supply is nearly 12.7 V and is commonly called a 12 V battery [140].

Lead-acid batteries are mostly used in automotive systems because they are robust against high discharge current amplitudes and temperatures. Especially in the start phase of the ICE, the battery can be significantly discharged by the starter.

The battery is an important component to be considered for the integration of the TEG into the electrical grid. Temporary excess energy of the TEG must be buffered in order to supply the electrical load with the TEG in time spans where the recovered power of the TEG is not sufficient. For the analysis of the electrical power grid, the state of charge (SOC) of the battery is required, which is determined with a model-based approach.

Parametrization of Battery

The modeling and parametrization of an electrochemical battery uses physical, mathematical, and electrical models. The highest accuracy can be achieved with physical models, which are difficult to handle because of the involvement of time-variant partial differential equations. Furthermore, the parameters of this model must be estimated with complex measurements. [138]

Mathematical models mostly are abstract and do not include all electrical characteristic information of the battery. The most commonly used approach is the modeling based on electrical models because the

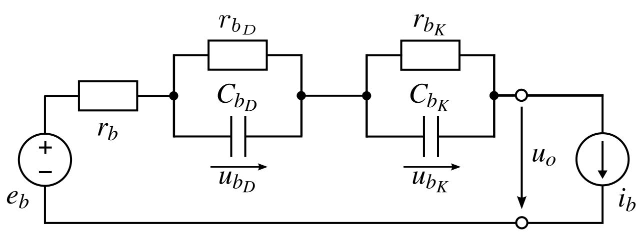

Figure 6.6.: Equivalent circuit network for a lead-acid battery.

parameters can be estimated through electrical simple test signals. [25]
An overview of different electrical models is presented in [25].
In this thesis, the Thévenin's theorem-based model is selected because the parameters can be identified by measurements of the electrical discharge signal. In Figure 6.6, the assumed equivalent circuit of the lead-acid battery is presented. The electrical behavior of the circuit can be described as [31]

$$\begin{aligned} u_o &= e_b + i_b\, r_b + u_{b_D} + u_{b_k} && (6.2)\\ C_{b_K}\frac{du_{b_K}}{dt} &= i_b - \frac{u_{b_K}}{r_{b_K}} && (6.3)\\ C_{b_D}\frac{du_{b_D}}{dt} &= i_b - \frac{u_{b_D}}{r_{b_D}}\ , && (6.4) \end{aligned}$$

where u_o is the terminal voltage, e_b the nominal voltage, r_b presents the ohmic contact resistance, C_{b_D} and r_{b_D} describe the double layer capacity effect on the electrode, and C_{b_K} and r_{b_K} present the diffusion process in the electrolyte [138]. The parameters depend on the SOC and the temperature of the battery. The SOC is defined as

$$\begin{aligned} \mathrm{SOC}(t) &= \frac{Ah_{nom} - \int i_b(t)dt}{Ah_{nom}} && (6.5)\\ 0 &\leq SOC(t) \leq 1 \quad \forall t\ , && (6.6) \end{aligned}$$

where Ah_{nom} is the nominal cell capacity of the battery.
An identification method for the parameters is based on the measurement of the terminal voltage u_o of the battery at a stepwise change of the current load i_b for all SOCs at constant temperature [154].
From these measurements, the parameters can be estimated by a linear regression analysis [119]. The System Identification Toolbox™ from MATLAB® is used for the regression analysis. The identified parameters and model verification of the Thévenin model (6.2) - (6.4) of a 72 A h lead-acid battery from Varta® at 25 °C, is presented in Figure 6.7. It is assumed that discharge and charge characteristics are identical. The RMS error between the simulated terminal battery voltage u_o and the measured voltage is 0.047 V, which corresponds to a relative RMS error of 0.41 %. The highest mismatch between the model and the measurement is caused by a non-ideal initial state of the SOC, which results in an increased discharge at the end of the measurement.

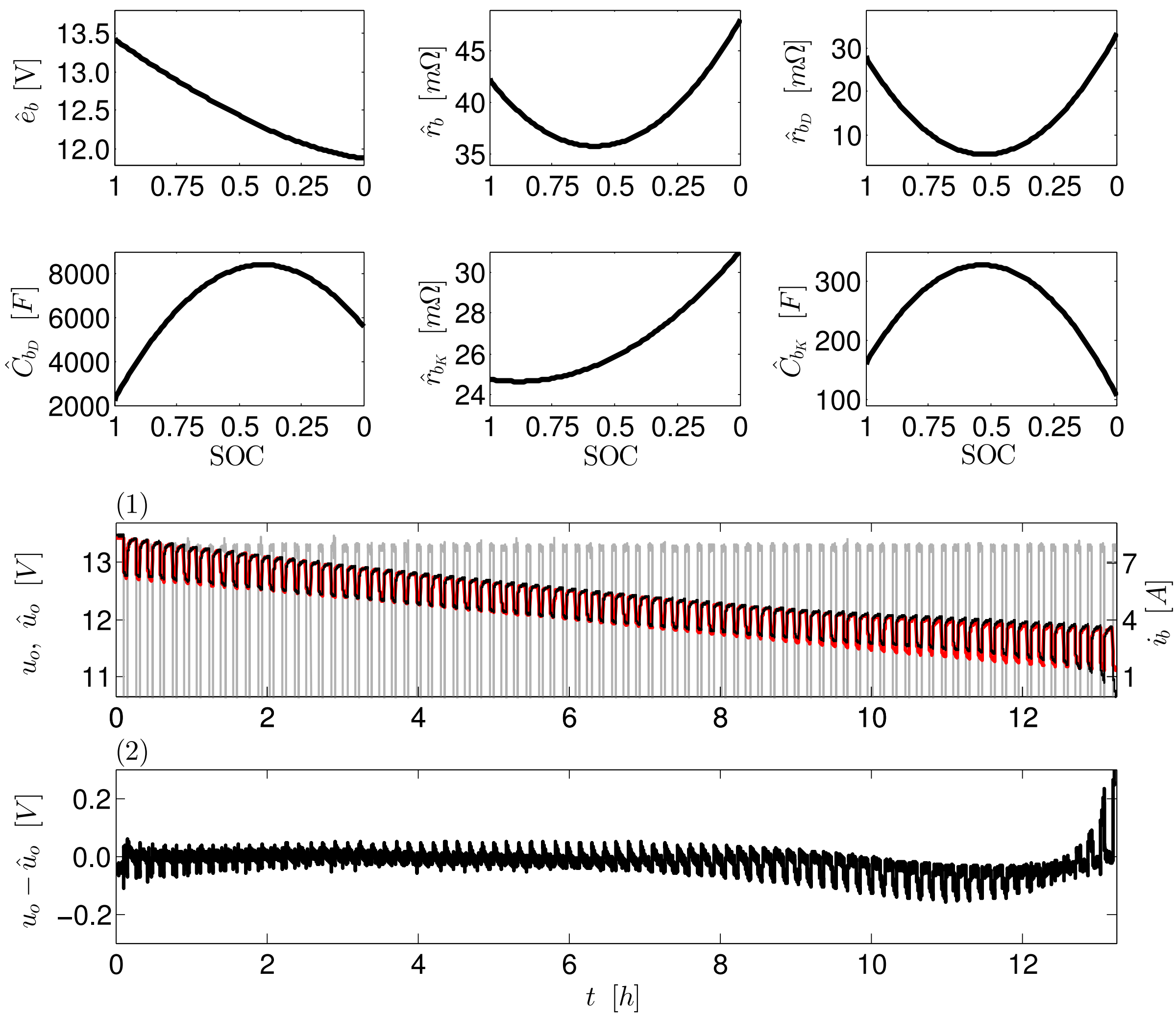

Figure 6.7.: Identified parameters and verification test of lead-acid battery at 25 °C. The predicted parameters $\hat{e}_b$, $\hat{r}_b$, $\hat{r}_{b_D}$, $\hat{C}_{b_D}$, $\hat{r}_{b_K}$, and $\hat{C}_{b_K}$ are identified in relation to the SOC of the battery. (1) the verification test between the simulated (black line) and the measured (red line) terminal voltage u_o for a square-wave current load i_b (gray line) are presented. (2) the error between measured (u) and estimated terminal voltage ($\hat{u}_o$) of the verification is presented.

6.1.3. Electrical Load

The electrical load in an on-board power supply depends on electrical consumers. Generally, the electrical power of the electrical power grid is time-dependent in a driver cycle, which in its turn depends on the engine management system, the influences of the environment, and the driver. During the start phase, the electrical load of the power grid reaches its maximum amplitude. This is caused by the starting current of the auxiliaries like pumps, fans, and the starter. [12, 15]

However, in this time span, the TEG system generates no power and has no influence on the on-board power supply.

After the start phase of the engine, the electrical power load decreases and converges to a nearly constant

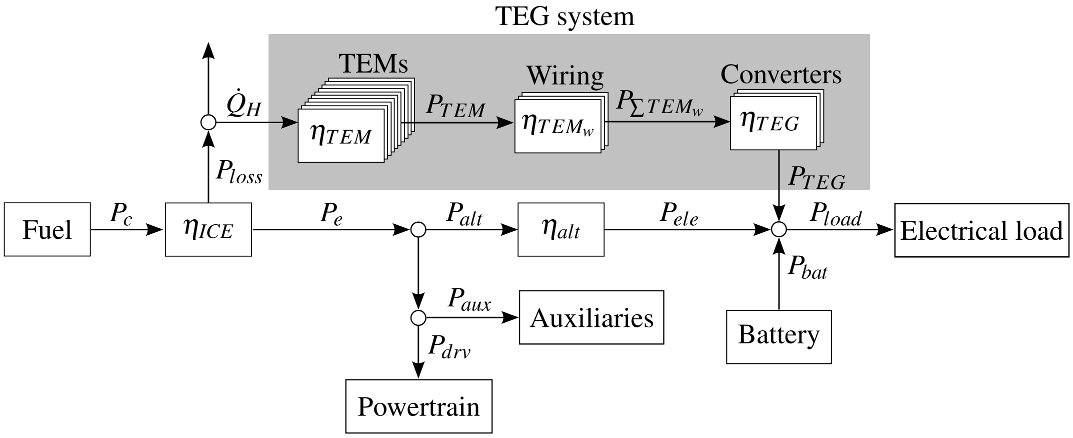

Figure 6.8.: Quality presentation of the power flow from the ICE and the TEG to the electrical load of the on-board power supply. The variables are described in the following: P_c is the power of fuel and P_e is the mean effective power of the ICE. P_{loss} is the loss of the ICE (such as waste heat and friction). $\dot{Q}_H$ is the heat power of the waste heat. η_{tem} is the efficiency of the thermoelectric material of the TEMs. P_{TEM} is the electrical power of the TEMs. η_{TEM_w} is the efficiency of the wiring of the TEMs. η_{TEG} is the efficiency of wired DC-DC converters. P_{TEG} is the electrical power of the TEG. P_{alt} is the drive power of the alternator. η_{alt} is the efficiency of alternator. P_{ele} is the electrical output power of alternator. P_{bat} is the power of the battery. P_{load} is the necessary power to supply the electrical load. P_{aux} is the power to drive the auxiliaries and P_{drv} is the resulted drive power for the powertrain.

value. Additionally, depending on the driver, the electrical consumers can be turned on or off. The driver causes a stochastic influence of the power consumption in a driver cycle.
Therefore, for generalization of the simulation results, it is assumed that the electrical load of the on-board power supply is a constant power P_{load} in the driver cycle.

6.1.4. TEG with DC-DC Converters

The optimized electrical wiring of the TEMs and the DC-DC converters is presented in Chapter 5. These results are used in this chapter to simulated the TEG system.

6.2. Analysis of Fuel Consumption

Consumption analyses usually refer to a specific application or explicit consumption characteristic map of an ICE. It is characteristic to a combustion engine that for each speed only one maximum efficiency respectively one minimum fuel consumption exists (cf. Figure 5.2). If the engine has an operation point with a mean effective pressure, which is below the minimal consumption curve, a load shift can significantly improve the efficiency of the engine at a constant speed.
However, the efficiency map of an ICE only indicates where the relation from input power to output power is minimal. The aim of this chapter is to analyze the additional fuel economy with a TEG system in a drive cycle. Figure 6.8 presents the power flow of the ICE and the TEG to the on-board power supply.

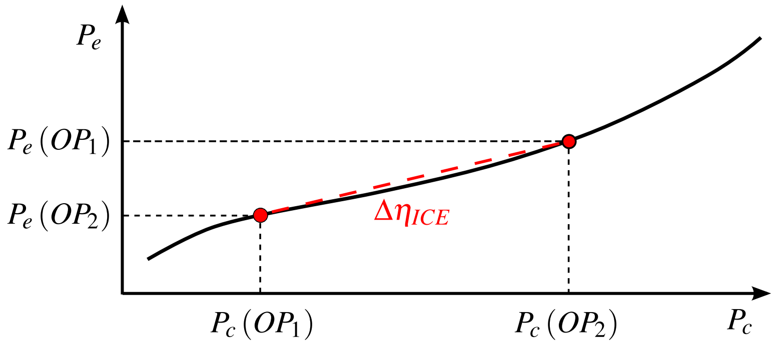

Figure 6.9.: Quality presentation of efficiency increase for a load shift from operation point OP_1 to OP_2.

Besides from the alternator, the recovered electric energy of the TEG is used to supply the vehicle power grid. Consequently, the alternator is relieved, which means that the necessary electrical power and also the mechanical drive power of the alternator decreases.
The drive power for the alternator is supplied by the ICE. Hence, the relief of the alternator from TEG also decreases the necessary drive power of the ICE and the fuel consumption in particular.
The power flow (see Figure 6.8) implies that the fuel economy depends on the function chain of the alternator and the ICE. Therefore, the influence of a load shift of the ICE, which is caused by the alternator, is analyzed below.

6.2.1. Load Shift of ICE

The effective mean power P_e of a four-stroke engine is defined as

$$P_e = 0.5\, p_{me}\, n\, V_c\ , \tag{6.7}$$

where V_c is the engine displacement. The fuel consumption corresponds to the power consumption P_c of the ICE

$$P_c = FC\, \rho_f\, B_f\ , \tag{6.8}$$

where B_f is the heat value of gasoline. In this thesis, $B_f = 11.5\ \mathrm{kW\,h\,kg^{-1}}$ is selected.
The relation of the power consumption to the output power when the operation point of the ICE changes from OP_1 to OP_2 for a constant engine speed is defined as the additional efficiency increase of the ICE [12]:

$$\Delta\eta_{ICE} = \frac{\Delta P_e}{\Delta P_c} = \frac{P_e(OP_2) - P_e(OP_1)}{P_c(OP_2) - P_c(OP_1)} \tag{6.9}$$

Figure 6.9 shows a quality presentation of the additional efficiency increase, which is caused by a load change. The additional efficiency increase of the ICE for a positive load change is estimated (see Figure 6.10) with the BSFC map (cf. Figure 5.2). External losses (eg., ancillary units) are not considered. The following statements can be formulated for the additional fuel consumption from Figure 6.10:

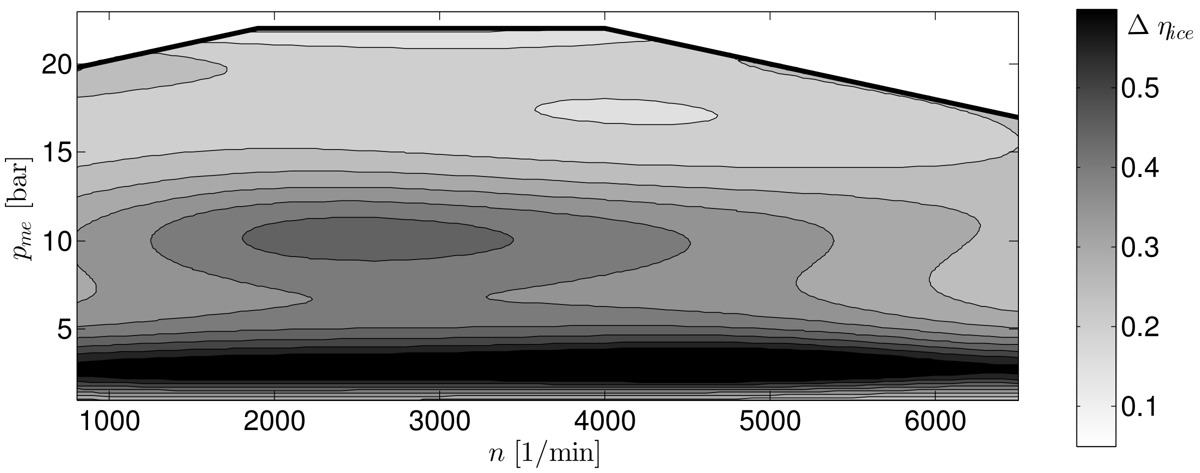

Figure 6.10.: Influence of the fuel consumption on the load shifting for the ICE.

- A load shifting between 0 and 5 bar is advantageous.
- A load shifting between 5 and 13 bar for 1500 min^{-1} up to 4500 min^{-1} is advantageous.
- A load shifting over 13 bar is suboptimal.

6.2.2. Load Shift of Alternator

How significant the load shift of the engine is depends on the energy recovered from the TEG and, especially, on the actual operation point of the alternator. The electric power of the TEG is used to supply the electric power grid. Therefore, the necessary output current of the alternator, which is required to supply the load, decreases. Consequently, this load current shift of the alternator results in the shifting of the alternator efficiency $\Delta\eta_{alt}$:

$$\Delta\eta_{alt} = \frac{\Delta P_{ele}}{\Delta P_{alt}} = \frac{P_{ele}(OP_2) - P_{ele}(OP_1)}{P_{alt}(OP_2) - P_{alt}(OP_1)} , \tag{6.10}$$

where P_{alt} is the mechanical driving power and P_{ele} is the electric power of the alternator. Figure 6.11 shows the differential efficiency map for a current load shifting of the alternator. The following statements can be formulated regarding to the efficiency shift from Figure 6.11:

- A current load shifting below 800 min^{-1} is suboptimal.
- A load shifting over 900 min^{-1} is advantageous.
- A current load shifting over 60 A is suboptimal.

Nevertheless, the load shifting of an alternator is most advantageous for current load shifts below 40 A and speed between 900 min^{-1} and 2200 min^{-1}.

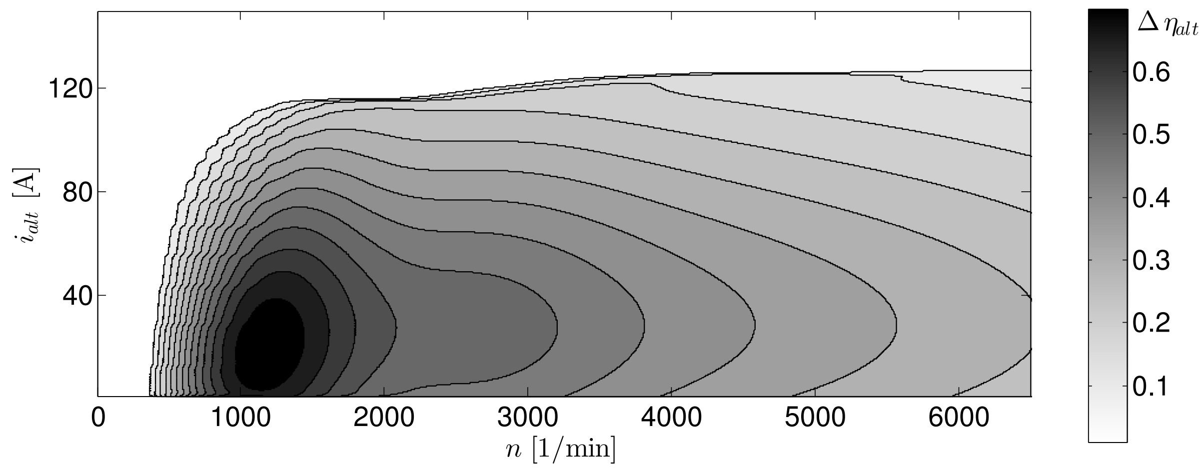

Figure 6.11.: Differential efficiency increases for current load shifting of the alternator at $u_o = 11.5$ V.

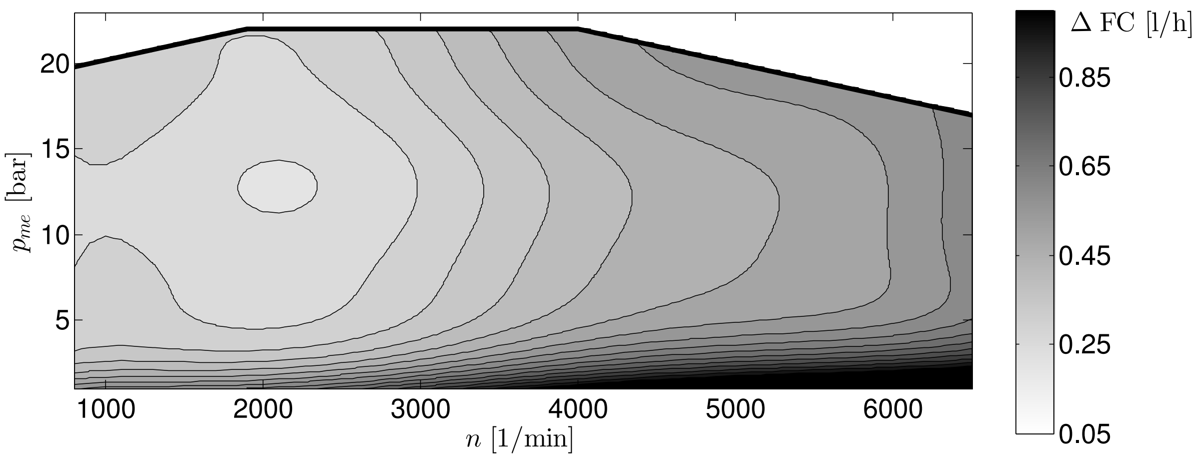

Figure 6.12.: Additional fuel consumption of the ICE for constant electrical load of 500 W at $u_o = 11.5$ V.

6.2.3. Additional Fuel Consumption of Alternator

The mechanical necessary drive power of the alternator depends on the desired electrical power P_{ele} and the engine speed. At constant speed, the load shift of the alternator results in a change of the necessary mean pressure of the ICE. Using the power flow diagram (see Figure 6.8), the change of the fuel consumption ΔFC for a load shift of the alternator can be estimated by [12]:

$$\Delta FC = \frac{P_{alt}}{B_f \rho_f \eta_{alt} \Delta\eta_{alt}} \tag{6.11}$$

The additional fuel consumption, causes by the alternator to supply a 500 W electrical load, is presented in Figure 6.12. This illustration suggests that the alternator has a minimum additional fuel consumption at middle mean effective pressures and engine speed between 1500 min^{-1} and 3000 min^{-1}.
However, the TEG also has the highest efficiency in this operation range of the engine. This means, that the potential of fuel economy with the TEG is in this operation points minimal.

6.2.4. Conclusion

The additional electrical power of the TEG can be used to supply the power grid in the automobile. Therefore, the alternator can be relieved, and the necessary mechanical drive power of the alternator decreases. Consequently, the effective mean power of the engine decreases and the fuel consumption in particular increase.

In this section, the influence of the load shift caused by the alternator and the ICE are analyzed. The results show that the efficiency of the alternator and the ICE increases significantly only within a limited operating range.

The lowest additional fuel consumption, to generate electrical power with the alternator is in the operating range of 1500 min^{-1} - 3000 min^{-1}, and 5 bar - 15 bar. Consequently, the alternator causes a minimal additional fuel consumption to generate electrical power in this operating range. However, within this operating range the TEG can significantly recover thermal power of the waste heat. Consequently, at operation points where the fuel consumption of the alternator is marginal, the TEG recovered a significant amount of electrical power. This means, that the recovered power has only a marginal influence of the entered fuel consumption in these operation points. It follows that the energy of the TEG must be stored in battery to relief the alternator in time spans, where the fuel consumption of the alternator is significant.

6.3. Electrical Energy Management Strategy

To ensure the functioning of the electrical components in the on-board power supply, it is necessary to provide sufficient amounts of electrical energy. To satisfy this requirement, the use of an EEMS is required. The energy grid of vehicles is a closed energy system. In this energy system, different measures can be accomplished for the EEMS. Some options and strategies which can be used for the EEMS are presented in [12].

In [12], the EEMS is subdivided into efficient use and the efficient provision of energy. In this thesis, the focus only lies on the provision of energy in relation to the fuel consumption.

From the analysis of Section 6.2 it follows that the fuel consumption of the alternator is minimal in the operation points where the electrical output power of the TEG is high. Therefore, the relief of the alternator in these operation points does not account for a significant fuel economy in contrast to operation points where the fuel consumption of the alternator is high. Therefore, to maximize the fuel economy of the TEG, different EEMSs should be analyzed in the following in order to estimate the maximum fuel economy.

In relation to [12], the following strategies are investigated:

EEMS 1 **Initial situation**
The power supply of the vehicle power grid is ensured through the alternator. The alternator uses a hysteresis voltage controller to regulate the exciting current of the rotor. The

controller has a characteristic curve to compensate for the influence of the temperature on the hysteresis voltage control values.

EEMS 2 **Direct integration of the TEG**
The TEG is integrated into the on-board power supply of the automobile without any variation of the power grid structure. The trickle charge controller of the DC-DC converters reduce the recovered power of the TEG once the SOC of the battery reaches one.

EEMS 3 **Ranking of recovered energy from the TEG**
The recovered electric energy should preferably be used to supply the electric load. For this reason, the battery must have enough charge capacity to store excess energy from the TEG if the load power is less than the recovered power from the TEG. Furthermore, sufficient charge capacity must be reserved in case the TEG recovers more energy than the power load consumes.
From this it follows that the control of the alternator must be manipulated by the EEMS. Thus, the exciting current of the rotor could be disabled and, consequently, the alternator would not supply the power grid. The on and off-states of the alternator is determined and optimized with an evolutionary algorithm for the driver cycle in order to minimize the fuel consumption of the ICE to supply the drive torque for the alternator.

EEMS 4 **Start-stop function and kinetic energy recovery**
It is determined in Section 6.2 that the alternator has a low efficiency at speed ranges below 900 min^{-1}. For this reason, the start-stop-function can be used to turn off the ICE during the time spans when no drive power is required. During this time period, the electric load is supplied only by the battery.
Furthermore, the alternator can use the kinetic energy of the ICE during the brake phase without an increase of the fuel consumption. The alternator is controlled by the hysteresis voltage controller. The TEG is not integrated in this power grid configuration.

EEMS 5 **Combined strategy**
The strategy of the start-stop-function and the kinetic energy recovery are combined with the prioritization of the recovered energy from the TEG. To minimize the fuel consumption, the on and off-state of the alternator are optimized using an evolutionary algorithm for the driver cycle (cf. EEMS 3).

6.3.1. Simulation of Fuel Consumption

The selected driver cycle for this simulation is the WLTC. The following conditions are defined for all fuel consumption simulations with the different EEMSs:

COND.1 Steady-state dynamic
The transient dynamic of the alternator and electrical load are neglected. This means that the magnetic excitement of the alternator is static and the measured characteristics map of Section 6.1.1 can be used to model the generator. Furthermore, the electrical load P_{load} is assumed to be constant. Dynamic changes of the electric loads during the start phase and from the starter are neglected.

COND.2 Temperature
For the EEMS, a constant ambient temperature of 25 °C is assumed.

COND.3 Battery conditions
For all simulations and analyses, it is assumed, that the battery is charged and the SOC equals one at the beginning of the driver cycle. The battery must be fully charged at the end of the cycle. In the sequence of the driver cycle, the battery can be charged and discharged within the limits of the SOC. The ageing process of the battery is not considered. The voltage amplitude of the terminal voltage u_o of the battery must be between 10.9 V and 14.9 V at 25 °C. These values are selected to protect the battery from exhaustive discharge and overvoltage.
For all analyses, the lead-acid battery model from Subsection 6.1.2 with a nominal capacity of 72 A h is selected.

COND.4 Specification of vehicle weight
The simulated vehicle has a total weight of 1470 kg, excluding the TEG system. The weight of the TEG system is assumed to be 30 kg.

COND.5 Cooling
The cooling water for the TEG must be cooled within the water circuit of the vehicle. The necessary additional electric power for the cooling and the pump is assumed to be 50 W.

COND.6 Back pressure
The TEG causes a back pressure in the exhaust gas system. The back pressure is particularly affected by the heat exchanger of the TEG. In relation to the mass flow of the exhaust gas, the back pressure is neglected in this thesis [67].

Beside from EEMS 1, EEMS 2, EEMS 4, EEMS 3 and EEMS 5 can directly control the state of $S_{alt}(1\,|\,0)$, which enables or disables the current flow i_{alt} for the exciter inductor (see Figure 6.3). The aim of EEMS 3 and EEMS 5 is to minimize the normalized fuel consumption FC_n in relation to the control statues S_{alt} of the alternator

$$\underset{S_{alt}}{\operatorname{argmin}}\ FC_n\left(t,n,P_e,SOC,P_{load},S_{alt}\right)\ , \tag{6.12}$$

where FC_n corresponds to the fuel consumption in liters per 100 km and is defined for the WLTC as:

$$FC_n = \frac{100\ \text{km}}{23.2\ \text{km}} \frac{1}{\rho_f} \int_0^{1800\ \text{s}} P_e(t)\ BSFC(P_e, n)\, dt \tag{6.13}$$

The WLTC is defined for a desired vehicle speed and acceleration. The necessary drive power P_{drv} for the powertrain is estimated with a mass model (see Appendix A.8) and a rotation speed n of the vehicle (cf. Figure 5.4). In this thesis, the auxiliaries are neglected. Consequently, the necessary mean effective power of the engine results into:

$$P_e = P_{drv} + P_{alt} \tag{6.14}$$

The fuel consumption FC_n is simulated for the electrical load P_{load} from 0 up to 1500 W because the load influences the necessary drive power of the alternator.
From (6.12) it follows that the state of the switch S_{alt} can be manipulated by the EEMS. In the simulation, the EEMS can change the state of this variable every second. For the EEMS 1, EEMS 2, and EEMS 4 S_{alt} is regulated by the alternators hysteresis controller. Additionally, in EEMS 4, the states of S_{alt} are zero if the no-load speed is reached and S_{alt} is one if the ICE is in the breaking phase.
In contrast, the state S_{alt} of alternator is a degree of freedom in EEMS 3 and EEMS 5, which can be used to optimize the fuel economy. Hence, an EA algorithm is used to estimated the states of S_{alt} in the driver cycle, in relation to maximize the fuel economy. The method and the function of the EA is explained in Subsection 5.4.1. The same structure is used for the optimization of the fuel consumption; only the selection criterion for the individuals is adapted to the stochastic universal sampling method. This method gives individuals of the population with a lower fitness a chance to be chosen for the next iteration step [8]. The population initially includes 40 individuals, and the EA algorithm is terminated after 40 iterations.
The simulated fuel consumption and CO_2 emissions results for all EEMSs are presented in Figure 6.13 and Table 6.1. The results are summarized in the following:

Results of EEMS 1

The fuel consumption increases almost proportionally to the power load of the on-board power system in relation to the fuel consumption map (cf. Figure 5.2). For every 100 W of electrical power the fuel consumption increases by 0.14 L/100 km.

The proportionality between fuel consumption and load power can be explain with the results from the fuel consumption analysis (cf. Section 6.2). The additional fuel consumption is nearly constant for the rotation ranging from 1500 min^{-1} to 3500 min^{-1} and the brake mean effective pressure ranging from 5 bar to 20 bar (cf. Figure 6.12). This means that an increase of the effective power of the ICE results in nearly proportional to the additional fuel consumption. At WLTC, 69 % of the operation points are in this area.

In comparison to [94, 134, 140, 173], the consumption of 0.1 L/100 km - 0.15 L/100 km per 100 W is specified. The values available in literature suggest that the simulation results

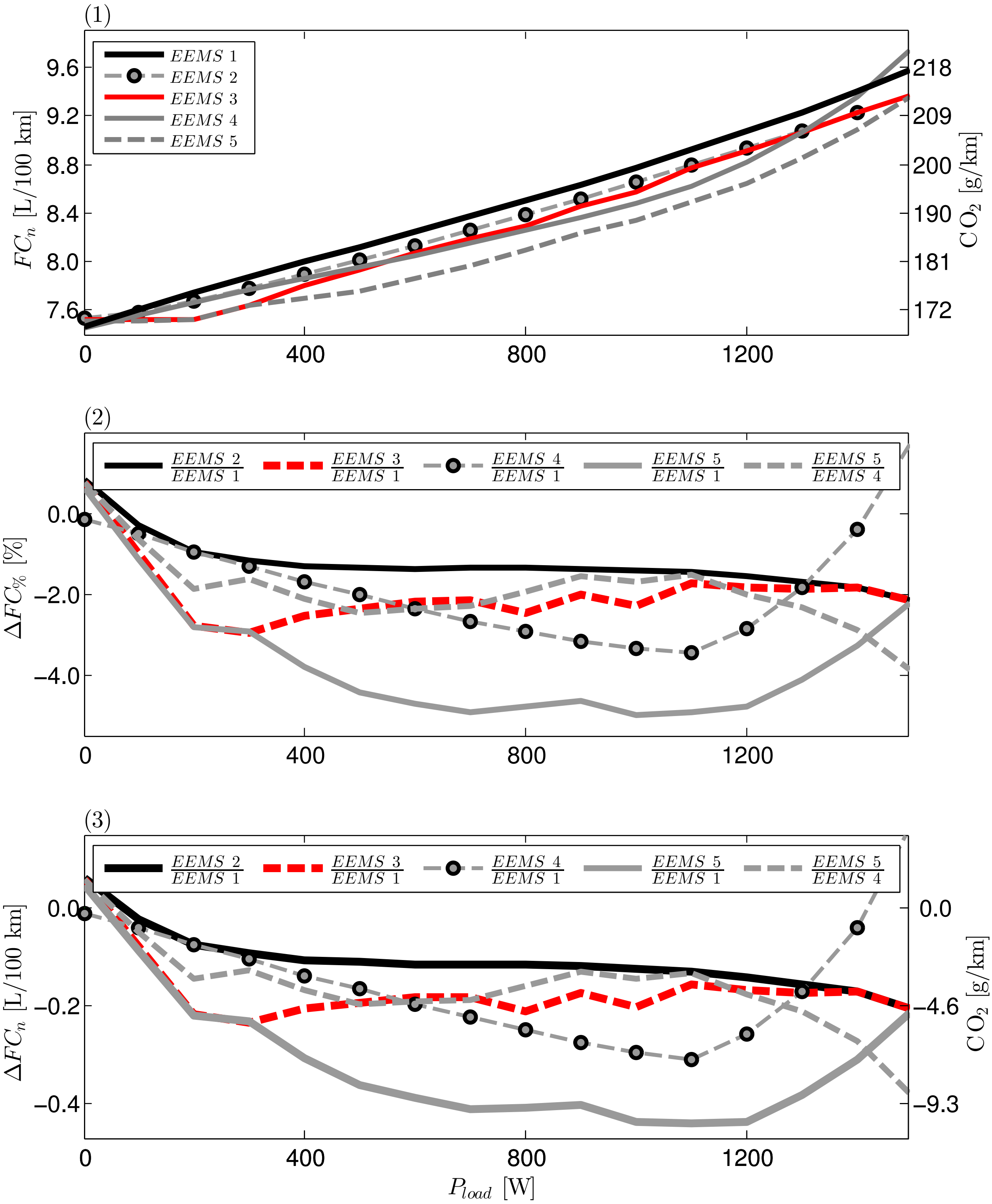

Figure 6.13.: Simulation results of fuel consumption depending on the load power for different EEMSs. In (1) the absolute fuel consumption FC_n normalized to 100 km is presented. In (2) the relative saved fuel consumption $\Delta FC_{\%}$ and in (3) the absolute saved fuel consumption ΔFC and the corresponding CO_2 values is presented.

	FC_n [L/100 km]				
P_{load} [W]	EEMS 1	EEMS 2	EEMS 3	EEMS 4	EEMS 5
0	7.47	7.53	7.53	7.46	7.51
100	7.60	7.58	7.53	7.56	7.51
200	7.74	7.67	7.53	7.67	7.52
300	7.87	7.78	7.64	7.77	7.64
400	8.00	7.90	7.80	7.87	7.70
500	8.12	8.01	7.93	7.96	7.76
600	8.25	8.13	8.07	8.05	7.86
700	8.37	8.26	8.19	8.15	7.96
800	8.50	8.39	8.29	8.25	8.09
900	8.64	8.52	8.46	8.36	8.23
1000	8.78	8.66	8.58	8.48	8.34
1100	8.93	8.80	8.77	8.62	8.49
1200	9.08	8.94	8.91	8.82	8.64
1300	9.23	9.08	9.06	9.06	8.85
1400	9.40	9.23	9.23	9.36	9.09
1500	9.59	9.39	9.38	9.77	9.38

Table 6.1.: Normalized fuel consuption FC_n in WLTC for different electrical energy management strategies.

of Figure 6.13 are plausible.

Results of EEMS 2 and EEMS 3

The integration of the TEG system leads to an additional fuel consumption of 0.06 L/100 km, which is caused by the weight of the TEG and the power for the additional cooling. To compensate this additional fuel consumption the TEG must recover approximately 100 W electric power. In the load range up to 200 W, the TEG can supply a significant part of the electrical load. Consequently, fossil fuel required to drive the alternator can be saved. At a power load above 200 W, the alternator can only offer a partial relief. Between 200 W and 1200 W, the fuel consumption increases with nearly the same gradient as for EEMS 1 since the maximal recoverable electrical power of the TEG is reached. In contrast to EEMS 1, the TEG prevents a full load of the alternator. Consequently, the fuel economy increases up to 2.12 % for power loads about 1200 W.

Furthermore, the results for EEMS 2 and EEMS 3 are significant different at a power load between 100 W and 1200 W. In this range, the EEMS 3 yields up to 2.96 % fuel economy in comparison to 1.45 % in EEMS 2. The significant higher fuel economy in EEMS 3 was reached through the deactivation of the alternator, by the switch S_{alt}. In contrast, the alternator is always active in EEMS 2.

Above 1200 W power load, the alternator must be continuously active in the drive cycle in order to supply the on-board power supply. Consequently, the alternator is only relieved when the TEMs generate power. The most electric power is generated at those operation points of the ICE where the additional fuel consumption of the alternator is minimal. This leads to a stagnation of the fuel economy for EEMS 2 and EEMS 3. In summary, EEMS 2 can save fuel up to 1.54 % for power loads between 100 W and 1200 W. This fuel economy corresponds to 0.13 L/100 km (3.2 $\mathrm{g\,km^{-1}}$ CO_2). By a fuel load of the alternator, the fuel economy increase up to 2.12 %, which corresponds to 0.20 L/100 km (4.6 $\mathrm{g\,km^{-1}}$ CO_2). In contrast, EEMS 3 can save fuel up to 2.96 % which corresponds to 0.23 L/100 km (5.4 $\mathrm{g\,km^{-1}}$ CO_2).

Results of EEMS 4

The strategy of the start-stop function is state of the art and useful for the low speed phase of the ICE and for power loads, which can be supported by the battery in this phase. Additionally, the alternator can preferably be activated in the engine brake phase because its drive energy does not effect the fuel consumption. With these mechanisms, up to 100 W electrical power can be recovered without a significant increase of the fuel consumption. However, for higher power loads, the fuel consumption of EEMS 4 converges continuously to EEMS 1 and increases beyond the consumption of EEMS 1 at 1400 W. The reason of this effect is that the battery is significantly discharged at higher power loads in the start-stop phase of the ICE. The alternator has to charge the battery after the start-stop phase, which causes a full load of the alternator. At full load, the alternator has the worst efficiency at a constant engine speed. Consequently, the brief discharge and recharge of the battery in case of a high power load results in a disproportionate increases of the drive torque and fuel consumption in relation to a continuous activation of the alternator.

However, in relation to EEMS 1, EEMS 4 can save up to 3.5 % fuel, which corresponds to 0.31 L/100 km (7.2 $\mathrm{g\,km^{-1}}$ CO_2). This positive effect to the fuel economy can be invert for high power loads, causes by the necessary drive power of the alternator to compensate the discharge energy of the battery in the start-stop phase.

Results of EEMS 5

The EEMS 5 is the combination of EEMS 3 and EEMS 4. For the on-board power supply, the start-stop function and engine brake recuperation can be used to supply up to 100 W electrical power. Above 100 W, the recovered electric energy from the TEG can additionally supply nearly 150 W of the load before the alternator must be used. Consequently, up to 250 W electrical power can be supplied without use of the alternator. As already pointed out in the results of EEMS 2 and EEMS 3, the fuel economy is almost stagnating for electric power loads between 600 W and 1200 W. Loads above 1200 W decrease fuel saving due to the negative effect of the start-stop function. In relation to EEMS 1, EEMS 5 can save up to 5 % fuel. This corresponds to 0.44 L/100 km (10.12 $\mathrm{g\,km^{-1}}$ CO_2).

6.4. Conclusions and Discussion

This chapter presented the fossil fuel consumption and potential fuel economy of an ICE with a TEG system which relieves the alternator. To simulate the on-board power supply, the alternator, the battery, the electric load, and the TEG system were modeled and characterized. The electric load was assumed as constant power load in the driver cycle.

The TEG system was modeled and simulated for the WLTC with the results of Chapter 5. Furthermore, the battery was modeled with a Thévenin model and the parameters were identified by measurements. In contrast, the alternator was measured and the characteristic map was determined with the measurement results.

The alternator is the primary power supply for a classic 12 V on-board power supply. The drive torque of the alternator results in load shifting of the ICE. With the efficiency map from Chapter 5, the additional fuel consumption for the current load shifting was analyzed. The results show that the ratio of the generated electric power to the additional fossil fuel has a minimum at the middle load and speed range of the ICE. In contrast, the TEG system also has the highest electric output magnitude also in this range. Consequently, the relive of the alternator by the TEG system causes only a marginal fuel economy.

This fact leads to the necessity to use an electric energy management system, which coordinates alternator, state of charge of the battery and TEG system. In comparison to an optimized management system with a maximum fuel economy of 2.96 %, the system without a management system reaches only 1.45 % for power loads up to 1200 W. At full load of the alternator, the relive of the alternator through the TEG system can save up to 2.12 % fuel.

An alternative to the use of TEGs is the use of the start-stop function and the braking energy recuperation. When compared to the TEG system, the start-stop function and the braking energy recuperation has almost the same effect on the additional fossil fuel consumption. In both cases, up to 100 W can be supplied without a significant increase of the fuel consumption. However, in the start-stop phase, the current stress of the battery increases proportionally with the power load. This must be compensated through high loads of the alternator which cause a significant increase in the fuel consumption.

The combination of the TEG system, the start-stop function, and the braking engine recuperation leads to fuel economy by up to 5 %. However, only the TEG has a positive effect on the fuel consumption whenever the start-stop function and the braking energy recuperation cannot supply the power consumption of the load.

In summary, the simulation results show that the TEG system can save fossil fuel by up to 2.96 %. This value depends on the recovered mean power of the TEG system and the power load from the on-board power supply. In relation to explicit energy consumption, the TEG system can be adapted (size, material, electric power) to the desired on-board power system. However, simple and low-cost mechanisms like start-stop function can be directly used to reduce the additional fossil fuel consumption from the alternator. Furthermore, those mechanisms are limited by the current stress of the battery and the alternator. Consequently, the break-even point of a TEG system can be shifted to higher loads by a smart energy grid. Hence, the combination of the TEG system, the start-stop, and the braking energy recuperation reach a significant fuel economy between 4 % and 5 % for a wide electric power load range.

7. Conclusions and Future Work

The aim of this thesis was to analyze and optimize the electrical functional chain of a TEG for the waste heat recovery in an automobile. In this context, the required components were modeled, analyzed, and optimized.

The electrical interface between a TEM and an on-board power supply is a DC-DC converter. In relation to the presented requirement criteria, the buck-boost, the boost-buck, the Ćuk, and the SEPIC converters were studied. To estimate the efficiency of the converter, a model which includes the dynamic and static losses of the electric circuit was derived. The parametrization of this model was performed with characteristics received from data sheets in order to avoid extensive measurements. By means of the model, individual losses in relation to the nominal input and output power, components, and the switching frequency were analyzed.

The TEMs are dependent of the temperature gradient from the application or the specific thermoelectric characteristics and the electrical characteristic of TEMs are difficult to generalize.

Therefor, the mean efficiency of the DC-DC converters was selected for the evaluation of different converter topologies, which can be used for TEMs. With the mean efficiency, the converter topologies can be easier compared.

In comparison to other DC-DC topologies, the boost-buck converter has the highest mean efficiency. Furthermore, the loss model was verified by the measurements at the developed boost-buck converter prototype. The results revealed a consistency between the measurements and the model. Additionally, the presented loss model of the converter can used as a guideline in designing the electrical parameters of DC-DC converters.

The maximum power point of the TEM needed to be tracked for the application in an exhaust gas system. Therefore, a P&O MPPT algorithm was implemented, which is based on a digital control of the boost-buck converter. An additional feedback controller was implemented in order to regulate the trickle charge of the battery once the charge voltage is reached. Based on the analytical model of the converter, the control parameters were designed to satisfy the requirement of stability for all operation points for the desired power range of the TEM. The adaptive control concept is one approach to compensates automatically parameter variations of the TEM. An experiment, with an adaptive current controller in the control concept of the DC-DC converter, confirmed this approach.

However, this method could not have been fully implemented due to limited computing capacity of the used microcontroller. An alternative successful approach is to design control parameters for those operating points at which the disturbances show the highest sensitivity to the closed-loop control stability of

the controller. Detailed analyses confirmed the stability and robustness of the control loops for the entire possible range of the TEG performance.
The selected cascade control structure allowed to control the voltage amplitude between the boost and the buck converter. The loss of the converter was reduced significantly by the adaption of the reference value from the this voltage.
Different experiments and measurements verify the developed and designed control. The designed boost-buck converter prototype reached an efficiency up to 98.1 %.

The interconnection between TEMs and DC-DC converter is an important aspect, which influence the electrical efficiency of the TEG system for temperature changes across the TEMs. The temperature distribution of waste heat results in a nonlinearity between individual TEMs. This means that the individuals TEMs have significantly different operation points, where the output of the modules is maximal. A neglect of this behavior by the wiring of the TEMs results in power loss in this interconnection. An evolutionary algorithm was used to optimize the wiring of the TEM with the aim to minimize the loss of the interconnection between the TEMs and the DC-DC converter. Therefore, a series connection of the TEMs was preferred over a parallel connection since the Joule heating loss is lower.
The analysis of the alternator showed that the lowest fuel consumption per watt is reached at middle speeds and torques of the ICE. At these operating points, the TEG supports the highest electrical power. The existing energy management system of the electrical system was adapted for integration using an optimization algorithm. Otherwise, the recovered power from the TEG might not be used or stored. For simulations, the necessary components of a classical 12 V on-board power supply were modeled and measured. Simulation results showed that the TEG with an average power of nearly 200 W saved fuel up to 0.2 L/100 km (4.6 $\mathrm{g\,km^{-1}}$ CO_2). An optimized electrical energy management, which combined the TEG with a star-stop and break energy recuperation function, saved fuel up to 0.44 L/100 km (10.12 $\mathrm{g\,km^{-1}}$ CO_2). The efficiency of the alternator, the electric energy requirement of the vehicle, and the weight of the TEG essentially determine the savings potential. The TEG can only save as much CO_2 as the ICE consumes to drive the alternator, which supplies the necessary electrical power.

The following research topics regarding the electrical integration of a TEG are proposed:

MPPT

The performance of the MPPT and the control structure is designed to track the MPP from the TEMs with an optimal accuracy. The measurement noise and disturbances of the sensor result in a mismatch of the maximum power. An adapted signal filtering or the use of predictive estimation algorithms, such as Kalman filter, should be studied to improve the signal quality. Furthermore, alternative MPPT algorithms which only use the voltage or current signals, like the fractional open circuit, offer possibilities to reduce the number of necessary sensors.

Active wiring network

At a series connection of TEMs, a defective module could lead to a total failure. By using a switching network, it is possible to configure the internal wiring of the TEMs for a DC-DC converter. Additionally, a switching network allows an adaptive optimization of the wiring without a previous knowledge of the electrical states of the TEMs and the temperature of the waste heat. This advantage must be compared to the technical complexity and energy consumption.

Optimization of electric efficiency

The developed boost-buck converter is a prototype. The loss model showed that the DC loss is the dominant loss in a DC-DC converter. An optimization of the semiconductors and the PCB layout should be studied to decrease the ohmic loss and, consequently, to increase the power efficiency of a DC-DC converter. Additionally, the use of a common core of an inductive or a snubber network for the MOSFETs could minimize the loss.

Economic efficiency

The costs of a TEG, including the DC-DC converter, is the decisive factor for industrial applications. Simplification of the presented control structure reduces the technical requirements for the sensors and the microcontroller. There is also the question of which power range should be selected in order to design a converter with regards to an economic criterion. The DC-DC converters with lower power range can be flexibly used for different applications, but it would increase the number of required converters.

Bibliography

[1] M. O. Abdullah, I. A. W. Tan, and L. S. Lim. Automobile adsorption air-conditioning system using oil palm biomass-based activated carbon: A review. *Renewable and Sustainable Energy Reviews*, 15(4):2061 – 2072, May 2011.

[2] K. Ahn, K. Biswas, J. He, I. Chung, V. Dravid, and M. G. Kanatzidis. Enhanced thermoelectric properties of p-type nanostructured PbTe-MTe (M = Cd, Hg) materials. *Energy & Environmental Science*, 6(5):1529 – 1537, Apr. 2013.

[3] M. Albach, T. Durbaum, and A. Brockmeyer. Calculating core losses in transformers for arbitrary magnetizing currents a comparison of different approaches. In *27th Annual IEEE Power Electronics Specialists Conference, 1996. PESC '96 Record*, volume 2, pages 1463 – 1468, June 1996.

[4] A. Altowati, T. Suntio, and K. Zenger. Input filter interactions in multi-module parallel switching-mode power supplies. In *IEEE International Conference on Industrial Technology, 2005. ICIT 2005*, pages 851 – 856, Dec. 2005.

[5] L. Anatychuk. On the discovery of thermoelectricity by Volta. *Journal of Thermoelectricity*, (2):5 – 11, 2004.

[6] K. J. Aström and B. Wittenmark. *Computer-Controlled Systems: Theory and Design*. Prentice Hall, Upper Saddle River, N.J, 3rd edition, Nov. 1996.

[7] K. J. Aström and B. Wittenmark. *Adaptive Control*. Dover Publications, 2008.

[8] T. Back, U. Hammel, and H.-P. Schwefel. Evolutionary computation: comments on the history and current state. *IEEE Transactions on Evolutionary Computation*, 1(1):3 – 17, Apr. 1997.

[9] L. Balogh. Design and application guide for high speed mosfet gate drive circuits. Application Note Slup169, Texas Instuments, 2001.

[10] R. C. Bansal. Optimization Methods for Electric Power Systems: An Overview. *International Journal of Emerging Electric Power Systems*, 2(1), Mar. 2005.

[11] J. C. Bass, N. B. Elsner, and F. A. Leavitt. Performance of the 1 kW thermoelectric generator for diesel engines. In *AIP Conference Proceedings*, volume 316, pages 295 – 298. AIP Publishing, Aug. 1994.

[12] S. Büchner. *Energiemanagement-Strategien für elektrische Energiebordnetze in Kraftfahrzeugen*. PhD thesis, Technische Universität Dresden, 2008.

[13] G. Bertotti. Physical interpretation of eddy current losses in ferromagnetic materials. I. Theoretical considerations. *Journal of Applied Physics*, 57(6):2110 – 2117, Mar. 1985.

[14] D. Biel, F. Guinjoan, E. Fossas, and J. Chavarria. Sliding-mode control design of a boost-buck switching converter for AC signal generation. *IEEE Transactions on Circuits and Systems I: Regular Papers*, 51(8):1539 – 1551, Aug. 2004.

[15] Bosch Robert GmbH. *Automotive Handbook*. Wiley, Plochingen, 8th edition, May 2011.

[16] E. K. Boukas and Z. K. Liu. Robust Stability and H-∞ Control of Discrete-Time Jump Linear Systems With Time-Delay: An LMI Approach. *Journal of Dynamic Systems, Measurement, and Control*, 125(2):271 – 277, June 2003.

[17] W. Boyes. *Instrumentation Reference Book*. Butterworth-Heinemann, Nov. 2009.

[18] S. Chattopadhyay and S. Das. A Digital Current-Mode Control Technique for DC DC Converters. *IEEE Transactions on Power Electronics*, 21(6):1718 – 1726, Nov. 2006.

[19] H. Chen, D. Y. Goswami, and E. K. Stefanakos. A review of thermodynamic cycles and working fluids for the conversion of low-grade heat. *Renewable and Sustainable Energy Reviews*, 14(9):3059 – 3067, Dec. 2010.

[20] J. Chen, D. Maksimovic, and R. Erickson. A new low-stress buck-boost converter for universal-input PPC applications. In *Applied Power Electronics Conference and Exposition, 2001. APEC 2001*, pages 343 – 349. IEEE, 2001.

[21] J. Chen, D. Maksimovic, and R. Erickson. Buck-boost PWM converters having two independently controlled switches. In *Power Electronics Specialists Conference, 2001. PESC*, volume 2, pages 736 – 741. IEEE, 2001.

[22] J. Chen, D. Maksimovic, and R. W. Erickson. Analysis and design of a low-stress buck-boost converter in universal-input PFC applications. *IEEE Transactions on Power Electronics*, 21(2):320 – 329, Mar. 2006.

[23] J. Chen, Z. Yan, and L. Wu. The influence of Thomson effect on the maximum power output and maximum efficiency of a thermoelectric generator. *Journal of Applied Physics*, 79(11):8823 – 8828, June 1996.

[24] M. Chen. Adaptive Removal and Revival of Underheated Thermoelectric Generation Modules. *IEEE Transactions on Industrial Electronics*, 61(11):6100 – 6107, Nov. 2014.

[25] M. Chen and G. Rincon-Mora. Accurate electrical battery model capable of predicting runtime and I-V performance. *IEEE Transactions on Energy Conversion*, 21(2):504 – 511, June 2006.

[26] B. H. Cho, H. Bae, and J. Lee. Review of current mode control schemes and introduction of a new digital current mode control method for the parallel module DC-DC converters. In *Power Electronics and Motion Control Conference, 2009. IPEMC '09. IEEE 6th International*, pages 202 – 210, May 2009.

[27] S. Cho, N. Kim, S. Park, and S. Kim. A coreless maximum power point tracking circuit of thermoelectric generators for battery charging systems. In *Solid State Circuits Conference (A-SSCC), 2010 IEEE Asian*, pages 1 – 4. IEEE, Nov. 2010.

[28] T. Christ. *Rekuperation in elektrischen Energiebordnetzen von Kraftfahrzeugen*. PhD thesis, Technische Universität Berlin, 2006.

[29] L. O. Chua. *Linear and Nonlinear Circuits*. Mcgraw-Hill College, New York, 1st edition, Mar. 1987.

[30] H. Chung, F. N. K. Poon, C. Liu, and M. Pong. Analysis of buck-boost converter inductor loss using a simple online B-H curve tracer. In *Fifteenth Annual IEEE Applied Power Electronics Conference and Exposition, 2000. APEC 2000*, volume 2, pages 640 – 646, 2000.

[31] F. Codeca, S. Savaresi, and G. Rizzoni. On battery State of Charge estimation: A new mixed algorithm. In *IEEE International Conference on Control Applications, 2008. CCA 2008*, pages 102 – 107, Sept. 2008.

[32] J. C. Conklin and J. P. Szybist. A highly efficient six-stroke internal combustion engine cycle with water injection for in-cylinder exhaust heat recovery. *Energy*, 35(4):1658 – 1664, Apr. 2010.

[33] D. J. Costinett. *Analysis and Design of High Efficiency, High Conversion Ratio, DC-DC Power Converters*. PhD thesis, University of Colorado, 2013.

[34] J. Creveling. Means for utilizing waste energy., Nov. 1914. US Patent 1118269 A.

[35] S. Ćuk. *Modelling, analysis, and design of switching converters*. PhD thesis, California Institute of Technology, 1977.

[36] S. Dalola, M. Ferrari, V. Ferrari, M. Guizzetti, D. Marioli, and A. Taroni. Characterization of Thermoelectric Modules for Powering Autonomous Sensors. *IEEE Transactions on Instrumentation and Measurement*, 58(1):99 – 107, Jan. 2009.

[37] A. Davoudi, J. Jatskevich, and T. De Rybel. Numerical state-space average-value modeling of PWM DC-DC converters operating in DCM and CCM. *IEEE Transactions on Power Electronics*, 21(4):1003 – 1012, July 2006.

[38] A. Domingues, H. Santos, and M. Costa. Analysis of vehicle exhaust waste heat recovery potential using a Rankine cycle. *Energy*, 49:71 – 85, Jan. 2013.

[39] E. Duran, M. Sidrach-de Cardona, J. Galan, and J. M. Andujar. Comparative analysis of buck-boost converters used to obtain I-V characteristic curves of photovoltaic modules. In *Power Electronics Specialists Conference, 2008. PESC 2008*, pages 2036 – 2042. IEEE, June 2008.

[40] J. Eakburanawat and I. Boonyaroonate. Development of a thermoelectric battery-charger with microcontroller-based maximum power point tracking technique. *Applied Energy*, 83(7):687 – 704, July 2006.

[41] W. A. T. Eberle. *Mosfet Current Source Gate Drivers, Switching Loss Modeling and Frequency Dithering Control for MHz Switching Frequency DC-DC Converters*. PhD thesis, Queen's University Kingston, Ontario, 2008.

[42] A. Eder and J. Fröschl. Integration of a Thermoelectric Generator into the On-board Vehicle Electrical Systems. In *IAV - Sympsoium - Symposium Steuerungssysteme für automobile Antriebe*, 2009.

[43] H. El Fadil and F. Giri. Backstepping Based Control of PWM DC-DC Boost Power Converters. In *IEEE International Symposium on Industrial Electronics, 2007. ISIE 2007*, pages 395 – 400, June 2007.

[44] R. W. Erickson and D. Maksimovic. *Fundamentals of Power Electronics*. Springer, 2nd edition, Jan. 2001.

[45] T. Esram and P. Chapman. Comparison of Photovoltaic Array Maximum Power Point Tracking Techniques. *IEEE Transactions on Energy Conversion*, 22(2):439 – 449, June 2007.

[46] P. M. Felix Antritter. Flatness-Based Control of a Buck-Converter Driven DC Motor. In *4th IFAC Symposium on Mechatronic Systems (2006)*, pages 36 – 41, 2006.

[47] J. Fu, J. Liu, Y. Yang, C. Ren, and G. Zhu. A new approach for exhaust energy recovery of internal combustion engine: Steam turbocharging. *Applied Thermal Engineering*, 52(1):150 – 159, Apr. 2013.

[48] Y. Gelbstein, Z. Dashevsky, and M. P. Dariel. High performance n-type PbTe-based materials for thermoelectric applications. *Physica B: Condensed Matter*, 363(1-4):196 – 205, June 2005.

[49] H. J. Goldsmid. *Introduction to Thermoelectricity*. Springer, Mar. 2012.

[50] G. C. Goodwin, S. Greabe, and M. Salgado. *Control System Design*. Addison Wesley Pub Co Inc, Upper Saddle River, N.J., Dec. 2000.

[51] M. Hallworth and S. Shirsavar. Microcontroller-Based Peak Current Mode Control Using Digital Slope Compensation. *IEEE Transactions on Power Electronics*, 27(7):3340 – 3351, July 2012.

[52] M. Hamid Elsheikh, D. A. Shnawah, M. F. M. Sabri, S. B. M. Said, M. Haji Hassan, M. B. Ali Bashir, and M. Mohamad. A review on thermoelectric renewable energy: Principle parameters that affect their performance. *Renewable and Sustainable Energy Reviews*, 30:337 – 355, Feb. 2014.

[53] M. Hankaniemi. *Dynamical Profile of Switched-Mode Converter - Fact or Fiction*. PhD thesis, Tampere University of Technology, 2007.

[54] J. G. Hawley, C. D. Bannister, C. J. Brace, S. Akehurst, I. Pegg, and M. R. Avery. The effect of engine and transmission oil viscometrics on vehicle fuel consumption. *Proceedings of the Institution of Mechanical Engineers, Part D: Journal of Automobile Engineering*, 224(9):1213 – 1228, Sept. 2010.

[55] U. Hopmann and M. C. Algrain. Diesel Engine Electric Turbo Compound Technology. SAE Technical Paper 2003-01-2294, Warrendale, PA, June 2003.

[56] Y. Huleihel, A. Cervera, and S. Ben-Yaakov. A high gain DC-DC converter for energy harvesting of thermal waste by thermoelectric generators. In *2012 IEEE 27th Convention of Electrical Electronics Engineers in Israel (IEEEI)*, pages 1 – 5, Nov. 2012.

[57] IAV GmbH. Thermoelectric Generator 2020. http://www.teg2020.com/de/projekt/teg-demonstrator/, Dec. 2014.

[58] A. F. Ioffe. *Semiconductor Thermoelements and Thermoelectric Cooling*. Pion Ltd, Dec. 1958.

[59] J. Jadhao and D. Thombare. Review on Exhaust Gas Heat Recovery for I.C. Engine. *International Journal of Engineering and Innovative Technology*, 12(2):93 – 100, 2013.

[60] S. Jain and V. Agarwal. A new algorithm for rapid tracking of approximate maximum power point in photovoltaic systems. *IEEE Power Electronics Letters*, 2(1):16 – 19, Mar. 2004.

[61] T. A. Johansen, K. J. Hunt, P. J. Gawthrop, and H. Fritz. Off-equilibrium linearisation and design of gain-scheduled control with application to vehicle speed control. *Control Engineering Practice*, 6(2):167 – 180, Feb. 1998.

[62] M. M. Jovanovic. Power supply technology-past, present, and future. In *Power Conversion and Intelligent Motion China Conference for Power Electronics (PCIM China)*, pages 3 – 15, Shanghai, 2007.

[63] J. Kassakian, J. Miller, and N. Traub. Automotive electronics power up. *IEEE Spectrum*, 37(5):34 – 39, 2000.

[64] M. K. Kazimierczuk. *Pulse-width Modulated DC-DC Power Converters*. Wiley, 1st edition, Oct. 2008.

[65] M. K. Kazimierczuk. *High-Frequency Magnetic Components*. John Wiley & Sons, Oct. 2013.

[66] H. K. Khalil. *Nonlinear Systems*. Prentice Hall PTR, 2002.

[67] R. Kühn, O. Koeppen, and J. Kitte. Influence of an Optimized Thermoelectric Generator on the Back Pressure of the Subsequent Exhaust Gas System of a Vehicle. *Journal of Electronic Materials*, 43(6):1521 – 1526, June 2014.

[68] R. Kühn, O. Koeppen, P. Schulze, and D. Jänsch. Comparison between a Plate and a Tube Bundle Geometry of a Simulated Thermoelectric Generator in the Exhaust Gas System of a Vehicle. *Materials Today: Proceedings*, 2(2):761 – 769, 2015.

[69] H. Kiehne. *Battery Technology Handbook*. CRC Press, 2nd edition, Aug. 2003.

[70] R.-Y. Kim. *Improved Renewable Energy Power System using a Generalized Control Structure for Two-Stage Power Converters*. PhD thesis, Virginia State University, 2009.

[71] R.-Y. Kim and J.-S. Lai. A Seamless Mode Transfer Maximum Power Point Tracking Controller for Thermoelectric Generator Applications. In *Conference Record of the 2007 IEEE Industry Applications Conference, 2007. 42nd IAS Annual Meeting*, pages 977 – 984. IEEE, Sept. 2007.

[72] R.-Y. Kim and J.-S. Lai. A Seamless Mode Transfer Maximum Power Point Tracking Controller For Thermoelectric Generator Applications. *IEEE Transactions on Power Electronics*, 23(5):2310 – 2318, Sept. 2008.

[73] R.-Y. Kim and J.-S. Lai. Aggregated modeling and control of a boost-buck cascade converter for maximum power point tracking of a thermoelectric generator. In *Twenty-Third Annual IEEE Applied Power Electronics Conference and Exposition, 2008. APEC 2008*, pages 1754 – 1760. IEEE, Feb. 2008.

[74] R.-Y. Kim, J.-S. Lai, B. York, and A. Koran. Analysis and Design of Maximum Power Point Tracking Scheme for Thermoelectric Battery Energy Storage System. *IEEE Transactions on Industrial Electronics*, 56(9):3709 – 3716, Sept. 2009.

[75] S. Kim, S. Park, S. Kim, and S.-H. Rhi. A Thermoelectric Generator Using Engine Coolant for Light-Duty Internal Combustion Engine-Powered Vehicles. *Journal of Electronic Materials*, 40(5):812 – 816, May 2011.

[76] J. Kimball and P. Krein. Analysis and design of switched capacitor converters. In *Twentieth Annual IEEE Applied Power Electronics Conference and Exposition, 2005. APEC 2005*, volume 3, pages 1473 – 1477, 2005.

[77] J. Kitte, F. Beck, and D. Jänsch. The Virtual Continuous TEG Model: Efficient Optimization of Thermogenerators. *Journal of Electronic Materials*, 42(7):2257 – 2268, July 2013.

[78] J. Klein. Synchronous buck MOSFET loss calculations with Excel model. Applicaton AN-6005, Fairchild Semiconductor, Apr. 2006.

[79] A. Krings and J. Soulard. Overview and Comparison of Iron Loss Models for Electrical Machines. *Journal of Electrical Engineering*, 10(3):162 – 169, 2010.

[80] S. Kumar, S. D. Heister, X. Xu, J. R. Salvador, and G. P. Meisner. Thermoelectric Generators for Automotive Waste Heat Recovery Systems Part I: Numerical Modeling and Baseline Model Analysis. *Journal of Electronic Materials*, 42(4):665 – 674, Apr. 2013.

[81] S. Kumar, S. D. Heister, X. Xu, J. R. Salvador, and G. P. Meisner. Thermoelectric Generators for Automotive Waste Heat Recovery Systems Part II: Parametric Evaluation and Topological Studies. *Journal of Electronic Materials*, 42(6):944 – 955, June 2013.

[82] M. J. Kurtz and M. A. Henson. Feedback linearizing control of discrete-time nonlinear systems with input constraints. *International Journal of Control*, 70(4):603 – 616, 1998.

[83] M. A. Lambert and B. J. Jones. Automotive Adsorption Air Conditioner Powered by Exhaust Heat. Part 1: Conceptual and Embodiment Design. 220(7):959 – 972, July 2006.

[84] I. D. Landau and A. Karimi. Recursive algorithms for identification in closed loop: A unified approach and evaluation. *Automatica*, 33(8):1499 – 1523, Aug. 1997.

[85] I. D. Landau, R. Lozano, M. M'Saad, and A. Karimi. *Adaptive Control: Algorithms, Analysis and Applications*. Springer, London ; New York, 2nd edition, June 2011.

[86] I. D. Landau and G. Zito. *Digital Control Systems: Design, Identification and Implementation*. Springer, May 2007.

[87] F. J. G. Landgraf, J. Teixeira, M. Emura, M. F. de Campos, and C. Muranaka. Separating Components of the Hysteresis Loss of Non-Oriented Electrical Steels. 302-303:440 – 445, 1999.

[88] A. Legros, L. Guillaume, M. Diny, H. Zaïdi, and V. Lemort. Comparison and Impact of Waste Heat Recovery Technologies on Passenger Car Fuel Consumption in a Normalized Driving Cycle. *Energies*, 7(8):5273 – 5290, Aug. 2014.

[89] M. Li, S. Xu, Q. Chen, and L.-R. Zheng. Thermoelectric-Generator-Based DC-DC Conversion Networks for Automotive Applications. *Journal of Electronic Materials*, 40(5):1136 – 1143, Mar. 2011.

[90] D. Liebal, P. Vijayraghavan, and N. Sreenath. Control of DC-DC buck-boost converter using exact linearization techniques. In *, 24th Annual IEEE Power Electronics Specialists Conference, 1993. PESC '93 Record*, pages 203 – 207, June 1993.

[91] J. Liebl, M. Lederer, K. Rohde-Brandenburger, J.-W. Biermann, M. Roth, and H. Schäfer. *Energiemanagement im Kraftfahrzeug: Optimierung von CO2-Emissionen und Verbrauch konventioneller und elektrifizierter Automobile*. Springer Vieweg, Wiesbaden, Oct. 2014.

[92] F. Liu, S. Duan, F. Liu, B. Liu, and Y. Kang. A Variable Step Size INC MPPT Method for PV Systems. *IEEE Transactions on Industrial Electronics*, 55(7):2622 – 2628, July 2008.

[93] Y.-F. Liu and X. Liu. Recent developments in digital control strategies for DC/DC switching power converters. In *Power Electronics and Motion Control Conference, 2009. IPEMC '09. IEEE 6th International*, pages 307 – 314, May 2009.

[94] M. Lunanova. *Optimierung von Nebenaggregaten: Maßnahmen zur Senkung der CO2-Emission von Kraftfahrzeugen*. Vieweg+Teubner Verlag, Wiesbaden, Jan. 2009.

[95] J. Mahdavi, A. Emadi, and H. A. Toliyat. Application of state space averaging method to sliding mode control of PWM DC/DC converters. In *Conference Record of the 1997 IEEE Industry Applications Conference, 1997. Thirty-Second IAS Annual Meeting, IAS '97*, volume 2, pages 820 – 827. IEEE, Oct. 1997.

[96] E. A. Man, E. Schaltz, and L. Rosendahl. Thermoelectric Generator Power Converter System Configurations: A Review. In A. Amaldi and F. Tang, editors, *Proceedings of the 11th European Conference on Thermoelectrics*, pages 151 – 166. Springer International Publishing, Jan. 2014.

[97] A. A. Manzela, S. M. Hanriot, L. Cabezas-Gómez, and J. R. Sodré. Using engine exhaust gas as energy source for an absorption refrigeration system. *Applied Energy*, 87(4):1141 – 1148, Apr. 2010.

[98] H. Mao, L. Yao, C. Wang, and I. Batarseh. Analysis of Inductor Current Sharing in Nonisolated and Isolated Multiphase DC-DC Converters. *IEEE Transactions on Industrial Electronics*, 54(6):3379 – 3388, Dec. 2007.

[99] S. Mappus. Optimizing MOSFET Characteristics by Adjusting Gate Drive Amplitude. Application Report SLUA341, Texas Instuments, 2005.

[100] A. Martínez, J. G. Vián, D. Astrain, A. Rodríguez, and I. Berrio. Optimization of the Heat Exchangers of a Thermoelectric Generation System. *Journal of Electronic Materials*, 39(9):1463 – 1468, Sept. 2010.

[101] P. Mayer and R. Ram. Optimization of Heat Sink-Limited Thermoelectric Generators. *Nanoscale and Microscale Thermophysical Engineering*, 10(2):143 – 155, July 2006.

[102] B. Mazar. *Gesamtsystemoptimierung eines thermoelektrischen Generators für eine Fahrzeuggruppe*. PhD thesis, Technische Universität Dresden, Feb. 2011.

[103] G. Meisner. Skutterudite thermoelectric generator for automotive waste heat recovery. 3rd Thermoelectrics applications workshop. Baltimore, MD: US Department of Energy, 2012.

[104] T. Meyer. *DC/DC-Wandler mit kleiner Eingangsspannung für photovoltaische elektrochemische und thermoelektrische Zellen*. VDI-Verlag GmbH, 2000.

[105] R. D. Middlebrook and S. Cuk. A general unified approach to modelling switching-converter power stages. In *Power Electronics Specialists Conference*, pages 18 – 34, 1976.

[106] N. Mohan, T. M. Undeland, and W. P. Robbins. *Power electronics: converters, applications, and design*. John Wiley & Sons, 2003.

[107] A. Montecucco. *Efficiently maximising power generation from thermoelectric generators*. PhD thesis, University of Glasgow, 2014.

[108] A. Montecucco, J. R. Buckle, and A. R. Knox. Solution to the 1-D unsteady heat conduction equation with internal Joule heat generation for thermoelectric devices. *Applied Thermal Engineering*, 35:177 – 184, Mar. 2012.

[109] A. Montecucco and A. Knox. Maximum Power Point Tracking Converter Based on the Open-Circuit Voltage Method for Thermoelectric Generators. *IEEE Transactions on Power Electronics*, 30(2):828 – 839, Feb. 2015.

[110] A. Montecucco, J. Siviter, and A. Knox. Simple, fast and accurate maximum power point tracking converter for thermoelectric generators. In *2012 IEEE Energy Conversion Congress and Exposition (ECCE)*, pages 2777 – 2783, Sept. 2012.

[111] A. Montecucco, J. Siviter, and A. R. Knox. The effect of temperature mismatch on thermoelectric generators electrically connected in series and parallel. *Applied Energy*, 123:47 – 54, June 2014.

[112] C. Moslacher and O. Guillemant. Improving Efficiency of Synchronous Rectification by Analysis of the MOSFET Power Loss Mechanism. Application Note AN 2012-03, Infineon Technologies, Mar. 2012.

[113] M. Mu. *High Frequency Magnetic Core Loss Study*. PhD thesis, Virginia Polytechnic Institute and State University, 2013.

[114] J. Muhlethaler, J. Biela, J. Kolar, and A. Ecklebe. Improved core loss calculation for magnetic components employed in power electronic system. In *2011 Twenty-Sixth Annual IEEE Applied Power Electronics Conference and Exposition (APEC)*, pages 1729 – 1736, Mar. 2011.

[115] J. Nachtrab. *Herstellung thermoelektrischer Generatoren mit textilen Methoden*. Shaker, Herzogenrath, Dec. 2013.

[116] H. Nagayoshi, T. Nakabayashi, H. Maiwa, and T. Kajikawa. Development of 100-W High-Efficiency MPPT Power Conditioner and Evaluation of TEG System with Battery Load. *Journal of Electronic Materials*, 40(5):657 – 661, May 2011.

[117] A. B. Neild. Portable Thermoelectric Generators. SAE Technical Paper 630019, Warrendale, PA, Jan. 1963.

[118] A. B. Neild. Thermoelectric Generators for Military Portable Power. SAE Technical Paper 670452, Warrendale, PA, Feb. 1967.

[119] O. Nelles. *Nonlinear System Identification: From Classical Approaches to Neural Networks and Fuzzy Models*. Springer, Jan. 2001.

[120] J. Neubert. Powering up [42 V automotive electronics]. *IEE Review*, 46(5):21 – 25, 2000.

[121] L.-X. Ni, K. Sun, H.-f. Wu, Z. Chen, and Y. Xing. A high efficiency step-up DC-DC converter for thermoelectric generator with wide input voltage range. In *2012 IEEE International Symposium on Industrial Electronics (ISIE)*, pages 52 – 57, May 2012.

[122] L.-X. Ni, K. Sun, L. Zhang, Y. Xing, M. Chen, and L. Rosendahl. A power conditioning system for thermoelectric generator based on interleaved Boost converter with MPPT control. In *2011 International Conference on Electrical Machines and Systems (ICEMS)*, pages 1 – 6, Aug. 2011.

[123] C. Nizzola. *Modellierung und Verbrauchsoptimierung von ottomotorischen Antriebskonzepten*. PhD thesis, Eidgenössische Technische Hochschule, Zürich, 2000.

[124] G. S. Nolas, J. Sharp, and J. Goldsmid. *Thermoelectrics: Basic Principles and New Materials Developments*. Springer, Berlin ; New York, June 2001.

[125] V. Pandiyarajan, M. Chinna Pandian, E. Malan, R. Velraj, and R. V. Seeniraj. Experimental investigation on heat recovery from diesel engine exhaust using finned shell and tube heat exchanger and thermal storage system. *Applied Energy*, 88(1):77 – 87, Jan. 2011.

[126] R. Pelster, I. Hüttl, and R. Pieper. Thermospannungen - viel genutzt und fast immer falsch erklärt. *PhyDid A - Physik und Didaktik in Schule und Hochschule*, 1(4):10 – 22, Jan. 2005.

[127] F. Peng, F. Zhang, and Z. Qian. A novel compact DC-DC converter for 42 V systems. In *Power Electronics Specialist Conference, 2003. PESC '03. 2003 IEEE 34th Annual*, volume 1, pages 33 – 38, 2003.

[128] F. Z. Peng, F. Zhang, and Z. Qian. A magnetic-less DC-DC converter for dual-voltage automotive systems. volume 39, pages 511 – 518, 2003.

[129] D. J. Perreault and V. Caliskan. Automotive power generation and control. *IEEE Transactions on Power Electronics*, 19(3):618 – 630, May 2004.

[130] D. Petitjean, L. Bernardini, C. Middlemass, and S. M. Shahed. Advanced Gasoline Engine Turbocharging Technology for Fuel Economy Improvements. SAE Technical Paper 2004-01-0988, Warrendale, PA, Mar. 2004.

[131] D. Polenov. *DC-DC-Wandler zur Einbindung von Doppelschichtkondensatoren in das Fahrzeugenergiebordnetz*. PhD thesis, 2010.

[132] H. Qiao, Y. Zhang, Y. Yao, and L. Wei. Analysis of Buck-Boost Converters for Fuel Cell Electric Vehicles. pages 109 – 113. IEEE, Dec. 2006.

[133] T. B. Reddy and D. Linden. *Linden's handbook of batteries*. McGraw-Hill, New York, NY, 4th edition, 2011.

[134] W. Reimann and R. Männel. Verbrauchseinfluss der elektrischen Energie im Fahrzeug. *ATZelektronik*, 3(1):6 – 11, Feb. 2008.

[135] J. Reinert, A. Brockmeyer, and R. De Doncker. Calculation of losses in ferro- and ferrimagnetic materials based on the modified Steinmetz equation. *IEEE Transactions on Industry Applications*, 37(4):1055 – 1061, July 2001.

[136] T. M. Reiter. *Reglerentwicklung und Optimierungsmethoden für DC/DC-Wandler im Kraftfahrzeug*. PhD thesis, Technische Universität München, 2012.

[137] Y. Ren, M. Xu, J. Zhou, and F. Lee. Analytical loss model of power MOSFET. *IEEE Transactions on Power Electronics*, 21(2):310 – 319, Mar. 2006.

[138] W. Renhart, C. Magele, and B. Schweighofer. FEM-Based Thermal Analysis of NiMH Batteries for Hybrid Vehicles. *IEEE Transactions on Magnetics*, 44(6):802 – 805, June 2008.

[139] S. Risse. *Motornahe thermoelektrische Rekuperation der Abgasenergie an einem turboaufgeladenen direkteinspritzenden Ottomotor*. PhD thesis, Technische Universität Dresden, Dresden, Jan. 2013.

[140] Robert Bosch GmbH. *Autoelektrik/Autoelektronik*. Vieweg+Teubner Verlag, Wiesbaden, 5th edition, Jan. 2007.

[141] Robert Bosch GmbH and H. Bauer. *Generatoren und Starter: Energieerzeugung und Bordnetz - Physikalische Grundlagen - Geräteausführungen für Pkw und Nkw - Qualitätsmanagement - Werkstatt-Technik*. Stuttgart, Oct. 2002.

[142] M. Rodríguez, A. Rodríguez, P. Miaja, D. Lamar, and J. Zúniga. An Insight into the Switching Process of Power MOSFETs: An Improved Analytical Losses Model. *IEEE Transactions on Power Electronics*, 25(6):1626 – 1640, 2010.

[143] D. M. Rowe. *Thermoelectrics Handbook: Macro to Nano*. CRC Press, Dec. 2006.

[144] D. M. Rowe. *Materials, Preparation, and Characterization in Thermoelectrics*. CRC Press, Apr. 2012.

[145] D. M. Rowe. *Modules, Systems, and Applications in Thermoelectrics*. CRC Press, Apr. 2012.

[146] A. Safari and S. Mekhilef. Simulation and Hardware Implementation of Incremental Conductance MPPT With Direct Control Method Using Cuk Converter. *IEEE Transactions on Industrial Electronics*, 58(4):1154 – 1161, Apr. 2011.

[147] R. Saidur, M. Rezaei, W. K. Muzammil, M. H. Hassan, S. Paria, and M. Hasanuzzaman. Technologies to recover exhaust heat from internal combustion engines. *Renewable and Sustainable Energy Reviews*, 16(8):5649 – 5659, Oct. 2012.

[148] V. Salas, E. Olías, A. Barrado, and A. Lázaro. Review of the maximum power point tracking algorithms for stand-alone photovoltaic systems. *Solar Energy Materials and Solar Cells*, 90(11):1555 – 1578, July 2006.

[149] K. Saqr and M. Musa. Critical review of thermoelectrics in modern power generation applications. *Thermal Science*, 13(3):165 – 174, 2009.

[150] T. Schauer. *Feedback Control of Cycling in Spinal Cord Injury using Functional Electrical Stimulation*. PhD thesis, Glasgow University, 2005.

[151] A. Schmidhofer, J. Horvat, T. Gabriel, H. Lanzenberger, D. Prix, and M. Bichler. Highly integrated power electronics for a 48 V hybrid drive application. In *2013 15th European Conference on Power Electronics and Applications (EPE)*, pages 1 – 7, 2013.

[152] D. Schröder. *Leistungselektronische Bauelemente*. Springer, 2nd edition, 2006.

[153] D. Schwartz. A maximum-power-point-tracking control system for thermoelectric generators. In *2012 3rd IEEE International Symposium on Power Electronics for Distributed Generation Systems (PEDG)*, pages 78 – 81, June 2012.

[154] B. Schweighofer, K. Raab, and G. Brasseur. Modeling of high power automotive batteries by the use of an automated test system. *IEEE Transactions on Instrumentation and Measurement*, 52(4):1087 – 1091, Aug. 2003.

[155] G. Shu, Y. Liang, H. Wei, H. Tian, J. Zhao, and L. Liu. A review of waste heat recovery on two-stroke IC engine aboard ships. *Renewable and Sustainable Energy Reviews*, 19:385 – 401, Mar. 2013.

[156] G. J. Snyder and E. S. Toberer. Complex thermoelectric materials. *Nature Materials*, 7(2):105 – 114, Feb. 2008.

[157] J. R. Sootsman, Y. Chung, Duck, and M. G. Kanatzidis. New and Old Concepts in Thermoelectric Materials. *Angewandte Chemie International Edition*, 48(46):8616 – 8639, Nov. 2009.

[158] C. Sprouse and C. Depcik. Review of organic Rankine cycles for internal combustion engine exhaust waste heat recovery. *Applied Thermal Engineering*, 51:711 – 722, Mar. 2013.

[159] C. Steinmetz. On the law of hysteresis. *Proceedings of the IEEE*, 72(2):197 – 221, Feb. 1984.

[160] R. Stobart and R. Weerasinghe. Heat Recovery and Bottoming Cycles for SI and CI Engines - A Perspective. SAE Technical Paper 2006-01-0662, Warrendale, PA, Apr. 2006.

[161] R. K. Stobart, A. Wijewardane, and C. Allen. The Potential for Thermo-Electric Devices in Passenger Vehicle Applications. SAE Technical Paper 2010-01-0833, Warrendale, PA, Apr. 2010.

[162] J. Sun, D. M. Mitchell, M. F. Greuel, P. T. Krein, and R. M. Bass. Modeling of PWM converters in discontinuous conduction mode. A reexamination. In *29th Annual IEEE Power Electronics Specialists Conference, 1998. PESC 98 Record*, volume 1, pages 615 – 622. IEEE, May 1998.

[163] T. Suntio. *Dynamic Profile of Switched-Mode Converter*. John Wiley & Sons, Apr. 2009.

[164] S.-C. Tan, Y. Lai, and C. Tse. General Design Issues of Sliding-Mode Controllers in DC-DC Converters. *IEEE Transactions on Industrial Electronics*, 55(3):1160 – 1174, Mar. 2008.

[165] S.-C. Tan, Y. Lai, and C. Tse. Indirect Sliding Mode Control of Power Converters Via Double Integral Sliding Surface. *IEEE Transactions on Power Electronics*, 23(2):600 – 611, Mar. 2008.

[166] S.-C. Tan, Y. Lai, C. Tse, and M. Cheung. A fixed-frequency pulsewidth modulation based quasi-sliding-mode controller for buck converters. *IEEE Transactions on Power Electronics*, 20(6):1379 – 1392, Nov. 2005.

[167] M. Telkes. The Efficiency of Thermoelectric Generators. *Journal of Applied Physics*, 18(12):1116 – 1127, Dec. 1947.

[168] P. Thounthong and S. Pierfederici. A New Control Law Based on the Differential Flatness Principle for Multiphase Interleaved DC-DC Converter. *IEEE Transactions on Circuits and Systems II: Express Briefs*, 57(11):903 – 907, Nov. 2010.

[169] H. Q. Tserng. *Design Parameters for Thermoelectric Generators*. PhD thesis, Rice University, Houston, 1968.

[170] V. I. Utkin, J. Guldner, and J. Shi. *Sliding Mode Control in Electromechanical Systems*. Taylor & Francis, 1999.

[171] A. Van den Bossche, V. Valchev, and G. Georgiev. Measurement and loss model of ferrites with non-sinusoidal waveforms. In *Power Electronics Specialists Conference, 2004. PESC 04. 2004 IEEE 35th Annual*, volume 6, pages 4814–4818 Vol.6, June 2004.

[172] J. A. Vieira and A. M. Mota. Thermoelectric generator using water gas heater energy for battery charging. In *2009 IEEE Control Applications, (CCA) & Intelligent Control, (ISIC)*, pages 1477 – 1482. IEEE, July 2009.

[173] H. Wallentowitz and M. Crampen. Einfluss von Nebenaggregaten auf den Kraftstoffverbrauch bei unterschiedlichen Fahrzyklen. *Automobiltechnische Zeitschrift*, 96(11), 1994.

[174] H. Wallentowitz and K. Reif. *Handbuch Kraftfahrzeugelektronik: Grundlagen - Komponenten - Systeme - Anwendungen*. Vieweg+Teubner Verlag, Wiesbaden, Sept. 2006.

[175] J. Wang, H. S.-h. Chung, and R. T.-h. Li. Characterization and Experimental Assessment of the Effects of Parasitic Elements on the MOSFET Switching Performance. *IEEE Transactions on Power Electronics*, 28(1):573 – 590, Jan. 2013.

[176] T. Wang, Y. Zhang, J. Zhang, G. Shu, and Z. Peng. Analysis of recoverable exhaust energy from a light-duty gasoline engine. *Applied Thermal Engineering*, 53(2):414 – 419, May 2013.

[177] W. M. S. R. Weerasinghe, R. K. Stobart, and S. M. Hounsham. Thermal efficiency improvement in high output diesel engines a comparison of a Rankine cycle with turbo-compounding. *Applied Thermal Engineering*, 30:2253 – 2256, Oct. 2010.

[178] G. W. Wester. *Low-Frequency characterization of Switched dc-dc Converters*. PhD thesis, California Institute of Technology, Pasadena, 1972.

[179] G. W. Wester and R. D. Middlebrook. Low-Frequency Characterization of Switched dc-dc Converters. *IEEE Transactions on Aerospace and Electronic Systems*, AES-9(3):376 – 385, May 1973.

[180] D. E. Wilson. The Design of a Low Specific Fuel Consumption Turbocompound Engine. SAE Technical Paper 860072, Warrendale, PA, Feb. 1986.

[181] H. Wu, K. Sun, M. Chen, Z. Chen, and Y. Xing. Hybrid centralized-distributed power conditioning system for thermoelectric generator with high energy efficiency. In *2013 IEEE Energy Conversion Congress and Exposition (ECCE)*, pages 4659 – 4664, Sept. 2013.

[182] H. Wu, K. Sun, J. Zhang, and Y. Xing. A TEG Efficiency Booster with Buck-Boost Conversion. *Journal of Electronic Materials*, 42(7):1737 – 1744, July 2013.

[183] K. Zenger, K. Altowati, and T. Suntio. Stability and Performance of Interconnected DC/DC Converter Systems. In *Advances in Computer, Information, and Systems Sciences, and Engineering*, pages 14 – 18. Springer Netherlands, Jan. 2006.

[184] K. Zhang, G. Subramanian, P. Audebert, and S. Akehurst. Method of Turbocharger Emulation on Engine Test and Application to Turbocompound System Optimisation. Technical report, Dresden, Sept. 2012.

[185] M. T. Zhang. *Electrical, Thermal, and EMI Designs of High-Density, Low-Profile Power Supploes*. PhD thesis, Virginia Polytechnic Institute and State University, 1997.

[186] X. Zhang, C. Chan, and W. Li. An automotive thermoelectric energy system with parallel configuration for engine waste heat recovery. In *2011 International Conference on Electrical Machines and Systems (ICEMS)*, pages 1 – 6, Aug. 2011.

[187] X. F. Zheng, C. X. Liu, Y. Y. Yan, and Q. Wang. A review of thermoelectrics research - Recent developments and potentials for sustainable and renewable energy applications. *Renewable and Sustainable Energy Reviews*, 32:486 – 503, Apr. 2014.

Puplications

[P1] J. H. Carstens and C. Gühmann. Simulative Analysis and Evaluation of DC/DC Converters for Thermoelectric Generators. In *Simulation und Test für die Automobilelektronik IV*, pages 145 – 155. Expert Verlag, 2012.

[P2] J. H. Carstens and C. Gühmann. Control concept for the electrical integration of thermoelectric generators into a vehicle power supply. In *14. Internationales Stuttgarter Symposium, Proceedings*, pages 627 – 642. Springer, 2014. doi: 10.1007/978-3-658-05130-3_43.

[P3] J. H. Carstens and C. Gühmann. Adaptive Control of a Boost-Buck Converter for Thermoelectric Generators. In *European Control Conference (ECC)*, pages 2121 – 2126. IEEE, June 2014. doi: 10.1109/ECC.2014.6862328, self archiving: 10.1109/ECC.2014.6862328.

[P4] J. H. Carstens and C. Gühmann. Maximum Power Point Controller for Thermoelectric Generators to Support a Vehicle Power Supply. *In Materials Today: Proceedings*, 2(2). pages 790 – 803. Elsevier, 2015. doi: 10.1016/j.matpr.2015.05.099, self archiving: 10.1016/j.matpr.2015.05.099..

[P5] C. Gühmann and J. H. Carstens. TEG2020 - Entwicklung modularer leistungsstarker und flexibel einsetzbarer thermoelektrischer Generatoren zur thermischen Rekuperation in Verbrennungskraftmaschinen und -anlagen, pages 1 – 82, 2015. Report 03X3552E, doi: 10.2314/GBV:832362794.

Nomenclature

Notations

notation	description
x^+	maximal value of variable x
x^-	minimal value of variable x
$\overline{x}$	average value of variable x
$x_{\%}$	relative value of variable x
$\hat{x}$	estimation of variable x
$\tilde{x}$	AC component of signal x
X	DC component of signal x
Δx	Amplitude ripple of signal x

Symbols

symbol	description	unit
α	Seebeck coefficient	$\mathrm{V\,K^{-1}}$
α_c	fitting parameter for core loss	
α_n	Seebeck coefficient of n-doted material	$\mathrm{V\,K^{-1}}$
α_p	Seebeck coefficient of p-doted material	$\mathrm{V\,K^{-1}}$
α_{pn}	Seebeck coefficient of p- and n-doted material	
β_c	fitting parameter for core loss	$\mathrm{V\,K^{-1}}$
η	efficiency	
η_{alt}	efficiency of alternator	
η_{ICE}	efficiency of ICE	
η_{tem}	efficiency of thermoelectric material conversion	
η_{TEM}	efficiency of a single TEM	
η_{TEM_w}	efficiency of wired TEMs	
η_{TEG}	efficiency of TEG system	
ε_{cl}	prediction error	
κ	thermal conductance	$\mathrm{W\,K^{-1}\,m^{-1}}$
κ_{tem}	thermal conductance of TEM	$\mathrm{W\,K^{-1}\,m^{-1}}$
$\mathscr{L}$	Laplace-Transform	
λ	forgetting factor	
μ	step size	
μ_c	chemical potential	eV
μ_0	vacuum permeability	$\mathrm{N\,A^{-2}}$

ρ	electrical resistivity	$\Omega\,\mathrm{m}$
ρ_f	mass density of the fuel	$\mathrm{kg\,L^{-1}}$
ρ_n	electrical resistivity of n-doted material	$\Omega\,\mathrm{m}$
ρ_p	electrical resistivity of p-doted material	$\Omega\,\mathrm{m}$
ρ_w	AC electrical resistivity	$\Omega\,\mathrm{m}$
φ_m	phase margin	°C
τ	confidence interval	
τ_d	rise time of gate voltage	s
τ_i	fall time of gate voltage	s
τ_{tem}	thermal efficiency	
ω	radial frequency	$\mathrm{rad\,s^{-1}}$
ω_0	closed-loop radial frequency	$\mathrm{rad\,s^{-1}}$
ω_{gc}	radial frequency at $\left\|G_{ol}\left(e^{-j180°}\right)\right\| = 1$	$\mathrm{rad\,s^{-1}}$
ω_c	cut-off radial frequency	$\mathrm{rad\,s^{-1}}$
ξ	damping factor	
ξ_c	cut-off damping factor	
Π	Peltier coefficient	V
$\mathscr{Z}$	z-Transform	

$b(k)$	time-discrete measuring noise signal	
d	duty cycle	
d_e	time delay	
d_m	time delay margin	
e	error	
$e(k)$	time-discrete error signal	
e_c	elementary charge	e
e_b	nominal voltage of battery	V
e_{bl}	equivalent constant voltage source of battery and load	V
e_{rms}	RMS error	
f_c	cut-off frequency	$\mathrm{s^{-1}}$
f_{eq}	equivalent sinusoidal frequency	$\mathrm{s^{-1}}$
f_o	closed loop frequency	$\mathrm{s^{-1}}$
f_s	sample frequency	$\mathrm{s^{-1}}$
f_{sw}	switching frequency	$\mathrm{s^{-1}}$
g_m	gain margin	dB
i	current	A
i_{alt}	current of alternator	A
i_b	current of battery	A
i_{ex}	excitation current of alternator	A
i_d	drain to source current	A
i_g	gate current	A
i_{in}	input current of DC-DC converter	A
i_L	inductor current	A
i_o	output current of DC-DC converter	A

i_{tem}	load current of TEM	A
k_c	fitting parameter of core loss	
k_{ce}	fitting parameter of core loss	
l_n	length of n-doted material	m
l_p	length of p-doted material	m
l_w	length of wire	m
m_m	modulus margin	dB
n	speed	min^{-1}
$p(k)$	time-discrete output disturbance signal	
p_{me}	brake mean effective pressure	bar
$p_{sw}(t)$	switch loss signal	
r	resistor	Ω
$r(k)$	time-discrete reference signal	
r	resistor	Ω
r_{b_D}	resistor of diffusion process	Ω
r_{b_K}	resistor of double layer capacity effect	Ω
r_b	equivalent resistor of battery	Ω
r_{bl}	equivalent resistor of battery and load	Ω
r_{ds}	resistor of drain to source	Ω
r_{df}	diode forward resistor	Ω
r_{dl}	low-side resistor of driver	Ω
r_{dh}	high-side resistor of driver	Ω
r_g	resistor of gate	Ω
r_l	load resistor	Ω
r_{load}	load resistor of on-boar power supply	Ω
r_{tem}	series resistor of TEM	Ω
r_w	radius of wire	m
t	time	s
t_{dt}	dead time of driving signal for MOSFETs	s
t_{fi}	fall-time of current signal	s
t_{fu}	fall-time of voltage signal	s
t_{off}	off-time of switch element	s
t_{on}	on-time of switch element	s
t_{ri}	rise-time of current signal	s
t_{ru}	rise-time of voltage signal	s
t_{rr}	reverse recovery time	s
u	voltage	V
$u(k),\ u(t)$	time-discrete and continuous control input signal	
u_{b_D}	voltage of diffusion process	V
u_{b_K}	voltage of double layer capacity effect	V
u_C	voltage of capacitor	V
u_{ds}	drain to source voltage	V
u_{gd}	gate to drain voltage	V
u_{gs}	gate to source voltage	V
u_L	voltage of inductor	V

u_{ld}	voltage of drain inductor to source	V
u_{in}	terminal voltage of TEM or input voltage of DC-DC converter	V
u_{mil}	Miller voltage	V
u_o	output voltage of DC-DC converter	V
u_{sat}	output of saturation	
u_{te}	open circuit voltage of TE	V
u_{tem}	open circuit voltage of TEM	V
u_{th}	threshold voltage	V
v	velocity	$\mathrm{m\,s^{-1}}$
$v(k)$	time-discrete input disturbance signal	
$y(k),\ y(t)$	time-discrete and continuous output signal	

$A(z^{-1}),\ A(q^{-1})$	polynomial of denominator	
$A_{aw}(z^{-1}),\ A_{aw}(q^{-1})$	characteristic polynomial for anti-wind-up	
$A_{cl}(z^{-1}),\ A_{cl}(q^{-1})$	characteristic polynomial of closed-loop	
A_p	cross section of p-doted material	$\mathrm{m^3}$
A_n	cross section of n-doted material	$\mathrm{m^3}$
$B(z^{-1}),\ B(q^{-1})$	polynomial of numerator	
B	flux density	T
B_f	heat value of gasoline	$\mathrm{kW\,h\,kg^{-1}}$
B_{pp}	peak-to-peak value of flux density	T
B_t	Thomson coefficient	$\mathrm{V\,K^{-1}}$
$BSFC$	brake specific fuel consumption	$\mathrm{g\,kW^{-1}\,h^{-1}}$
C	capacitance	F
C_{b_D}	capacitance of diffusion process	F
C_{b_K}	capacitance of double layer capacity effect	F
C_{ds}	capacitance of drain to source	F
C_{gd}	capacitance of gate to drain	F
C_{gs}	capacitance of gate to source	F
C_{iss}	input small signal capacitance	F
$C_{i_{L1}}$	controller of i_{L_1}	
$C_{i_{L2}}$	controller of i_{L_2}	
$C_{u_{C2}}$	controller of u_{C_2}	
$C_{u_{C3}}$	controller of u_{C_3}	
D_f	freewheeling diode	
F_C	fuel consumption	$\mathrm{L\,h^{-1}}$
F_{C_n}	fuel consumption per 100 km	L/100 km
$G(z^{-1}),\ G(q^{-1}),\ G(s)$	time-discrete and continuous transfer function / plant	
$G_f(z^{-1}),\ G_f(s)$	time-discrete and continuous transfer function of anti-aliasing filter	
$G_{ol}(z^{-1}),\ G_{ol}(q^{-1}),\ G_{ol}(s)$	time-discrete and continuous open-loop transfer function	
$G_{PT2}(z^{-1}),\ G_{PT2}(s)$	time-discrete and continuous transfer function of second order system	

$H_S(z^{-1}),\ H_S(q^{-1})$	time-discrete pre-specify polynomial of controller	
$H_R(z^{-1}),\ H_R(q^{-1})$	time-discrete pre-specify polynomial of controller	
L	inductor	H
L_d	inductor of drain	H
M	torque	N m
M_{alt}	torque of alternator	N m
Q_g	charge of gate	C
Q_{gd}	charge of gate to drain terminal	C
Q_{gs}	charge of gate to source terminal	C
Q_{ir}	charge at current rise time	C
Q_{rr}	reverse recovery charge	C
$\dot{Q}_C$	heat current of cold side	J
$\dot{Q}_H$	heat current of hot side	J
$\dot{Q}_p$	Peltier heat current	J
$\dot{Q}_t$	Thomson heat current	J
$R(z^{-1})$	control polynomial	
$R'(z^{-1})$	control polynomial	
RN	confidence value	
S_μ	tuning factor	
$S(z^{-1}),\ S(q^{-1})$	control polynomial	
$S'(z^{-1}),\ S'(q^{-1})$	control polynomial	
S_{alt}	switch signal for excitation current	
S_C	logical switch of control signal	
$S_{bu}(z^{-1})$	(noise) control signal sensitivity function	
$S_{by}(z^{-1})$	noise-output sensitivity function	
$S_{pu}(z^{-1})$	(output) control signal sensitivity function	
$S_{py}(z^{-1})$	(output) sensitivity function	
$S_{vy}(z^{-1})$	input-disturbance output-sensitivity function	
$S_{vu}(z^{-1})$	(input-disturbance) control signal sensitivity function	
SOC	state of charge	
T	temperature	K
$T(z^{-1})$	time-discrete pre-filter transfer function	
T_C	temperature of cold side	K
T_{C_s}	temperature of cold side at substrate	K
T_H	temperature of hot side	K
T_{H_s}	temperature of hot side at substrate	K
$T_{ry}(z^{-1})$	complementary sensitivity function	
$T_{ru}(z^{-1})$	(input) control sensitivity function	
T_s	temperature at substrate	K
T_S	sample time	s
T_{sw}	switching time	s
T_{tem}	temperature of TEM	K
U_{DD}	open circuit voltage of MOSFET	V
U_{drv}	supply voltage of driver	V
S	switch element	

S_μ	tuning factor	
P_{ac}	dynamic frequency dependent loss	W
P_{alt}	electric power of alternator	W
P_{bat}	electric power of battery	W
P_c	input power for combustion process of ICE	W
P_{core}	core power loss	W
P_{dc}	ohmic power loss	W
P_{drv}	driver power loss	W
$P_{drv,on}$	driver power loss for switch on-time	W
$P_{drv,off}$	driver power loss for switch off-time	W
P_e	effective power of ICE	W
P_{ele}	electric power of alternator	W
P_{eddy}	eddy power loss	W
P_{exe}	excess power loss	W
P_{hys}	hysteresis power loss	W
P_{in}	input power	W
P_{ind}	total AC loss of inductor	W
$P_{l_{ac}}$	AC power loss of resistor	W
P_{load}	electric power of load	W
P_{loss}	electric power loss	W
P_{out}	electric output power	W
P_{sw}	MOSFET power loss	W
$P_{sw,off}$	MOSFET power loss at switch off-time	W
$P_{sw,on}$	MOSFET power loss at switch on-time	W
$P_{sw,sy}$	SY-MOSFET power loss	W
P_{sydt}	forward-biased loss of SY-MOSFET	W
P_{syrr}	reverse recovery loss of SY-MOSFET	W
P_{TEM}	electric power of TEM	W
P_{TEM_w}	electric power of wired TEMs	W
P_{TEG}	electric output power of TEG	W
$P_{\sum TEM_w}$	output power of interconnected DC-DC converters from the TEG system	W
V_c	engine displacement	m^3
Z	figure of merit	K^{-1}
$Z\overline{T}$	normalized figure of merit	

$\boldsymbol{\theta}$	parameter vector
$\boldsymbol{\Theta}$	measurement vector
$\mathbf{c}$	output matrix
$\mathbf{u}$	input vector
$\mathbf{x}$	state vector
$\mathbf{y}$	output vector
$\mathbf{A}$	system matrix
$\mathbf{B}$	input matrix

$\mathbf{L}$	adaption gain
$\mathbf{F}_a$	acceleration force vector
$\mathbf{F}_r$	friction force vector
$\mathbf{F}_{ro}$	rolling friction force vector
$\mathbf{F}_{st}$	slope friction force vector
$\mathbf{U}$	small signal input vector
$\mathbf{P}$	covariance matrix
$\mathbf{X}$	state vector at operation point

Abbreviations

2DOF	two degree of freedom controller
ADC	analog digital converter
ARTEMIS	Assessment and Reliability of Transport Emission Models and Inventory Systems
B&B	branch and bound
BMEP	brake mean effective pressure
BoBu	boost-buck converter
BuBo	buck-boost converter
BSFC	brake specific fuel consumption
CAT	catalytic converter
CCM	continuous conduction mode
CO_2	carbon dioxide
CRC	Clausius-Rankine cycle
DAC	digital analog converter
DAQ	data acquisition
DCM	discontinuous conduction mode
DFT	discrete Fourier transformation
DMOSFET	double-diffused metal-oxide semiconductor field effect transistor
EA	evolution algorithm
EEMS	electrical energy management strategy
EMI	electromagnetic interferences
EP	evolutionary programming
ES	evolution strategy
ESR	equivalent series resistance
GA	genetic algorithm
GSE	generalized steinmetz equation
HC	hill climbing
ICE	internal combustion engine
iGSE	improves generalized Steinmetz equation
i^2GSE	improved-improved generalized Steinmetz equation
MOSFET	metal-oxide-semiconductor field-effect transistor
MPP	maximum power point
MPPT	maximum power point tracking
MSE	modified Steinmetz equation
NEDC	new European driving cycle
RLS	recursive least-square
RMS	root-mean-square
S	starter of ICE
SA	simulated annealing
SE	Steinmetz equation
SEPIC	single-ended primary-inductor converter
SMD	surface-mounted device
SSA	state-space-averaging
SY-MOSFET	synchronous metal-oxide-semiconductor field-effect transistor
TCC	trickle charge control
TE	thermoelectric element
TEG	thermoelectric generator
TEG2020	Thermoelectric Generator 2020
TEM	thermoelectric module

TEMN	thermoelectric module network
TS	tabu search
P&O	perturb and observe
PWM	pulse-width modulation
PCB	printed circuit board
WLTC	worldwide harmonized light vehicles test cycle
ZOH	zero-order hold
μC	microcontroller

A. Appendix

A.1. Models of DC-DC Converters

Buck-Boost

$$\frac{d\bar{u}_{C_1}}{dt} = -\alpha_1 u_{C_1} + \alpha_2 d i_L + \alpha_1 u_{tem} \tag{A.1}$$

$$\frac{d\bar{u}_{C_2}}{dt} = -\beta_1 u_{C_2} + \beta_1 e_{bl} - \beta_2 d i_L + \beta_2 i_L \tag{A.2}$$

$$\begin{aligned}\frac{d\bar{i}_L}{dt} = {} & \gamma_1 d u_{C_2} - \gamma_1 u_{C_2} + \gamma_2 d i_L + \gamma_3 d^2 i_L + \gamma_4 i_L \\ & + \gamma_5 d e_{bl} - \gamma_5 e_{bl} + \gamma_6 u_{tem} ,\end{aligned} \tag{A.3}$$

where α_{1-2}, β_{1-2} and γ_{1-6} are system parameters:

$$\alpha_1 = \frac{1}{C_1 \left(r_{C_1} + r_{tem}\right)} \tag{A.4}$$

$$\alpha_2 = \frac{r_{C_1}}{C_1 \left(r_{C_1} + r_{tem}\right)} \tag{A.5}$$

$$\beta_1 = \frac{1}{C_2 \left(r_{C_2} + r_{bl}\right)} \tag{A.6}$$

$$\beta_2 = \frac{r_{bl}}{C_2 \left(r_{C_2} + r_{bl}\right)} \tag{A.7}$$

$$\gamma_1 = \frac{r_{bl}}{L \left(r_{C_2} + r_{bl}\right)} \tag{A.8}$$

$$\gamma_2 = \frac{\left(r_{ds_2} - r_{ds_1} + r_{bl}\right) r_{C_2} + \left(r_{ds_2} - r_{ds_1}\right) r_{bl}}{L \left(r_{C_2} + r_{bl}\right)} \tag{A.9}$$

$$\gamma_3 = \frac{r_{tem}}{L} \tag{A.10}$$

$$\gamma_4 = \frac{\left(r_{C_2} + r_{bl} + r_{bl}\right) r_L + \left(r_{bl} + r_{ds_2}\right) r_{C_2} + r_{ds_2} r_{bl}}{L \left(r_{C_2} + r_{bl}\right)} \tag{A.11}$$

$$\gamma_5 = \frac{r_{C_2}}{L \left(r_{C_2} + r_{bl}\right)} \tag{A.12}$$

$$\gamma_6 = \frac{1}{L} \tag{A.13}$$

Ćuk

$$
\begin{aligned}
\frac{d\bar{u}_{C_1}}{dt} &= -\alpha_1 u_{C_1} + \alpha_2 i_{L_1} - \alpha_1 u_{tem} && \text{(A.14)}\\
\frac{d\bar{u}_{C_2}}{dt} &= -\beta_1 d i_{L_1} - \beta_1 d i_{L_2} + \beta_1 i_{L_1} && \text{(A.15)}\\
\frac{d\bar{u}_{C_3}}{dt} &= -\gamma_1 u_{C_3} + \gamma_2 i_{L_2} - \gamma_1 e_{bl} && \text{(A.16)}\\
\frac{d\bar{i}_{L_1}}{dt} &= \delta_1 d u_{C_2} + \delta_1 d u_{C_3} + \delta_2 u_{C_2} + \delta_3 d i_{L_1} - \delta_4 i_{L_1}\\
&\quad + \delta_5 u_{tem} + \delta_6 d i_{L_2} - \delta_7 i_{L_2} && \text{(A.17)}\\
\frac{d\bar{i}_{L_2}}{dt} &= -\varepsilon_1 u_{C_3} + \varepsilon_2 d u_{C_2} - \varepsilon_3 d i_{L_2}\\
&\quad - \varepsilon_4 i_{L_2} - \varepsilon_5 e_{bl} + \varepsilon_6 d i_{L_1} - \varepsilon_7 i_{L_1}\ , && \text{(A.18)}
\end{aligned}
$$

where α_{1-2}, β_1, γ_{1-2}, δ_{1-7} and ε_{1-7} are system parameters:

$$
\begin{aligned}
\alpha_1 &= \frac{1}{C_1\ (r_{C_1} + r_{tem})} && \text{(A.19)}\\
\alpha_2 &= \frac{r_{tem}}{C_1\ (r_{C_1} + r_{tem})} && \text{(A.20)}\\
\beta_1 &= \frac{1}{C_2} && \text{(A.21)}\\
\gamma_1 &= \frac{1}{C_3\ (r_{C_3} + r_{bl})} && \text{(A.22)}\\
\gamma_2 &= \frac{r_{bl}}{C_3\ (r_{C_3} + r_{bl})} && \text{(A.23)}\\
\delta_1 &= \frac{1}{L_1} && \text{(A.24)}\\
\delta_2 &= \frac{r_{tem}}{L_1\ (r_{C_1} + r_{tem})} && \text{(A.25)}\\
\delta_3 &= \frac{r_{C_2} + r_{bl} + r_{ds_2} - r_{ds_1}}{L_1} && \text{(A.26)}\\
\delta_4 &= \frac{(r_{C_1} + r_{tem})\, r_{L_1} + (r_{C_1} + r_{tem})\, r_{C_2} + (r_{tem} + r_{ds_2})\, r_{C_1} + r_{ds_2} r_{tem}}{L_1\ (r_{C_1} + r_{tem})} && \text{(A.27)}\\
\delta_5 &= \frac{r_{C_1}}{L_1\ (r_{C_1} + r_{tem})} && \text{(A.28)}\\
\delta_6 &= \frac{r_{ds_2} - r_{ds_1}}{L_1} && \text{(A.29)}\\
\delta_7 &= \frac{r_{ds_2}}{L_1} && \text{(A.30)}
\end{aligned}
$$

$$\varepsilon_1 = \frac{r_{bl}}{L_2\,(r_{C_3}+r_{bl})} \tag{A.31}$$
$$\varepsilon_2 = \frac{1}{L_2} \tag{A.32}$$
$$\varepsilon_3 = \frac{r_{C_2}+(r_{ds_1}-r_{ds_2})}{L_2} \tag{A.33}$$
$$\varepsilon_4 = \frac{(r_{C_3}+r_{bl})\,r_{L_2}+(r_{bl}+r_{ds_2})\,r_{C_3}+r_{ds_2}r_{bl}}{L_2\,(r_{C_3}+r_{bl})} \tag{A.34}$$
$$\varepsilon_5 = \frac{r_{C_3}}{L_2\,(r_{C_3}+r_{bl})} \tag{A.35}$$
$$\varepsilon_6 = \frac{r_{ds_2}-r_{ds_1}}{L_2} \tag{A.36}$$
$$\varepsilon_7 = \frac{r_{ds_2}}{L_2} \tag{A.37}$$

SEPIC

$$\frac{d\bar{u}_{C_1}}{dt} = -\alpha_1 u_{C_1}+\alpha_2 i_{L_1}-\alpha_1 u_{tem} \tag{A.38}$$
$$\frac{d\bar{u}_{C_2}}{dt} = -\beta_1 di_{L_1}+\beta_1 di_{L_2}+\beta_1 i_{L_1} \tag{A.39}$$
$$\frac{d\bar{u}_{C_3}}{dt} = -\gamma_1 u_{C_3}+\gamma_2 i_{L_1}+\gamma_2 i_{L_2}-\gamma_1 e_{bl}+\gamma_2 di_{L_1}+\gamma_2 di_{L_2} \tag{A.40}$$
$$\begin{aligned}\frac{d\bar{i}_{L_1}}{dt} &= -\delta_1 u_{C_3}+\delta_1 du_{C_3}+\delta_2 du_{C_2}-\delta_2 u_{C_2}+\delta_3 u_{C_1}+\delta_4 di_{L_1}\\ &\quad +\delta_5 di_{L_2}-\delta_6 i_{L_1}-\delta_7 i_{L_2}+\delta_8 de_{bl}-\delta_8 e_{bl}-\delta_8 u_{tem}\end{aligned} \tag{A.41}$$
$$\begin{aligned}\frac{d\bar{i}_{L_2}}{dt} &= \varepsilon_1 du_{C_3}+\varepsilon_1 u_{C_3}+\varepsilon_2 du_{C_2}+\varepsilon_3 di_{L_2}-\varepsilon_4 i_{L_2}\\ &\quad +\varepsilon_5 di_{L_1}-\varepsilon_6 i_{L_1}+\varepsilon_7 de_{bl}-\varepsilon_7 e_{bl}\ ,\end{aligned} \tag{A.42}$$

where α_{1-2}, β_1, γ_{1-2}, δ_{1-8} and ε_{1-7} are system parameters:

$$\alpha_1 = \frac{1}{C_1\,(r_{C_1}+r_{tem})} \tag{A.43}$$
$$\alpha_2 = \frac{r_{tem}}{C_1\,(r_{C_1}+r_{tem})} \tag{A.44}$$
$$\beta_1 = \frac{1}{C_2} \tag{A.45}$$
$$\gamma_1 = \frac{1}{C_3\,(r_{C_3}+r_{bl})} \tag{A.46}$$
$$\gamma_2 = \frac{r_{bl}}{C_3\,(r_{C_3}+r_{bl})} \tag{A.47}$$
$$\delta_1 = \frac{r_{bl}}{L_1\,(r_{C_3}+r_{bl})} \tag{A.48}$$
$$\delta_2 = \frac{1}{L_1} \tag{A.49}$$
$$\delta_3 = \frac{r_{tem}}{L_1\,(r_{C_1}+r_{tem})} \tag{A.50}$$
$$\delta_4 = \frac{r_{C_2}+r_{bl}+(r_{ds_2}-r_{ds_1})r_{C_3}+r_{bl}r_{C_2}+(r_{ds_2}-r_{ds_1})r_{bl}}{L_1\,(r_{C_3}+r_{bl})} \tag{A.51}$$

$$\delta_5 = \frac{r_{bl} + (r_{ds_2} - r_{ds_1})\, r_{C_3} + (r_{ds_2} - r_{ds_1}) r_{bl}}{L_1\, (r_{C_3} + r_{bl})} \tag{A.52}$$

$$\delta_6 = \frac{r_{L_1} + r_{C_2} + r_{ds_2}}{L_1} + \frac{r_{bl} r_{C_3}}{L_1\, (r_{C_3} + r_{bl})} + \frac{r_{tem} r_{C_1}}{L_1\, (r_{C_1} + r_{tem})} \tag{A.53}$$

$$\delta_7 = \frac{(r_{bl} + r_{ds_2})\, r_{C_3} + r_{ds_2} r_{bl}}{L_1\, (r_{C_3} + r_{bl})} \tag{A.54}$$

$$\delta_8 = \frac{r_{C_3}}{L_1\, (r_{C_3} + r_{bl})} \tag{A.55}$$

$$\varepsilon_1 = \frac{r_{bl}}{L_2\, (r_{C_3} + r_{bl})} \tag{A.56}$$

$$\varepsilon_2 = \frac{1}{L_2} \tag{A.57}$$

$$\varepsilon_3 = \frac{(-r_{C_2} + r_{bl} + (r_{ds_2} - r_{ds_1}))\, r_{C_3} - r_{bl} r_{C_2} + (r_{ds_2} - r_{ds_1})\, r_{bl}}{L_2\, (r_{C_3} + r_{bl})} \tag{A.58}$$

$$\varepsilon_4 = \frac{(r_{C_3} + r_{bl})\, r_{L_2} + (r_{bl} + r_{ds_2})\, r_{C_3} + r_{ds_2} r_{bl}}{L_2\, (r_{C_3} + r_{bl})} \tag{A.59}$$

$$\varepsilon_5 = \frac{(r_{bl} + r_{ds_2} r_{C_3} + r - ds_2 r_{bl})}{L_2, (r_{C_3} + r_{bl})} \tag{A.60}$$

$$\varepsilon_6 = \frac{(r_{bl} + r_{ds_2} r_{C_3})\, r_{C_3} + r_{ds_2} r_{bl}}{L_2, (r_{C_3} + r_{bl})} \tag{A.61}$$

$$\varepsilon_7 = \frac{r_{C_3}}{L_2\, (r_{C_3} + r_{bl})} \tag{A.62}$$

Boost-Buck

$$\frac{d\bar{u}_{C_1}}{dt} = -\beta_1 u_{C_1} - \beta_2 i_{L_1} + \beta_3 u_{tem} \tag{A.63}$$

$$\frac{d\bar{u}_{C_2}}{dt} = \delta_1 i_{L_1} - \delta_2 i_{L_1} d_1 - \delta_3 i_{L_2} d_2 \tag{A.64}$$

$$\frac{d\bar{u}_{C_3}}{dt} = \gamma_1 i_{L_2} - \gamma_2 u_{C_3} + \gamma_3 e_{BL} \tag{A.65}$$

$$\begin{aligned} \frac{d\bar{i}_{L_1}}{dt} = {} & \alpha_1 i_{L_1} + \alpha_2 u_{C_1} - \alpha_3\, u_{C_2} + \alpha_4 u_{tem} \\ & + \alpha_5\, d_1\, i_{L_1} + \alpha_6\, d_2\, i_{L_2} - \alpha_3\, d_1 u_{C_2} \\ & - \alpha_6 d_1\, d_2\, i_{L_2} \end{aligned} \tag{A.66}$$

$$\begin{aligned} \frac{di_{L_2}}{dt} = {} & -\varepsilon_1 i_{L_2} - \varepsilon_2 u_{C_3} + \varepsilon_3 e_{BL} - \varepsilon_4 i_{L_2} d_2 \\ & + \varepsilon_5 d_2 i_{L_1} - \varepsilon_6 d_1 d_2 i_{L_1}\ , \end{aligned} \tag{A.67}$$

where α_{1-6}, β_{1-3}, γ_{1-3}, δ_{1-3} and ε_{1-5} are system parameters:

$$\alpha_1 = \frac{(r_{C_1}+r_{tem})\,r_{L_1}+(r_{C_1}+r_{tem})\,r_{C_2}+(r_{ds_2}+r_{tem})\,r_{C_1}+r_{ds_2}r_{tem}}{L_1\,(r_{C_1}+r_{tem})} \tag{A.68}$$

$$\alpha_2 = \frac{r_{tem}}{L_1\,(r_{C_1}+r_{tem})} \tag{A.69}$$

$$\alpha_3 = \frac{1}{L_1} \tag{A.70}$$

$$\alpha_4 = \frac{r_{C_1}}{L_1\,(r_{C_1}+r_{tem})} \tag{A.71}$$

$$\alpha_5 = \frac{r_{C_2}+(r_{ds_2}-r_{ds_1})}{L_1} \tag{A.72}$$

$$\alpha_6 = \frac{r_{C_2}}{L_1} \tag{A.73}$$

$$\beta_1 = \frac{\beta_2}{r_{tem}} = \beta_3 = \frac{1}{C_1\,(r_{C_1}+r_{tem})} \tag{A.74}$$

$$\delta_1 = \delta_2 = \delta_3 = \frac{1}{C_2} \tag{A.75}$$

$$\gamma_2 = \frac{\gamma_1}{r_{bl}} = \gamma_3 = \frac{1}{C_3\,(r_{C_3}+r_{bl})} \tag{A.76}$$

$$\varepsilon_1 = \frac{r_{C_3}\,r_{L_2}+r_{bl}\,r_{L_2}+r_{bl}\,r_{C_3}+r_{ds_3}\,r_{C_3}+r_{ds_3}r_{bl}}{L_2\,(r_{C_3}+r_{bl})} \tag{A.77}$$

$$\varepsilon_2 = \varepsilon_3 = \frac{r_{bl}}{L_2\,(r_{C_3}+r_{bl})} \tag{A.78}$$

$$\varepsilon_4 = \frac{r_{C_2}+(r_{ds_4}-r_{ds_3})}{L_2} \tag{A.79}$$

$$\varepsilon_5 = = \frac{r_{C_2}}{L_2} \tag{A.80}$$

A.2. Analysis of Converters for Switching Frequency and Load Voltage

In this appendix, the separated mean losses of the DC-DC converters in relation to the switching frequency and the battery voltage are presented. Figures A.1 - A.7 are structured as follows: The ohmic loss $\bar{P}_{dc}$ is presented in (1). The switch loss $\bar{P}_{sw}$ with the driver losses $\bar{P}_{drv}$ is presented in (2). The inductor loss $\bar{P}_{ind}$ is presented in (3). The synchronous switch loss $\bar{P}_{sw,sy}$ is presented in (4). Whole loss is presented in (5) and the mean efficiency $\bar{\eta}$ presented in (6).

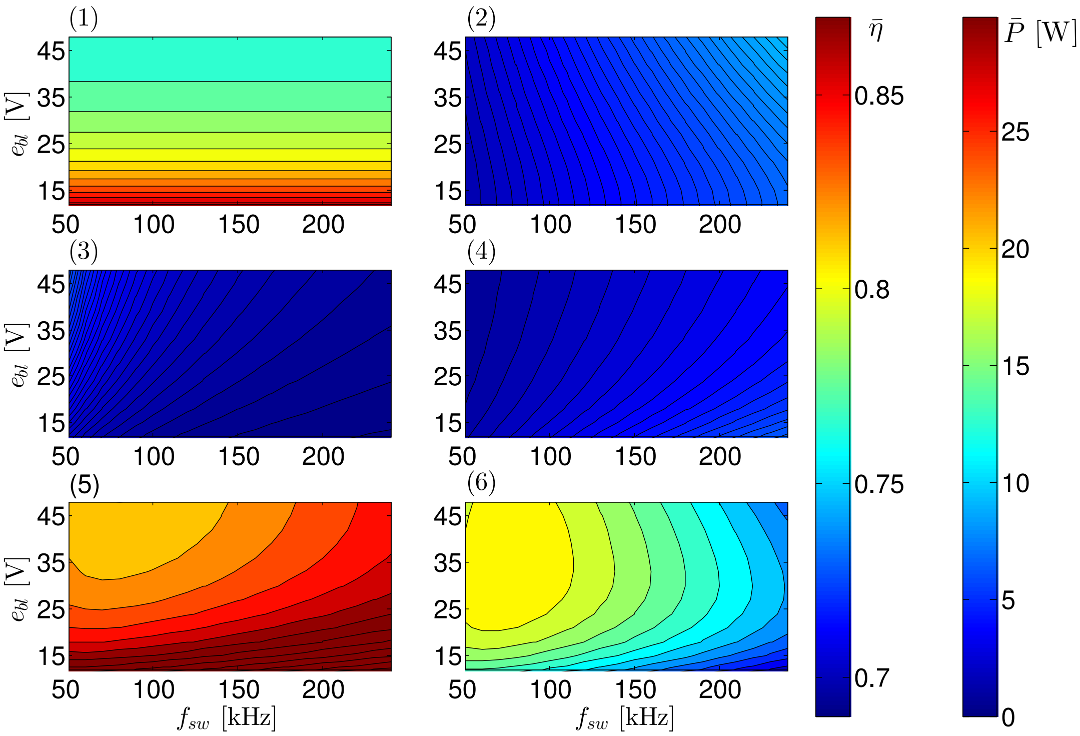

Figure A.1.: Separated mean losses of the buck-boost converter.

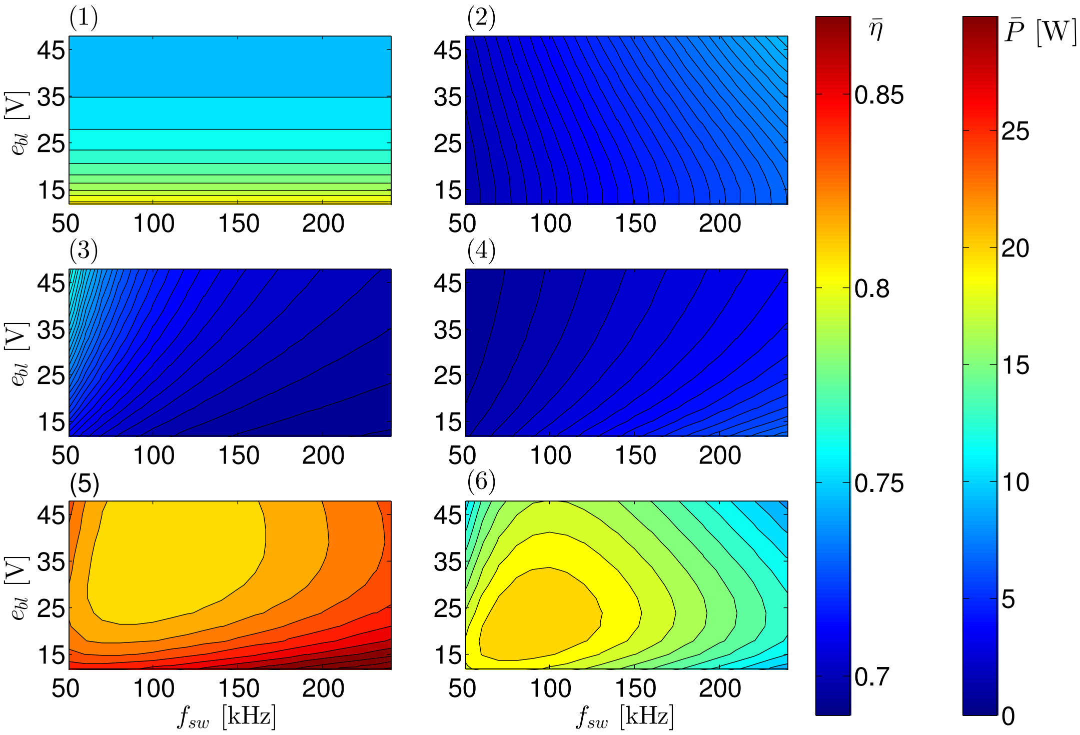

Figure A.2.: Separated mean losses of the Ćuk converter.

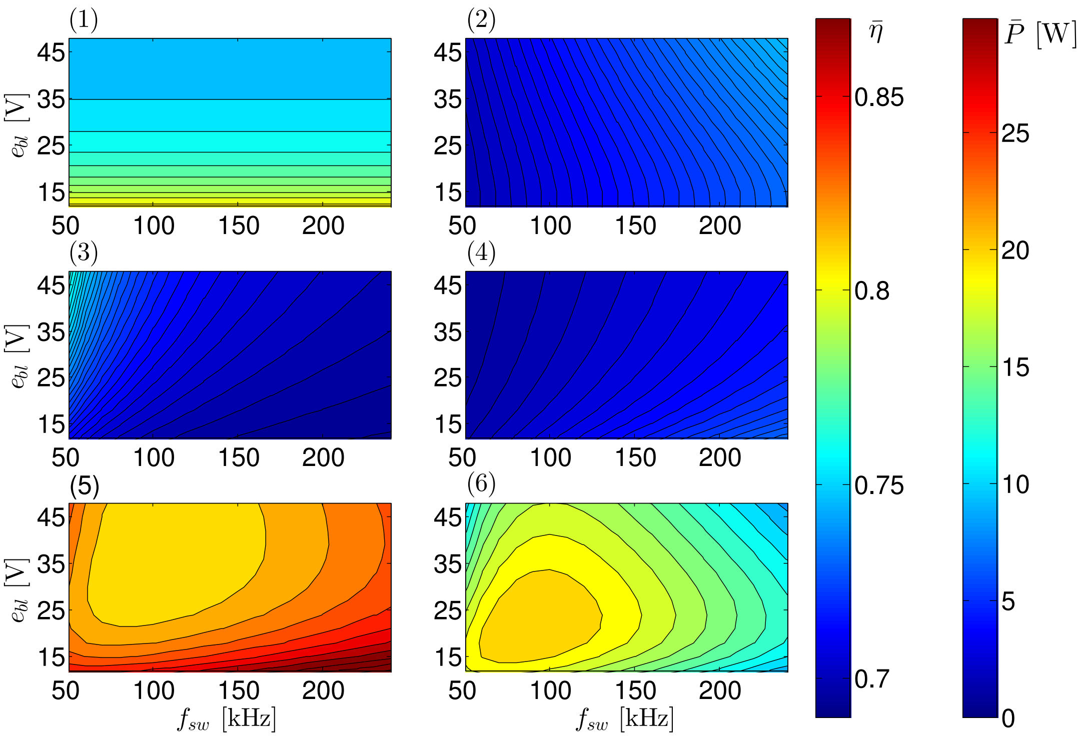

Figure A.3.: Separated mean losses of the SEPIC converter.

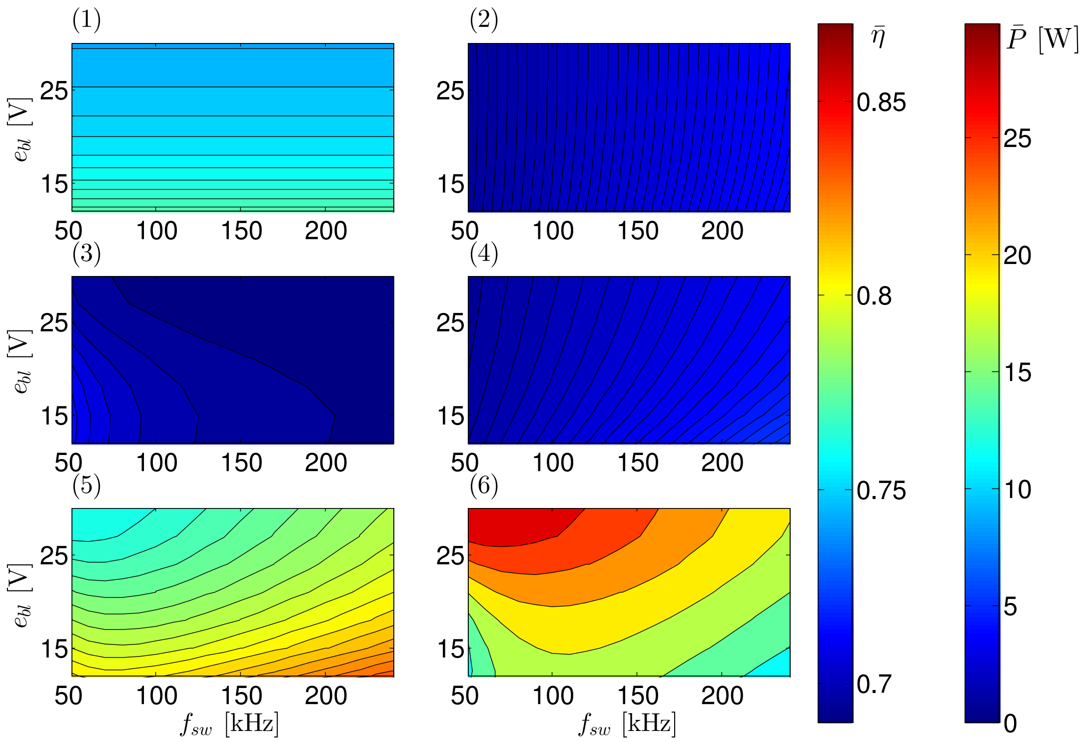

Figure A.4.: Separated mean losses of the boost-buck converter for $u_{C_2} = 30$ V.

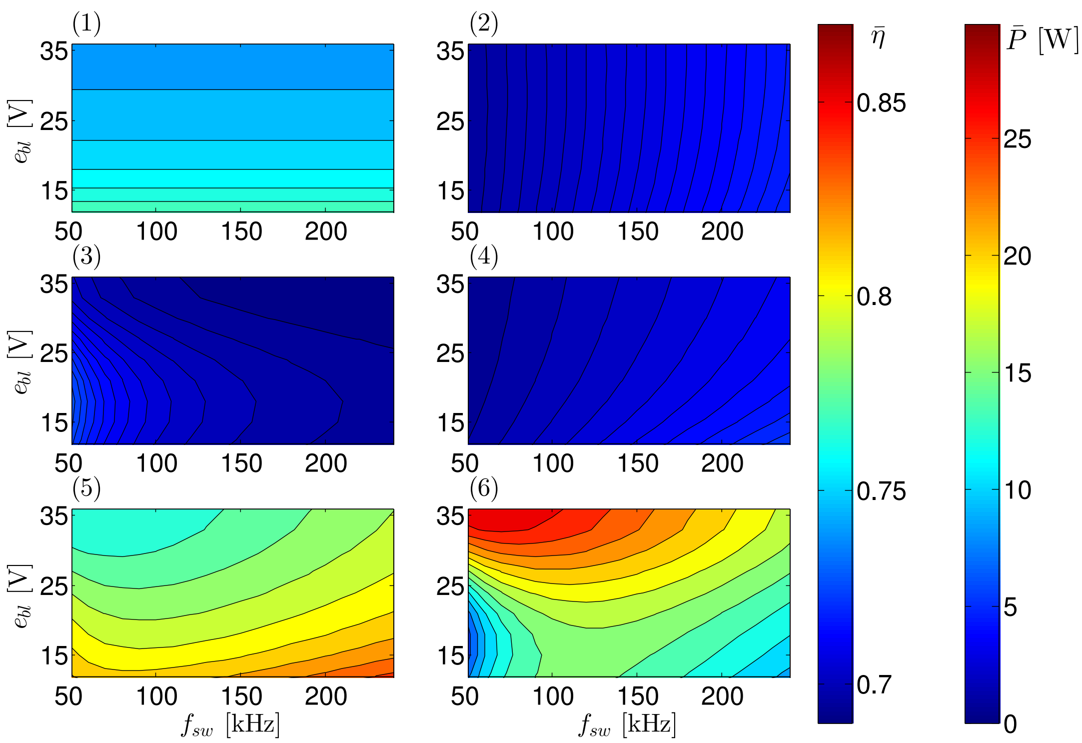

Figure A.5.: Separated mean losses of the boost-buck converter for $u_{C_2} = 36$ V.

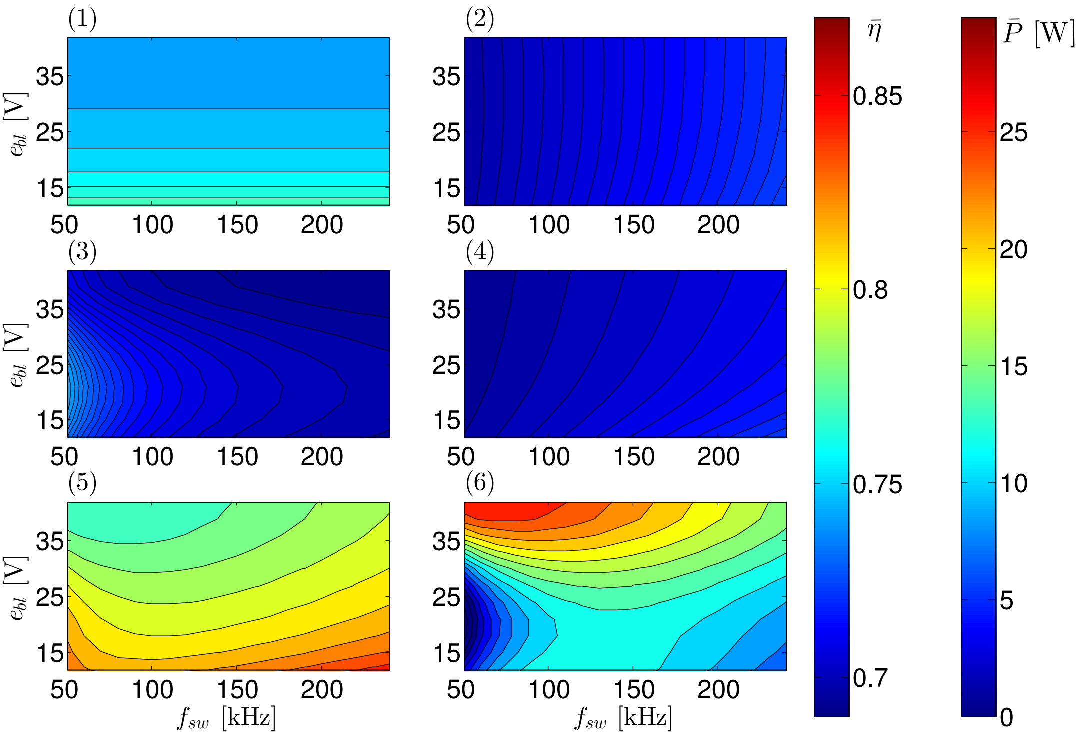

Figure A.6.: Separated losses of the boost-buck converter for $u_{C_2} = 42$ V.

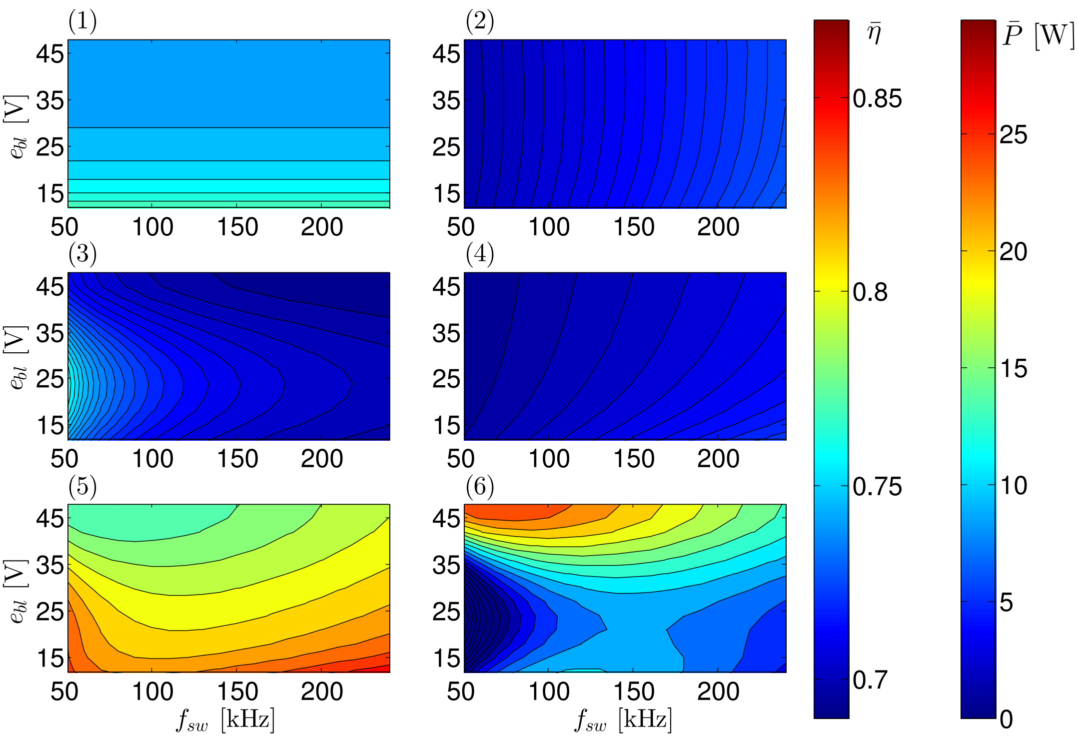

Figure A.7.: Separated losses of the boost-buck converter for $u_{C_2} = 48$ V.

A.3. Analysis of Converters in Relation to Input Power and Output Voltage

In this appendix, the separated losses of the converters are presented at $f_{sw} = 100$ kHz. For detailed analyses, different output voltages e_{bl} are selected: 12 V, 24 V, and 48 V. The Appendices A.3.1 - A.3.3 present absolute losses and efficiency of the DC-DC converters. These figures are structured as follows: The ohmic loss P_{dc} is presented in (1). The switch loss P_{sw} with the driver losses P_{drv} is presented in (2). The inductor loss P_{ind} is presented in (3). The synchronous switch loss $P_{sw,sy}$ is presented in (4). The whole loss is presented in (5). The efficiency is presented in (6).
The Appendices A.3.4 - A.3.6 present the relative losses and efficiency of the DC-DC converters. The figures in this appendix are structured as follows: The ohmic loss $P_{\%_{dc}}$ is presented in (1). The switch loss $P_{\%_{sw}}$ with the driver losses $P_{\%_{drv}}$ is presented in (2). The inductor loss $P_{\%_{ind}}$ is presented in (3). The synchronous switch loss $P_{\%_{sw,sy}}$ is presented in (4).
The mean loss and maximum loss as well as the efficiency values are tabulated in Appendix A.3.7.

A.3.1. Absolute Losses and Efficiency of 12 V Vehicle Voltage Supply

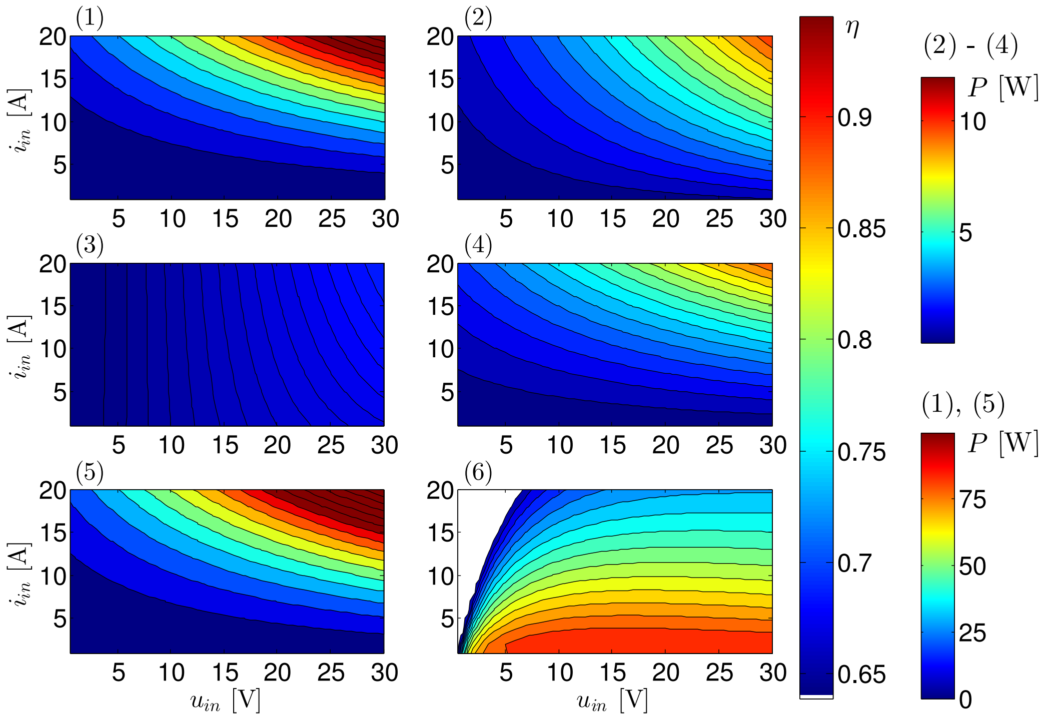

Figure A.8.: Separated losses of the buck-boost converter for $e_{bl} = 12$ V.

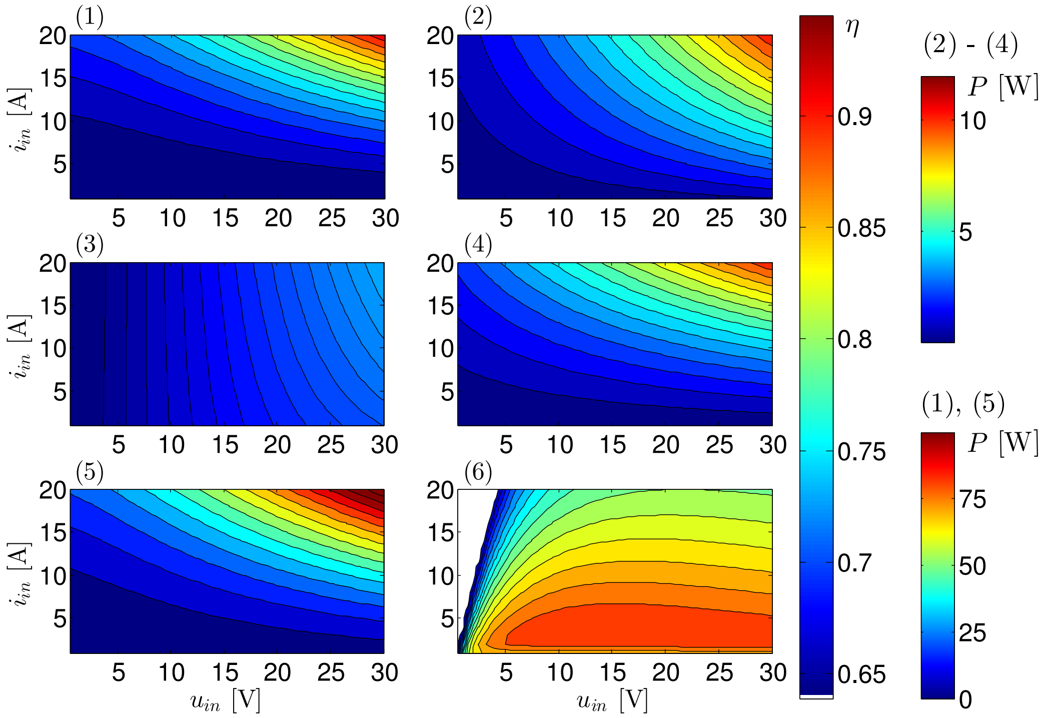

Figure A.9.: Separated losses of the Ćuk converter for $e_{bl} = 12$ V.

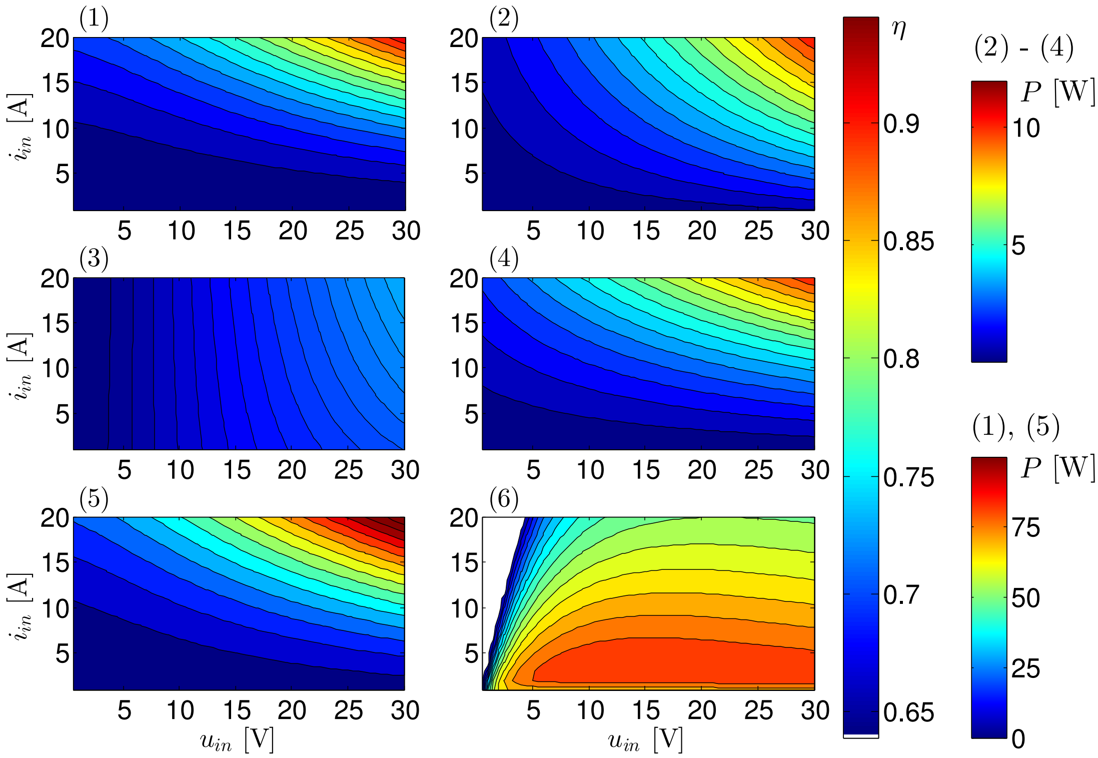

Figure A.10.: Separated losses of the SEPIC converter for $e_{bl} = 12$ V.

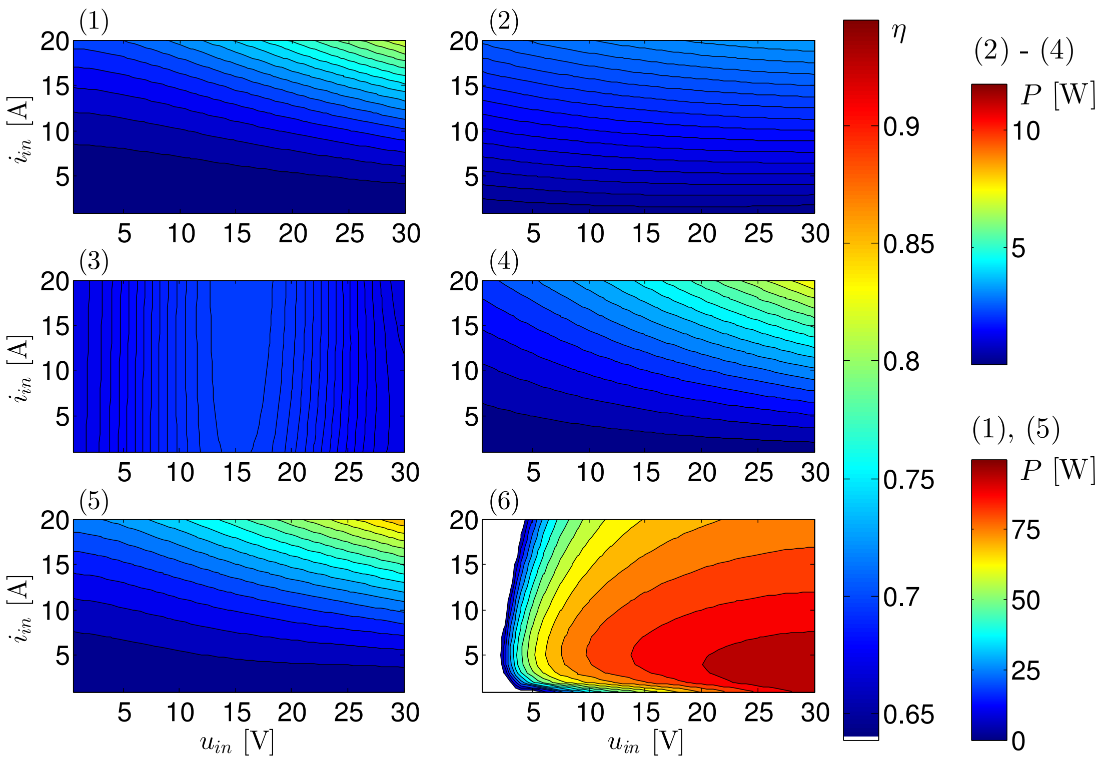

Figure A.11.: Separated losses of the boost-buck converter for $u_{C_2} = 30$ V and $e_{bl} = 12$ V.

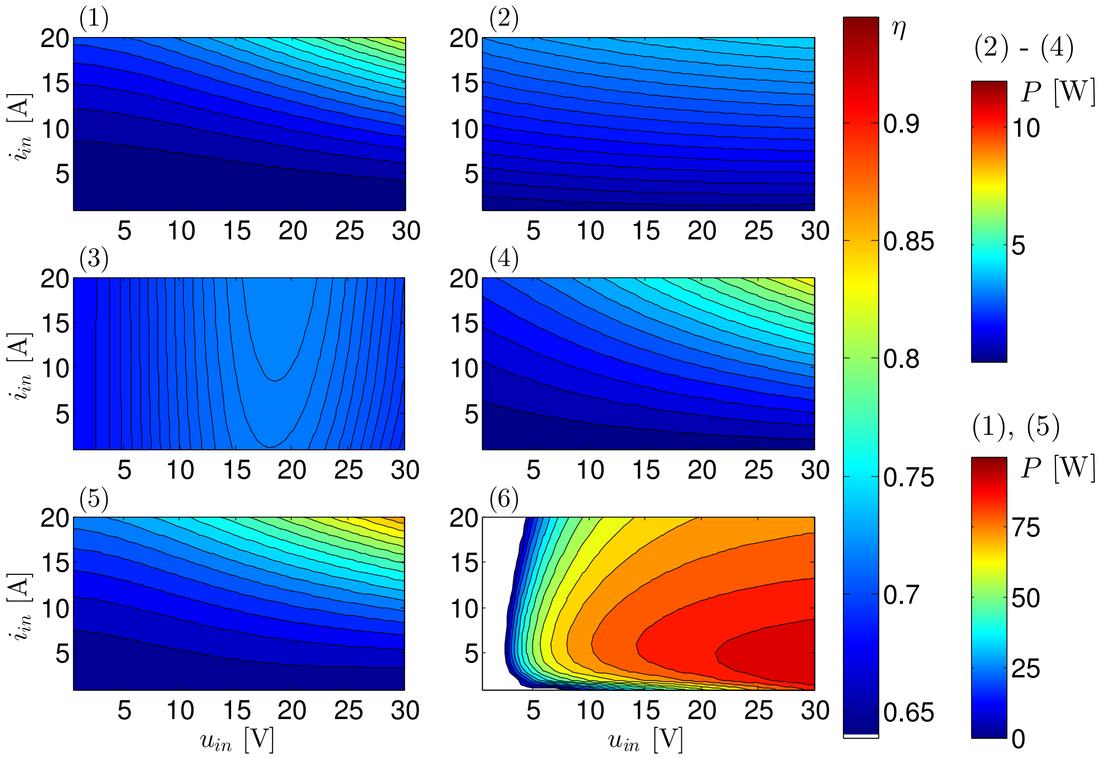

Figure A.12.: Separated losses of the boost-buck converter for $u_{C_2} = 36$ V and $e_{bl} = 12$ V.

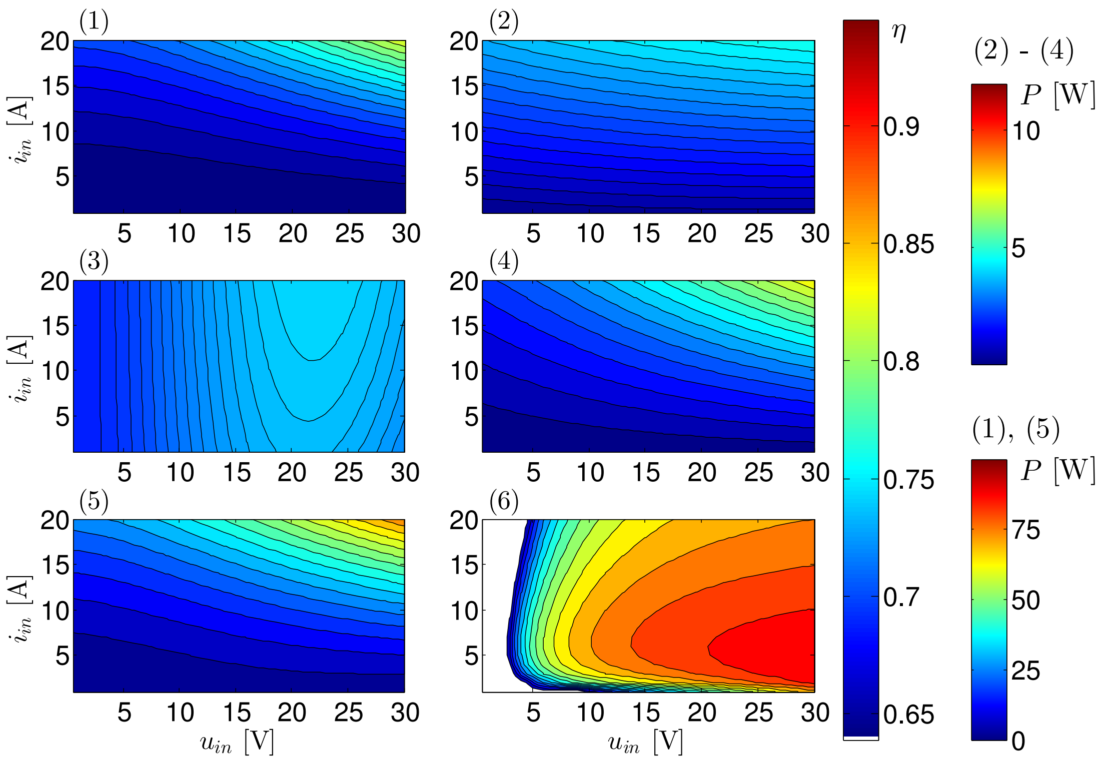

Figure A.13.: Separated losses of the boost-buck converter for $u_{C_2} = 42$ V and $e_{bl} = 12$ V.

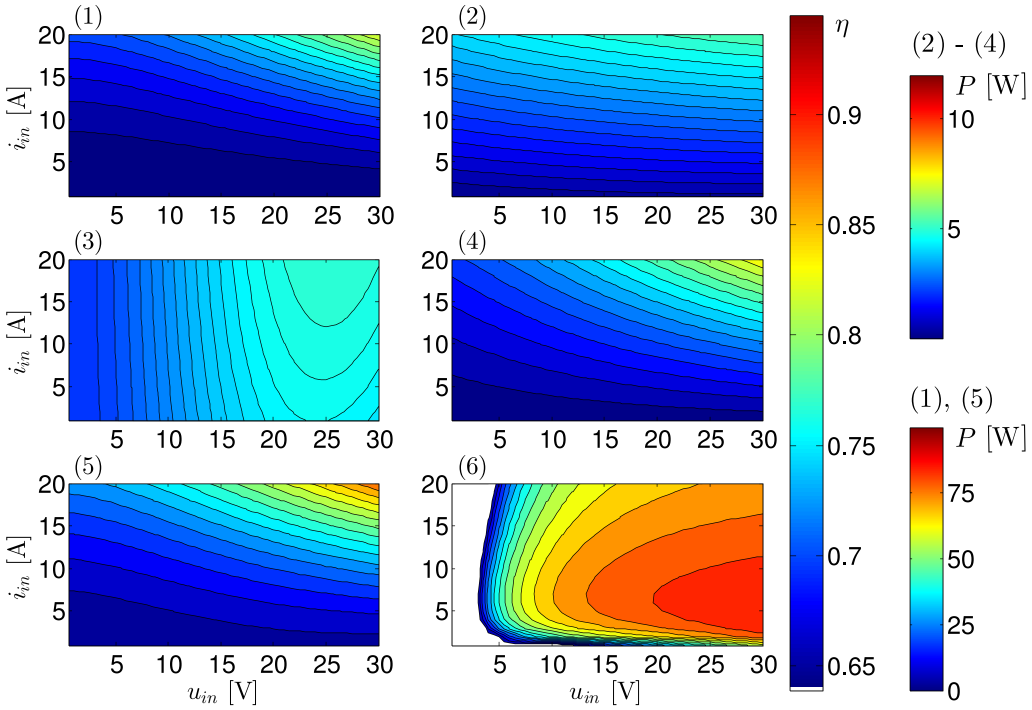

Figure A.14.: Separated losses of the boost-buck converter for $u_{C_2} = 48$ V and $e_{bl} = 12$ V.

A.3.2. Absolute Losses and Efficiency of 24 V Vehicle Voltage Supply

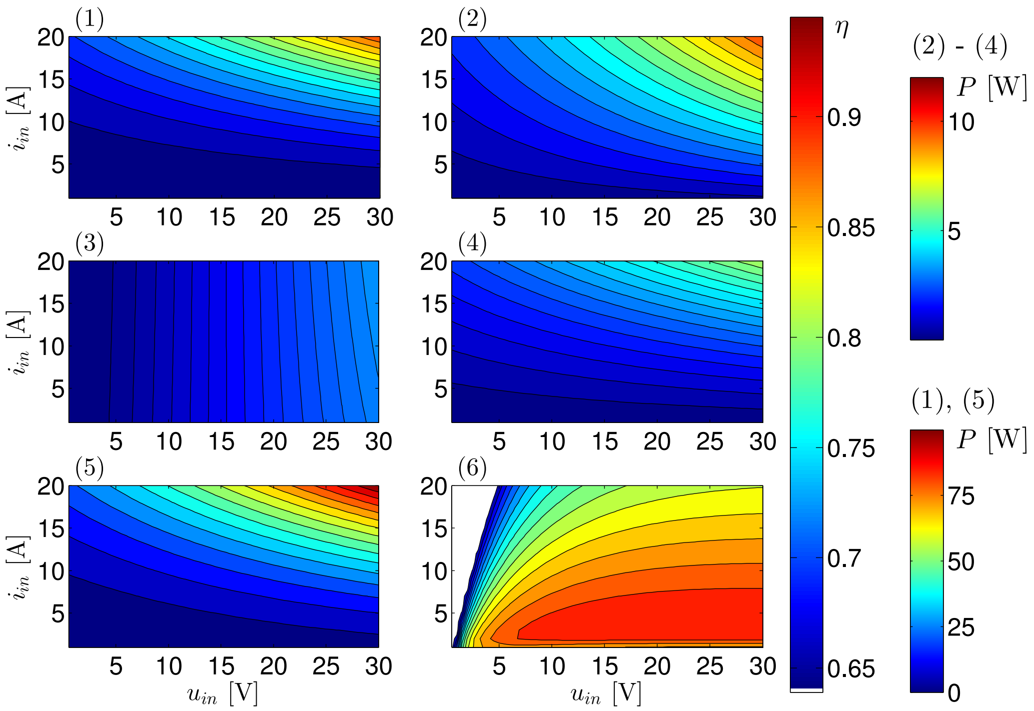

Figure A.15.: Separated losses of the buck-boost converter for $e_{bl} = 24$ V.

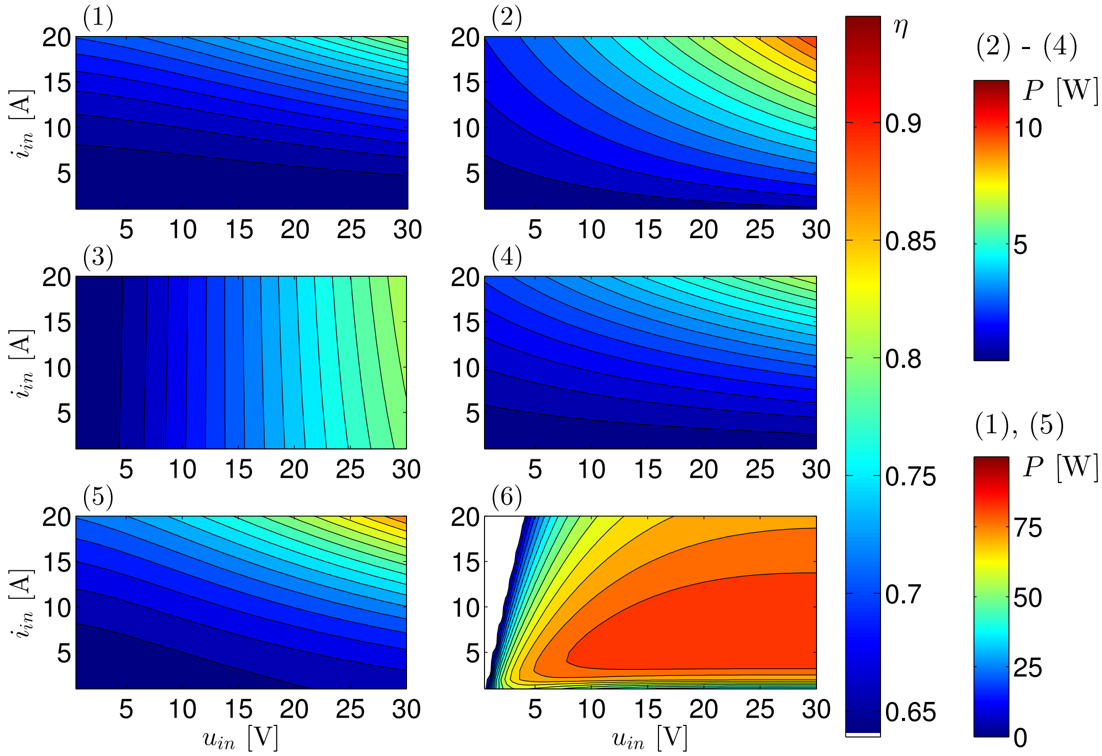

Figure A.16.: Separated losses of the Ćuk converter for $e_{bl} = 24$ V.

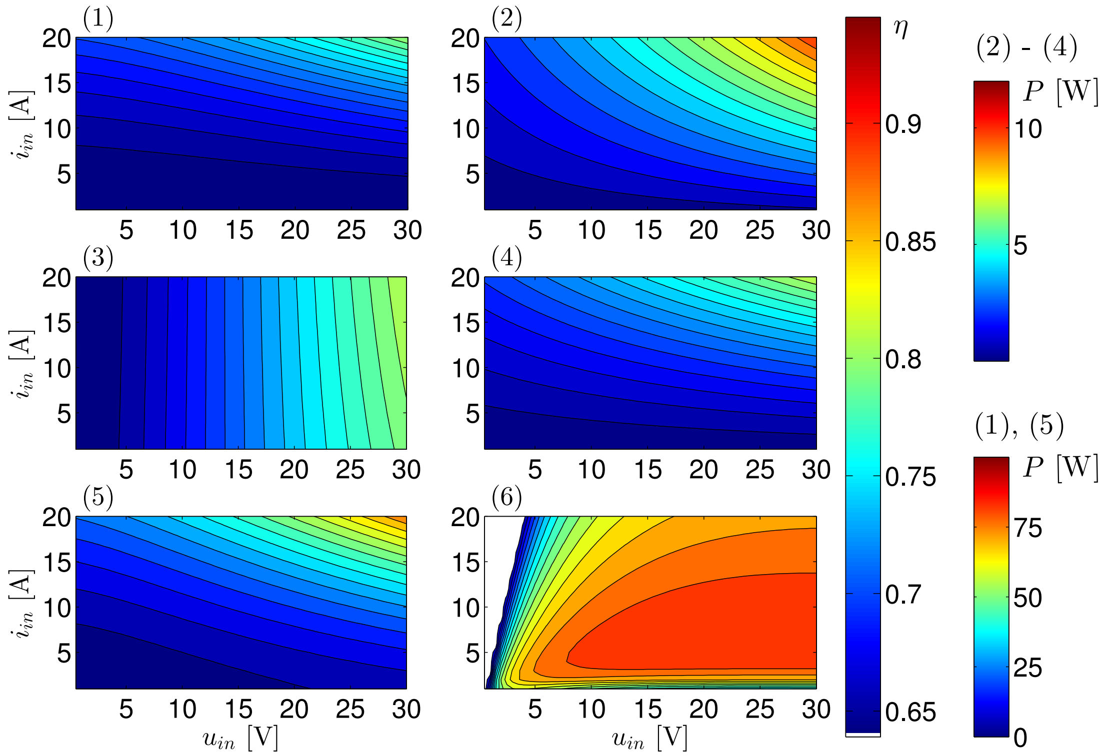

Figure A.17.: Separated losses of the SEPIC converter for $e_{bl} = 24$ V.

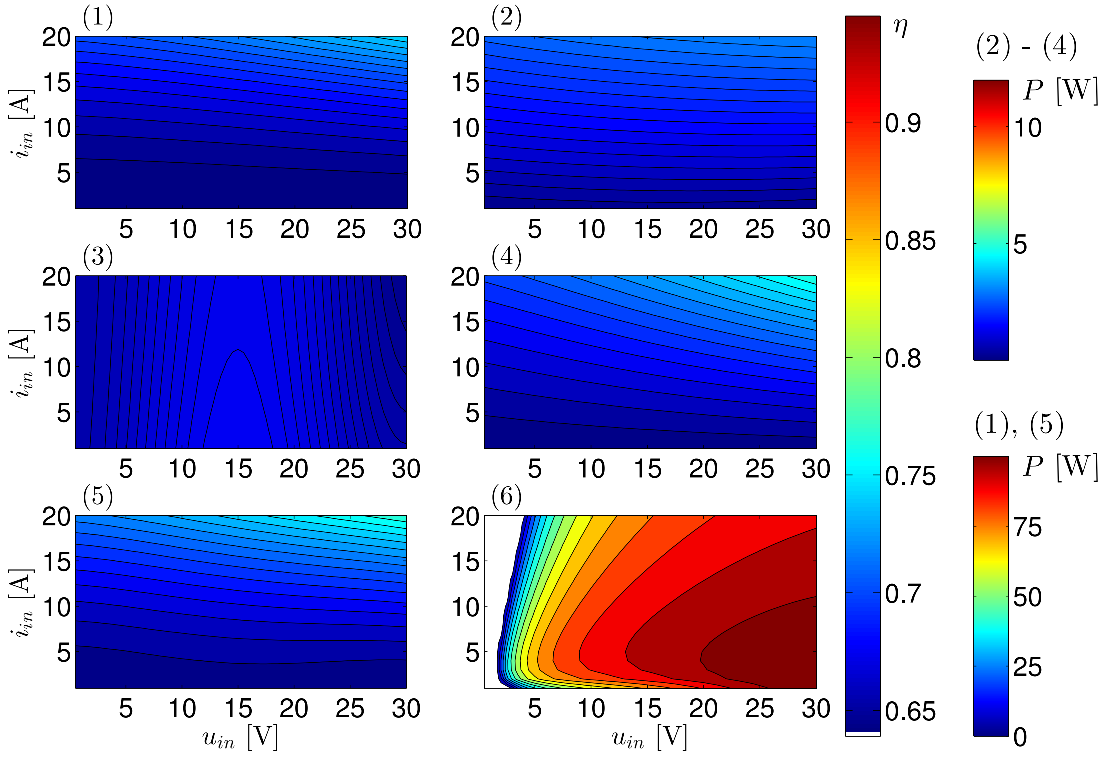

Figure A.18.: Separated losses of the boost-buck converter for $u_{C_2} = 30$ V and $e_{bl} = 24$ V.

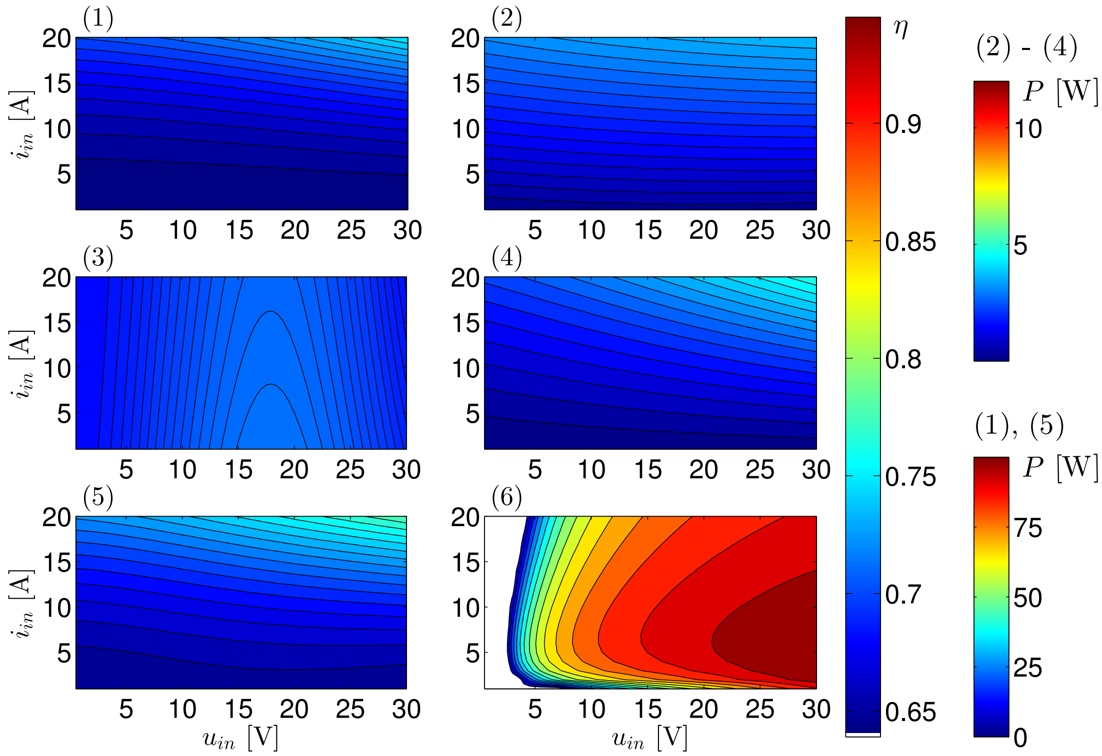

Figure A.19.: Separated losses of the boost-buck converter for $u_{C_2} = 36$ V and $e_{bl} = 24$ V.

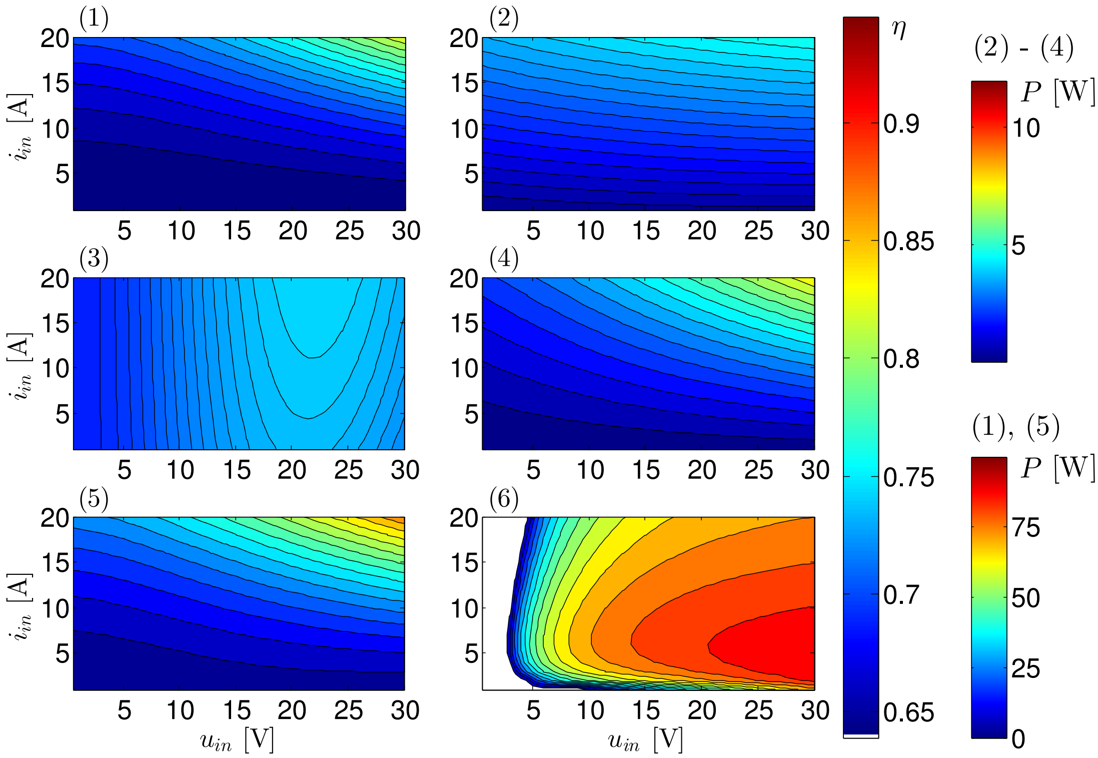

Figure A.20.: Separated losses of the boost-buck converter for $u_{C_2} = 42$ V and $e_{bl} = 24$ V.

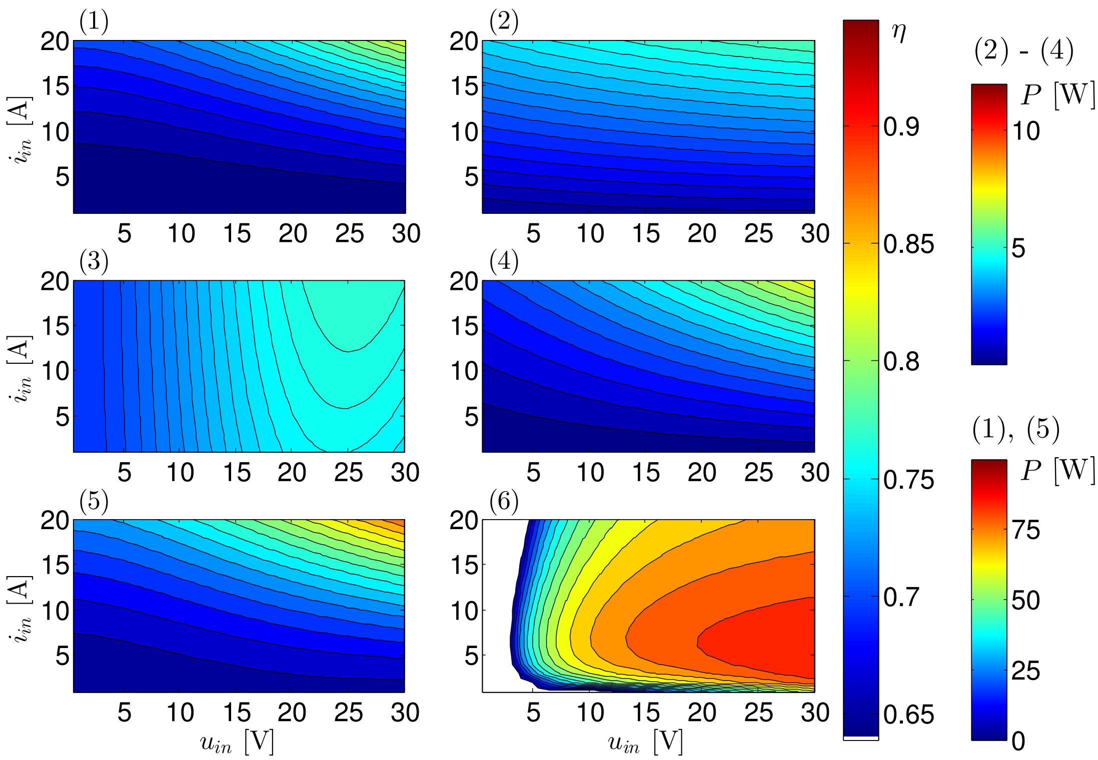

Figure A.21.: Separated losses of the boost-buck converter for $u_{C_2} = 48$ V and $e_{bl} = 24$ V.

A.3.3. Absolute Losses and Efficiency of 48 V Vehicle Voltage Supply

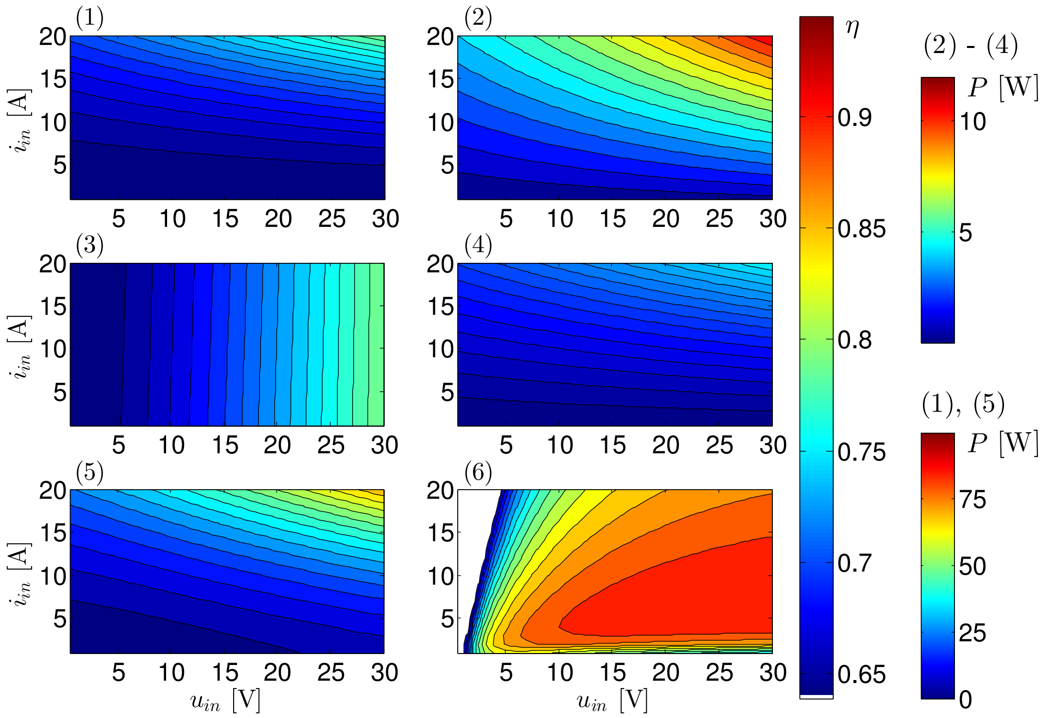

Figure A.22.: Separated losses of the buck-boost converter for $e_{bl} = 48$ V.

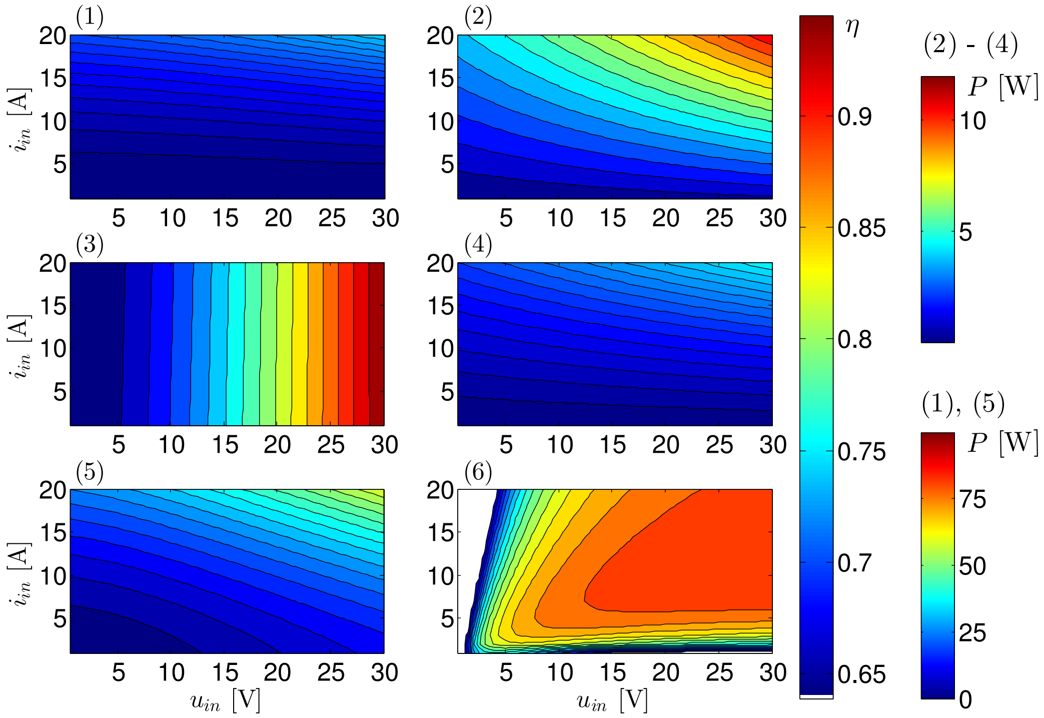

Figure A.23.: Separated losses of the Ćuk converter for $e_{bl} = 48$ V.

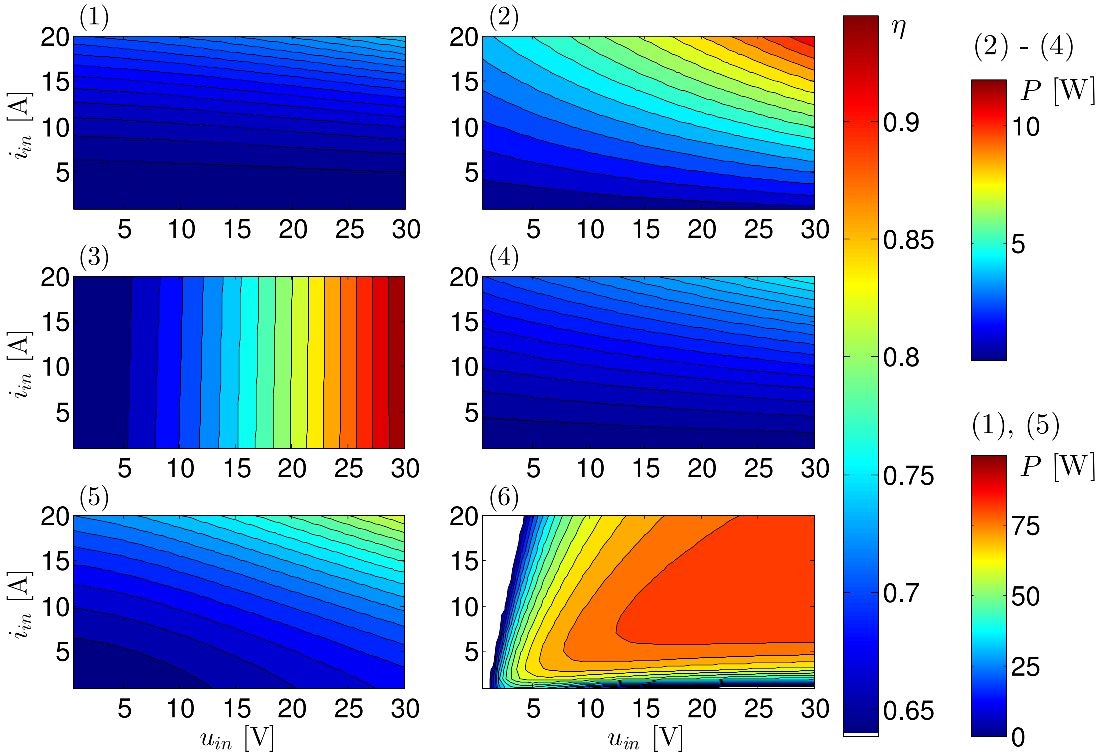

Figure A.24.: Separated losses of the SEPIC converter for $e_{bl} = 48$ V.

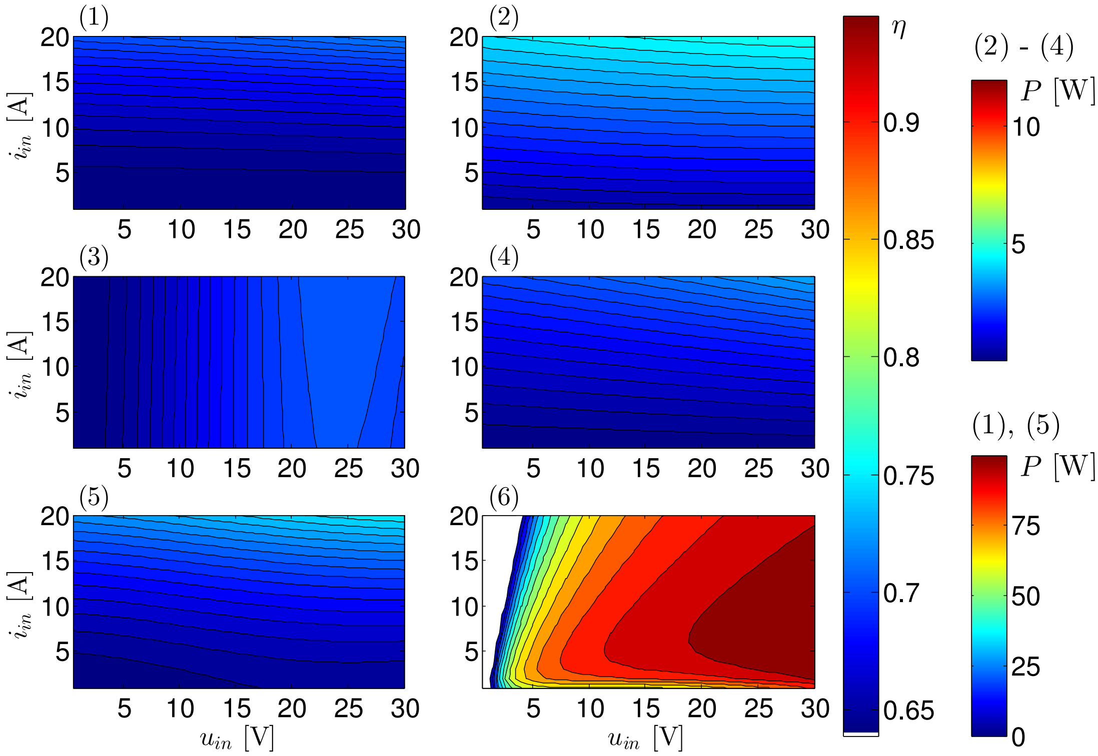

Figure A.25.: Separated losses of the boost-buck converter for $u_{C_2} = 48$ V and $e_{bl} = 48$ V.

A.3.4. Relative Losses and Efficiency for 12 V Vehicle Voltage Supply

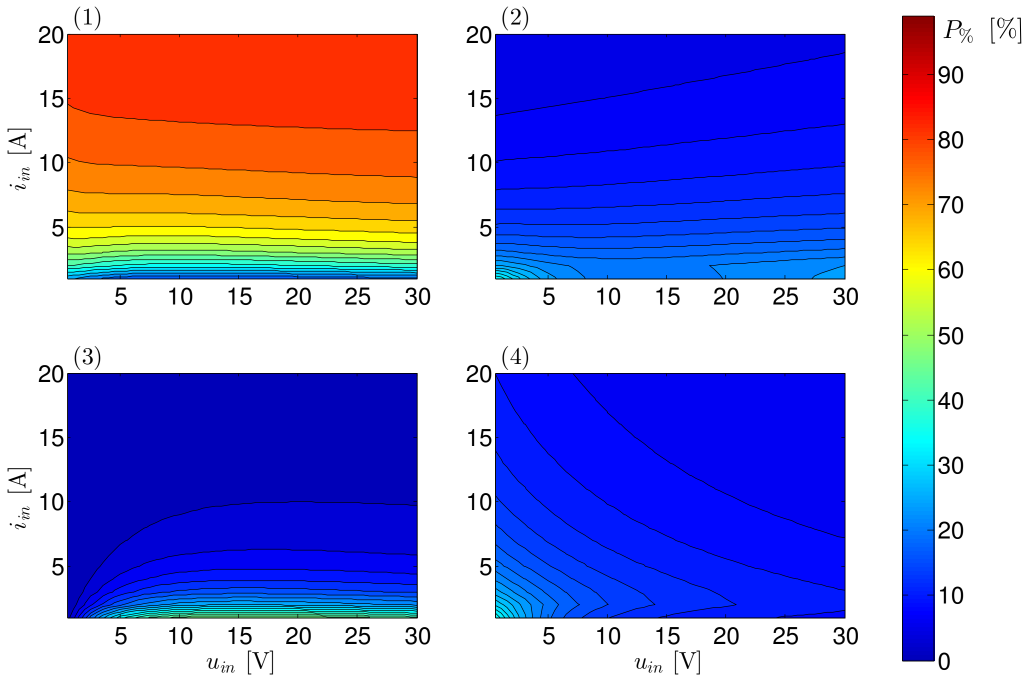

Figure A.26.: Separated losses of the buck-boost converter for $e_{bl} = 12$ V.

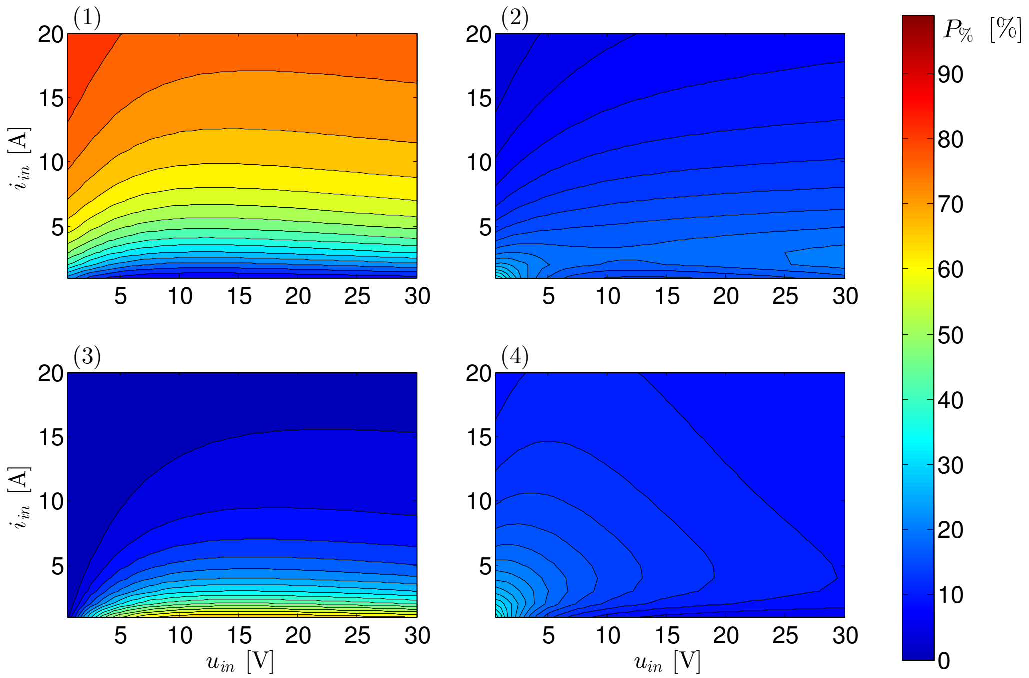

Figure A.27.: Separated losses of the Ćuk converter for $e_{bl} = 12$ V.

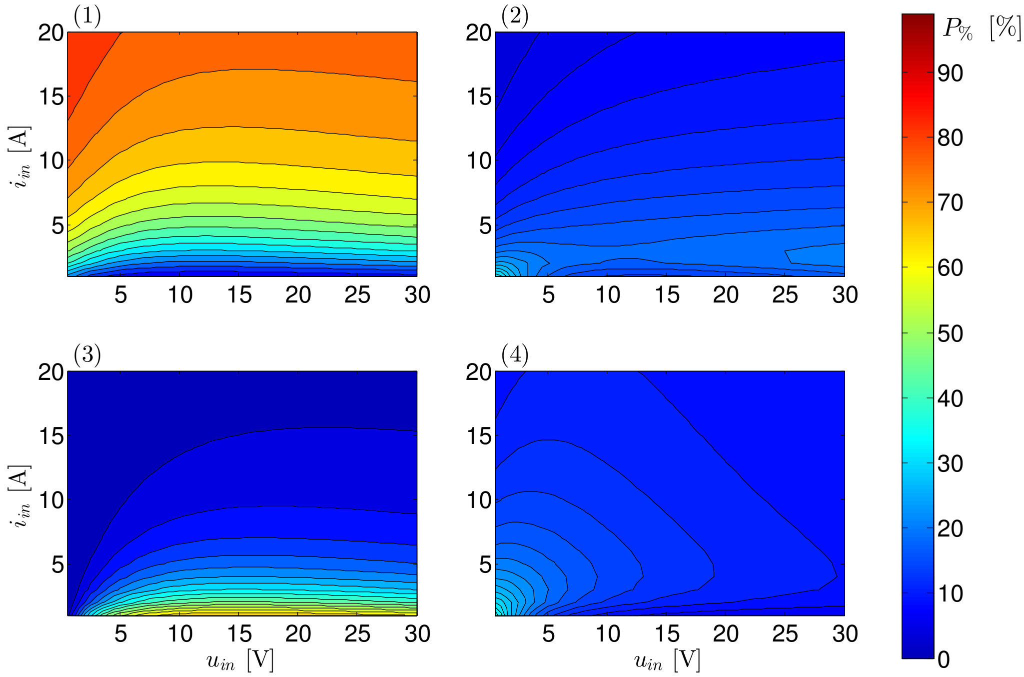

Figure A.28.: Separated losses of the SEPIC converter for $e_{bl} = 12$ V.

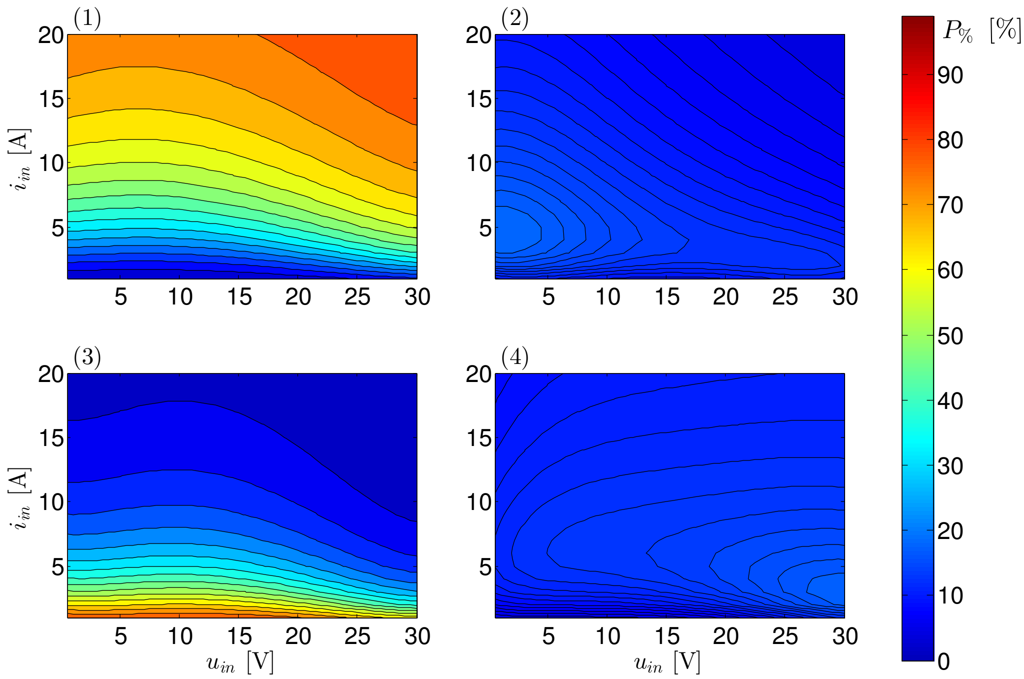

Figure A.29.: Separated losses of the boost-buck converter for $u_{C_2} = 30$ V and $e_{bl} = 12$ V.

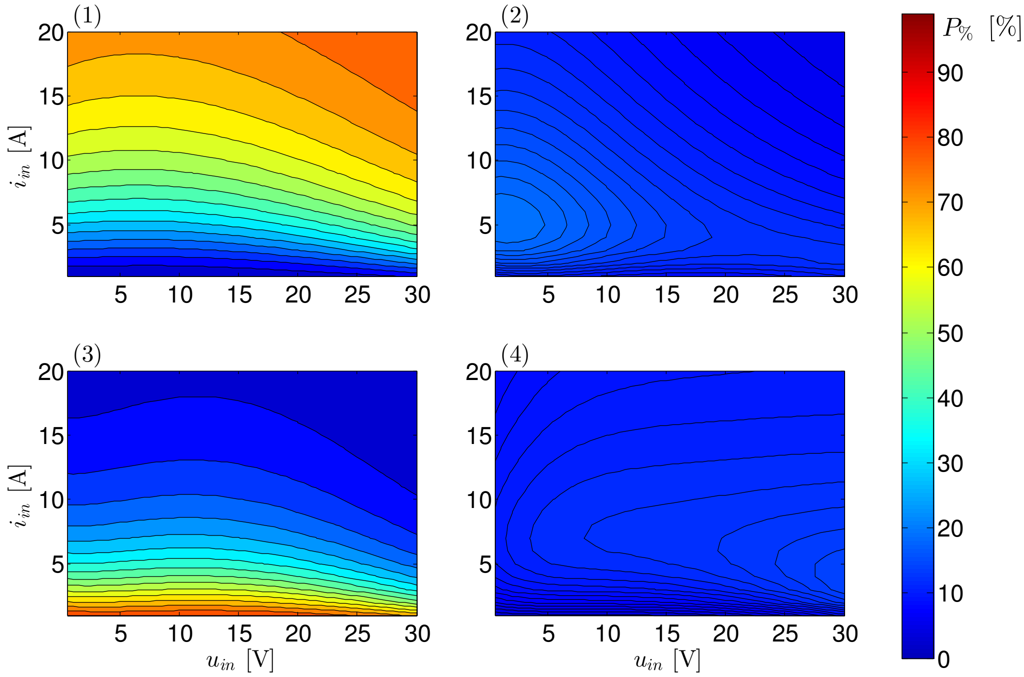

Figure A.30.: Separated losses of the boost-buck converter for $u_{C_2} = 36$ V and $e_{bl} = 12$ V.

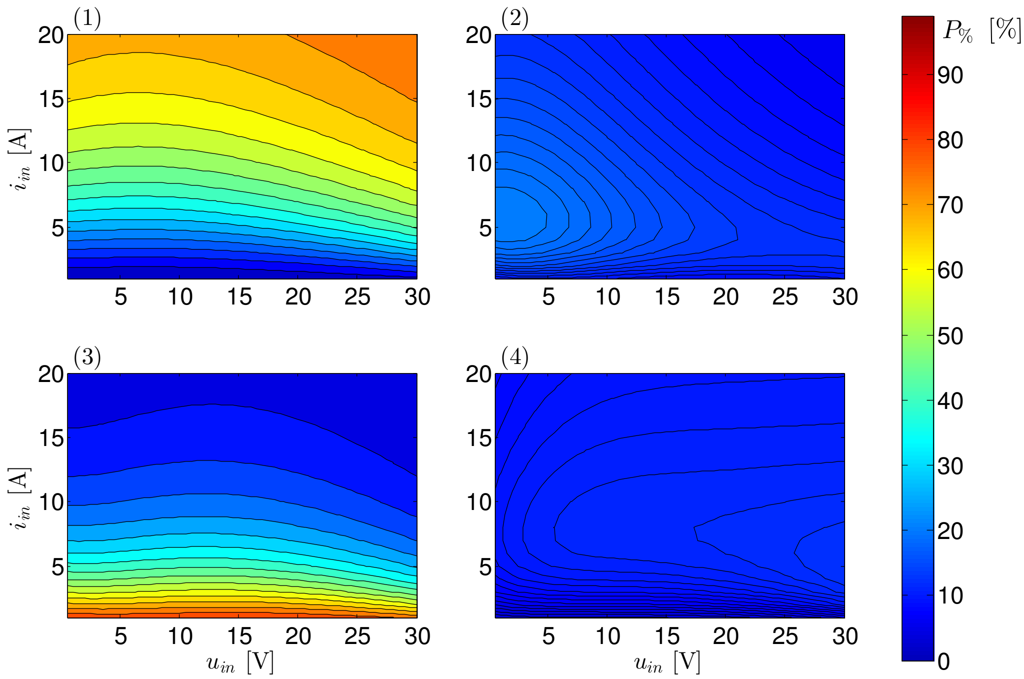

Figure A.31.: Separated losses of the boost-buck converter, for $u_{C_2} = 42$ V and $e_{bl} = 12$ V.

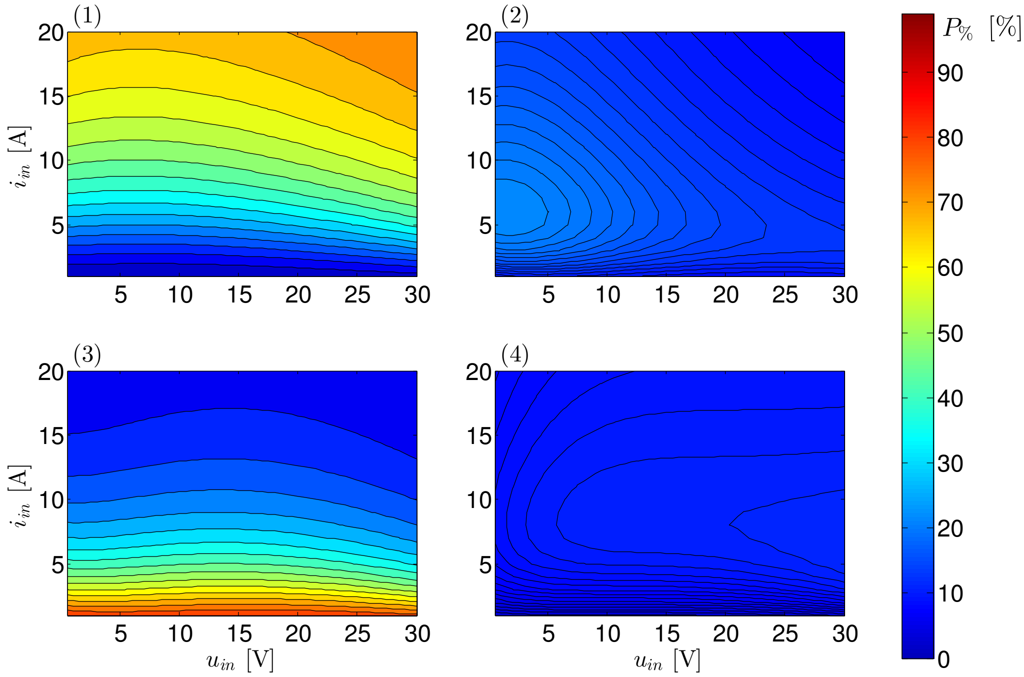

Figure A.32.: Separated losses of the boost-buck converter for $u_{C_2} = 48$ V and $e_{bl} = 12$ V.

A.3.5. Relative Losses and Efficiency for 24 V Vehicle Voltage Supply

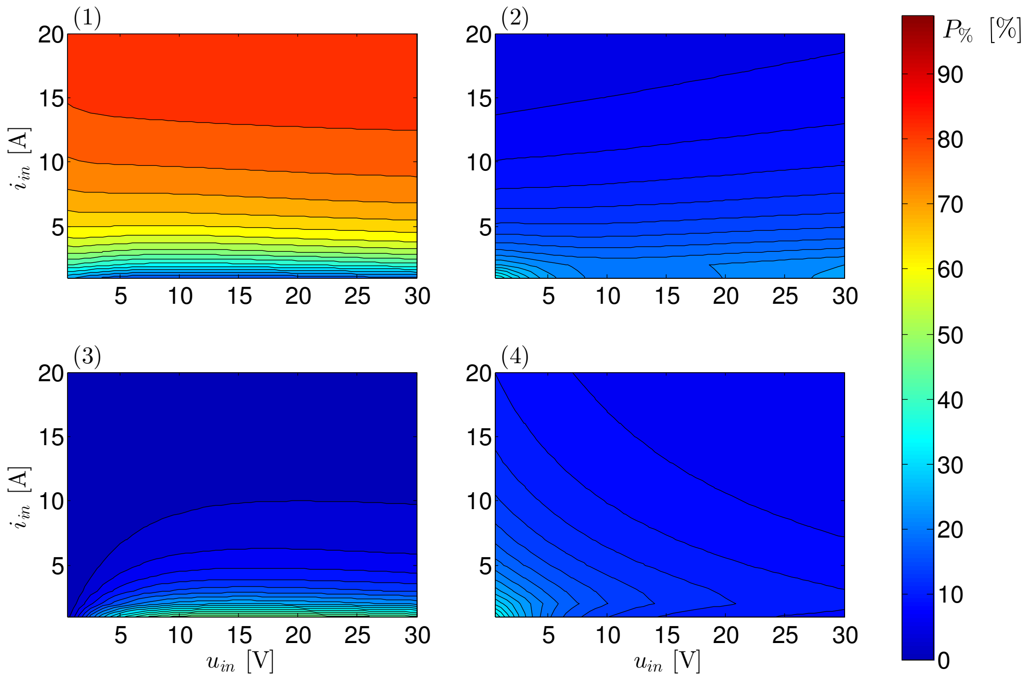

Figure A.33.: Separated losses of the buck-boost converter for $e_{bl} = 24$ V.

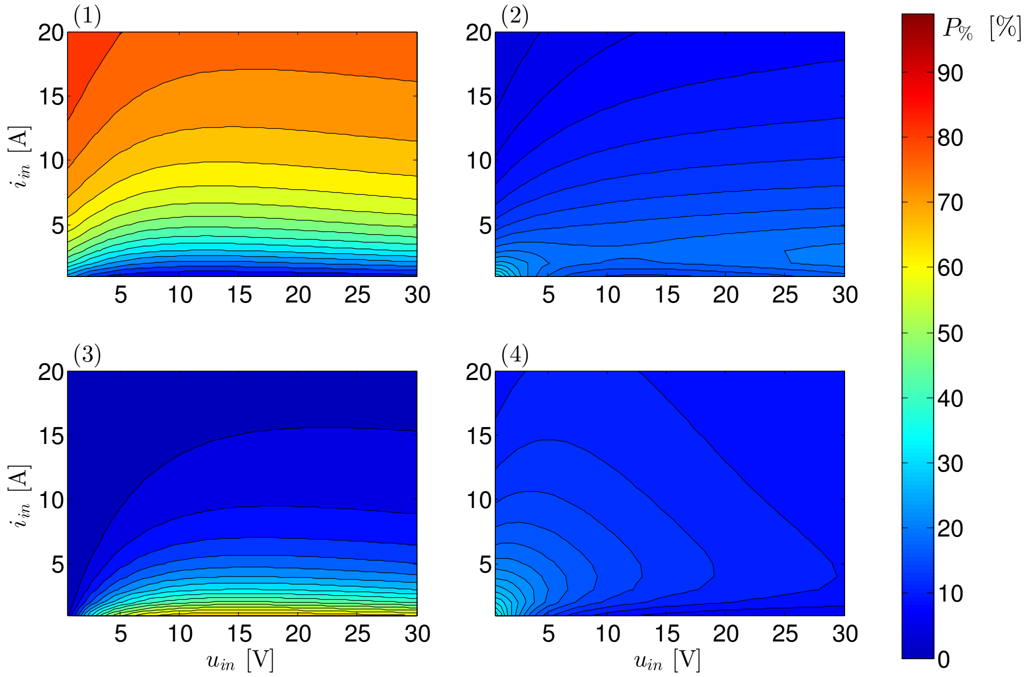

Figure A.34.: Separated losses of the Ćuk converter for $e_{bl} = 24$ V.

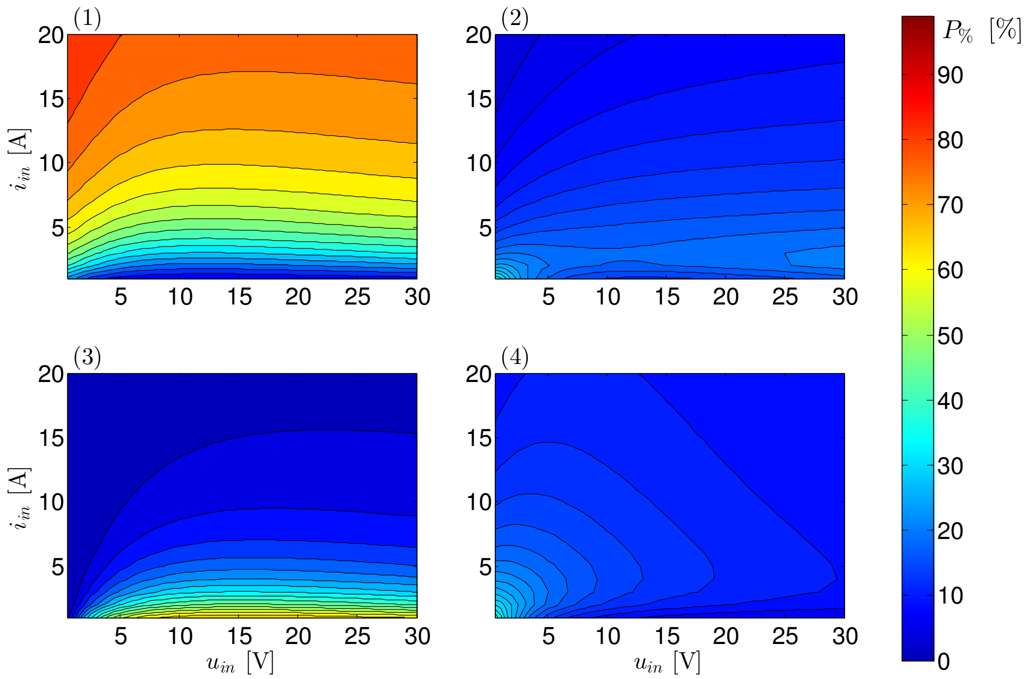

Figure A.35.: Separated losses of the SEPIC converter for $e_{bl} = 24$ V.

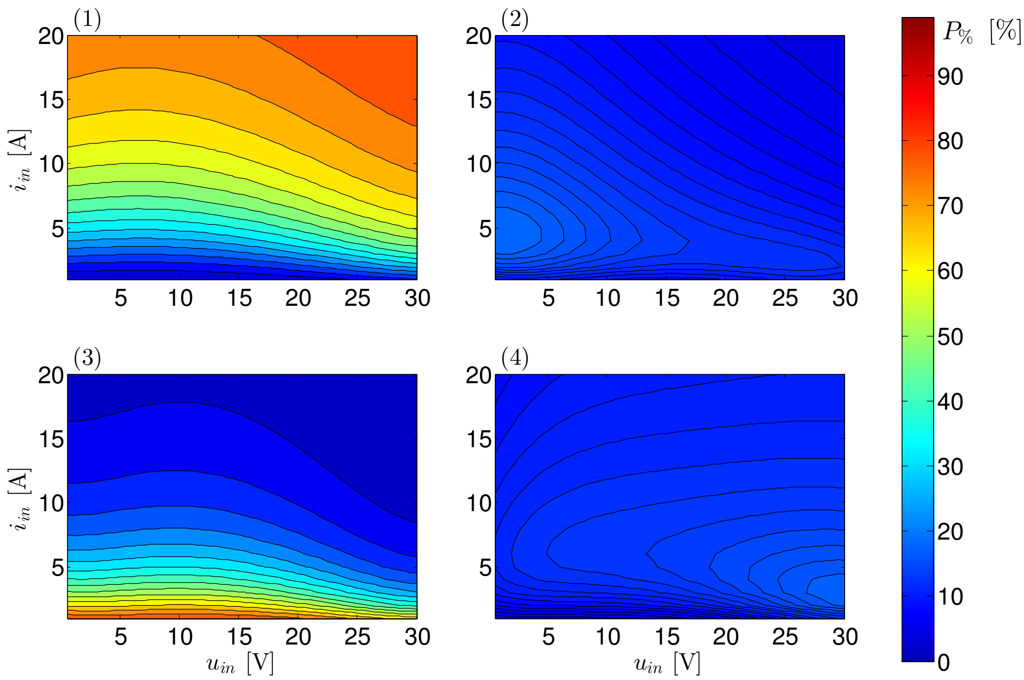

Figure A.36.: Separated losses of the boost-buck converter for $u_{C_2} = 30$ V and $e_{bl} = 24$ V.

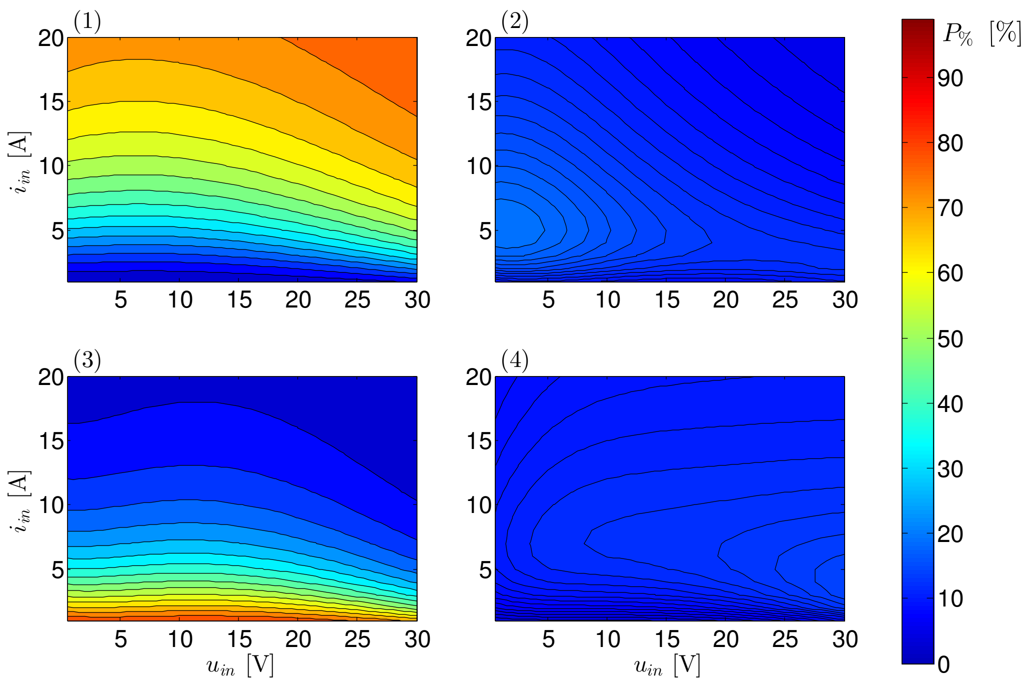

Figure A.37.: Separated losses of the boost-buck converter for $u_{C_2} = 36$ V and $e_{bl} = 24$ V.

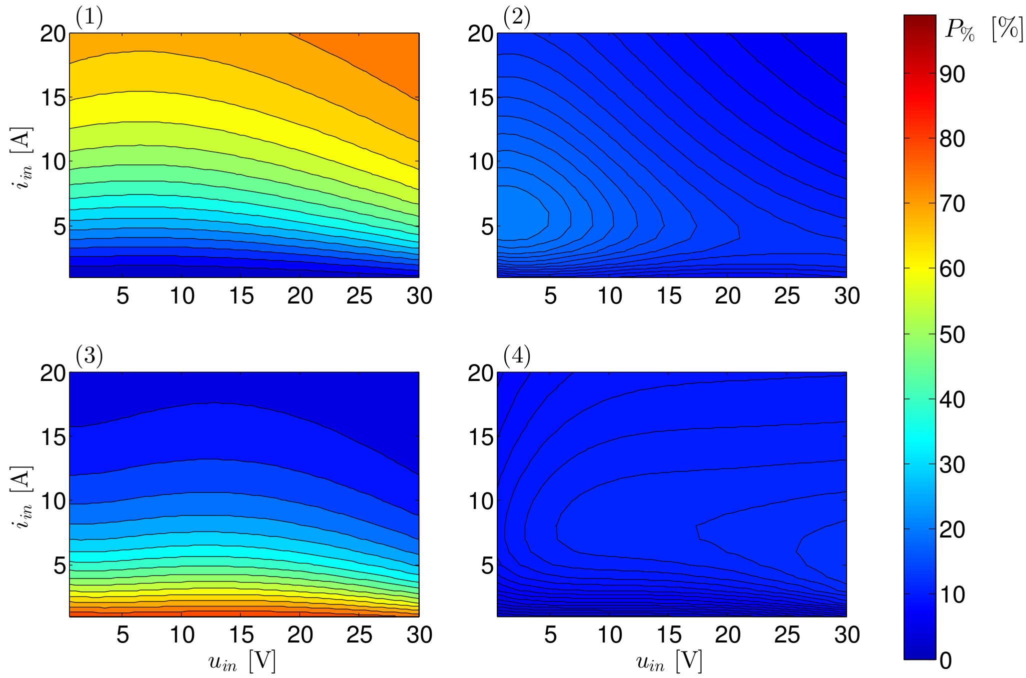

Figure A.38.: Separated losses of the boost-buck converter for $u_{C_2} = 42$ V and $e_{bl} = 24$ V.

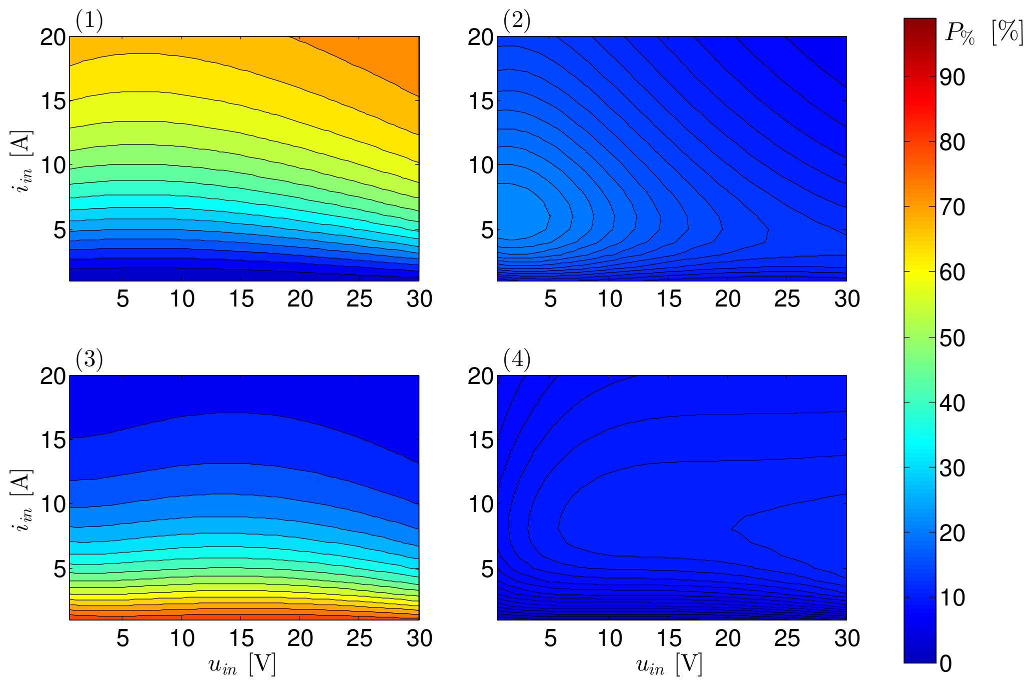

Figure A.39.: Separated losses of the boost-buck converter for $u_{C_2} = 48$ V and $e_{bl} = 24$ V.

A.3.6. Relative Losses and Efficiency for 48 V Vehicle Voltage Supply

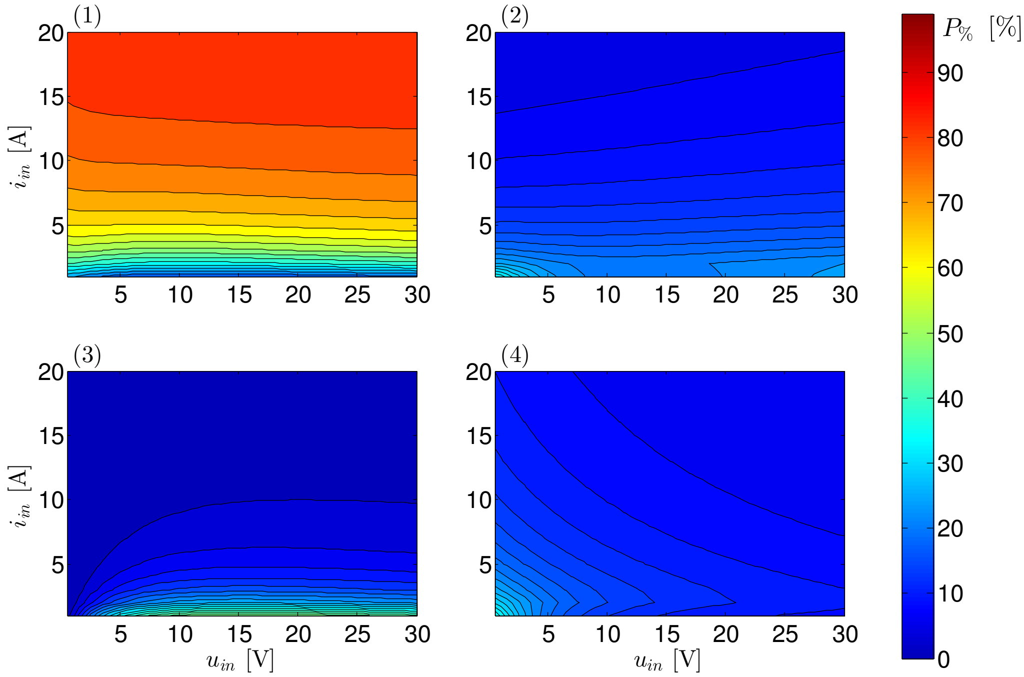

Figure A.40.: Separated losses of the buck-boost converter for $e_{bl} = 48$ V.

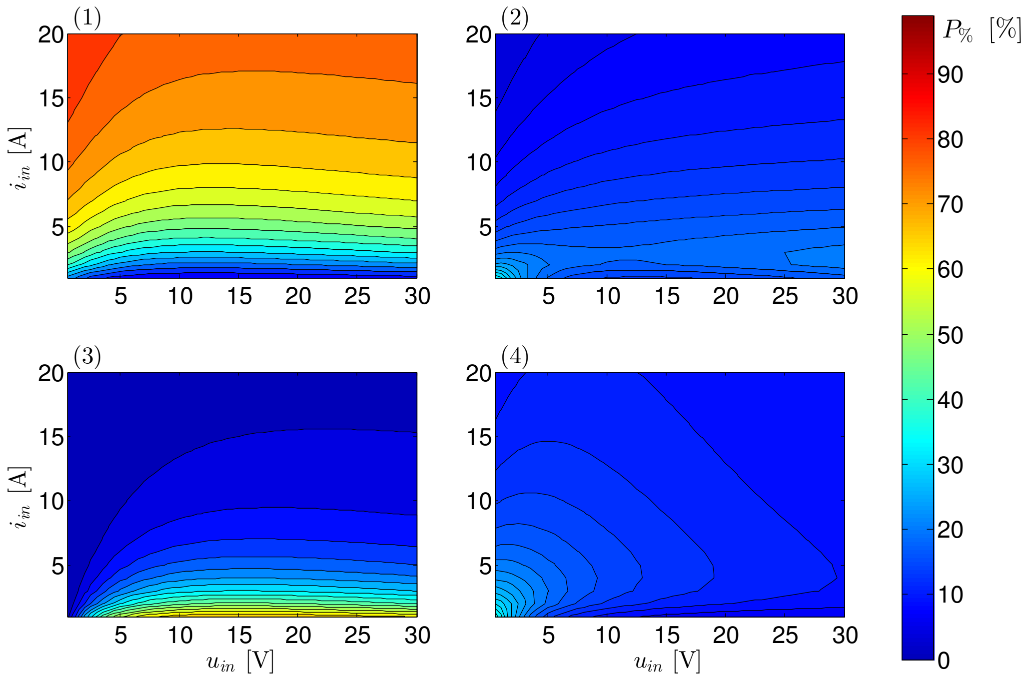

Figure A.41.: Separated losses of the Ćuk converter for $e_{bl} = 48$ V.

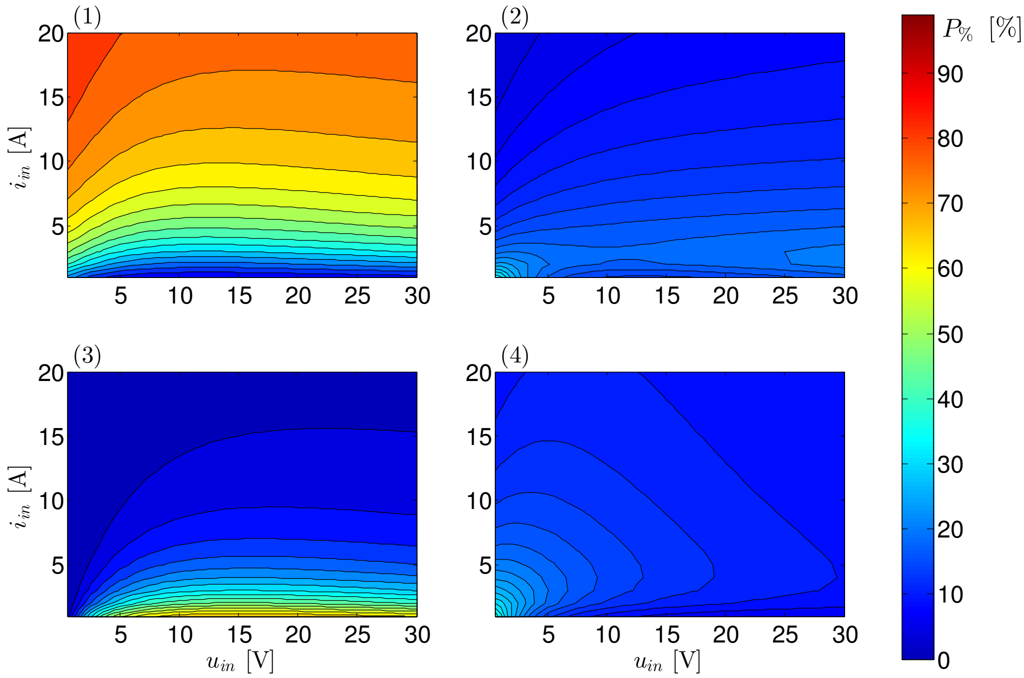

Figure A.42.: Separated losses of the SEPIC converter for $e_{bl} = 48$ V.

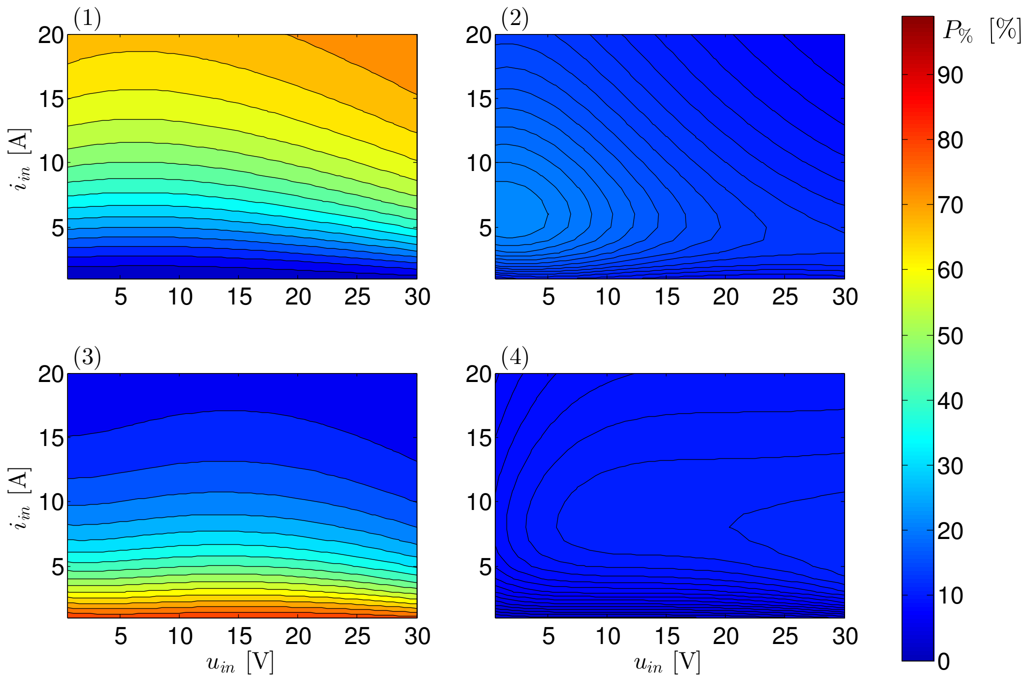

Figure A.43.: Separated losses of the boost-buck converter for $u_{C_2} = 48$ V and $e_{bl} = 48$ V.

A.3.7. Performance Level of Converters

In this subsection, the mean power loss $\overline{P}$ and the maximum values of the power loss P^+ from Appendix A.3.1 - A.3.6 are summarized in tables. The loss are separated in the ohmic loss P_{dc}, the switch loss P_{sw} (inclusive the driver loss), the inductor loss P_{ind}, and the synchronous switch loss $P_{sw,sy}$. Furthermore, the mean efficiency $\overline{\eta}$ and the maximum efficiency η^+ are summarized.

Nominal Vehicle Voltage Supply 12 V

converter	$\overline{P}_{dc}$ [W]	$\overline{P}_{sw}$ [W]	$\overline{P}_{ind}$[W]	$\overline{P}_{sw,sy}$[W]
BuBo	28.773	2.857	0.798	2.773
Ćuk	19.674	2.886	1.579	2.905
SEPIC	19.673	2.886	1.579	2.905
$\text{BoBu}\vert_{u_{C_2}=30\text{ V}}$	13.819	1.688	1.756	2.310
$\text{BoBu}\vert_{u_{C_2}=36\text{ V}}$	13.832	2.047	2.512	2.310
$\text{BoBu}\vert_{u_{C_2}=42\text{ V}}$	13.792	2.406	3.213	2.310
$\text{BoBu}\vert_{u_{C_2}=48\text{ V}}$	13.736	2.766	3.838	2.311

Table A.1.: Mean losses of converters for $e_{bl} = 12$ V.

converter	P^+_{dc} [W]	P^+_{sw} [W]	P^+_{ind} [W]	$P^+_{sw,sy}$ [W]
BuBo	135.262	10.304	1.879	9.856
Ćuk	93.928	10.750	3.698	10.578
SEPIC	93.921	10.750	3.698	10.578
$\text{BoBu}\vert_{u_{C_2}=30\text{ V}}$	60.151	3.411	2.222	7.827
$\text{BoBu}\vert_{u_{C_2}=36\text{ V}}$	60.938	4.156	3.144	7.817
$\text{BoBu}\vert_{u_{C_2}=42\text{ V}}$	61.109	4.901	4.124	7.815
$\text{BoBu}\vert_{u_{C_2}=48\text{ V}}$	61.023	5.648	5.168	7.816

Table A.2.: Maximum value of losses for $e_{bl} = 12$ V.

converter	$\overline{P}_{\%_{dc}}$	$\overline{P}_{\%_{sw}}$	$\overline{P}_{\%_{ind}}$	$\overline{P}_{\%_{sw,sy}}$
BuBo	0.499	0.228	0.192	0.081
Ćuk	0.397	0.217	0.307	0.079
SEPIC	0.396	0.216	0.308	0.080
$\mathrm{BoBu}\vert_{u_{C_2}=30\ \mathrm{V}}$	0.565	0.109	0.205	0.121
$\mathrm{BoBu}\vert_{u_{C_2}=36\ \mathrm{V}}$	0.527	0.120	0.244	0.110
$\mathrm{BoBu}\vert_{u_{C_2}=42\ \mathrm{V}}$	0.490	0.130	0.272	0.102
$\mathrm{BoBu}\vert_{u_{C_2}=48\ \mathrm{V}}$	0.471	0.140	0.292	0.017

Table A.3.: Mean relative losses of converters for $e_{bl} = 12$ V

converter	$P^{+}_{\%_{dc}}$	$P^{+}_{\%_{sw}}$	$P^{+}_{\%_{ind}}$	$P^{+}_{\%_{sw,sy}}$
BuBo	0.858	0.362	0.511	0.361
Ćuk	0.862	0.347	0.705	0.370
SEPIC	0.861	0.348	0.705	0.369
$\mathrm{BoBu}\vert_{u_{C_2}=30\ \mathrm{V}}$	0.827	0.187	0.817	0.180
$\mathrm{BoBu}\vert_{u_{C_2}=36\ \mathrm{V}}$	0.808	0.197	0.837	0.151
$\mathrm{BoBu}\vert_{u_{C_2}=42\ \mathrm{V}}$	0.786	0.209	0.848	0.130
$\mathrm{BoBu}\vert_{u_{C_2}=48\ \mathrm{V}}$	0.764	0.222	0.854	0.118

Table A.4.: Maximum value of relative losses for $e_{bl} = 12$ V.

converter	$\overline{\eta}$	η^{+}
BuBo	0.777	0.912
Ćuk	0.812	0.905
SEPIC	0.812	0.905
$\mathrm{BoBu}\vert_{u_{C_2}=30\ \mathrm{V}}$	0.821	0.949
$\mathrm{BoBu}\vert_{u_{C_2}=36\ \mathrm{V}}$	0.806	0.938
$\mathrm{BoBu}\vert_{u_{C_2}=42\ \mathrm{V}}$	0.794	0.926
$\mathrm{BoBu}\vert_{u_{C_2}=48\ \mathrm{V}}$	0.782	0.915

Table A.5.: Averaged and maximum efficiency of converter for $e_{bl} = 12$ V.

Nominal Vehicle Voltage Supply 24 V

converter	$\overline{P}_{dc}$ [W]	$\overline{P}_{sw}$ [W]	$\overline{P}_{ind}$[W]	$\overline{P}_{sw,sy}$[W]
BuBo	18.327	3.091	1.44	1.488
Ćuk	12.491	3.079	2.988	2.049
SEPIC	12.490	3.079	2.988	2.050
$\text{BoBu}\vert_{u_{C_2}=30\text{ V}}$	9.734	1.602	0.949	1.681
$\text{BoBu}\vert_{u_{C_2}=36\text{ V}}$	9.854	1.931	2.310	1.680
$\text{BoBu}\vert_{u_{C_2}=42\text{ V}}$	9.889	2.260	3.806	1.680
$\text{BoBu}\vert_{u_{C_2}=48\text{ V}}$	9.887	2.589	5.245	1.680

Table A.6.: Mean losses of converters for $e_{bl} = 24$ V.

converter	P^+_{dc} [W]	P^+_{sw} [W]	P^+_{ind}	$P^+_{sw,sy}$ [W]
BuBo	83.335	10.038	3.395	6.689
Ćuk	53.877	10.207	6.807	6.968
SEPIC	53.871	10.207	6.807	6.968
$\text{BoBu}\vert_{u_{C_2}=30\text{ V}}$	34.865	3.148	1.453	5.075
$\text{BoBu}\vert_{u_{C_2}=36\text{ V}}$	36.401	3.825	2.916	5.066
$\text{BoBu}\vert_{u_{C_2}=42\text{ V}}$	37.080	4.503	4.549	5.062
$\text{BoBu}\vert_{u_{C_2}=48\text{ V}}$	37.363	5.182	6.223	5.060

Table A.7.: Maximum value of losses for $e_{bl} = 24$ V.

converter	$\overline{P}_{\%_{dc}}$	$\overline{P}_{\%_{sw}}$	$\overline{P}_{\%_{ind}}$	$\overline{P}_{\%_{sw,sy}}$
BuBo	0.623	0.157	0.125	0.095
Ćuk	0.511	0.165	0.220	0.105
SEPIC	0.510	0.164	0.219	0.105
$\text{BoBu}\vert_{u_{C_2}=30\text{ V}}$	0.561	0.139	0.174	0.127
$\text{BoBu}\vert_{u_{C_2}=36\text{ V}}$	0.492	0.134	0.271	0.103
$\text{BoBu}\vert_{u_{C_2}=42\text{ V}}$	0.440	0.133	0.338	0.089
$\text{BoBu}\vert_{u_{C_2}=48\text{ V}}$	0.401	0.135	0.384	0.080

Table A.8.: Mean relative losses of converters for $e_{bl} = 24$ V.

converter	$P^+_{\%_{dc}}$	$P^+_{\%_{sw}}$	$P^+_{\%_{ind}}$	$P^+_{\%_{sw,sy}}$
BuBo	0.819	0.503	0.732	0.283
Ćuk	0.828	0.491	0.854	0.286
SEPIC	0.829	0.490	0.854	0.287
$\mathrm{BoBu}\vert_{u_{C_2}=30\text{ V}}$	0.806	0.241	0.780	0.213
$\mathrm{BoBu}\vert_{u_{C_2}=36\text{ V}}$	0.776	0.196	0.855	0.146
$\mathrm{BoBu}\vert_{u_{C_2}=42\text{ V}}$	0.738	0.183	0.890	0.118
$\mathrm{BoBu}\vert_{u_{C_2}=48\text{ V}}$	0.7023	0.181	0.913	0.103

Table A.9.: Maximum value of relative losses for $e_{bl} = 24$ V.

converter	$\overline{\eta}$	η^+
BuBo	0.812	0.915
Ćuk	0.826	0.909
SEPIC	0.826	0.908
$\mathrm{BoBu}\vert_{u_{C_2}=30\text{ V}}$	0.852	0.972
$\mathrm{BoBu}\vert_{u_{C_2}=36\text{ V}}$	0.824	0.956
$\mathrm{BoBu}\vert_{u_{C_2}=42\text{ V}}$	0.799	0.943
$\mathrm{BoBu}\vert_{u_{C_2}=48\text{ V}}$	0.776	0.932

Table A.10.: Averaged and maximum efficiency of converter for $e_{bl} = 24$ V.

Nominal Vehicle Voltage Supply 48 V

converter	$\overline{P}_{dc}$ [W]	$\overline{P}_{sw}$ [W]	$\overline{P}_{ind}$ [W]	$\overline{P}_{sw,sy}$ [W]
BuBo	12.632	4.006	2.513	1.555
Ćuk	9.372	3.992	5.074	1.566
SEPIC	9.371	3.992	5.074	1.566
$\text{BoBu}\|_{u_{C_2}=30\text{ V}}$ V	-	-	-	-
$\text{BoBu}\|_{u_{C_2}=36\text{ V}}$ V	-	-	-	-
$\text{BoBu}\|_{u_{C_2}=42\text{ V}}$ V	-	-	-	-
$\text{BoBu}\|_{u_{C_2}=48\text{ V}}$	8.381	2.574	1.550	1.366

Table A.11.: Mean losses of converters for $e_{bl} = 48$ V.

converter	P^{+}_{dc} [W]	P^{+}_{sw} [W]	P^{+}_{ind} [W]	$P^{+}_{sw,sy}$ [W]
BuBo	50.913	11.093	6.107	4.578
Ćuk	33.389	11.132	12.307	4.657
SEPIC	33.386	11.133	12.307	4.660
$\text{BoBu}\|_{u_{C_2}=30\text{ V}}$	-	-	-	-
$\text{BoBu}\|_{u_{C_2}=36\text{ V}}$	-	-	-	-
$\text{BoBu}\|_{u_{C_2}=42\text{ V}}$	-	-	-	-
$\text{BoBu}\|_{u_{C_2}=48\text{ V}}$	26.211	4.933	2.593	3.567

Table A.12.: Maximum value of losses for $e_{bl} = 48$ V.

converter	$\overline{P}_{\%_{dc}}$	$\overline{P}_{\%_{sw}}$	$\overline{P}_{\%_{ind}}$	$\overline{P}_{\%_{sw,sy}}$
BuBo	0.499	0.228	0.192	0.081
Ćuk	0.397	0.217	0.307	0.079
SEPIC	0.396	0.216	0.308	0.08
$\text{BoBu}\|_{u_{C_2}=30\text{ V}}$	-	-	-	-
$\text{BoBu}\|_{u_{C_2}=36\text{ V}}$	-	-	-	-
$\text{BoBu}\|_{u_{C_2}=42\text{ V}}$	-	-	-	-
$\text{BoBu}\|_{u_{C_2}=48\text{ V}}$	0.481	0.224	0.190	0.100

Table A.13.: Mean relative losses of converters for $e_{bl} = 48$ V.

converter	$P^{+}_{\%_{dc}}$	$P^{+}_{\%_{sw}}$	$P^{+}_{\%_{ind}}$	$P^{+}_{\%_{sw,sy}}$
BuBo	0.753	0.671	0.860	0.187
Ćuk	0.761	0.663	0.922	0.188
SEPIC	0.760	0.664	0.923	0.188
$\text{BoBu}\|_{u_{C_2}=30\text{ V}}$	-	-	-	-
$\text{BoBu}\|_{u_{C_2}=36\text{ V}}$	-	-	-	-
$\text{BoBu}\|_{u_{C_2}=42\text{ V}}$	-	-	-	-
$\text{BoBu}\|_{u_{C_2}=48\text{ V}}$	0.755	0.706	0.781	0.173

Table A.14.: Maximum value of relative losses for $e_{bl} = 48$ V.

converter	$\overline{\eta}$	η^{+}
BuBo	0.810	0.915
Ćuk	0.809	0.907
SEPIC	0.809	0.907
$\text{BoBu}\|_{u_{C_2}=30\text{ V}}$	-	-
$\text{BoBu}\|_{u_{C_2}=36\text{ V}}$	-	-
$\text{BoBu}\|_{u_{C_2}=42\text{ V}}$	-	-
$\text{BoBu}\|_{u_{C_2}=48\text{ V}}$	0.853	0.961

Table A.15.: Averaged and maximum efficiency of converter for $e_{bl} = 48$ V.

A.4. Parameters and Specifications of the Boost-Buck Converter Prototype

parameter	value	tolerance	component
L_1	45 μH	±%20	3 ×IHLP-6767GZ-11 15 μH (Vishay) (series)
L_2	24.6 μH	±%20	3 × IHLP-6767GZ-01 8.2 μH (Vishay) (series)
r_{L_1}	43.2 mΩ	–	-
r_{L_2}	31.98 mΩ	–	-
C_1	20 μF	±%20	2 × CGA9N 10 μF (TDK) (parallel)
C_2	88 μF	±%20	4 × CKG57N 22 μF (TDK) (parallel)
C_3	30 μF	±%20	3 × CGA9N 10 μF (TDK) (parallel)
r_{C_1}	1.2 mΩ	-	-
r_{C_2}	2.1 mΩ	-	-
r_{C_3}	0.8 mΩ	-	-
$S_1 - S_4$	–	-	IPP80N06S2L-07 (Infineon)
$r_{ds1} - r_{ds4}$	11.1 mΩ	-	-
$r_{g1} - r_{g4}$	1.5 Ω	-	-
$Driver$	-	-	UCC27201 (TI)
μC	-	-	TMS320F28069 (TI)
f_c	1 kHz	–	
f_{sw}	100 kHz	–	

Table A.16.: Parameters and specifications of the boost-buck converter prototype. The parameters are specified for 25 °C. The ESR values are obtained from the data sheets of the manufacturers.

A.5. Influence of Component Tolerance and Quantization Error

Different mismatches of assumed parameters of the hardware or inaccuracies of actuator and sensors can influence the efficiency of the development of the boost-buck converter. The following presents three potential factors which caused a mismatch between the analytical efficiency and the measured efficiency of the boost-buck converter.

- **PWM Quantization**
  The PWMs of the boost-buck converter are generated by a μC. The accuracy of PWM resolution depends on the hardware specification of μC. A quantization error of the PWMs results in a mismatch between the desired and the actual control signal for the MOSFETs. This can cause an error between the assumed and actual operation point of the converter. Consequently, this error results in a mismatch of the analytically caculated and the measured efficiency. In Figure A.44. the errors between the analytical efficiency of the converter with a simple quantization error of the duty cycle and the measured efficiency are presented.

- **Tolerance of Electrical Components**
  For the efficiency analysis of the developed boost-buck converter, the nominal values of the data sheets are selected by the manufacturers. The difference between the assumed and the actual parameters of the boost-buck converter results in a mismatch between the loss calculation and in the measured efficiency of the converter. In Figure A.44 the errors between the measured efficiency and the analytical efficiency of the converter with 20 % tolerance of the ohmic values from the capacitors, the inductors, and the MOSFETs are presented.

- **Tolerance and Quantization Error**
  Generally, there may be more than one fault at the same time. The efficiency of the combination with 20 % component tolerance and a simple quantization error of the boost-buck converter with the error between this efficiency map and the measured efficiency is presented in Figure A.46.

The characteristic error values of these three potential mismatches between analytical efficiency and measured efficiency are presented in Table A.17.

case	$\overline{\lvert e\rvert}$	$\lvert e\rvert^+$	$\overline{\lvert e_\%\rvert}$	$\lvert e_\%\rvert^+$
quantization error	0.03	0.10	3.86 %	17.37 %
tolerance	0.03	0.11	4.18 %	17.52 %
tolerance and quantization error	0.01	0.09	3.41 %	13.19 %

Table A.17.: Errors between the measured and the analytical efficiency of boost-buck converter with a variation of component values and quantization errors. $\overline{|e|}$ is the mean absolute error, $|e|^+$ is the maximal absolute error, $\overline{|e_\%|}$ is the mean absolute relative error, and$|e_\%|^+$ is the maximal absolute relative error.

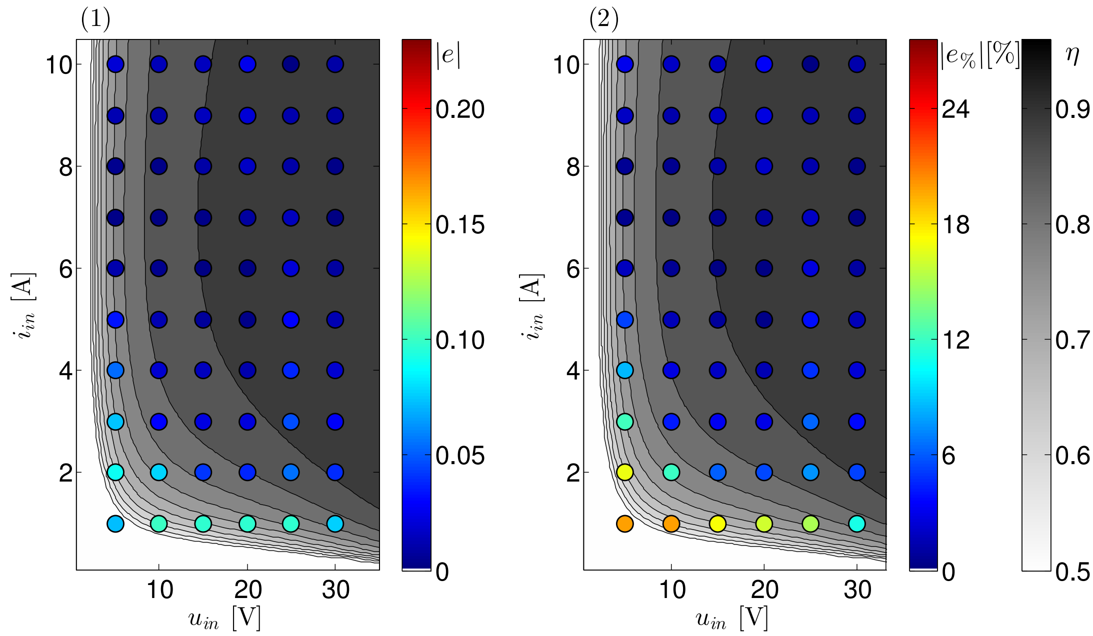

Figure A.44.: Comparison between the experimental measurement and the analytical efficiency model of the converter with a simple quantization error of the duty cycles from the converter. The dotted markers present the measurement points in relation to the error between the measurement and the model. (1) the absolute error e between the measurement and the model. (2) the relative error $e_{\%}$ between the measurement and the model.

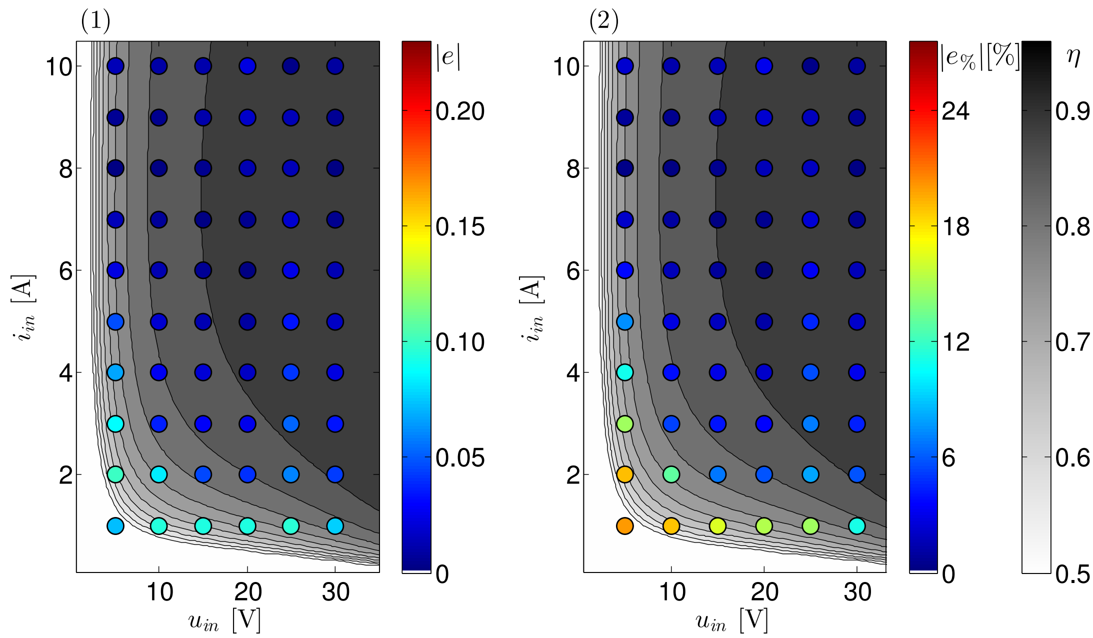

Figure A.45.: Comparison between the experimental measurement and the analytical efficiency model of the converter with 20 % tolerance of the ohmic values from the capacitors, the inductors, and the MOSFETs. The dotted markers present the measurement points in relation to the error between the measurement and the model. (1) the absolute error e between the measurement and the model. (2) the relative error $e_{\%}$ between the measurement and the model.

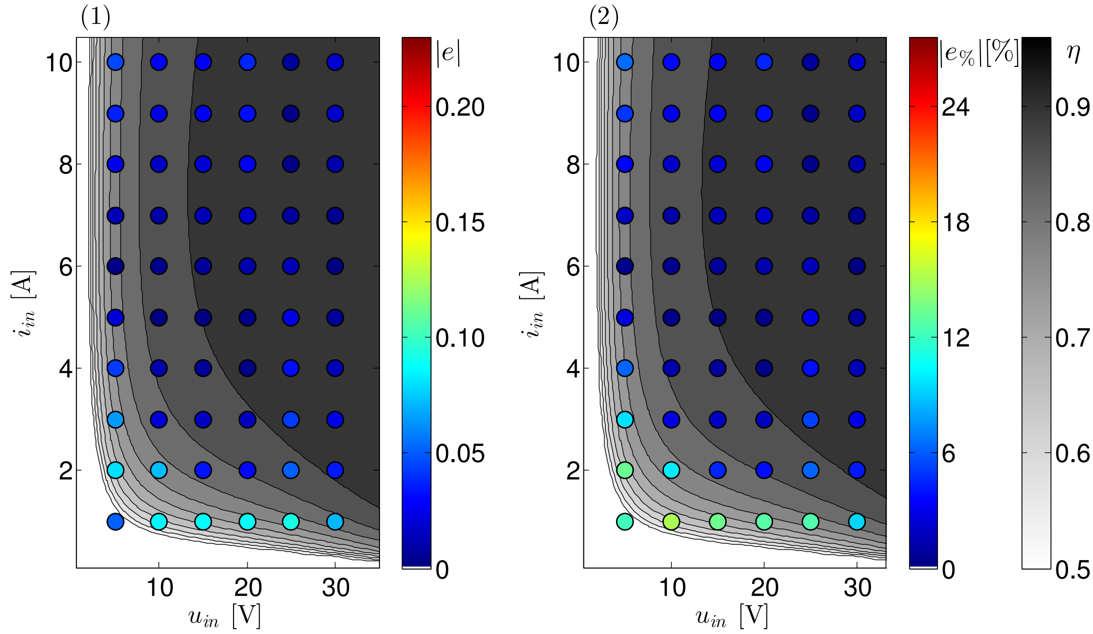

Figure A.46.: Comparison between the experimental measurement and the analytical efficiency model of the converter with 20 % tolerance of the ohmic values from the capacitors, the inductors, the MOSFETs, and a simple quantization error of the duty cycles. The dotted markers present the measurement points in relation to the error between the measurement and the model. (1) the absolute error e between the measurement and the model. (2) the relative error $e_{\%}$ between the measurement and the model.

A.6. Influence of Parameter Variations

The comparison between the Bode plots from the measurements and the model of the DC-DC converter with desired nominal parameters (see Table A.18) are presented in Figure A.47.
The confidential interval of the measurements is defined as the least significant bit voltage of ADC from the test bench. The RMS errors of amplitude and phase between measurements and simulations are presented in Table A.19.
The transfer functions of the DC-DC converter can be influenced through an incorrect assumption of the nominal parameters from the DC-DC converter. In case of an additional uncounted contact resistor of 80 mΩ the resistor value of the TEM results in $r_{tem} = 0.18\ \Omega$. The Bode plots from the measurements and the model of DC-DC converter with the uncounted contact resistor are presented in Figure A.48. The resulting RMS errors of amplitude and phase are presented in Table A.20. The difference between the transfer functions of the DC-DC converter for $r_{tem} = 0.1\ \Omega$ and $r_{tem} = 0.18\ \Omega$ are presented in Figure A.49.

operation point	value	operation point	value
U_{tem}	30 V	r_{tem}	0.1 Ω
E_{bl}	12.5 V	U_{C_1}	29.5 V
I_{L_1}	5 A	U_{C_2}	48 V
I_{L_2}	10.6 A	U_{C_3}	13.6 V
D_1	0.40	D_2	0.28
$\tilde{d}_1$	0.020	$\tilde{d}_2$	0.014

Table A.18.: Nominal parameters and specification of the boost-buck converter for the frequency analysis.

transfer function	e_{rms_a} [dB]	e_{rms_p} [°]
$G_{d_1 i_{L1}}$	1.27	7.23
$G_{d_1 u_{C3}}$	2.22	23.86
$G_{d_2 i_{L2}}$	2.61	6.62
$G_{d_2 u_{C2}}$	3.41	5.13

Table A.19.: RMS errors between the model and the measurement of the frequency analysis. The error of the amplitude is e_{rms_a} and of the phase is e_{rms_p}.

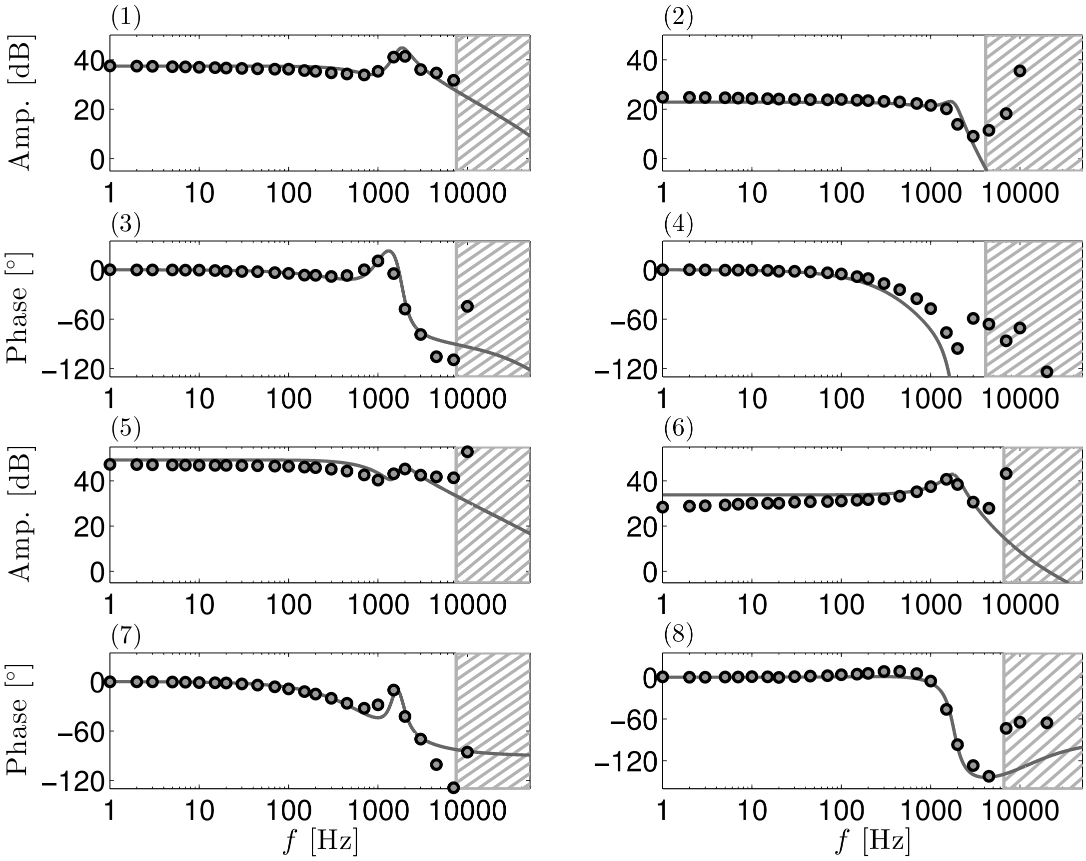

Figure A.47.: Bode plot of $G_{d_1 i_{L1}}$, $G_{d_1 u_{C3}}$, $G_{d_2 i_{L2}}$, $G_{d_2 u_{C2}}$ (black line) in relation to the experimental measurements (dotted markers). The amplitude and the phase of $G_{d_1 i_{L1}}$ are presented in (1) and (3). The amplitude and the phase of $G_{d_1 u_{C3}}$ are presented in (2) and (4). The amplitude and the phase of $G_{d_2 i_{L2}}$ are presented in (5) and (7). The amplitude and the phase of $G_{d_2 u_{C2}}$ are presented in (6) and (8). The measurements in the criss-cross gray are outside of the confidence interval.

transfer function	e_{rms_a} [dB]	e_{rms_p} [°]
$G_{d_1 i_{L1}}$	0.89	7.24
$G_{d_1 u_{C3}}$	1.82	23.25
$G_{d_2 i_{L2}}$	1.80	5.82
$G_{d_2 u_{C2}}$	5.29	7.78

Table A.20.: RMS errors between the model and the measurement of the frequency analysis with uncounted contact resistor. The error of the amplitude is e_{rms_a} and of the phase is e_{rms_p}.

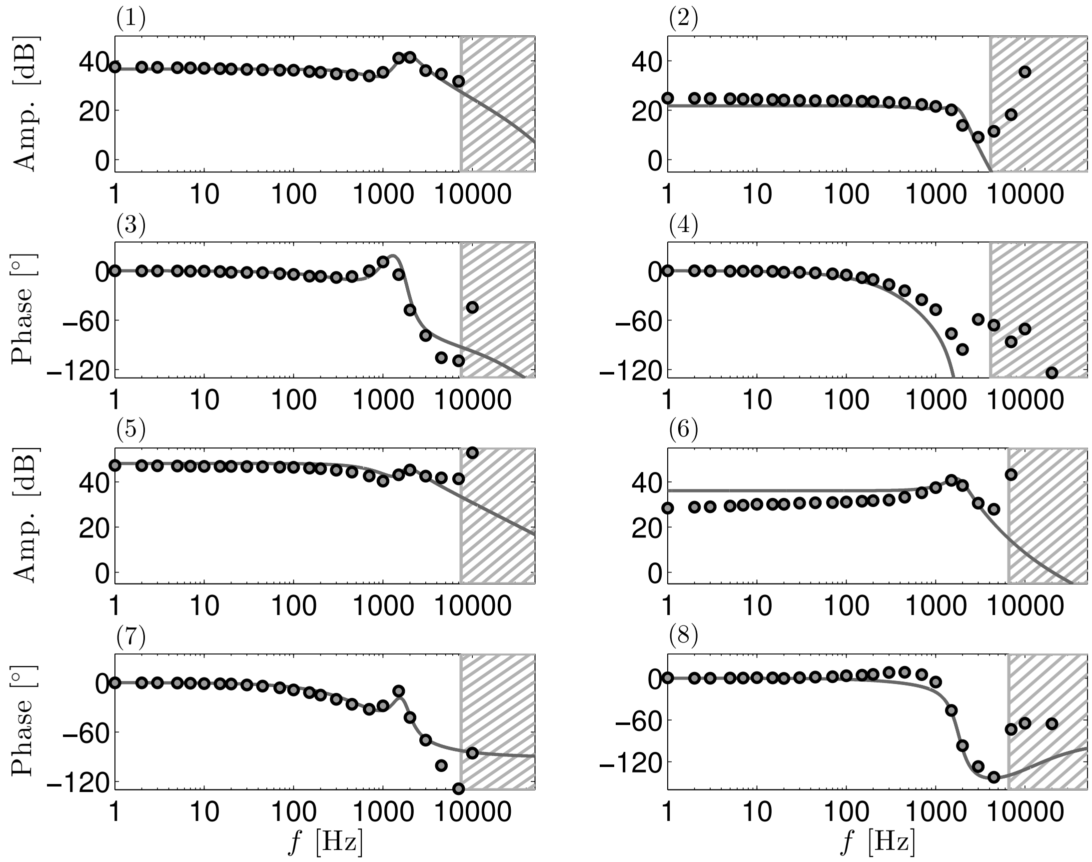

Figure A.48.: Bode plot of $G_{d_1 i_{L1}}$, $G_{d_1 u_{C3}}$, $G_{d_2 i_{L2}}$, $G_{d_2 u_{C2}}$ (black line) with additional contact resistor in relation to the experimental measurements results (dotted markers). The amplitude and the phase of $G_{d_1 i_{L1}}$ are presented in (1) and (3). The amplitude and the phase of $G_{d_1 u_{C3}}$ are presented in (2) and (4). The amplitude and the phase of $G_{d_2 i_{L2}}$ are presented in (5) and (7). The amplitude and the phase of $G_{d_2 u_{C2}}$ are presented in (6) and (8). The measurements in the criss-crossed gray area are outside of the confidence interval.

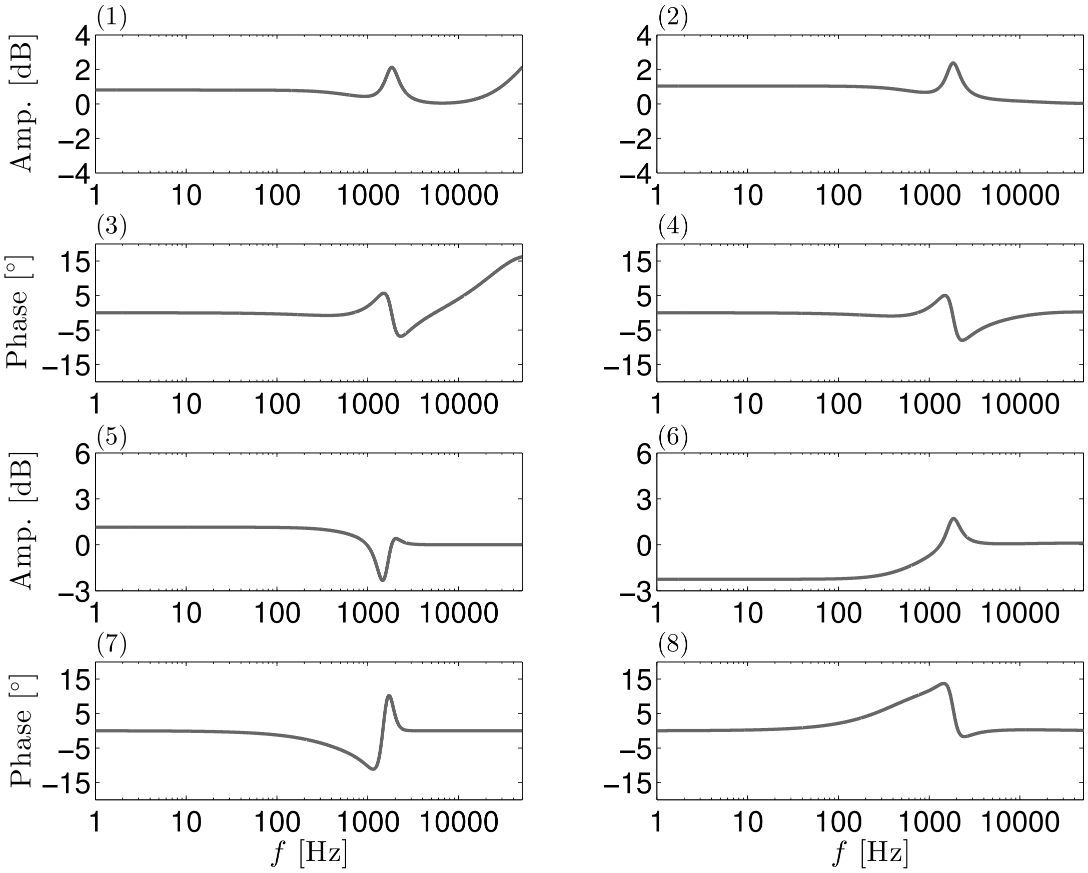

Figure A.49.: Difference between $G_{d_1 i_{L1}}$, $G_{d_1 u_{C3}}$, $G_{d_2 i_{L2}}$, $G_{d_2 u_{C2}}$ with $r_{tem} = 0.1\ \Omega$ and $r_{tem} = 0.18\ \Omega$. The error of amplitude and phase between $G_{d_1 i_{L1}}\big|_{r_{tem}=0.1\,\Omega}$ and $G_{d_1 i_{L1}}\big|_{r_{tem}=0.18\,\Omega}$ are presented in (1) and (3). The error of amplitude and phase between $G_{d_1 u_{C3}}\big|_{r_{tem}=0.1\,\Omega}$ and $G_{d_1 u_{C3}}\big|_{r_{tem}=0.18\,\Omega}$ are presented in (2) and (4). The error of amplitude and phase between $G_{d_2 i_{L2}}\big|_{r_{tem}=0.1\,\Omega}$ and $G_{d_2 u_{L2}}\big|_{r_{tem}=0.18\,\Omega}$ are presented in (5) and (7). The error of amplitude and phase between $G_{d_2 u_{C2}}\big|_{r_{tem}=0.1\,\Omega}$ and $G_{d_2 u_{C2}}\big|_{r_{tem}=0.18\,\Omega}$ are presented in (6) and (8).

A.7. Control Parameters

For the control design, the criterions in Table A.21 are selected. From these criterions, the control polynomials are determined (see Table A.22).

controller	f_o [Hz]	ξ	t_r [ms]
$C_{i_{L1}}$	500	0.95	1
$C_{i_{L2}}$	500	0.95	1
$C_{u_{C2}}$	100	0.95	5
$C_{u_{C3}}$	250	0.95	2.5

Table A.21.: Design parameters for the cascaded controllers. The natural frequency f_o and the damping factor ξ of the reference system $G_{CL}(s)$ for the closed loop polynomial of $T_{ry}(q^{-1})$ are presented. The equivalent rising time t_r of the closed loop is the time needed for the output signal to pass 10 % to 90 % of the reference value.

polynomials	coefficients
T_{i_1}	0.003
S_{i_1}	$1-0.713\,z^{-1}-0.288\,z^{-2}$
R_{i_1}	$0.017-0.021\,z^{-1}+0.007\,z^{-2}$
T_{u_3}	0.597
S_{u_3}	$1-0.868\,z^{-1}-0.132\,z^{-2}$
R_{u_3}	$13.150-21.714\,z^{-1}+9.161\,z^{-2}$
T_{i_2}	$5.02\cdot10^{-4}$
S_{i_2}	$1-0.777\,z^{-1}-0.204\,z^{-2}-0.019\,z^{-3}$
R_{i_2}	$0.002-0.003\,z^{-1}+0.002\,z^{-2}-5\cdot10^{-4}\,z^{-3}$
T_{u_2}	-0.234
S_{u_2}	$1-z^{-1}$
R_{u_2}	$-4.887+4.6526\,z^{-1}$

Table A.22.: Coefficients of designed control polynomials.

A.8. Vehicle Model

The vehicle can be assumed as a simple mass model (see Figure A.50). In order to accelerate the mass m of the vehicle to a desired speed $\mathbf{v}$, static and dynamic friction must be compensated. The whole fractional resistance $\mathbf{F}_r$ can simplified to

$$\mathbf{F}_r = \mathbf{F}_{ro} + \mathbf{F}_{air} + \mathbf{F}_{st} \ , \tag{A.81}$$

where $\mathbf{P}_r = \mathbf{F}_r\mathbf{v}$ is fractional resistance power. The rolling fraction $\mathbf{F}_{ro}$ is assumed as a static component:

$$\mathbf{F}_{ro} = c_{ro}\ m\ \mathbf{g} \tag{A.82}$$

Only the deformation of the wheels dynamically affects the friction, which is only significant for a soft underground and is neglected in this thesis. The coefficient c_{ro} depends on the underground and the wheels. Generally, this value is between 0.002 and 0.08. For the simulations in this thesis, $c_{ro} = 0.02$ is selected.
The air resistance $\mathbf{F}_{air}$ for a direct upstream flow is defined as:

$$\mathbf{F}_{air} = c_{air}\ A\ \rho\ \frac{\mathbf{v}^2}{2} \tag{A.83}$$

Due to the quadratic weighting of velocity, this fraction is the dominant value for higher speeds. For this reason, the drag coefficient c_{air} is an important factor which can be minimized by the aerodynamic design of the vehicle. Depending on the across area A of the vehicle, the c_{air} ranges between 0.25 and 0.4. The air density ρ is 1.18 kg m^{-3} at 25 °C. In this thesis, $c_{air} = 0.38$ and $A = 2.64$ m^2 is selected.
The third friction part is the slope friction

$$\mathbf{F}_{st} = m\ \mathbf{g} \sin\beta_s \ , \tag{A.84}$$

which is neglected in this thesis.
The actual necessary forces $\mathbf{F}_a$ to accelerate the mass without any friction is as follows:

$$\mathbf{F}_a = m\ \mathbf{a} \ , \tag{A.85}$$

where $\mathbf{a}$ is the acceleration. Consequently, the resulting necessary power to accelerate the vehicle to a velocity $\mathbf{v}$ is defined as:

$$\mathbf{P} = (\mathbf{F}_a + \mathbf{F}_r)\ \mathbf{v} \tag{A.86}$$

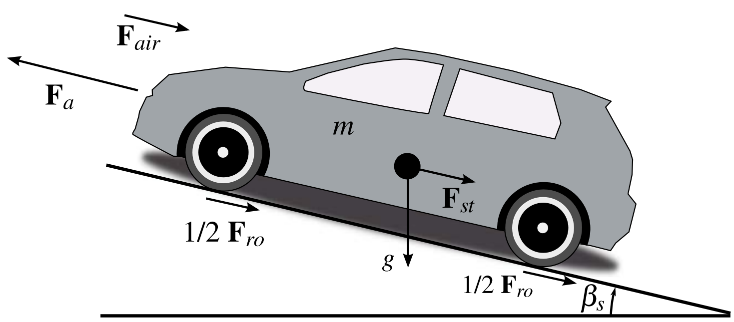

Figure A.50.: Forces of vehicle.

Finally, the required motor torque **M** follows to

$$\mathbf{M} = \frac{m\,\mathbf{a} + c_{ro}\,m\,\mathbf{g} + c_{air}\,A\,\rho\,\frac{\mathbf{v}^2}{2} + m\,\mathbf{g}\sin\beta_s}{2\pi n}\mathbf{v}\,, \tag{A.87}$$

which also can express with the mean effective pressure p_{me} for a four cylinder engine as

$$p_{me} = \frac{4\pi\mathbf{M}}{Vc}\,, \tag{A.88}$$

where Vc is the engine displacement.